ISSN 0911-5730
UVSOR-35
June 2008

UVSOR ACTIVITY REPORT 2007

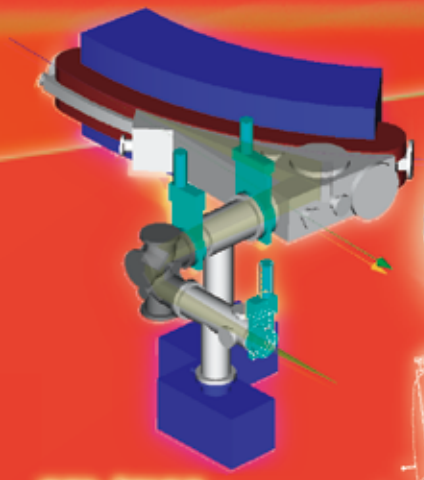

IR/THz Spectroscopy

UVSOR II since 2003

Multi Extreme Conditions

UVSOR Facility
Institute for Molecular Science
National Institutes of Natural Sciences

BL6B

UVSOR
ACTIVITY REPORT
2007

edited by
T. Ito, Y. Hikosaka, H. Hagiwara,

Preface

This Activity Report covers the research activities carried out at the UVSOR facility in FY2007 (April 2007-March 2008). This is the fifth volume in the new series for the third decade of UVSOR, corresponding to the fifth year of the use of the low-emittance UVSOR-II storage ring. The UVSOR-II ring has been very stable in operation at the initial beam current of 350 mA for every 6-hour 0.75-GeV full-energy injection and the beam emittance of 27 nm-rad for these three years. We will start the top-up operation as a daily routine soon in FY2008.

The UVSOR facility is exclusively responsible for the high-brilliant VUV light source as a low-energy third generation ring of the three major SR facilities (SPring-8 and Photon Factory) which are supported by the Ministry of Education, Culture, Sports, Science and Technology (MEXT). There are four 4 m-long long straight sections and four 1.5 m-long short straight sections in the present UVSOR-II ring of 53 m in circumference. We already installed three long undulators at BL3U, BL5U and BL7U, all of which are internationally competitive beamlines. We are now constructing a new short-undulator beamline BL6U. After successful beamline commissioning of BL6U, in order to keep the total number of beamlines reasonable, we will shut down a dipole beamline BL8B1 covering the same photon energy range. The next plan may be to construct BL1U with a long straight section after change of the injection point.

In UVSOR, we have four research positions for accelerator physics (1 full prof., 1 assoc. prof., and 2 assist. profs.) and four research positions for photophysics and photochemistry (2 assoc. profs. and 2 assist. profs.). In the accelerator physics division, there have been two vacancies for 1 assoc. prof. and 1 assist. prof. In addition, Assist. Prof. Dr. Akira Mochihashi moved to the SPring-8 accelerator team in August 2007. Fortunately, in March 2008, Dr. Masahiro Adachi joined the accelerator division as a new assistant professor from JAEA.

It is our pleasure to report two awards regarding outstanding achievements carried out in UVSOR (see this back page). In December 2007, Assist. Prof. Dr. Yasumasa Hikosaka of UVSOR was awarded The Young Scientist Award of the Physical Society of Japan for his multiple photoionization study of atoms and molecules. In April 2008, Prof. Dr. Takao Nanba of Kobe University and Assoc. Prof. Dr. Shin-ichi Kimura of UVSOR were awarded The Prize for Science and Technology, by Minister of MEXT Mr. Kisaburo Tokai, for their pioneering development of the highly brilliant infrared synchrotron radiation including realization of the world's first infrared beamline at UVSOR and its application to materials science.

We look forward to more exciting achivements in the coming years of UVSOR-II.

April, 2008

Nobuhiro Kosugi
Director of UVSOR

Professors Takao Nanba and Shin-ichi Kimura won The Prize for Science and Technology in Research Category, the Commendation for Science and Technology by the Minister of Education, Culture, Sports, Science and Technology.

Professor Takao NANBA of Kobe University and Associate Professor Shin-ichi KIMURA of UVSOR were awarded The Prize for Science and Technology in Research Category, the Commendation for Science and Technology by the Minister of Education, Culture, Sports, Science and Technology. The reasons of the prize are the development of the highly brilliant infrared synchrotron radiation including the realization of the world's first infrared beamline at UVSOR and applications to materials science.

The Young Scientist Award of The Physical Society of Japan Given to Dr. Yasumasa Hikosaka

Dr. Yasumasa HIKOSAKA, Assistant Professor at UVSOR, won the Young Scientist Award of the Physical Society of Japan in 2008, for his outstanding scientific achievements on “Multiple photoionization studies of atoms and molecules utilizing a multi-electron coincidence method”. Inner-shell photoionization of atoms and molecules produces a variety of multiply-charged ions that is energetically allowed. Coincidence observation of emitted electrons enables one to gain clear identification of the multiple photoionization process. Thanks to the successful results recently obtained by Dr. HIKOSAKA and his co-workers by introducing a magnetic bottle electron spectrometer, our knowledge on the mechanisms of the multiple photoionization has considerably deepened. Congratulations!

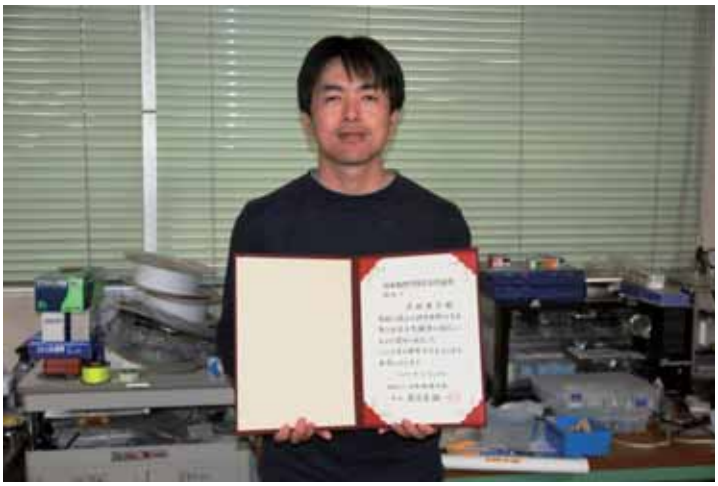

UVSOR Organization (April 1st, 2008)

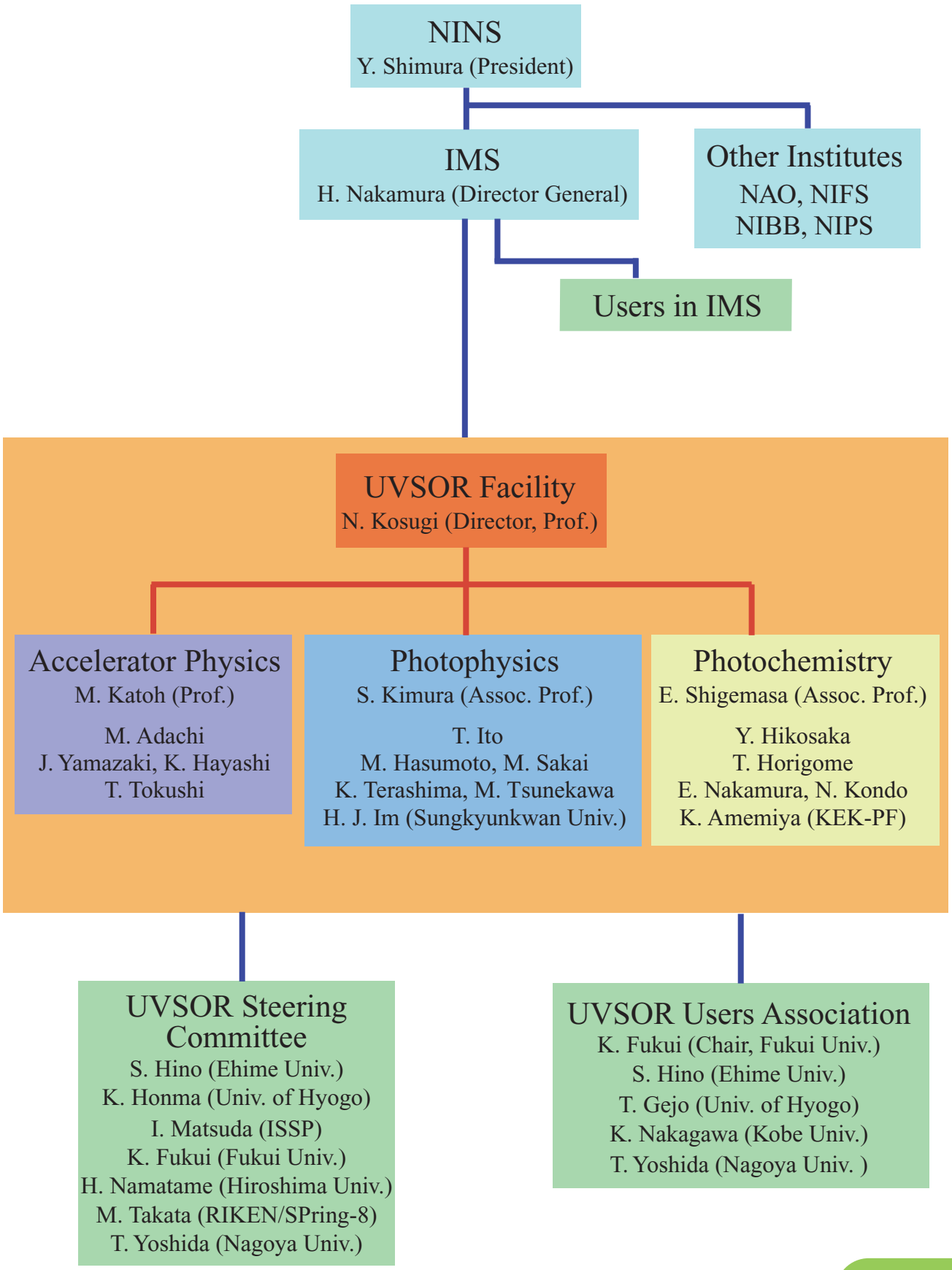

UVSOR Staff

Director

KOSUGI, Nobuhiro	Professor	kosugi@ims.ac.jp	

Light Source Division (Accelerator Physics)

KATOH, Masahiro	Professor	mkatoh@ims.ac.jp	
ADACHI, Masahiro	Assistant Professor	adachi@ims.ac.jp	(since Mar. 2008)
MOCHIHASHI, Akira	Assistant Professor		(until Aug. 2007)
YAMAZAKI, Jun-ichiro	Unit Chief Engineer	yamazaki@ims.ac.jp	
HAYASHI, Kenji	Engineer	h-kenji@ims.ac.jp	
SHIMADA, Miho	IMS Fellow (PD)		(until Mar. 2008)
TOKUSHI, Tetsuzyo	Supporting Engineer	tetsuzyo@ims.ac.jp	

Beamline Division (Photophysics)

KIMURA, Shin-ichi	Associate Professor	kimura@ims.ac.jp	
ITO, Takahiro	Assistant Professor	tito@ims.ac.jp	
HASUMOTO, Masami	Unit Chief Engineer	hasumoto@ims.ac.jp	
SAKAI, Masahiro	Engineer	sakai@ims.ac.jp	
TERASHIMA, Kensei	JSPS Fellow (PD)	kensei@ims.ac.jp	(since Apr. 2008)
IM, Hojun	Guest Researcher	hojun@ims.ac.jp	
SUMII, Ryohei	Guest Researcher		(until Sept. 2007)
TSUNEKAWA, Masanori	Guest Researcher	tsunekaw@ims.ac.jp	(since Mar. 2008)
SODA, Kazuo	Adjunct Professor		(until Mar. 2008)

Beamline Division (Photochemistry)

SHIGEMASA, Eiji	Associate Professor	sigemasa@ims.ac.jp	
HIKOSAKA, Yasumasa	Assistant Professor	hikosaka@ims.ac.jp	
HORIGOME, Toshio	Facility Chief Engineer	horigome@ims.ac.jp	
NAKAMURA, Eiken	Unit Chief Engineer	eiken@ims.ac.jp	
KONDO, Naonori	Engineer	nkondo@ims.ac.jp	
KANEYASU, Tatsuo	IMS Fellow (PD)		(until Mar. 2008)
AMEMIYA, Kenta	Adjunct Associate Professor		(since Apr. 2008)

Secretary

HAGIWARA, Hisayo		hagiwara@ims.ac.jp	

Graduate Students

MIZUNO, Takafumi	Grad. Univ. Adv. Studies	tmizuno@ims.ac.jp	
MIYAZAKI , Hidetoshi	Nagoya Univ.	hmiyazak@ims.ac.jp	
IIZUKA, Takuya	Grad. Univ. Adv. Studies	takuizk@ims.ac.jp	
TANIKAWA, Takanori	Grad. Univ. Adv. Studies	tanikawa@ims.ac.jp	
KOIKE, Masashi	Nagoya Univ.		
SUZUKI, Yasuhiro	Nagoya Univ.		
YOSHIDA, Mitsuhiro	Nagoya Univ.		
HASE, Atsumune	Nagoya Univ.		
FURUI, Yuta	Nagoya Univ.		
ITO, Masahiro	Niigata Univ.		(until Mar. 2008)

Visiting Scientists

SIMON, Marc	LCPMR, France	(Mar. 2007)
GUILLEMIN, Reaud	LCPMR, France	(Mar. 2007)
KWON, Yong-Seung	Sungkyunkwan Univ., Korea	(July-Aug. 2007, Jan 2008)
LEE, Kyeng Eun	Sungkyunkwan Univ., Korea	(July 2007, Jan 2008)
SONG, Yun Young	Sungkyunkwan Univ., Korea	(July-Aug. 2007)
LEE, Yunsang	Sungkyunkwan Univ., Korea	(July 2007)
BIELAWSKI, Serge	Lille Univ., France	(Sept.-Oct. 2007)
SZWAJ, Christophe	Lille Univ., France	(Sept.-Oct. 2007)
ELAND, John	University of Oxford, UK	(Oct.-Nov. 2007)
FENG, Donglai	Fudan University, P. R. China	(Dec. 2007)
SHEN, Dawei	Fudan University, P. R. China	(Dec. 2007)
WEI, Jia	Fudan University, P. R. China	(Dec. 2007)
COUPRIE, Marie-Emmanuelle	SOLEIL, France	(Dec. 2007)
LABAT, Marie	SOLEIL, France	(Dec. 2007)

UVSOR Steering Committee

KOSUGI, Nobuhiro	UVSOR, IMS	Chair
KIMURA, Shin-ichi	UVSOR, IMS	
KATOH, Masahiro	UVSOR, IMS	
SHIGEMASA, Eiji	UVSOR, IMS	
SODA, Kazuo	Nagoya Univ. (Adj. Prof., IMS)	(until Mar. 2008)
AMEMIYA, Kenta	KEK-PF (Adj. Assoc. Prof., IMS)	(since Apr. 2008)
YOKOYAMA, Toshihiko	IMS	
OHMORI, Kenji	IMS	
NAKAMURA, Toshikazu	IMS	
MITSUKE, Koichiro	IMS	
KAKIZAKI, Akito	Univ. of Tokyo	(until Mar. 2008)
MASE, Kazuhiko	KEK-PF	(until Mar. 2008)
YOSHIDA, Hisao	Nagoya Univ.	(until Mar. 2008)
TAKATA, Masaki	RIKEN/SPring-8	
NAMATAME, Hirofumi	Hiroshima Univ.	
HONMA, Kenji	Univ. of Hyogo	
HINO, Shojun	Ehime Univ.	
MATSUDA, Iwao	Univ. of Tokyo	(since Apr. 2008)
FUKUI, Kazutoshi	Fukui Univ.	(since Apr. 2008)
YOSHIDA, Tomoko	Nagoya Univ.	(since Apr. 2008)

Light Source in 2007

Masahiro KATOH

UVSOR Facility, Institute for Molecular Science

1. Status of UVSOR-II

In the fiscal year 2007, we have operated the UVSOR-II accelerators from April ’07 to March ’08. We had totally 36 weeks for the users operation, 34 weeks in multi-bunch mode and 2 weeks in single-bunch mode. We had 9 weeks dedicated for machine studies, although one week was canceled as described later. The monthly statistics of the operation time and the integrated beam current are shown in Figure 1.

The weekly operation schedule is as follows. On Monday, the machine is operated for machine studies. From Tuesday to Friday, the machine is operated for users, from 9am to 9pm. The beam injection is twice a day, at 9am and 3pm. The filling beam current is 350 mA in the multi-bunch mode and 100 mA in the single bunch mode. Occasionally, we operate the machine after 9pm for beam-line conditioning, free electron laser experiments and so on.

In this fiscal year, we had no major reconstruction on accelerators. Thus, we only had short shut-downs for maintenance works and for holidays. We had three 1-week shut-down, in May, September and March, and two 2-week ones in August and around the New Years Day.

In this fiscal year, we had two rather serious troubles. In May, the power supply for the septum magnet of the storage ring was malfunctioned. Many power transistors were broken and it took about one week to recover. We exchanged a machine study week, which had been planned in the next week of this happening, with the users’ week. In October, we had a trouble on a booster synchrotron magnet. We had an electrical short of a bus bar of the bending magnet to the ground. It was partly melted down. Fortunately, it was recovered within a few days.

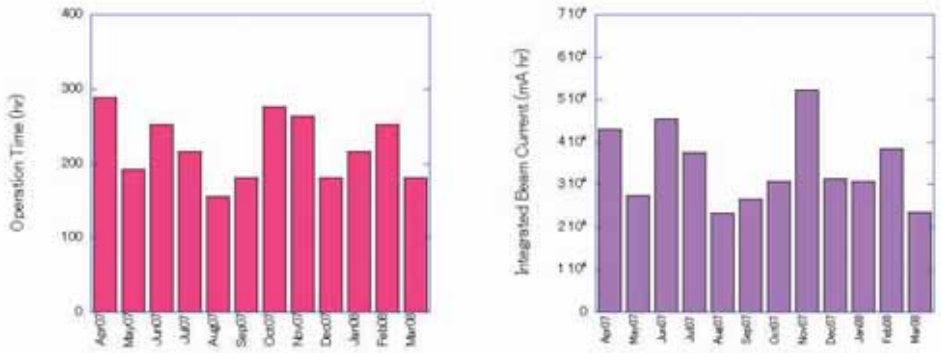

Fig. 1. Monthly statistics of the operation time (left) and of the integrated beam current (right).

2. Improvements

Full Energy Injection

The bending magnet power supply of the beam transport line was replaced in the last March, as shown in Figure 2. The new power supply is capable of transporting the full energy (750 MeV) beam to the storage ring. The power supplies of the booster synchrotron had been already replaced last year, to be compatible with the full energy acceleration.

In April, we have started testing the full-energy acceleration on the booster synchrotron, the beam transport and the injection to the storage ring [1]. In July, we have started operating the machine with the full-energy injection in the users' runs. The injection rate is about 0.5 mA/sec and to reach the filling current, 350 mA, it takes about 15 minutes. The repetition rate of the injection at 750 MeV was reduced to 1 Hz, which had been 3 Hz at 600 MeV, not to increase the peak electric power of the booster synchrotron. Even with this lower repetition rate, the total time required for the injection procedure is almost the same as before, partly because the acceleration on the storage ring was not necessary and also because we re-fill the electrons on the remaining electrons at the second injection of the day.

In the machine studies, we have tested the top-up injection. The electron beam current was successfully kept constant for more than 30 minutes, as shown in Figure 3. This was just a demonstration and there are many subjects that we must prepare before introducing this technique to the users' runs.

Fig. 2. New Magnet Power Supply for Bending Magnets on Beam Transport Line

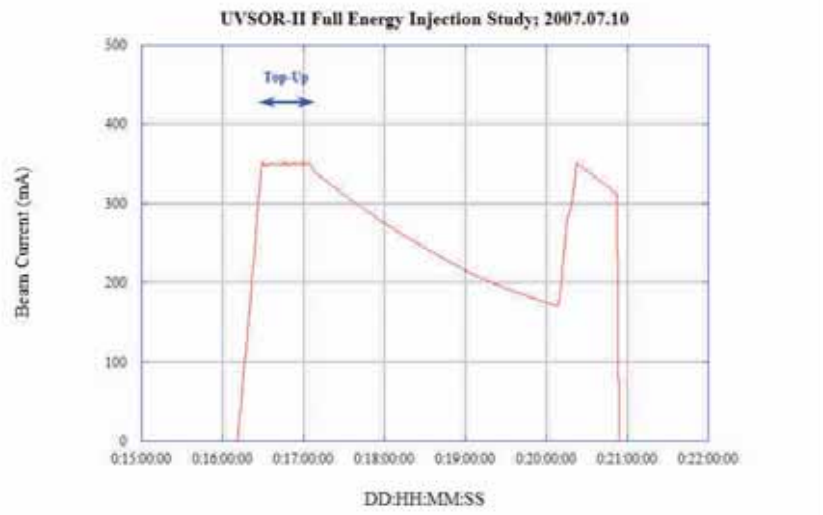

Fig. 3. Top-Up Operation Test. The beam current was kept constant for about 30 minutes.

Progress of New Undulator for BL7U

The new undulator for BL7U, a variable polarization undulator of APPLE-II type, is now opened for users. A feed-forward system to correct the orbit movement caused by the pole gap changes is successfully commissioned [2]. The orbit movement is corrected within 10 microns. The users can change the pole gap from the beam line anytime. They also can change the polarization at a fixed gap, 100 mm during the runs. A beam lifetime shortening is observed for vertically polarized mode, which may be caused by the non-linear effect of the undulator on the electron dynamics. Some sophisticated correction scheme should be introduced.

3. Researches and Developments

Free Electron Laser

The oscillating wavelength of the UVSOR-II Free Electron Laser is approaching the VUV region. In this fiscal year, an oscillation at 199 nm was realized, as shown in Figure 4 [3]. Laser oscillation around 190 nm, which seems promising, will be the target of the next fiscal year. By using this high power laser in deep UV region, some users' experiments are in progress [4].

To get coherent radiation in even shorter wavelength region, which seems hard to reach with the resonator type free electron laser, coherent harmonic generation (CHG) is under investigation, collaborating with French researchers. Coherent 3rd harmonics of Ti:Sa laser was successfully produced and the properties of the radiation and the mechanisms were investigated[5].

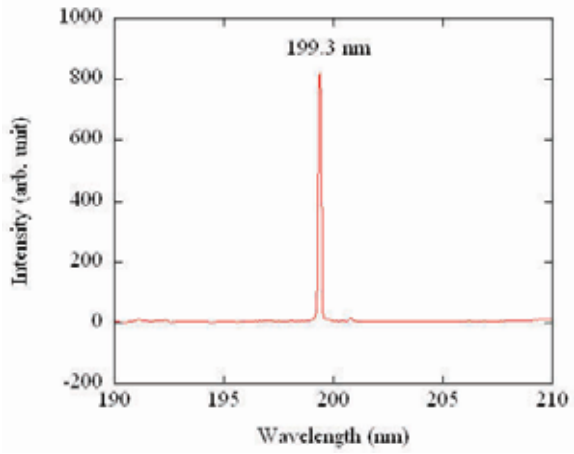

Fig. 4. Spectrum of the UVSOR-II Free Electron Laser at 199 nm

Laser Bunch Slicing

Terahertz coherent synchrotron radiation has been intensively studied by using laser bunch slicing technique [6]. In this scheme, ultra-short laser pulses are injected to the storage ring. As the result of the interaction between the laser pulses and an electron bunch in an undulator, a part of the electron bunch is energy-modulated. As this bunch is proceeding in the ring, the energy-modulated electrons escape from the interacting part of the bunch and finally a dip is created. Such an electron bunch emits coherent synchrotron radiation in the wavelength region longer than the dip width. If we use a femto-second laser pulse, we can create a dip of sub-millimeter width, which corresponds to the terahertz radiation wavelength. We have demonstrated that, by changing the laser pulse width, we could control the radiation spectra.

We have developed the laser slicing technique to produce periodic density structures by using amplitude modulated laser pulses [7]. We have succeeded in producing narrow-band coherent synchrotron radiation in the uniform magnetic field of the bending magnet. We have also demonstrated that we could control the spectral peak by changing the modulation frequency, and also that we could control the spectral width by changing the number of the modulation.

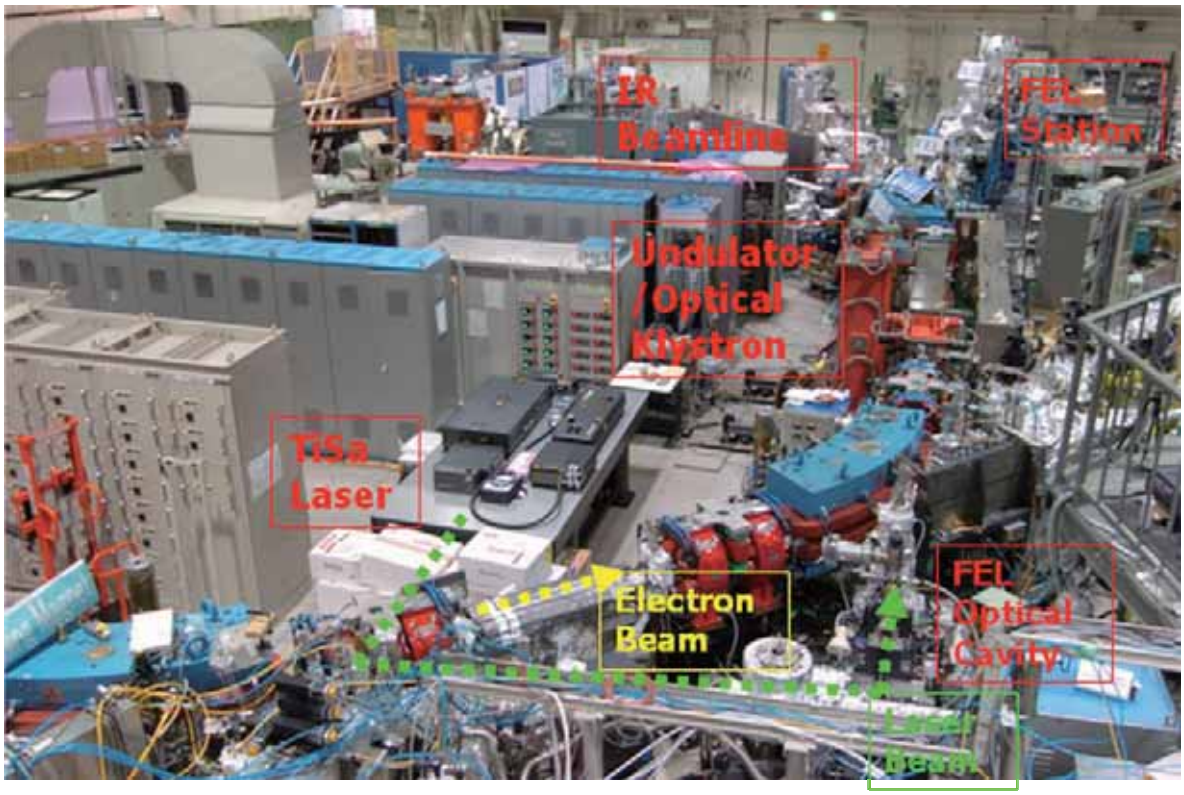

Fig. 5. Experimental set-up of the laser bunch slicing

REFERENCES

[1] A. Mochihashi et al., in this report

[2] K. Hayashi et al., in this report

[3] M. Hosaka et al., in this report

[4] K. Kobayashi et al., in this report

[5] M. Labat, M. Hosaka, A. Mochihashi, M. Shimada, M. Katoh, G. Lambert, T. Hara, Y. Takashima, M. E. Couprie, Euro. Phys. J. D Vol. 44, No. 1 (2007) 187-200

[6] M. Shimada et al., in this report

[7] M. Shimada et al., in this report

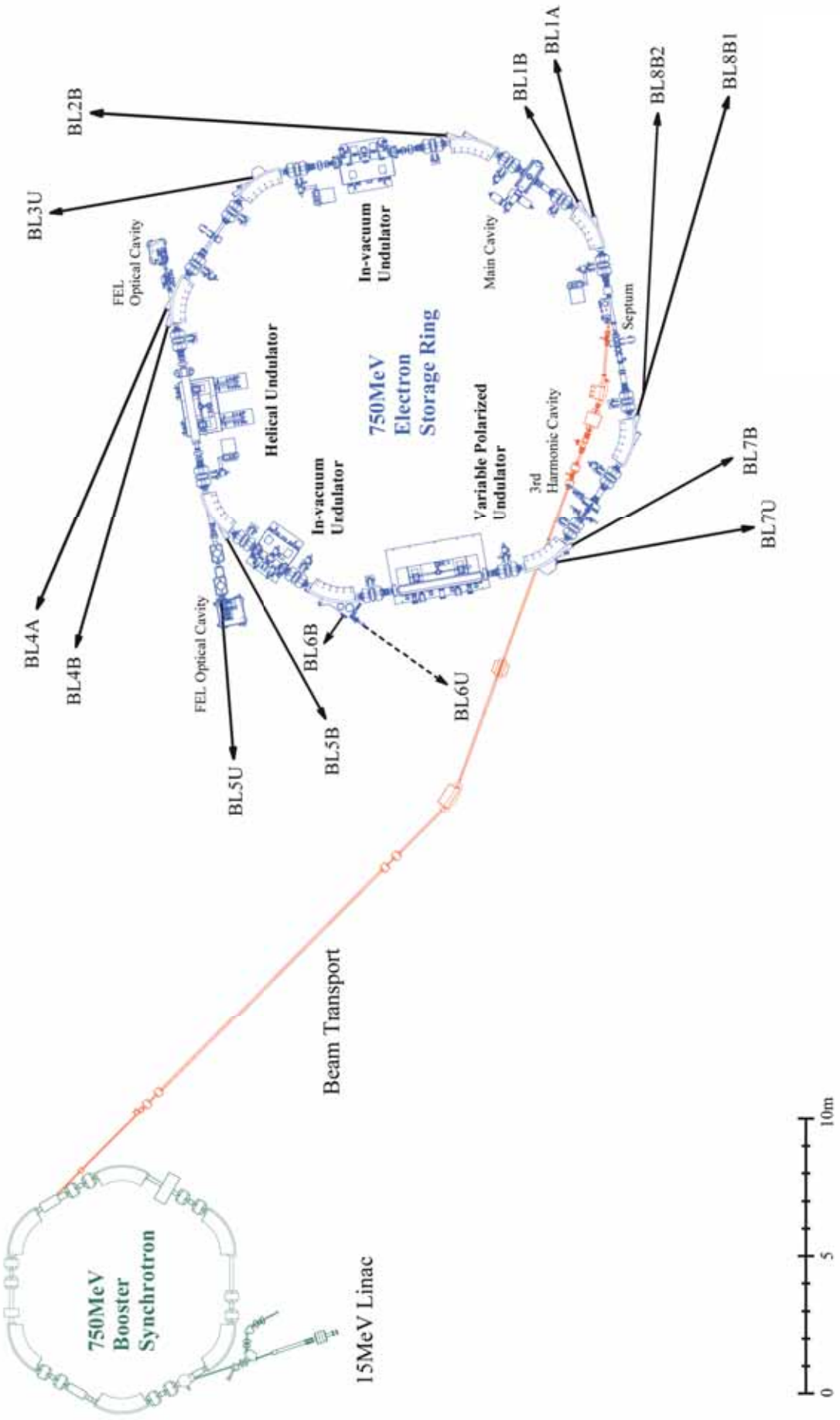
BL2B
BL3U
BL1B
BL1A
BL8B2
BL8B1
FEL Optical Cavity
In-vacuum Undulator
Main Cavity
Septum
Helical Undulator
750MeV Electron Storage Ring
3rd Harmonic Cavity
In-vacuum Urdulator
Variable Polarized Undulator
BL7B
BL7U
BL4A
BL4B
FEL Optical Cavity
BL6B
BL6U
BL5U
BL5B
Beam Transport
750MeV Booster Synchrotron
15MeV Linac
0
5
10m

Parameters of Injection Linear Accelerator

Energy	15 MeV
Length	2.5 m
Frequency	2856 MHz
Accelerating RF Field	2π/3 Traveling Wave
Klystron Power	1.8 MW
Energy Spread	~ 1.6 MeV
Repetition Rate	2.6 Hz

Parameters of Booster Synchrotron

Energy	750 MeV
Injection Energy	15 MeV
Beam Current	32 mA (uniform filling)
Circumference	26.6 m
RF Frequency	90.1 MHz
Harmonic Number	8
Bending Radius	1.8 m
Lattice	FODO × 8
Betatron Tune	
Horizontal	2.25
Vertical	1.25
Momentum Compaction	0.138
Repetition Rate	1 Hz (750 MeV)

Parameters of UVSOR-II Storage Ring

Energy	750 MeV
Injection Energy	750 MeV
Maximum Stored Current	500 mA (multi bunch) 100 mA (single bunch)
Natural Emittance	27.4 nm-rad
Circumference	53.2 m
RF Frequency	90.1 MHz
Harmonic Number	16
Bending Radius	2.2 m
Lattice	Extended DBA × 4
Straight Section	(4 m × 4) + (1.5 m × 4)
RF Voltage	100 kV
Betatron Tune	
Horizontal	3.75
Vertical	3.20
Momentum Compaction	0.028
Natural Chromaticity	
Horizontal	-8.1
Vertical	-7.3
Energy Spread	4.2×10^{-4}
Natural Bunch Length	108 ps

Electron Beam Optics of UVSOR-II Storage Ring

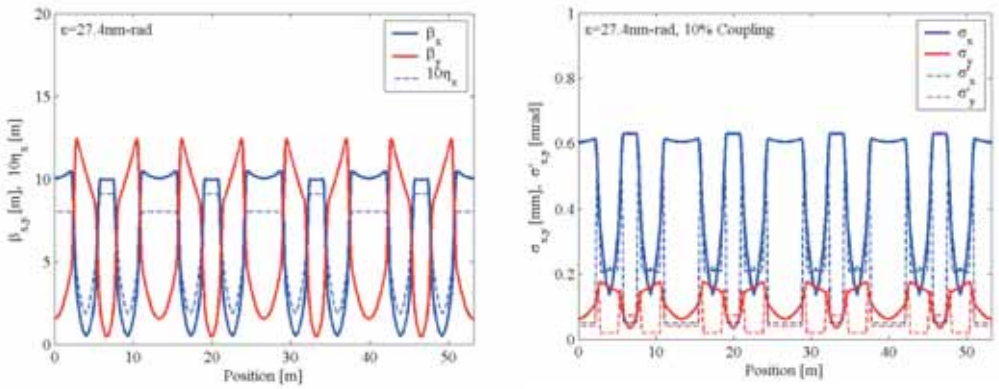

Horizontal/vertical betatron functions and dispersion function (left), and horizontal/vertical electron beam sizes and beam divergences (right) of UVSOR-II

Parameters of the insertion devices

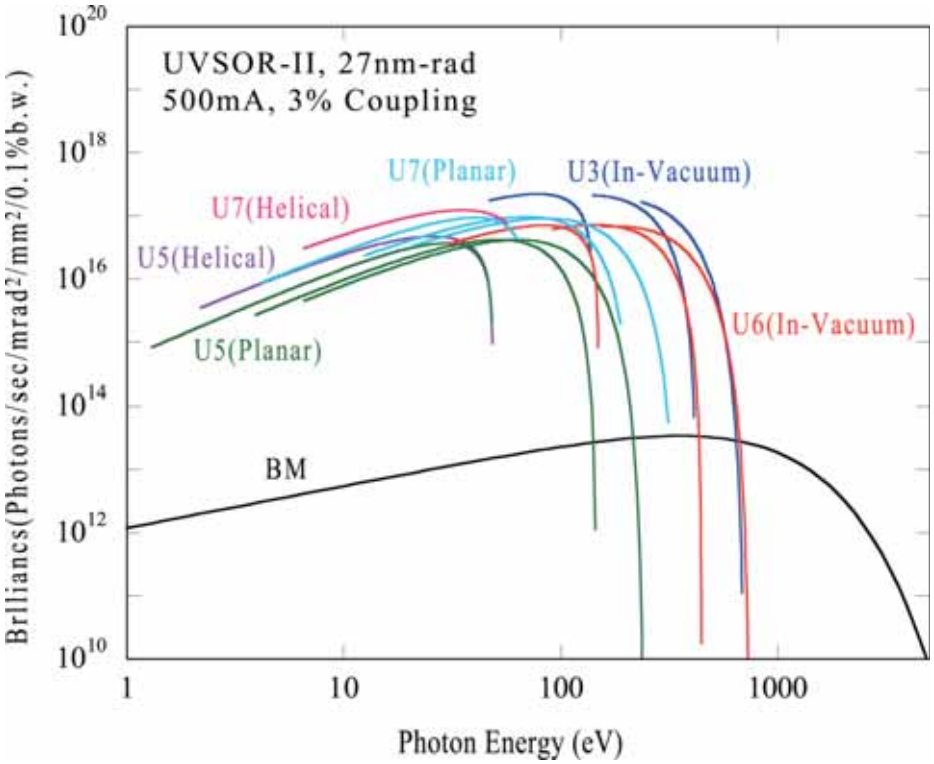

Brilliance of radiation from the insertion devices (U3, U5, U6 and U7) and a bending magnet of UVSOR-II

BL3U In-vacuum Undulator

Number of Periods	50
Period Length	38 mm
Pole Length	1.9 m
Pole Gap	15 - 40mm
Deflection Parameter	2.00 - 0.24

BL6U In-vacuum Undulator

Number of Periods	26
Period Length	36 mm
Pole Length	0.94 m
Pole Gap	15 - 40 mm
Deflection Parameter	1.78 - 0.19

BL5U Helical Undulator / Optical Klystron

Number of Periods	21 / 9+9(Opt. Kly.)
Period Length	110mm
Pole Length	2.35 m
Pole Gap	30 - 150 mm
Deflection Parameter	4.6 - 0.07(Helical) 8.5 - 0.15(Linear)

BL7U Apple-II variable polarization undulator

Number of Periods	40
Period Length	76mm
Pole Length	3.04 m
Pole Gap	24 - 200 mm
Deflection Parameter	5.4 (max. horizontal) 3.6 (max. vertical) 3.0 (max. helical)

Bending Magnets

Bending Radius	2.2 m
Critical Energy	425 eV

Beamlines in 2007

Eiji SHIGEMASA

UVSOR Facility, Institute for Molecular Science

Since the successful accomplishment of the upgrade project on the UVSOR storage ring (UVSOR-II project), in which the creation of four new straight sections and the achievement of much smaller emittance (27 nm-rad) were planned, the UVSOR facility has become one of the highest brilliance extreme-ultraviolet radiation sources among synchrotron radiation facilities with electron energy less than 1 GeV. Eight bending magnets and three insertion devices are available for utilizing synchrotron radiation at UVSOR. There is a total of fourteen operational beamlines in 2007, which are classified into two categories. Nine of them are so-called "Open beamlines", which are open to scientists of universities and research institutes belonging to the government, public organizations, private enterprises and those of foreign countries. The rest of the five beamlines are so-called "In-house beamlines", and are dedicated to the use of research groups within IMS. We have one soft X-rays station equipped with a double-crystal monochromator, seven extreme ultraviolet and soft X-rays stations with a grazing incidence monochromator, three vacuum ultraviolet stations with a normal incidence monochromator, one infrared (IR) station equipped with Fourier-Transform interferometers, one station with a multi-layer monochromator, and one non-monochromatized station for irradiation of white-light, as shown in the appended table for all available beamlines at UVSOR.

Keeping pace with the upgrade project, the improvements and upgrades of the beamlines at UVSOR have been continuously discussed with users in a series of UVSOR workshops. Newly constructed (BL3U) as well as upgraded (BL5U and BL6B) beamlines synchronized with the UVSOR-II project have routinely been operated, and a number of outcome has emerged through the utilization of these beamlines. Concerning the utilization for the long straight section between B06 and B07, a UVSOR workshop has been held in March 2005. A high resolution and high flux variable polarization beamline for spectroscopy in the VUV range has been proposed and possible scientific cases performed on this beamline have been discussed there. The construction of the new beamline BL7U has been completed during the regular summer shutdown in 2006 as planned. BL7U is composed of a modified Wadsworth-type monochromator with three interchangeable spherical gratings (R=10 m; 1200, 2400, and 3600 lines/mm), and a hemispherical photoelectron analyzer (MBS 'Peter' A-1), where high-resolution angle-resolved photoemission experiments can be performed. A new APPLE-II type undulator for the light source of BL7U has successfully been installed at the end of October 2006. Practical utilization by users at BL7U has begun, including a sort of performance tests for the experimental system by highly active and internationally appreciated users.

Regarding the utilization of the first in-vacuum type undulator, which has been relocated from the long straight section U7 to the short one between B05 and B06, a new project for constructing the undulator beamline BL6U has been initiated. BL6U will be initially prepared as an in-house beamline. The monochromator designed covers the photon energy ranging from 30 to 500 eV, with the resolving power higher than 10000 and the photon flux more than 10^{10} photons/sec. The practical construction of BL6U is expected to start from the summer of 2008. After the beamline commissioning of BL6U, BL4B will be allocated to an open beamline, and all users' activities continued at BL8B1 will be accepted at BL4B. Further serious discussion toward utilizing the

available straight sections most effectively and formulating a basic plan on the beamline construction, will be continued.

All users are required to refer to the beamline manuals and the UVSOR guidebook (the latest revision in PDF format was uploaded on the UVSOR web page in the summer of 2007), on the occasion of conducting the actual experimental procedures. Those wishing to use the open and in-house beamlines are recommended to contact the station master/supervisor and the representative, respectively. For updated information of UVSOR, http://www.uvsor.ims.ac.jp/.

Table I. Station masters and supervisors of open beamlines

Beamline	Station Master	Sub Master	Supervisor
1A	N. Kondo	E. Shigemasa	E. Shigemasa
1B	M. Hasumoto	S. Kimura	S. Kimura
5U	T. Ito	M. Sakai	S. Kimura
5B	M. Hasumoto	E. Nakamura	E. Shigemasa
6B	S. Kimura	E. Nakamura	S. Kimura
7U	T. Ito	M. Sakai	S. Kimura
7B	M. Hasumoto	S. Kimura	S. Kimura
8B1	Y. Hikosaka	E. Nakamura	E. Shigemasa
8B2	M. Tsunekawa	E. Nakamura	S. Kimura

Table II. Representatives of in-house beamlines

Beamline	Representative	Affiliation
2B	K. Mitsuke	Dep. Photo-Molecular Science
3U	N. Kosugi	Dep. Photo-Molecular Science
4A	T. Urisu	Dep. Life & Coordination-Complex Molecular Science
4B	E. Shigemasa	UVSOR

Beamlines at UVSOR-II

Beam-line	Monochromator, Spectrometer	Energy Region (eV)	Experiments	Beamline master
1A	Double-Crystal	600 eV – 4 keV	Solid (Absorption)	N. Kondo nkondo@ims.ac.jp
1B	1m Seya-Namioka	2 eV – 30 eV	Solid (Reflection, Absorption)	M. Hasumoto hasumoto@ims.ac.jp
2B	18m Spherical Grating (Dragon)	24 eV – 205 eV	Gas (Photoionization, Photodissociation)	K. Mitsuke mitsuke@ims.ac.jp
3U	Varied-Line-Spacing Plane Grating (Monk-Gillieson)	60 eV – 800 eV	Gas, Liquid, Solid (Absorption, Photoemission, Photon Emission)	N. Kosugi kosugi@ims.ac.jp
4A	Multi-Layered-Mirror	50 eV – 95 eV	Irradiation	T. Urisu urisu@ims.ac.jp
4B	Varied-Line-Spacing Plane Grating (Monk-Gillieson)	25 eV – 1 keV	Gas (Photoionization, Photodissociation) Solid (Photoemission)	E. Shigemasa sigemasa@ims.ac.jp
5U	Spherical Grating (SGM-TRAIN*)	5 eV – 250 eV	Solid (Photoemission)	T. Ito tito@ims.ac.jp
5B	Plane Grating	6 eV – 600 eV	Calibration Solid (Absorption)	M. Hasumoto hasumoto@ims.ac.jp
**6U	Variable-included-angle Varied-Line-Spacing Plane Grating	40 eV – 500 eV	Gas (Photoionization, Photodissociation) Solid (Photoemission)	E. Shigemasa sigemasa@ims.ac.jp
6B	Martin-Puplett FT-FIR Michelson FT-IR	2.5 eV – 0.1 meV	Solid (Reflection, Absorption)	S. Kimura kimura@ims.ac.jp
7U	10m Normal Incidence (Modified Wadsworth)	6 eV – 40 eV	Solid (Photoemission)	T. Ito tito@ims.ac.jp
7B	3m Normal Incidence	1.2 eV – 25eV	Solid (Reflection, Absorption)	M. Hasumoto hasumoto@ims.ac.jp
8B1	15m Constant Deviation Grazing Incidence	30 eV – 800eV	Solid (Absorption)	Y. Hikosaka hikosaka@ims.ac.jp
8B2	Plane Grating	1.9 eV – 150 eV	Solid (Photoemission)	M. Tsunekawa tsunekaw@ims.ac.jp
FEL	None	6.2 eV – 1.6 eV	Free Electron Laser	J. Yamazaki yamazaki@ims.ac.jp
CSR	None	5meV – 0.5meV	Coherent Synchrotton Radiation	M. Katoh mkatoh@ims.ac.jp

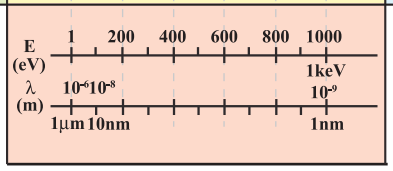

* Spherical Grating Monochromator with Translating and Rotating Assembly Including Normal incidence mount

**Under Construction

BL1A

Soft X-Ray Beamline for Photoabsorption Spectroscopy

BL1A is a soft X-ray beamline for photoabsorption spectroscopy. The beamline is equipped with a focusing premirror and a double crystal monochromator [1]. The monochromator serves soft X-rays in the energy region from 585 to 4000 eV by using several kinds of single crystals such as β-Al_2O_3, beryl, KTP ($KTiOPO_4$), quartz, InSb, and Ge. The throughput spectra measured by a Si photodiode (AXUV-100, IRD Inc.) are shown in Fig. 1. Typical energy resolution (E/ΔE) of the monochromator is about 1500 for beryl and InSb. There are no experimental setups specific of this beamline, except for a small vacuum chamber equipped with an electron multiplier (EM) detector. Photoabsorption spectra for powdery samples are usually measured in a total electron yield mode, with the use of the EM detector.

[1] Hiraya *at al*, Rev. Sci. Instrum. **63** (1992) 1264.

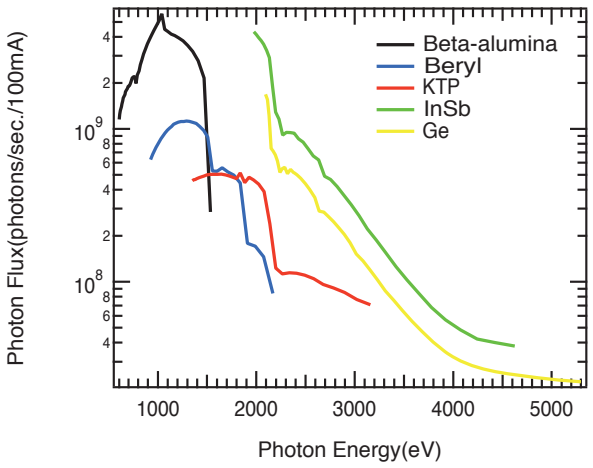

Fig. 1. Throughput spectra of the double crystal monochromator at BL1A.

Fig. 2. A side view of BL1A.

Beamline Specifications

Monochromator	Double crystal monochromator
Monochromator crystals: (2d value, energy range)	β-Al_2O_3 (22.53 Å, 585-1609 eV), beryl (15.965 Å, 826-2271 eV), KTP (10.95 Å, 1205-3310 eV), quartz (8.512 Å, 1550-4000 eV), InSb (7.481 Å, 1764-4000 eV), Ge (6.532 Å, 2094-4000 eV)
Resolution	E/ΔE = 1500 for beryl and InSb
Experiments	Photoabsorption spectroscopy

BL1B

Seya-Namioka Monochromator for General Purposes

BL1B has been constructed to perform various spectroscopic investigations such as absorption, reflectivity, and luminescence in condensed matters. This beamline consists of a pre-focusing mirror, a 1-m Seya-Namioka type monochromator, and post-focusing mirrors with different focal lengths. Three gratings of 600, 1200, and 2400 l/mm can cover the wavelength region ranging from 40 to 650 nm ($h\nu$ = 2 – 30 eV). The post mirror with a longer focal length is usually used with an LiF window to separate the vacuum condition of the monochromator from a main experimental station, which make experiments for liquids and bio-specimens possible, while the other is mainly utilized for solid-state spectroscopy. The output flux from this monochromator is about 10^{10} photons/sec. around 200 nm with 0.1 mm slit openings. The spectral distributions for two gratings measured by a conventional photomultiplyer are shown in Fig. 1. A second monochromator (Spex 270M) and a LN-cooled CCD detector (Princeton Inc.) are available for luminescence measurements, together with a liquid helium-flow type cryostat. To perform time-resolved experiments, a TAC system is also available.

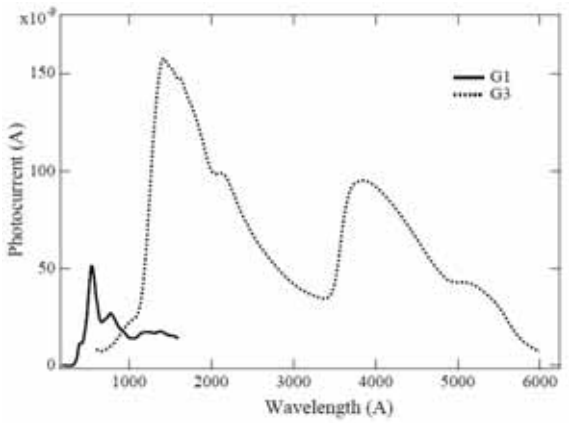

Fig. 1. Photocurrent at the sample position at BL1B.

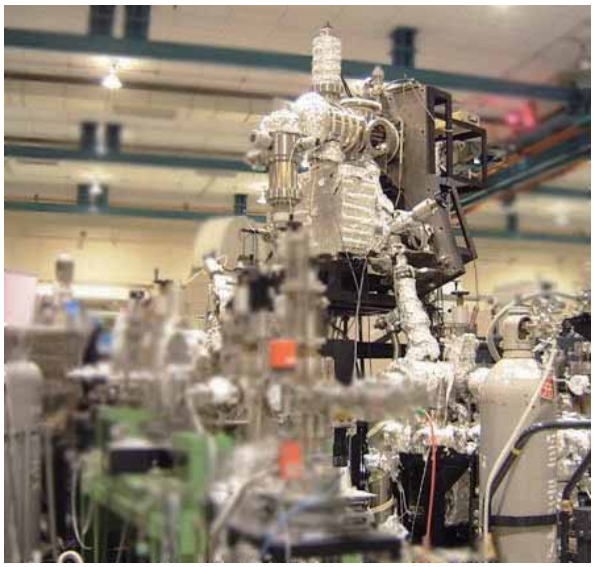

Fig. 2. Photo of BL1B.

Beamline Specifications

Monochromator	1-m Seya-Namioka type
Wavelength Range	40 to 600 nm (2-30 eV)
Resolution	E/ΔE~1000 at 100 nm (10 eV)
Experiment	Absorption, reflection, luminescence spectroscopy for solids

BL2B

Beamline for Gas Phase Photoionization and Reaction Dynamics

This beamline has been developed for the purpose of studying ionization, excitation and decay dynamics involving inner-valence electrons, 2*p* electrons of the third row atoms, and 4d electrons of the lanthanides. The monochromator is a spherical grating Dragon-type with 18-m focal length. High throughput (1×10^{10} photons s^{-1}) and high resolution ($E/\Delta E$ = 2000 - 8000) are achieved simultaneously under the condition of the ring current of 100 mA [1]. The optical system consists of two prefocusing mirrors, an entrance slit, three spherical gratings (G1 - G3), two folding mirrors, a movable exit slit and a refocusing mirror [2]. The monochromator is designed to cover the energy range of 23 - 205 eV with the three gratings: G1 (2400 lines mm^{-1}, R = 18 m) at 80 - 205 eV; G2 (1200 lines mm^{-1}, R = 18 m) at 40 - 100 eV; G3 (2400 lines mm^{-1}, R = 9.25 m) at 23 - 50 eV. The percentage of the second-order light contamination at $h\nu$ = 45.6 eV is 23 % for G2 or 7 % for G3.

We have been taking the yield curves of various fullerene ions [3]. Geometrical structures and electronic properties of fullerenes have attracted widespread attention because of their novel structures, novel reactivity, and novel catalytic behaviors as typical nanometer-size materials. However, spectroscopic information was very limited in the extreme UV region, owing to difficulties in acquiring enough amount of sample. This situation has been rapidly changed since the start of this century, because the techniques of syntheses, isolation, and purification have been advanced so rapidly that appreciable amount of fullerenes can be readily obtained.

Fig. 1. 18-m spherical grating monochromator at BL2B.

Fig. 2. End station of BL2B for gas phase spectroscopy of refractory materials.

[1] M. Ono, H. Yoshida, H. Hattori, K. Mitsuke, Nucl. Instrum. Meth. Phys. Res. A **467-468** (2001) 577.
[2] H. Yoshida, K. Mitsuke, J. Synchrotron Radiat. **5** (1998) 774.
[3] J. Kou, T. Mori, Y. Kubozono, K. Mitsuke, Phys. Chem. Chem. Phys. **7** (2005) 119.

Beamline Specifications

Monochromator	18-m spherical grating Dragon-type
Wavelength Range	6 – 55 nm; 24 – 205 eV
Resolution	2000 – 8000 depending on the gratings
Experiment	Mass spectrom.; Photoelectron spectrosc.; Momentum imaging spectrosc.; e^--Ion coincidence spectrosc.; Fullerene beam source

BL3U

Varied-Line-Spacing Plane Grating Monochromator for Molecular Soft X-Ray Spectroscopy

The beamline BL3U is equipped with an in-vaccum undulator composed of 50 periods of 3.8 cm period length. The emitted photons are monochromatized by the varied-line-spacing plane grating monochromator (VLS-PGM) designed for various spectroscopic investigations in the soft x-ray range including soft x-ray emission studies. Three holographically ruled laminar profile plane gratings are designed to cover the photon energy range from 60 eV to 800 eV. The beamline has two endstations, namely XES setup and Multi-purpose setup. The XES setup is used for soft x-ray emission spectroscopy. The beam is horizontally focused onto the sample position by plane-elliptical mirror, M2X. In the Multi-purpose setup, the beam is focused by the toroidal mirror M2. Between the sample position and M2, the differential pumping is placed.

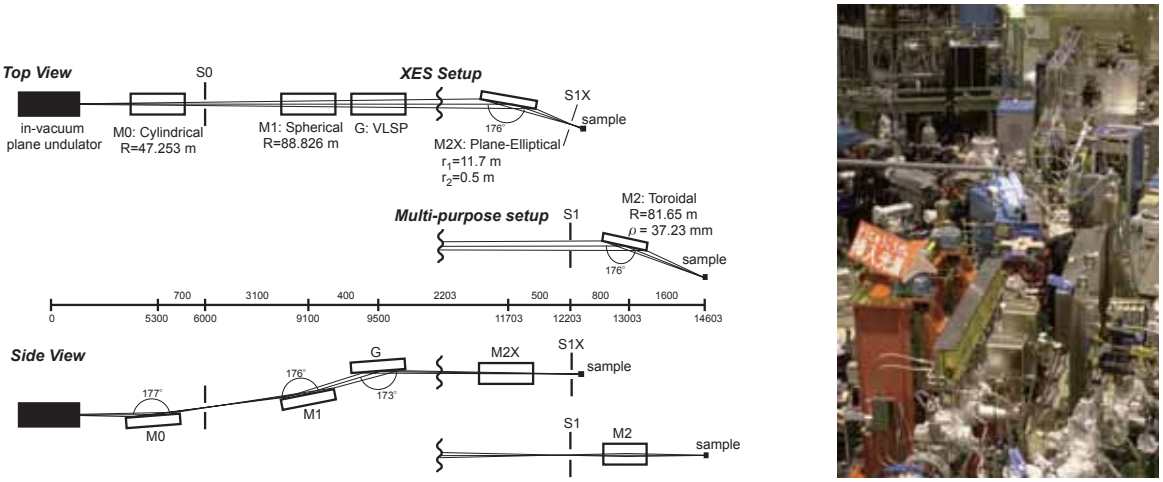

Fig. 1. Schematic layout (left) and the photography (right) of the BL3U. The distances along the beam from the center of the in-vacuum plane undulator are shown in mm. S1X and M2X can be replaced with the other exit slit S1 so that experiments can be carried out at either the XES or multi-purpose endstation. In the XES setup, the sample is placed at 5-10 mm downstream of S1X.

Beamline Specifications

Monochromator	Varied-line-spacing plane grating monochromator
Energy Range	60-800 eV
Resolution	E/ΔE > 10 000
Experiment	Soft X-ray spectroscopy (XPS, XES, XAS)
Beam Size (XES Endstation)	Gaussian shape Vertical 5-20 μm; Horizontal 41 μm (FWHM)

BL4A

Multilayered Mirror Monochromator for Photochemistry

BL4A1 has been constructed to perform the synchrotron radiation induced etching of Si and SiO_2 using XeF_2 as an etching gas. This beam-line is composed of a multilayered mirror (MLM) monochromator, a beam condenser system, and a differential pump system. The XeF_2 pressure during the etching will reach to 0.5 Torr, so a differential pump apparatus is installed in the vacuum system and the etching chamber as shown in Fig. 1. The etching chamber is evacuated independently and is designed to achieve high pressure (0.5 Torr) keeping other vacuum system at low pressure (< 10^{-5} Torr) by an aperture flange and a sequence of pressure stages. The condenser mirror focuses the divergent radiation onto the sample surface in the etching chamber, and obtains an extreme higher photon flux can be obtained.

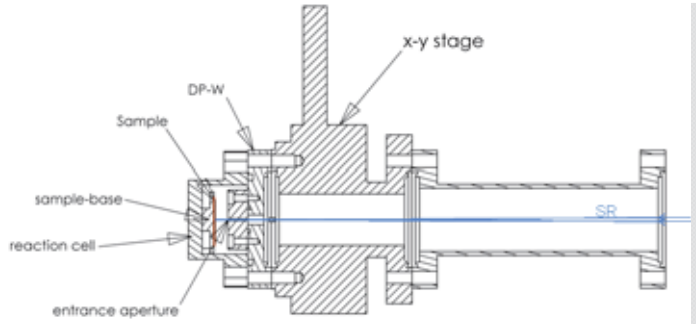

Fig. 1. Section view of differential pump apparatus installed in the etching chamber (reaction cell) and the entrance of beam.

Fig. 2. A side view of the end-station at BL4A1.

Beamline Specifications

Monochromator	Multilayered mirror monochromator
Wavelength Range	13.3 ~ 22.5 nm
Resolution	5 ~ 9 eV (FWHM)
Experiment	Irradiation
Miscellaneous	Not-in-use for SR users

BL4B

Varied-Line-Spacing Plane Grating Monochromator for Molecular Soft X-Ray Spectroscopy

The beamline BL4B equipped with a varied-line-spacing plane grating monochromator (VLS-PGM) was constructed for various spectroscopic investigations in a gas phase and/or on solids in the soft X-ray range. Three holographically ruled laminar profile plane gratings with SiO_2 substrates are designed to cover the photon energy range from 25 eV to 800 eV. The gratings with the groove densities of 100, 267, and 800 l/mm cover the spectral ranges of 25-100, 60-300, and 200-1000 eV, respectively, and are interchangeable without breaking the vacuum. Fig. 1 shows the absolute photon flux for each grating measured by a Si photodiode (IRD Inc.), with the entrance- and exit-slit openings set at 50 and 50 μm, respectively. The maximum resolving power (E/ΔE) achieved for each grating is more than 5000.

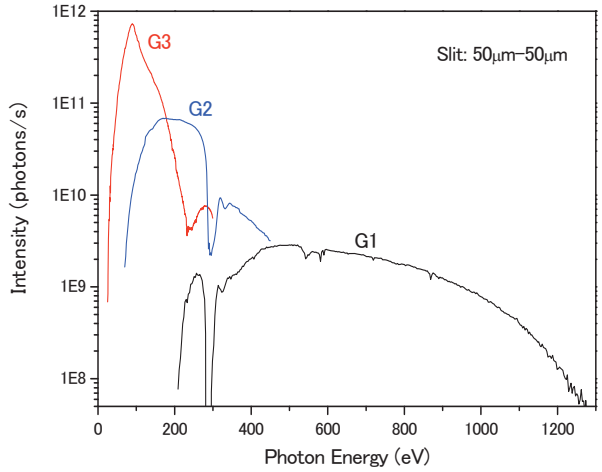

Fig. 1. Throughput from the VLS-PGM monochromator on BL4B.

Fig. 2. Photo of BL4B.

Beamline Specifications

Monochromator	Varied-line-spacing Plane Grating Monochromator
Energy range	25-1000 eV
Resolution	E/ΔE > 5000 (at maximum)
Experiments	Soft X-ray spectroscopy (mainly, angle-resolved photoion spectroscopy for gaseous targets and photoelectron spectroscopy for gaseous and solid targets)

BL5U

Photoemission Spectroscopy of Solids and Surfaces

This beamline is designed for a high-resolution angle-resolved photoemission study on solids and surfaces with horizontal-linearly and circularly (CW, CCW) polarized synchrotron radiation from a helical undulator. The beamline consists of a Spherical Grating Monochromator with Translational and Rotational Assembly Including a Normal incidence mount (SGM-TRAIN), and a high-resolution angle-resolved photoemission spectrometer.

The SGM-TRAIN is an improved version of a constant-length SGM to aim the following points; (1) covering the wide energy range of 5-250 eV, (2) high energy resolving power, (3) use of linearly and circularly polarized undulator light, (4) reduction of higher order light, and (5) two driving modes (rotation and translation of gratings) by computer control. The second-order light is well suppressed by using laminar profile gratings and ombinations of mirrors and gratings.

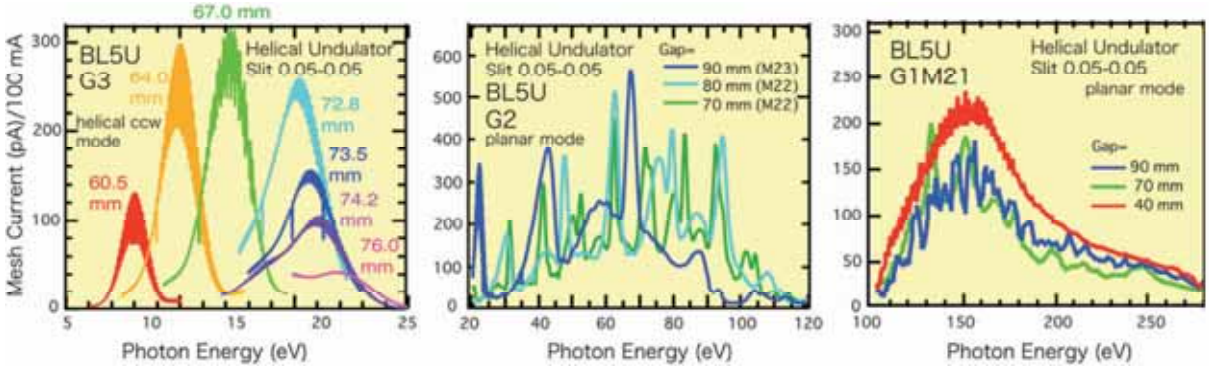

Fig. 1. Throughput spectra from the SGM-TRAIN monochromator at BL5U.

Beamline Specifications

Monochromator	SGM-TRAIN
Energy Range	5-250 eV
Resolution	hν/ΔE >2,000 for < 40μm slits
Experiment	ARPES, AIPES, XAS
Flux	$<10^{11}$ photons/s for < 40μm slits (at the sample position)
Main Instruments	Hemispherical photoelectron analyzer (MBS-Toyama 'Peter' A-1), LEED of reverse type (OMICRON), Liq-He flow cryostat (5 – 400 K)

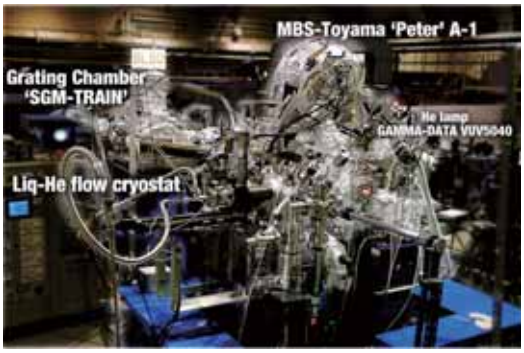

Fig. 2. High-resolution angle-resolved photoemission apparatus at BL5U.

BL5B

Calibration Apparatus for Optical Elements and Detectors

BL5B has been constructed to perform calibration measurements for optical elements and detectors. This beamline is composed of a plane grating monochromator (PGM) and three end stations in tandem. The most upstream station is used for calibration measurements of optical elements, the middle one for optical measurements for solids and the last for photo-stimulated desorption experiments. The experimental chamber at the most downstream station is sometimes changed to a chamber for photoemission spectroscopy.

The calibration chamber shown in Fig. 2 is equipped with a goniometer for the characterization of optical elements, which has six-degree-of-freedom; X-Y translation of a sample, and interchange of samples and filters. These are driven by pulse motors in vacuum. Since the polarization of synchrotron radiation is essential for such measurements, the rotation axis can be made in either horizontal or vertical direction (s- or p-polarization).

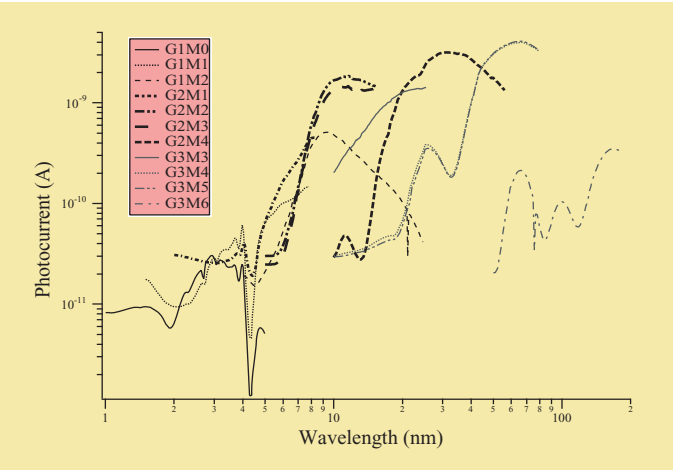

Fig. 1. Throughput spectra for possible combinations of gratings and mirrors at BL5B measured by a gold mesh.

Fig. 2. A side view of the experimental chamber for calibration measurements.

Beamline Specifications

Monochromator	Plane Grating Monochromator
Energy range	6-600 eV (2-200 nm)
Resolution	E/ΔE ~ 500
Experiments	Calibration of optical elements, absorption of solids, photo-stimulated desorption from rare gas solids

BL6B

Infrared and Terahertz Spectroscopy of Solids

SR has a good performance (high brilliance and high flux) not only in VUV and SX regions but also in IR and terahertz regions. This beamline covers in the IR and terahertz regions. The previous beamline BL6A1 that has been constructed in 1985 is the pioneer of the infrared SR research. The beamline was upgraded in the spring of 2004 and the name was changed to be BL6B (IR). The front-end part including the bending duct #6 was replaced to a new one with higher acceptance angle using a magic mirror as shown in Fig. 1.

The beamline is equipped with two interferometers, one is Michelson-type (Bruker IFS-66v) and the other Martin-Puplett-type (JASCO FARIS-1), for the wide spectral region from several to 20,000 cm^{-1} ($h\nu$ = several 100 μeV – 2.5 eV) as shown in Fig. 2. The experimental chamber in which users bring can be equipped at the free port. In the near future, an IR microscope covering down to terahertz region will be set up.

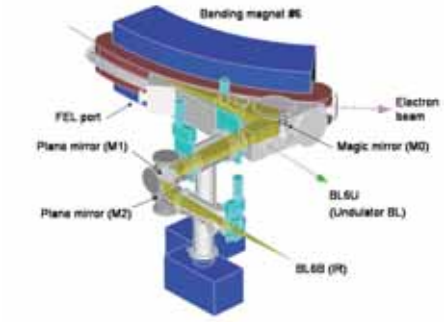

Fig. 1. The design of optics and front end of BL6B.

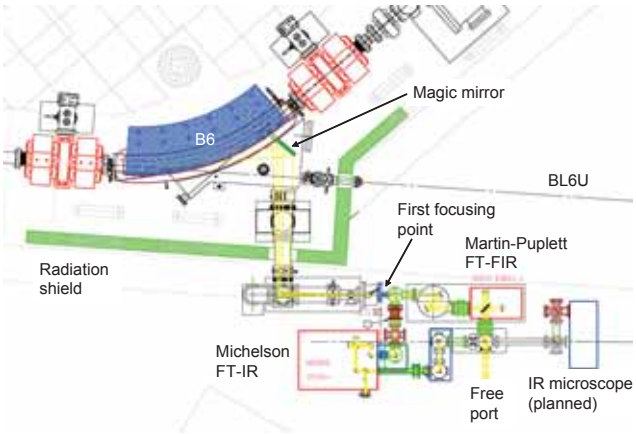

Fig. 2. Schematic figure of top view of BL6B.

Beamline Specifications

Interferometer	Michelson (Bruker IFS66v), Martin-Puplett (JASCO FARIS-1)
Wavenumber Range (Energy range)	several – 20,000 cm^{-1} (several 100 μeV – 2.5 eV)
Resolution in cm^{-1}	0.1cm^{-1} for IFS66v 0.25cm^{-1} for FARIS-1
Experiments	Reflectivity and transmission Magneto-optics (Microspectroscopy)
Miscellaneous	Users can bring their experimental system in this beamline.

BL7U

Angle-Resolved Photoemission of Solids in the VUV Region

The beamline 7U is constructed to provide the photon flux with high energy resolution and high flux mainly for high-resolution angle-resolved photoemission spectroscopy of solids. An APPLE-II-type variable polarization undulator is equipped for the light source. The undulator can make high intense VUV light with horizontal/vertical linear and right/left circular polarization. The undulator light is monochromatized by the modified Wadsworth-type monochromator with three gratings (R = 10 m; 1200, 2400 and 3600 lines/mm optimized at $h\nu$ = 10, 20, and 33 eV). The energy resolution of light ($h\nu/\Delta h\nu$) is more than 10^4 with the photon flux of more than 10^{11} ~ 10^{12} ph/s on samples in the whole energy region.

The beamline has a photoemission end station which equips a 200-mm-radius hemispherical photoelectron analyzer (MB Scientific AB, A-l analyzer) and a liquid-helium-cooled cryostat with a 6-axes pulse motor control (A-VC Co. Ltd., i-GONIO). The main purpose is to determine the three-dimensional Fermi surface and electronic structure of solids at low temperatures and their temperature dependence to reveal the origin of the physical properties.

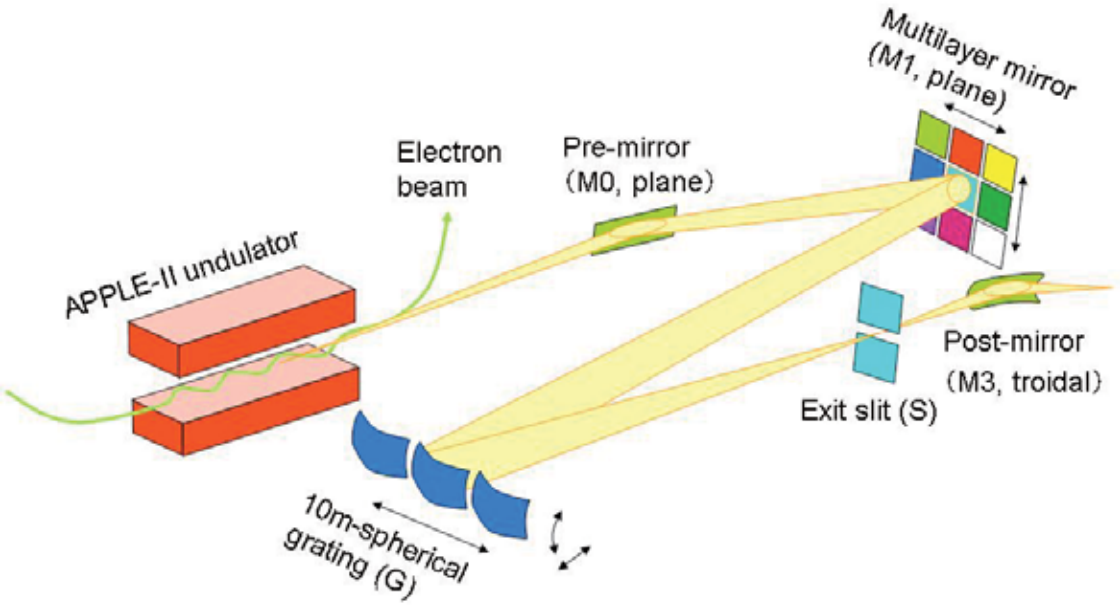

Fig.1. Schematic figure of BL7U.

Beamline Specifications

Light source	APPLE-II type undulator (λ_u = 76mm, N = 36)
Monochromator	10-m Normal Incidence Monochromator (modified Wadsworth-type)
Photon energy range	6 ~ 40 eV (λ = 30 ~ 200 nm)
Resolution ($h\nu/\Delta h\nu$)	1×10^4 ~ 5×10^4
Photon flux on sample	$\geq10^{12}$ ~ 10^{11} ph/s (depend on $h\nu$)
Beam size on sample	200(H)×50(V) μm^2
Experiments	Angle-resolved photoemission of solids (MB Scientific A-1 analyzer)

BL7B

3-m Normal Incidence Monochromator for Solid-State Spectroscopy

BL7B has been constructed to provide sufficiently high resolution for conventional solid-state spectroscopy, enough intensity for luminescence measurements, a wide wavelength coverage for Kramers-Kronig analyses, and the minimum deformation to the polarization characteristic of the incident synchrotron radiation. This beamline consists of a 3-m normal incidence monochromator which covers the vacuum ultraviolet, ultraviolet, visible and infrared, *i.e.* the wavelength region of 40 -1000 nm, with three gratings (1200, 600, and 300 l/mm). Two interchangeable refocusing mirrors provide two different focusing positions. For the mirror with the longer focal length, an LiF or a MgF2 window valve can be installed in between the end valve of the beamline and the focusing position. Figure 1 shows absolute photon intensity for each grating with the entrance and exit slit openings of 0.5 mm. A silicon photodiode (AXUV-100, IRD Inc.) was utilized for measuring the photon intensity and the absolute photon flux was estimated, taking the quantum efficiency of the photodiode into account.

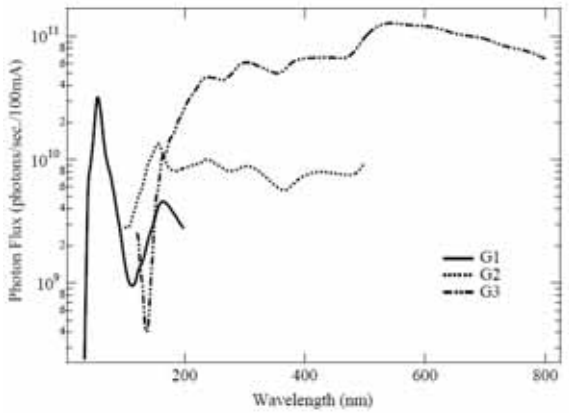

Fig. 1. Throughput spectra of BL7B measured by a silicon photodiode.

Fig. 2. Photo of BL7B.

Beamline Specifications

Monochromator	3-m Normal Incidence Monochromator
Wavelength Range	50 to 1000 nm (1.2 - 25 eV)
Resolution	$E/\Delta E$ = 4000 – 8000 for 0.01 mm slits
Experiment	absorption, reflection, fluorescence spectroscopy, mainly for solids

BL8B1

Spherical Grating Monochromator for Soft X-Ray Spectroscopic Studies on Solids and Surfaces

The beamline BL8B1 equipped with a constant-deviation constant-length spherical grating monochromator [1] provides soft X-ray photons in the energy range 30-800 eV with medium energy resolution. The photon energy range is covered by using three gratings (R=15 m; 1080 l/mm, R=15 m; 540l/m, and R=7.5m; 360 l/mm) which are interchangeable in vacuum. Figure 1 shows a throughput spectrum measured with the entrance- and exit-slit openings of 10 μm. Under this condition, the achievable resolving power is about 4000 at 400 eV and 3000 at 245 eV, respectively.

An experimental chamber is equipped for conventional measurements of electron yield spectra, or pseudo-photoabsorption spectra, under a ~1×10^{-6} Torr vacuum condition.

[1] Hiraya *et al*., Rev. Sci. Instrum. **66** (1995) 2104.

Fig. 1. Photo of BL8B1.

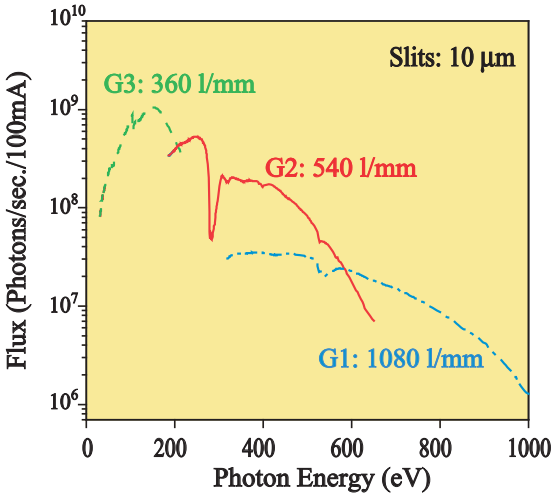

Fig. 2. Throughput of the monochromator at BL8B1.

Beamline Specifications

Monochromator	Constant-deviation constant-length spherical grating type
Energy range	30-800 eV
Resolution	E/ΔE = 4000 at 400 eV and 3000 at 245 eV
Experiments	Photoabsorption spectroscopy, electron spectroscopy and electron-ion coincidence spectroscopy for solids and surfaces

BL8B2

Angle-Resolved Ultraviolet Photoelectron Spectrometer for Solids

BL8B2 is a beamline for angle-resolved ultraviolet photoemission spectroscopy (ARUPS) system which is designed for measuring various organic solids such as molecular crystals, organic semiconductors, and conducting polymers. This beamline consists of a plane-grating monochromator (PGM), a sample preparation chamber with a fast entry Load-Lock chamber, a measurement chamber with an accurate for temperature dependence (base pressure 1×10^{-10}Torr), a cleaning chamber (base pressure 1×10^{-10}Torr), and a sample evaporation chamber (base pressure 3×10^{-10}Torr). The cleaning chamber is equipped with a back-view LEED/AUGER, an ion gun for Ar^+ sputtering, and an infrared heating unit. The PGM consists of premirrors, a plane grating, focusing mirror, and a post-mirror, with an exit slit. It covers the wide range from 2 to 130eV with exchanging two gratings (G1: 1200l/mm, G2: 450l/mm) and five cylindrical mirrors. The toroidal mirror focuses the divergent radiation onto the sample in the measurement chamber. The spot size of the zeroth-order visible light at the sample surface is about $1\times1mm^2$. Figure 1 shows the throughput spectra of PGM (slit=100μm). The energy resolution at a slit width of 100μm was found to be $E/\Delta E$ = 1000 in the wavelength range from 2 to 130eV. A hemi-spherical electron energy analyzer of 75mm mean radius with an angular resolution less than 2° can be rotated around vertical and horizontal axes. The sample mounted on a manipulator can be also rotated around two axes.

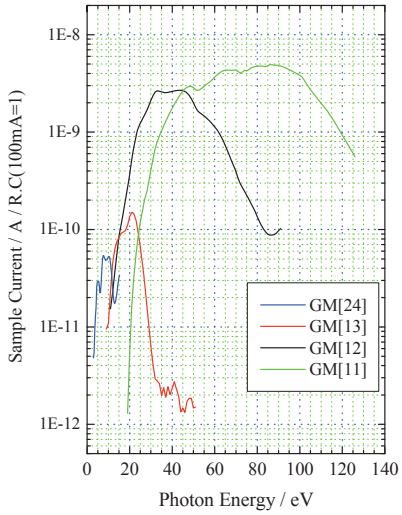

Fig. 1. Throughput spectra of plane-grating monochromator at BL8B2 (slit=100μm).

Fig. 2. A photo of BL8B2.

Beamline Specifications

Monochromator	Plane-grating monochromator
Wavelength Range	9- 600nm
Resolution	$E/\Delta E$ = 1000
Experiment	Angle-resolved ultraviolet photoemission spectroscopy

CSR

Tunable Narrowband Terahertz CSR from Electron Bunch Interacted with Modulated Laser Pulse

M. Shimada[1], M. Katoh[1], S. Kimura[1], M. Hosaka[2], Y. Takashima[2], S. Bielawski[3], C. Szwaj[3], C. Evain[3], A. Mochihashi[4], T. Hara[5], T. Takahashi[6]

[1]*UVSOR Facility, Institute for Molecular Science, Okazaki 444-8585 Japan*
[2]*Graduate School of Engineering, Nagoya University, Nagoya 464-8603 Japan*
[3]*Université des Sciences et Technologies de Lille, Villeneuve d'Ascq Cedex, France*
[4]*Japan Synchrotron Radiation Research Institute, SPring-8, Sayo-cho Hyogo 679-5198 Japan*
[5]*RIKEN SPring-8 Center, RIKEN Harima Institute, Sayo-cho Hyogo 679-5148 Japan*
[6]*Kyoto University Research Reactor Institute, Kumatori-cho Osaka 590-0494 Japan*

Powerful and tunable narrowband terahertz (THz) light source is expected to open a new field in biology, chemistry, medical sciences and so on. Recently, we have developed a new method to produce monochromatic synchrotron radiation in the terahertz region on storage rings [1]. In this method, a specially tailored electron bunch emits monochromatic radiation in a uniform magnetic field. This is in contrast with the ordinary technique to produce monochromatic radiation by utilizing periodic magnetic fields created by undulators.

At UVSOR-II, we have already succeeded in producing intense broadband THz emission by using the laser slicing technique [2]. In the feasibility study before starting this experiment, we had pointed out the possibility to produce monochromatic radiation by extending this technique. We had predicted that, by creating many dips periodically on an electron bunch, we could produce quasi-monochromatic synchrotron radiation through coherent synchrotron radiation (CSR) mechanism.

To create many dips periodically or, in other words, periodic density modulation, we developed a method to produce amplitude-modulated laser pulses by using a technique called 'chirped pulse beating' (see Fig. 1), in collaboration with a French team [1]. This is a robust technique which fits the accelerator circumstances and is easy to operate.

The amplitude modulated laser pulses are injected to the ring through a laser transport line which was constructed by utilizing a part of the existing optical cavity for free electron laser. The laser pulses interact with electron bunches in an undulator whose fundamental wavelength is tuned to the laser wavelength, 800 nm in this case.

In the undulator, the laser field and the electrons exchange their energy, and an energy modulation is created on the electron bunch. The energy modulation is larger/smaller where the electrons interact with laser field of larger/smaller amplitude. After this interaction the electron bunch proceeds in the ring. Since the higher/lower energy electrons go slow/fast., in other words, the time of flight depends on the energy, the energy modulation is converted to a density modulation. Electrons escape out from strongly modulated parts. Fig. 2 shows a result from numerical simulation on the formation of the density modulation. The period of the density modulation is exactly same as that of the amplitude modulation of the laser pulse.

The density modulated electron bunch emits CSR at the wavelength corresponds to the density modulation period. This can be understood by using a general expression of the power of the CSR;

$$P(\lambda) = P_0(\lambda)(N_e + N_e^2 f(\lambda)),$$

$$f(\lambda) = \left(\int \cos(2\pi z/\lambda) S(z) dz\right)^2$$

where the $P(\lambda)$ is the radiation power at the wavelength λ emitted by an electron bunch, the $P_0(\lambda)$ that emitted by a single electron, the N_e the number of the electrons, the $S(z)$ is the longitudinal density distribution of the electron bunch. If the bunch has a single dip, the $f(\lambda)$ has a value close to unity for the wavelength longer than the dip width. In this case, the CSR spectrum becomes broadband. On the other hand, when sinusoidal density modulation is created on the bunch, then the $f(\lambda)$ has a sharp peak at the wavelength corresponds to the density modulation period.

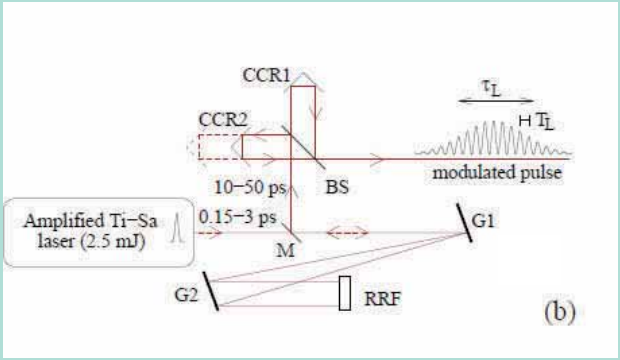

Fig. 1. Principle of Chirped Pulse Beating [1]. A femto-second laser pulse is stretched and separated into two pulses. They are merged with some delay on one pulse.

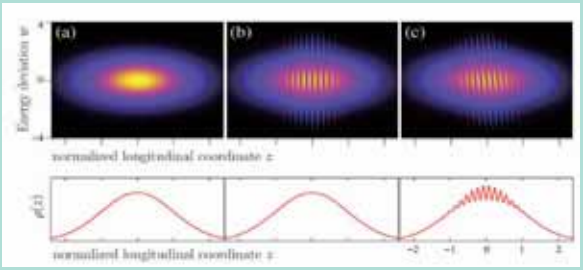

Fig. 2. Evolution of the electron distribution in longitudinal phase-space (upper) and their projection onto the longitudinal coordinate (lower), (a) before the interaction, (b) just after the interaction and (c) after traveling in the ring [1].

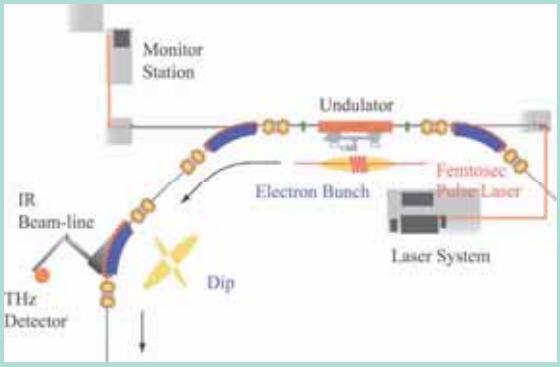

Fig. 3. Laser slicing system at UVSOR-II [2].

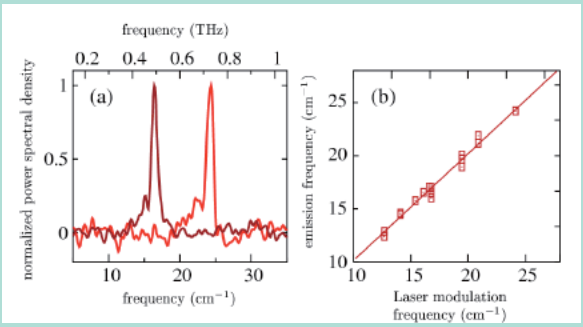

Fig. 4. Typical narrowband THz CSR spectra, and tunability curve [1]. (a) Two THz CSR spectra obtained with modulation frequencies of 16 cm^{-1} and 24cm^{-1}, respectively. (b) Peak frequency of THz CSR versus laser modulation frequency.

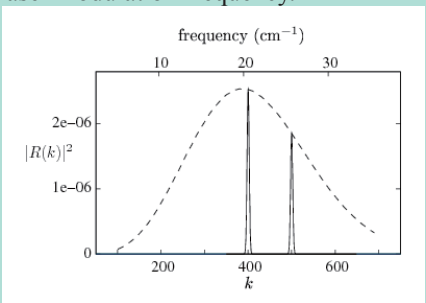

Fig. 5. Calculated CSR intensity versus modulation frequency [1]. The two peaks (full lines) are spectra associated to modulation frequencies of k_m=400 and k_m=500, respectively.

The experimental setup is illustrated in Fig. 3. The CSR was observed at the second bending magnet from the undulator section where the interaction between the electron bunch and the laser pulse took place. The THz spectrum is measured by the Martin-Puplett interferometer at the beam-line BL6B. We succeeded in observing the narrowband THz CSR as shown in Fig. 4(a). It was also confirmed that the larger number of the modulation gave the narrower line width.

Another important feature of this new technique, the 'tunability', was also successfully demonstrated. Just by adjusting the position of a retro-reflector, which is a component of 'chirped pulse beating' optical systems, we could change the modulation period. The radiation wavelength was found to exactly same as the modulation period as shown in Fig. 4(b). A detectable peak was in the 12-25 cm^{-1} range.

Intensity of THz CSR for given laser peak power and for the present experimental setup can be estimated analytically as a function of the modulation frequency. The result is bell shaped with the peak around 20 cm^{-1} as shown in Fig. 5 and qualitatively explains well the experimental results.

Acknowledgement

This work was supported by the Joint Studies Program (2005–2007) of the Institute for Molecular Science and the JSPS Fellowship Program for Research in Japan (grant S06215), by Grants-in-Aid for Scientific Research B15360038 and B15360039 from JSPS and by the research foundation for Opt-Science and Technology. CERLA is supported by the French Minist`ere charg´e de la Recherche, the R´egion Nord-Pas de Calais and FEDER.

[1] S. Bielawski, C. Evain, T. Hara, M. Hosaka, M. Katoh, S. Kimura, A. Mochihashi, M. Shimada, C. Szwaj, T. Takahashi, Y. Takashima (in alphabetic order), Nature Physics **4** (2008) 390.
[2] M. Shimada, M. Katoh, S. Kimura, A. Mochihashi, M. Hosaka, Y. Takashima, T. Hara, T. Takahashi, Jpn. J. Appl. Phys. **46** (2007) 7939.
[3] Y. Takashima, M. Katoh, M. Hosaka, A. Mochihashi, UVSOR Activity Report 2002 (2003) 56.
[4] Y. Takashima, M. Katoh, M. Hosaka, A. Mochihashi, S. Kimura, T. Takahashi, Jpn. J. Appl. Phys. **44** (2005) L1131.

Undulator

Independent Tuning of Variable Polarization Undulator U7

K. Hayashi, M. Katoh, J. Yamazaki, A. Mochihashi, M. Shimada
UVSOR Facility, Institute for Molecular Science, Okazaki 444-8585 Japan

Outline of U7

The variable polarization undulator, U7, was introduced in summer 2006 (Fig.1). It is a 3m Apple-II type undulator. It is the 4th undulator operational at UVSOR.

Fig. 1. Variable polarization U7 undulator.

All undulators of UVSOR can be controlled via Ethernet from beamlines. They have several steering magnets to cancel the closed orbit distortion (COD) caused by pole gap change. U7 has four correction magnets (two horizontal/vertical steerings and two quadrupoles) at the ends of the undulator. The controller commands DC power supply to provide feedforward current for steering magnets, referring both of the pole gap and the correction table in period less than one second.

Method of COD correction

We first prepared the correction table for the local quadrupole magnets to cancel the betatron tune shift caused by gap change based on measurements. Then, we prepared the correction table for the steering magnets to compensate the COD due to gap change [1].

As the first step, COD due to the gap change was measured by beam position monitors (BPM). Next, COD caused by the excitation of the steering magnets was measured. Then the currents of the steering magnets were determined so as to minimize the COD. We used least-square method, that is to find local minimum of S given below;

$$S = \sum_{i=1}^{N_{BPM}} \left\{ \begin{matrix} (x_i + u_i^H I_H)^2 \\ (y_i + v_i^V I_v)^2 \end{matrix} \right\}$$

where u_i^H, I_H and x_i represent horizontal COD at i-th BPM caused by the excitation of horizontal steering magnets at unit current, excitation current of horizontal steering magnets and horizontal COD of i-th BPM caused by gap change, respectively.

Result of COD correction

The result of COD correction is shown in Fig. 2 as to horizontal COD in horizontal polarization mode for example. COD without correction caused by gap change from 100mm to 24mm is larger than 100 microns, while smaller than 10 microns with correction. At present, horizontal polarization mode (gap 24mm-200mm) and vertical polarization mode (gap 35mm-200mm) are opened for users. In vertical mode, short gap (smaller than 35mm) causes beam life shortening, which should be improved by introducing more sophisticated correction for non-linear effects.

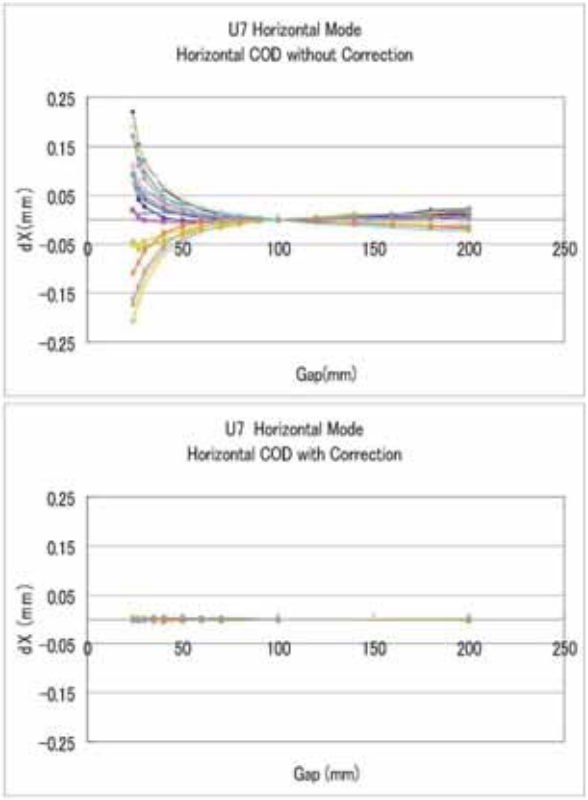

Fig. 2. COD without(up) and with(down) correction

Polarization change is also allowed at fixed gap, 100mm. The COD during the polarization change was successfully corrected to be less than 10 microns.

[1] K. Hayashi *et al.*, UVSOR Activity Report 2003 (2002) 51.

Lasing below 200 nm at the UVSOR-II FEL

M. Hosaka[1], M. Koike[1], N. Yamamoto[1], Y. Takashima[1], M. Katoh[2], M. Shimada[2], J, Yamazaki[2], A. Mochihashi[2,3]

[1]*Graduate School of Engineering, Nagoya University, Nagoya 464-8603 Japan*
[2]*UVSOR Facility, Institute for Molecular Science, Okazaki 444-8585 Japan*
[3]*RIKEN SPring-8 Center, RIKEN Harima Institute, Sayo Hyogo 679-5148 Japan*

The UVSOR-II FEL has been recognized as a useful tool for application experiments because of its high out-coupled average power in the deep UV region down to 215 nm. This fiscal year, application experiments, irradiation on bio-molecules and time resolve experiments on a scintillator have been performed. In the irradiation experiment, average power of 100 mW could be maintained and in the time resolved experiment, FEL of wavelengths of 215 nm and 240 nm was employed. In order to promote application experiments more extensively, FEL lasing in shorter wavelength below 200 nm is required.

The shortest wavelength attained in storage ring FELs is 176.4 nm at Elettra, Italy [1]. They employed fluoride multilayers for resonator mirrors and in-vacuum diagnostic system. At the UVSOR-II FEL, on the other side, attainable wavelength is limited by diagnostic system (out-of vacuum) now and therefore we decided to demonstrate an FEL lasing just below 200 nm.

The lasing experiment was made at electron beam energies of 600 MeV and 750 MeV. Multilayers of Al_2O_5/SiO_2 were employed for the cavity mirrors. The mirrors were designed to maximize reflectivity at 198 nm. The numbers of layers for the front and backward cavity mirrors are 41 and 51, respectively. In order to obtain high out-coupled power from the backward mirror, smaller number of layer was chosen for it. Calculated round trip reflectivity using the optical constant of Al_2O_5 and SiO_2 is 99.1 %. After degassing the mirror with synchrotron radiation from an optical klystron, the reflectivity was measured using cavity ring-down technique. The measured round-trip reflectivity was 98.5%. We suppose that the value is smaller than calculated one due to mirror degradation in the process of the degassing. The first lasing experiment was made with 600 MeV electron beam of 100 mA/2bunch. The shortest wavelength spectrum in the experiment is shown in figure 1. As seen in the figure, the shortest wavelength attained with the mirrors was 199.3 nm although the designed value was 198 nm. We suppose that the wavelength of maximum reflectivity of the mirrors was shifted toward longer wavelength due to the mirror degradation after irradiation of synchrotron radiation, which is often observed in other FEL experiments at UVSOR-II. The measured threshold beam current for the lasing was 28.9 mA/2bunch, which is almost consistent with the FEL gain calculation.

After lasing with 600 MeV electron beam, we raised it up to 750 MeV, which is favorable for a high power FEL operation [2]. An FEL lasing was obtained; however, the shortest wavelength was not shorter than 200 nm anymore. The out-coupled power around 202 nm was 18 mW at a beam current of 90 mA/2bunch. Since the aim of this experiment is to examine a lasing below 200nm, we did not store high beam current in the storage ring. However for users' applications, we will increase the beam current (~ 200 mA/2bunch), and higher out-coupled FEL power will be is obtained.

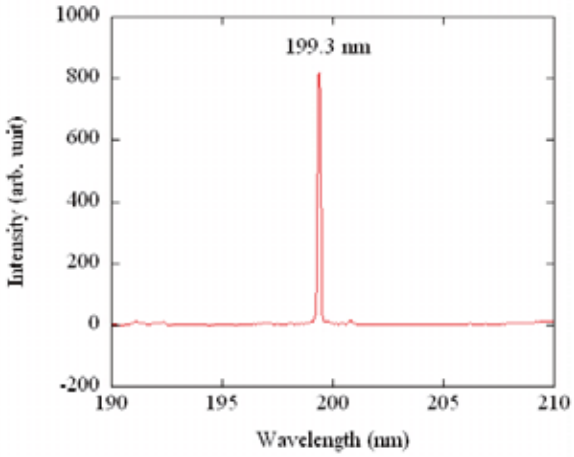

Fig. 1. Measured spectra of the FEL lasing at 199.3 nm. The gap length of the U5 optical klystron was 44.8 mm.

In conclusion, we have succeeded in an FEL lasing below 200 nm and found no technological barrier for the lasing. Further shortening of the lasing wavelength, a VUV diagnostic system and cavity mirror for the shorter wavelength is necessary. According to a gain estimation, an FEL lasing is possible at UVSOR-II with more than 96 % round trip reflectivity cavity mirrors.

[1] F. Curbis *et al.*, Proceeding of the 27th FEL conference (2005) 473.
[2] M. Hosaka *et al.*, UVSOR Activity Report 2006 (2007).

Full-Energy Injection in UVSOR-II

M. Katoh[1], K. Hayashi[1], J. Yamazaki[1], M. Shimada[1], A. Mochihashi[2]
[1]*UVSOR Facility, Institute for Molecular Science, Okazaki 444-8585 Japan*
[2]*Japan Synchrotron Radiation Research Institute, SPring-8, Sayo, Hyogo 679-5198 Japan*

In the previous report [1] we have mentioned replacement of power supplies for electromagnets of the booster synchrotron in UVSOR; aiming at the full-energy injection operation. Before the replacement, the maximum acceleration beam energy with the booster was restricted up to 600 MeV because of specifications of the power supplies for the electromagnet; after the beam injection we had to accelerate the beam up to 750 MeV in the storage ring for users operation. Such operation was not suitable for stabilization of the beam position in the storage ring, and moreover, it could become critical problem for 'top-up' operation which we are planning to do in the future. After the replacement and basic tuning of the power supplies for 600 MeV operation mode, we continued development of the operating condition for getting full-energy injection mode. In the development we settled the 750 MeV operating point of the booster on the extension of the 600 MeV operation; without changing beam optics. Figure 1 shows output patterns of the power supplies for the 750/600 MeV operations. The main power supply ('Main Coil' in the figure) supplies all of the magnets; bending, QF and QD magnets. Additional power supplies ('Sub Coil QF' and 'Sub Coil QD') are also used to control the quadrupole fields. During the additional acceleration the QF and QD magnets saturate because of the main power supply, so the QF and QD output had to decrease in the acceleration process. That means slight change in the beam optics, but we didn't have any serious problems in the operation. Because of the change in the operation pattern, a repetition rate of the booster in the 750 MeV operation is settled at 1Hz while the repetition in the 600 MeV is usually ~3 Hz. To compensate the additional beam loading and keep enough beam intensity in the booster, we have adopted a pattern operation for RF accelerating voltage. To transport the 750MeV beam from the booster to the storage ring, we have also replaced a power supply for bending magnets in the beam transport line at the end of FY2006.

After the upgrade of the beam transport line, soon we succeeded the full energy injection [2]. Figure 2 shows typical operation pattern of the booster synchrotron in 750 MeV operation. The beam current circulating in the booster was measured by an AC-CT via an linear wave detector for RF frequency (90.1 MHz) component; in the figure the beam current seems to change because of the change in the bunch length during the acceleration. At present, the extraction beam current from the booster to the storage ring is almost the same as that in the 600 MeV operation; typically it takes 3 times longer injection time to get the same beam current in the storage ring. In the daily users operation, however, we re-inject the beam upon the remaining beam in the full-energy injection operation; that shortens the time for the injection up to almost the same as that in the 600 MeV operation actually.

Now we are planning to perform 'top-up' operation in UVSOR near the future. The development the top-up systems including hardware and control systems are under way. Upgrade of radiation safety to cope with the continuous injection is also planning.

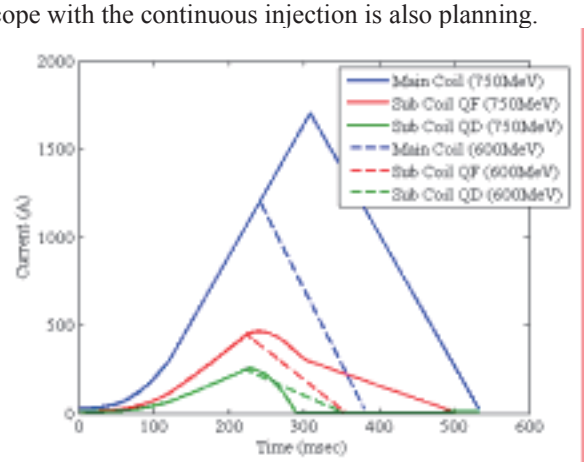

Fig. 1. The operation pattern of power sources for electromagnets in the booster. 750/600 MeV patterns are shown.

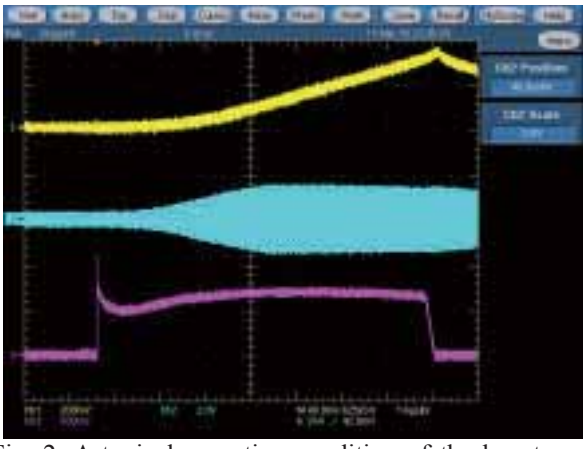

Fig. 2. A typical operating condition of the booster; magenta: beam current from AC-CT, yellow: output of the main power source, cyan: RF voltage from pick-up electrode in the RF cavity. The beam is accelerated up to 750 MeV at the top of the main power source output.

[1] M. Katoh,UVSOR Activity Report 2006 (2007) 8.
[2] K. Hayashi *et. al*., The 21st Jpn. Soc. on Syn. Rad. Res. Conf. (Kusatsu, 2008) 14P004.

Spectrum Measurement of Terahertz Synchrotron Radiation by Laser Bunch Slicing at UVSOR-II Electron Storage Ring

M. Shimada[1], M. Katoh[1], S. Kimura[1], M. Hosaka[2], Y. Takashima[2], N. Yamamoto[2], A. Mochihashi[3], T. Hara[4], T. Takahashi[5]

[1]*UVSOR Facility, Institute for Molecular Science, Okazaki 444-8585 Japan*
[2]*Graduate School of Engineering, Nagoya University, Nagoya 464-8603 Japan*
[3]*Japan Synchrotron Radiation Research Institute, SPring-8, Sayo Hyogo 679-5198 Japan*
[4]*RIKEN SPring-8, Sayo Hyogo 679-5148 Japan*
[5]*Kyoto University Research Reactor Institute, Sen-nan Osaka 590-0494 Japan*

Laser bunch slicing is a technique for producing intense coherent synchrotron radiation (CSR) in terahertz region by formation of a sub-millimeter dip on electron bunches. The intensity of CSR is enhanced at the wavelength longer than the longitudinal size of the dip. We have already been successful in observation of THz CSR signal train synchronized with the 1kHz laser trigger signal [1]. The intensity of the THz CSR is 10^4 – 10^5 times larger than that of the normal SR and proportional to square of the peak current of the electron beam.

The experimental setup is shown in Fig.1. A Ti:Sa laser pulse with sub-pico sec duration propagating from the upstream of an undulator interacts with an electron bunch under a resonance condition. Then the electron changes its energy and its orbit after the bending magnet. This is a process of dip formation.

Fig. 2 shows a schematic of the dip formation with various pulse durations. From the numerical results, you can see that a laser with shorter pulse duration makes a sharper dip. It means that the high frequency component of the THz CSR is enhanced with the shorter laser pulse duration.

THz CSR is gathered with large acceptance 215 mrad x 80 mrad at beamline BL6B installing a magic mirror [2]. A Martin-Puplett interferometer is placed in front of the bolometer for spectrum measurement. A gated integrator is used for reducing the background noise.

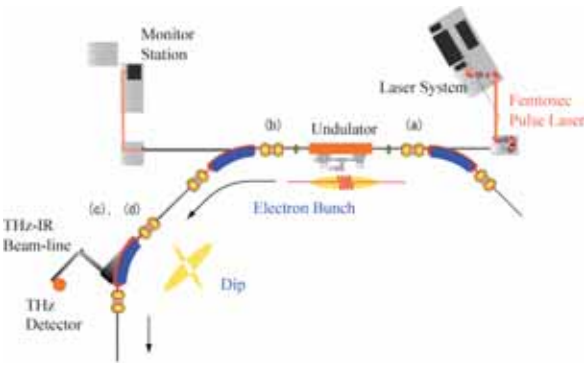

Fig. 1. Schematic of laser bunch slicing system in UVSOR-II

The experimental results of THz CSR spectra are shown in Fig.3. We demonstrated that the THz CSR spectrum depends on the laser pulse duration. High-frequency component of the THz CSR is more intense in the case of shorter laser pulse duration. This result is well explained by the numerical simulation.

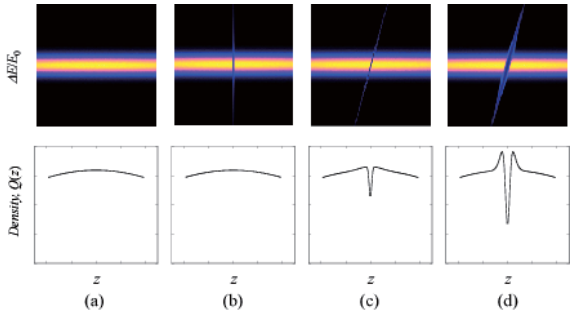

Fig. 2. Numerical simulations of longitudinal phase space (upper) and electron bunch density distribution (lower) in dip formation process. (a) : Before laser interaction, (b) : just after laser interaction, (c) : after passing through bending magnets, (d) : same as (c) but with longer laser pulse duration.

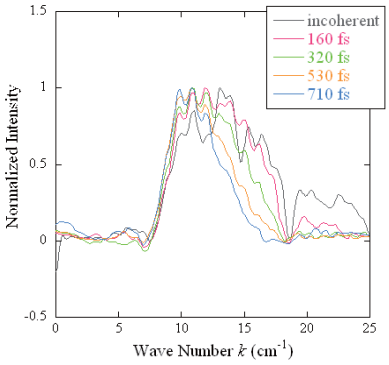

Fig. 3. Spectra of THz CSR obtained with various laser pulse durations, 160 (red), 320 (green), 530 (orange), and 710 fs (blue). For comparison, the spectrum of the normal SR obtained with the same system is also plotted but the intensity is normalized.

[1] M. Shimada *et al.*, UVSOR Activity Report 2006 (2007) 34.
[2] S. Kimura *et al.*, Infrared Phys. Technol. **49** (2006) 147.

Radiation Monitoring around Accelerator Using Nuclear Emulsion

Y. Taira, K. Morishima, K. Hamada, T. Nakano
F-lab, Department of Science, Nagoya University, Nagoya 464-8602, Japan

Nuclear Emulsion is a radiation detector, originally used for cosmic ray experiment, and high energy elementary particle experiment.

The structure of Nuclear Emulsion is that 45 micron emulsions applied both faces of 200 micron TAC bases. This type of Nuclear Emulsion is called "OPERA film".

Tracks of Charged particles in Emulsion read as 3-D information, which consists of position, angle and depth of tracks. The resolution of track is 0.05 micron for position and 0.3 mrad for angle. And scanning of tracks is done automatically, which speed is 5 min/cm^2 [1].

To monitor radiations of scattering around UVSOR Storage Ring, We set up detectors during operation (Fig. 1: circled red ring). The structure of the detector is 20 emulsions, 24*24 mm^2, stacked and vacuum-sealed in laminated sheet. Emulsions can measure angle, position, momentum, flux and particle ID (electron or gamma ray) of arrived radiations.

The angle distribution of the detector is Fig. 2. Electrons (include from gamma ray) arrived from right side to the detector. We checked blue print, confirmed electrons arrived from quadruple magnet and bending magnet. The structure of angle distribution is due to the matter of magnets.

Momentum is calculated from multiple electromagnetic scattering. Scattering is inversely proportional to momentum.

From this experiment, Nuclear Emulsion is very useful to measure leak radiations emitted from accelerator during operation.

Radiation monitoring using Nuclear Emulsion has a great possibility to expand. For example, first the detector for gamma ray CT. Second, monitor neutron at Heavy ion accelerators (RIKEN), Nuclear reactors and heavy particle cancer treatment facilities.

Fig. 1. Set up backward from quadruple and bending magnet.

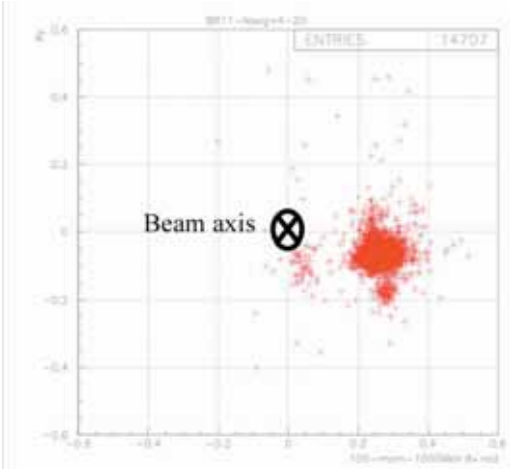

Fig. 2. Angle distribution of electrons that momentum more than 100 MeV/c.

[1] T. Nakano, *Proceedings of International Euro Physics Conference on High Energy Physics (Budapest, Hungary, 2001)* 1218.

FEL

Threshold Photoemission Magnetic Circular Dichroism Using Free Electron Laser

T. Nakagawa, T. Yokoyama, M. Hosaka, M. Katoh
Institute for Molecular Science (IMS), Okazaki 444-8585, Japan

Magnetic circular dichroism (MCD) in the x-ray regions (XMCD) has widespread over the synchrotron radiation facilities all over the world because of its high sensitivity to the element specific magnetism. The MCD depends on spin polarization and spin-orbit coupling.[1,2] Since the spin orbit coupling is strong in the core shell and the spin polarization in conduction band is large, x-ray MCD gives large MCD asymmetry. Now its high sensitivity combined with electron microscopy, called XMCD-photoemission electron microscopy (XMCD-PEEM), is used as a very powerful tool for the nano-scale magnetic domain imaging. XMCD-PEEM has been developed into time resolved imaging by using time structure of synchrotron radiation. On the other hand, MCD in the regions from infrared to ultraviolet (UV) is also a useful tool for the study of ferromagnetic ultrathin films. The magneto-optical Kerr effect (MOKE) detects the rotation and distortion of the polarization of reflected lights from magnetic materials. The Kerr effect in valence bands in thin films usually rotates the polarization and changes the ellipticity only by 10^{-2}-10^{-6} rad. This is because of its weak spin orbit coupling, although the spin polarization is large in the valence band. In the valence band photoemission, nevertheless, extensive works have been performed using circularly polarized synchrotron radiation and angle-resolved measurement, showing high (~10%) asymmetry [1,2]. The large asymmetry is attributed to the angle and energy selection of spin orbit split band. This requirement is not suitable for magnetic properties such as magnetization hysteresis curves or magnetic domain imaging because an electron analyzer is inevitable.

We have investigated the observation of enhanced MCD near the Fermi level using visible and ultraviolet lasers in a total yield mode [3]. Figure 1 shows MCD asymmetry as a function of workfunction subtracted by photon energy. Here the workfunction is varied by Cs adsorption and the photon energy is fixed. More than 10% MCD asymmetry is achieved on perpendicularly magnetized 12 ML Ni film on Cu(001), and magnetization curves are obtained. By changing the work function with the aid of cesium adsorption, the laser experiments show that the MCD asymmetry is enhanced only near the photoemission threshold, and that the asymmetry drops to 0.1% for photon energy larger than the work function by 0.6 eV. A theoretical calculation also shows enhanced dichroism near the photoemission threshold, in agreement with the experimental result.

While the above experiment changes workfunction to achieve high MCD asymmetry near the threshold, photon energy tuning is another possibility.

Our experiment needs two properties: *tunable wave length and high photon density*. As shown in Fig.1, to obtain high MCD asymmetry we have to tune the photon energy a little higher than the workfunction. We have used tunable free electron laser from UVSOR-II, which can deliver lower energy than $h\nu$ = 6.3 eV, close to typical workfunction for transition metal surfaces without surface modification such as alkali metal adsorption. Second, MCD method in magnetic field has to be measured by electron drain current from the ground to the sample since the trajectory of emitted electrons strongly depends on the magnetic field. This prevents the use of electron multiplier and needs high light intensity to give sufficient photoelectrons. The FEL in UVSOR can deliver ~100 mW around $h\nu$ = 5 eV [4], which is much stronger than usual laser output in this

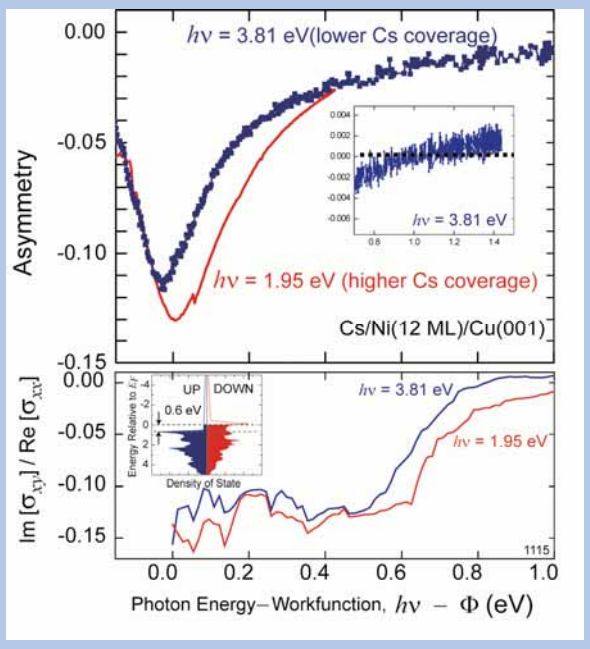

Fig. 1. (top) MCD asymmetry on Ni(12 ML)/Cu(001) surface as a function of workfunction – photon energy. Cs is used to change workfunction. The blue line is for hv = 3.25 eV, while the red 1.95 eV. The inset shows the inversion of MCD sign at 1 eV. (bottom) The corresponding theoretical calculation using Wien2k [6].

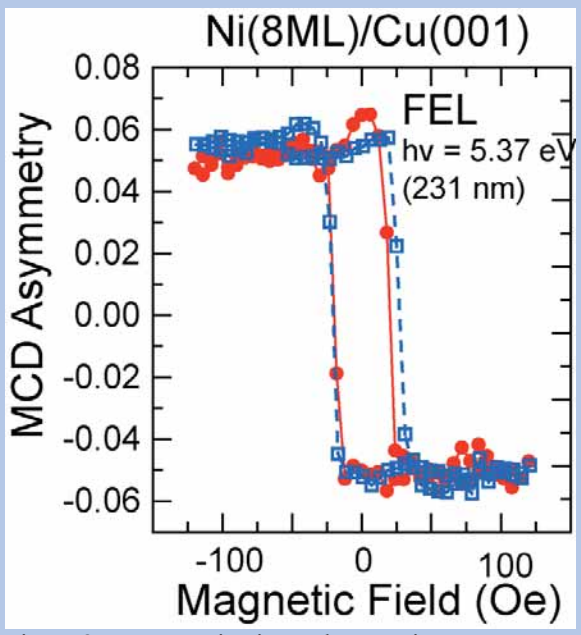

Fig. 2. Magnetization hysteresis curve on Ni(8ML)/Cu(001) taken by FEL-MCD. The plot gives 6% asymmetry. Also shown is the data taken by conventional MOKE.

wavelength region. Furthermore the light is circularly polarized inherently. Owing to its tunability and high intensity, FEL at UVSOR-II is a suitable source to threshold photoemission MCD measurements.

Figure 2 shows a magnetization hysteresis curve on Ni(8 ML)/Cu(001) using $h\nu$ = 5.37 eV, where the photoemission threshold for Ni is ~5.3 eV [5]. As expected from the result shown in Fig. 1, the asymmetry is high, ~6%, near the threshold. This result evidences that the clean Ni surface also shows high asymmetry near the photoemission threshold. The result from conventional magneto-optical Kerr effect is also shown together in Fig.2, having a similar hysteresis shape, which confirms the validity of the MCD method.

MCD in the valence band is strong enough for microscopic measurement. We can measure magnetic domain imaging using photoemission microscopy, which needs high brilliance. Figure 3 shows UVMCD-PEEM result. Unfortunately a FEL-PEEM measurement is still under construction, and here we show a result by a laptop laser. The laser used is LD laser, whose photon energy is 3.06 eV and output power is 5 mW. The magnetic domains (perpendicular to the surface) are clearly visible, giving good contrast. This result promises that FEL is brilliant enough for MCD-PEEM measurements, and MCD-PEEM with FEL is expected to be used for the real time imaging of the magnetic domains under surface modifications.

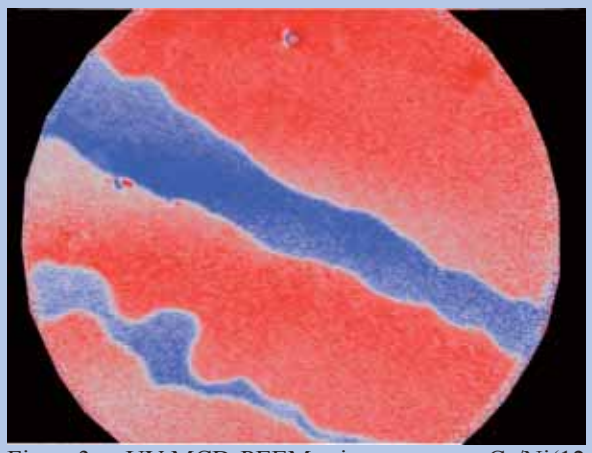

Fig. 3. UV-MCD-PEEM image on Cs/Ni(12 ML)/Cu(001). The field of view is 25 μm. The magnetic domain image is the processed result of the images by the right and left circular light. The red and blue regions are opposite magnetization directions.

[1] C. M. Schneider *et al.*, Phys. Rev. B **44** (1991) R12066.
[2] W. Kuch, C.M. Schneider, Rep. Prog. Phys. **64** (2001) 147.
[3] T. Nakagawa, T. Yokoyama, Phys. Rev. Lett. **96** (2006) 237402.
[4] M. Hosaka *et al.*, Nucl. Instrum. Methods A **483** (2002) 146.
[5] T. Nakagawa *et al.*, Rev. Sci. Instrum. **78** (2007) 023907.
[6] P. Blaha *et al.*, Computer code WIEN2k (Technische Universitat Wien, Vienna, 2002).

BL1A

Performance of CVD Diamond Photon Detectors in the Soft X-Ray Region

Y. Iwakaji, M. Kanasugi, S. Iguchi, O. Maida, T. Ito
Division of Electrical, Electronic and Information Engineering,
Graduate School of Engineering, Osaka University, Suita, Osaka 565-0871, Japan

Introduction

Since diamond with a bandgap of 5.5 eV has such various excellent properties as high breakdown electric field, high thermal conductivity and high chemical stability, it is considered as one of the electronic materials most suitable for high-performance radiation detectors working under severe environments. We have so far been investigating fabrication processes of high-quality single-crystalline diamond films using a high-power MWPCVD (microwave-plasma chemical vapor deposition) method [1], and have reported on performances of photon detectors fabricated with such high-quality diamond films for ultraviolet and soft-X-ray photons with energies below 2 keV [2-4]. In the present study, the room-temperature performance of such CVD diamond detectors has been investigated for soft-X-ray photons of 2.0 – 4.5 keV.

Experimental

Three high-quality homoepitaxial CVD diamond layers (undoped, boron-doped and undoped ones) were grown sequentially on a high-temperature / high-pressure-synthesized Ib (100) diamond substrate with a size of 3×3×0.5 mm^3. The typical thickness of the topmost undoped diamond layers used for the photon detection was ≈50 μm. After the homo-epitaxial growth processes, thin TiN electrodes were formed for the topmost layer using a standard photo-lithography technique and a magnetron sputtering method while Ti/Au bi-layer electrodes were deposited for the buried B-doped layer.

To one of detection areas of the diamond detector thus fabricated, photons with energies of 2.0 – 4.5 keV were irradiated through an aperture of ≈1 mm in diameter. Signal currents were measured at various bias voltages (V_b) of ≤ 100 V. The number of the incident photons was calibrated using a Si photon detector and the temporal storage ring currents.

Results and discussion

Although the number of the incident photons decreased significantly with the increasing photon energy (E_{ph}) in the energy region concerned in this study, the signal currents of the diamond detectors were able to be measured. The quantum efficiency of the photon detector (QE) is given by the quotient of the signal current divided by the product of the element charge and the number of incident photons. Figure 1 shows typical plots of QE versus E_{ph} for two different V_b. On one hand, QE at each E_{ph} is found to increased greatly (abnormally) with increasing V_b. This means that the diamond detector has an important function of increasing amplifications with the increasing V_b, as previously reported [3,4].

On the other hand, at each constant V_b, QE increases with increasing E_{ph} < ≈3 keV, above which QE decreases with increasing E_{ph}. At V_b = 10 V, QE is roughly proportional to E_{ph} below ≈3 keV, which well reflects the number of the electron-hole pairs created in the topmost undoped diamond layer by the incident photons. The critical E_{ph} (≈3 – 3.5 keV) corresponds roughly to the penetration depth of the photons in diamond which equals to the thickness of the detection (topmost undoped diamond) layer. It is also found that QE increases more strongly with the increasing E_{ph} at V_b = 100 V than at V_b = 10 V, indicating that both the location the excited carriers are created and the number of the excited carriers are important factors for the observed signal amplification phenomenon. A possible origin of the amplification is considered to be related to the local high fields formed near the thin TiN electrodes [3,4].

This work was partly supported by the JSPS, Grant-in-Aid for Scientific Research (B) (19360018).

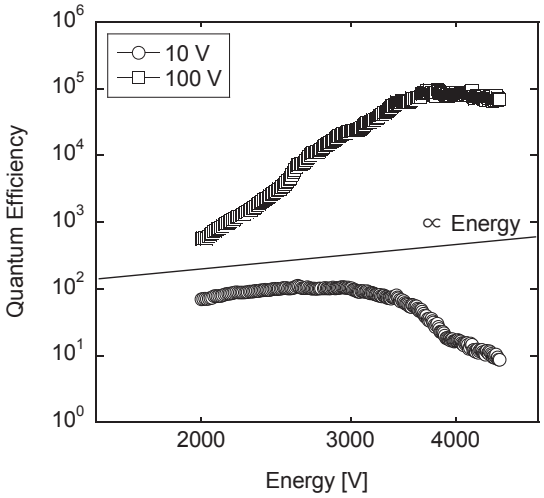

Fig. 1. Photon energy dependence of the quantum efficiency of a diamond detector at the detector bias voltages of 10 and 100 V.

[1] T. Teraji, T. Ito, J. Cryst. Growth **271** (2004) 409.
[2] T. Teraji *et al.*, Diamond Relat. Mater. **13** (2004) 858.
[3] H. Matsubara *et al.*, Diamond Relat. Mater. **16** (2007) 1044.
[4] Y. Iwakaji *et al.*, Appl. Surf. Sci. *in press*.

Evaluation of New Monochromatic Light Sources for ELEPES

G. Funabashi[1], A. Sekiyama[1], H. Fujiwara[1], M. Hasumoto[2], T. Ito[2], S. Kimura[2], P. Baltzer[3], S. Suga[1]

[1]*Graduate School of Engineering Science, Osaka University, Toyonaka, Osaka 560-8531, Japan*

[2]*UVSOR-II, Institute for Molecular Science, Okazaki, Aichi 444-8585, Japan*

[3]*MB Scientific AB, Seminariegatan 29B, SE-75228, Uppsala, Sweden*

In recent years, the extremely-low-energy (< ~12 eV) excitation photoemission study called ELEPES (extremely low energy photoelectron spectroscopy) has attracted much attentions due to its high potential for high bulk-sensitivity and high energy-resolution. However, this technique is not so popular because there are no conventional light sources at present. Therefore, we propose the new monochromatic light sources for ELEPES by means of rare-gas (Ar, Kr, and Xe) resonance lines and the low-energy-pass filters (LiF, CaF_2, and sapphire).

We performed the transmission measurement and the monochromatization experiment at BL1B and BL7B of UVSOR-II, respectively.

Ar I resonance lines appear at ~1040 and 1060 Å. The transmittance limit of LiF is located at ~1040 Å at room temperature (RT). This value is insufficient to realize a single monochromatic line. According to the transmission measurement, the limit wavelength is ~ 1045 Å at ~50 °C which should be sufficient to cut the 1040-Å component. Thus, Ar I resonance lines are monochromatized by LiF heated up to ~50 °C resulting in 1060-Å (11.7-eV) monochromatic light. Kr I resonance lines appear at ~1158 and 1230 Å. The transmittance limit of CaF_2 is located at ~1205 Å at RT and it is sufficient to monochromatize those lines. Thus, we can get the monochromatic light of 1230 Å (10.1 eV) from Kr. Finally, Xe I resonance lines appear at ~1464 Å and below 1300 Å (Fig. 1(a)). The transmittance limit of sapphire is located at ~1430 Å at RT and it is sufficient to monochromatize the lines. We can obtain the monochromatic light of 1464 Å (8.47 eV) from Xe (Fig. 1(b)).

Additionally, we measured the line width of Kr I and Xe I main lines. The line width of Kr I main line was measured not with the highest resolution setting. However, the obtained spectrum can be fitted by a Gaussian curve with the width of 1.34 meV. Considering the resolution, the intrinsic line width is estimated to better than 1 meV. On the other hand, the line width of Xe I main line was measured with the highest resolution setting (E/ΔE~20,000) at the sacrifice of the intensity. The obtained spectrum is fitted by a Gaussian with the width of ~600 μeV (Fig. 1(c)). The energy resolution at this wavelength (1464 Å) is ~423 μeV, so the intrinsic line width of Xe I main line is estimated to be ~426 μeV, which is, at least, much better than 500 μeV.

For the transmission efficiency, the transmittance of 1-mm-thick LiF heated up to ~50 °C is approximately 40% at 1060 Å (Ar I). Those of 1-mm-thick CaF_2 and 2-mm-thick sapphire at RT are approximately 50 and 45% at 1230 (Kr I) and 1464 Å, respectively. The thinner (0.5-mm-thick) filters are expected to be more transparent at each line (Ar I: ~55%, Kr I and Xe I: ~80%). Therefore, we can obtain the monochromatic lines with high intensity by using them.

In conclusion, we proposed the new monochromatic light sources for ELEPES using rare-gas (Ar, Kr, and Xe) resonance and the low-energy-pass filters. Performance test was performed. Thus, it was found that they are useful new ultrahigh-resolution monochromatic light sources for ELEPES.

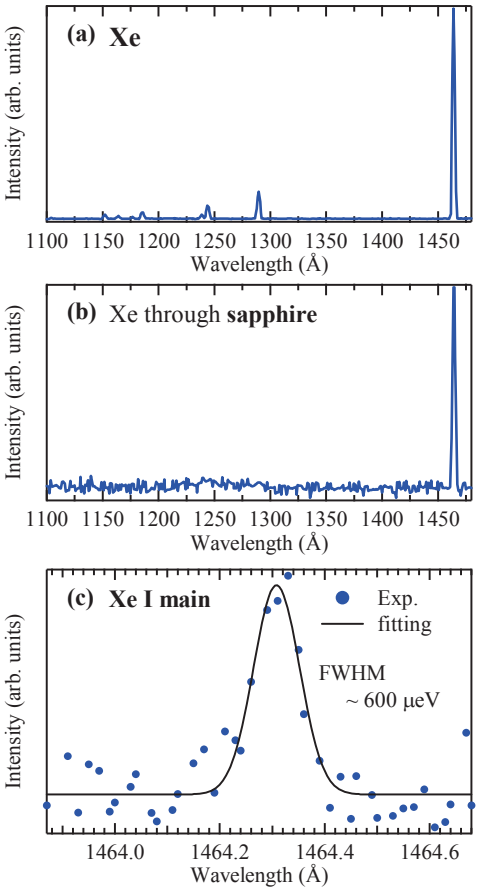

Fig. 1. (a) Xe resonance lines without filter, (b) monochromatized spectrum by using a sapphire filter at RT. (c) Major resonance line of Xe lamp for the highest resolution setting of the monochromator (~20,000).

BL4B

X-Ray Magnetic Circular Dichroism System Using Superconducting Magnet and Liquid He Cryostat

T. Nakagawa[1], Y. Takagi[1], Y. Matsumoto[2], T. Yokoyama[1]
[1]*Institute for Molecular Science, Okazaki 444-8585 Japan*
[2]*Japan Atomic Energy Institute, Tokai, Ibaraki 319-1195, Japan*

Introduction

The X-ray magnetic circular dichroism (XMCD) technique has become matured as a valuable element-specific tool for the determination of microscopic spin- and orbital magnetic moments method. The measurement under high magnetic field and low temperature is substantially important when one wants to investigate, for instance, magnetic anisotropy. This is because saturation magnetization is essential to estimate precisely the spin and orbital magnetic moments along a magnetically hard axis. Since the XMCD system with a superconducting magnet and a liquid He cryostat [1] is not popular around the world especially for public use, we have exploited a new system in this work [2].

Design and Performance

We have designed and fabricated a new XMCD measurement system with a 7 T UHV-compatible superconducting magnet. The system consists of two separated UHV chambers for XMCD measurement and sample preparation. The schematic view and image of the system are depicted in Fig. 1. The sample preparation chamber is equipped with metal evaporators, reflection high-energy electron diffraction (RHEED) or low-energy electron diffraction and Auger electron spectroscopy (LEED/AES) optics, an ion gun, a sample heating system, and so forth. The chamber is evacuated with a turbo molecular pump, a non-evaporation getter pump and a Ti sublimation pump. The base pressure is around 8×10^{-11} Torr.

The measurement chamber was constructed by JANIS Research Company. The system (model 7THM-ST-UHV) consists of a superconducting magnet and a variable temperature insert. The magnet is a 7 T (horizontal field) split multifilamentary NbTi superconducting magnet with a homogeneity of ±0.5% over a 1 cm diameter sphere. The sweep speeds are 1 T/min up to 5 T and 0.25 T/min from 5 to 7 T. A liquid helium reservoir with a 25 l capacity and a minimum of 12 h static hold time (24 h hold time without applying magnetic field) was used.

The sample cryostat has a built in heater and two calibrated Cernox thermometers plus a two-section high-efficiency continuous-flow-type liquid helium transfer line. This offers the lowest sample temperatures of ~4.8 K for accumulated He and ~3.8 K for pumped He.

The sample cryostat can be rotated 360°, allowing us to measure angle-dependent XMCD spectra. A sample holder is a hexagonal Mo with a screw. For future magneto-optical Kerr effect (MOKE) and/or laser-induced photoemission MCD measurements, the chamber possesses several ICF70 viewing ports accessible to the center of the magnet. These ports enable the MOKE measurements with the polar and transverse configurations. The chamber is pumped with a turbo molecular pump, which can be shut down during liquid He insertion. The base pressure is below 2×10^{-10} Torr at the ionization gauge position and should be much lower at the sample position.

The XMCD system was installed at Beamline 4B of UVOSR-II in IMS. The beamline is a bending-magnet soft X-ray station equipped with a varied line spacing grating monochromator, which covers the photon energies of 25–1000 eV. The circularly polarized X-rays were obtained by adjusting the vertical aperture upstream of the first mirror. The circularly polarization factor of P_c=0.70–0.85 can be obtained with a reasonable photon intensity.

The examples of measured spectra can be referred to in this booklet.

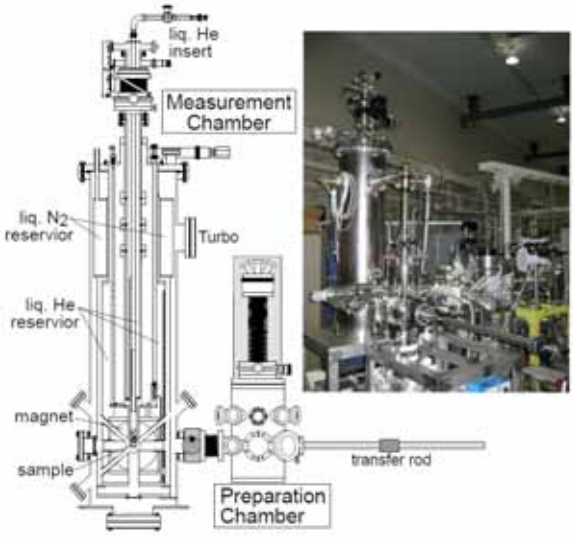

Fig. 1. Schematic rear view and image of XMCD measurement system. The X-rays come from the back surface with a configuration parallel to a magnetic field. The liquid He reservoir with a 25 *l* capacity is surrounded by a liquid nitrogen reservoir with a nominal 10 *l* capacity.

[1] T. Koide, T. Shidara, H. Fukutani, Rev. Sci. Instrum. **63** (1992) 1462.
[2] T. Nakagawa, Y. Takagi, Y. Matsumoto, T. Yokoyama, Jpn. J. Appl. Phys., *in press*.

BL4B

Sensitivity Calibration of a Compact Flat-Field EUV Spectrometer for the Development of Extreme Ultraviolet Light Sources

H. Tanuma[1], H. Ohashi[1], S. Suda[1], S. Fujioka[2], H. Nishimura[2], K. Nishihara[2], T. Kaneyasu[3]

[1]*Department of Physics, Tokyo Metropolitan University, Tokyo 192-0397, Japan*

[2]*Laser Engineering, Osaka University, Osaka 565-0871, Japan*

[3]*UVSOR Facility, Institute for Molecular Science, Okazaki 444-8585 Japan*

Extreme ultraviolet lithography (EUVL) is expected to be used as one of the key technologies in the next generation semiconductor device production. Noting that a Mo/Si multi-layer mirror has the highest reflectivity of about 70% at 13.5 nm of wavelength, a light source peaking of emission around 13.5 nm should be selected for the EUVL technology. For this purpose, a laser-produced plasma (LPP) of tin and xenon is an extremely attractive light source due to its compactness and high efficiency, and it has been investigated both experimentally and theoretically all over the world in this decade [1].

For the understanding of plasmas, spectroscopic data on ions composing the plasmas is definitely required as necessary information. The available spectroscopic data on tin and xenon ions, however, is fairly limited at this moment in time. Publishing works on xenon ions through December 2002 have been compiled by Saloman [2]. Even in this most detailed article about the energy levels and spectral lines of xenon ions, the numbers of levels and lines are not so many and not nearly as good as complete for the multiply charged states. On the other hand, the spectroscopic data of tin ions has not be compiled since the historical work by Moore [3] and is extremely scanty in particular for highly charged states.

In order to provide the fundamental spectroscopic data on tin and xenon ions, we have performed the measurement of various emission spectra from multiply charged tin and xenon ions with charge exchange spectroscopy in Tokyo Metropolitan University [4-6]. In a series of these experiments, we have used a compact flat-field grazing-incident spectrometer, which is equipped with a toroidal-type conversing mirror and a varied line spacing groove grating blazed at 100 nm, and a liquid nitrogen cooled CCD camera as a detector. Efficiencies of the spectrometer and the detector depend on the wavelength. To discuss not only absolute emission intensities also relative intensity distribution, the efficiency should be investigated by experimental measurements.

Absolute efficiency of a similar grating has been studied using bremsstrahlung continuum from LHD (Large Helical Devise) plasmas in NIFS [7], and the sensitivity of a similar CCD has been measured in the synchrotron radiation facility BESSY [8]. However, we wish to know the efficiency of the overall system.

Figure 1 shows a typical spectrum measured in this experiment. This spectrum was observed with injection of 14 nm as the first order light from UVSOR at BL4B with the grating G3 into the compact EUV spectrometer. As can be seen, the prominent peak is at 7 nm. This finding indicates that the second order of the diffraction at the G3 is significant. Not only the higher order light from the G3 but also higher order light from the grating GC in the compact spectrometer can be observed in this figure. For example, the weak peak at 8 nm can be assigned as the 4th order of the GC and the 7th order of the G3.

Because of the very complicated contribution of the higher order lights, the analysis of the obtained data has not be finished at all. We, however, wish to continue the analysis to obtain some results on the higher order diffraction of the gratings and the detection efficiency of the spectrometer.

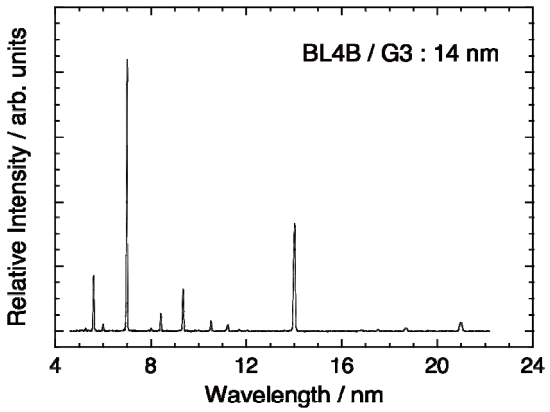

Fig. 1. Observed emission spectrum with injection of 14 nm into a compact EUV spectrometer.

[1] V. Bakshi, "EUV Light Sources for Lithography" (SPIE Press, Washington, 2005).
[2] E. B. Saloman, J. Phys. Chem. Ref. Data **33** (2004) 765.
[3] C. E. Moore, NSRDS-NBS **35** (1971).
[4] H. Tanuma *et al.*, Nucl. Instrum. Meth. B **235** (2005) 331.
[5] H. Tanuma *et al.*, J. Phys. Conf. **58** (2007) 231.
[6] H. Ohashi *et al.*, J. Phys. Conf. **58** (2007) 235.
[7] M. B. Chowdlhuri *et al.*, Rev. Sci. Instrum. **78** (2007) 023501.
[8] G. Schriever *et al.*, Rev. Sci. Instrum. **68** (1997) 3301.

BL5B

Design and Fabrication of Wide-Band Multilayer for 40 – 30 nm Region

T. Goto[1], T. Ejima[1], S. Kimura[2]

[1]*Institute for Multidisciplinary Research for Advanced Materials, Tohoku University, Sendai 980-8577 Japan*

[2]*UVSOR Facility, Institute for Molecular Science, Okazaki 444-8585 Japan*

Monochromators used in the vacuum ultraviolet region (λ<200nm) are normal-incidence one in longer wavelength region (λ>50nm) and grazing-incidence one in shorter wavelength region (λ<50nm) [1], because normal-incident reflectances of conventional mirrors decrease in the shorter wavelength region. Merit of the normal-incidence monochromators is high wavelength-resolution if both types of monochromators can be applied in a same wavelength region. Recently, some reflection multilayers were developed in 50 – 30 nm wavelength region, therefore possibility that normal incidence monochromators will be applied in this wavelength region was suggested [2, 3]. In this study, it were made that design and fabrication of wide-band reflection multilayer mirrors and applying developed-multilayers to the M1 mirror of BL7U at UVSOR-II [4].

Multilayers for normal incidence (ϕ=7.5°) were designed to increase the bandwidth while maintaining the reflectivity in 40 – 30 nm wavelength region. The first step of the design was to select material pairs that show high reflectance in the wavelength region. Among the selected pairs, the pairs to show wide bandwidth of reflectance were chosen. Finally, Mg/SiC pair was remained, because reflection multilayers using this material pair show both high reflectivity and wide band-width. Obtained design parameters are listed in Table 1, and the calculated reflectances using these parameters are shown as solid curves in Figure 1.

The multilayers were deposited on Si substrates (L25.4×W25.4×H10mm) for the M1 mirrors of BL7U beamline using a conventional magnetron sputtering system (ANELVE SPL-500). For evaluation of fabricated multilayer mirrors, the multilayers were deposited simultaneously on Si wafers. Deposition rates were controlled to keep periodic lengths of the multilayers constant in the mirror area. Obtained deposition rate of the Mg deposition was 5.8 nm/min, and of the SiC deposition, 0.87 nm/min in average. The error of the periodic lengths of fabricated multilayers estimated from XRD measurements was ±2% in the mirror area.

Reflectance measurements were made using the G3M4 combination of BL5B beamline. Wavelength resolution λ/Δλ was about 200. Obtained results are shown as squares and triangles in Fig. 1. Squares represent the reflectance of the center of the mirrors, and triangles, of the edge of the mirrors. The peak reflectances of the multilayers are about 0.3, and its values between the center and the edge of the mirrors are nearly equal to each other. Fabricated 4 multilayer mirrors cover 43 – 28 nm wavelength region with that their reflectances are 0.2 or more. These multilayer mirrors were installed in the M1 mirror of BL7U beamline. Throughput of this beamline in this wavelength region was about 10 times or more greater than the previous one, which used conventional Au mirror as the M1 mirror [4].

Table 1. Design parameters for wide-band multilayers in 40 – 30 nm wavelength region.

Multilayer No.	Periodic number	Periodic length D (nm)	Thickness ratio $\gamma=d_{SiC}/D$
1	7	16.6	0.42
2	7	18.0	0.41
3	6	19.8	0.40
4	6	22.2	0.40

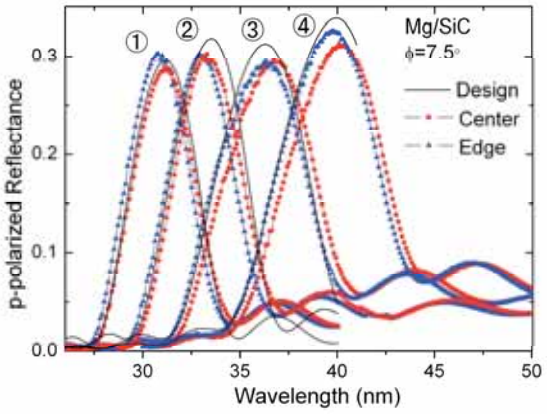

Fig. 1. Calculated and measured reflectances of wide-band multilayer mirrors. Numbers at the peaks represent the multilayer number in Table 1.

[1] Vacuum Ultraviolet Spectroscopy II, edited by J. A. Samson, D. L. Ederer (Academic Press, San Diego, CA, 2000), Chap. 1 & 2.

[2] Y. A. Uspenskii *et al.*, Optics Letters **23** (1998) 771.

[3] T. Ejima *et al.*, Jpn. J. Appl. Phys. **40** (2001) 376.

[4] S. Kimura *et al.*, UVSOR activity report 2006 (2007) 50.

BL5B

Evaluation of Higher Order Diffraction Light Contaminations at EUV Region by Using Transmission-Grating Spectrometer

F. Suzuki[1], T. Ito[1], K. Fukui[1], T. Hatsui[2], N. Kosugi[2]
[1]*Dept. Elec. Elec. Engi., Univ. of Fukui, Fukui 910-8507, Japan*
[2]*Institute for Molecular Science, Okazaki 444-8585, Japan*

Absolute measurement of physical properties generally requires quantitative information on the unwanted higher diffraction-order intensity in light sources. However, there are many difficulties to evaluate the higher diffraction-order intensity in EUV region. The energy analysis of the photoelectron emitted from the appropriate material which is irradiated by the target monochromatized light is one way to realize the evaluation of the higher-order contaminations, but the composition of the photo-electron spectrometer is complicated and the operation is not so easy. Another way to realize the evaluation is using the second monochromator. It means that the target monochromatized lights by the first monochromator are monochromatized again by the second monochromator. In EUV region, however, this method also has the difficulties, because the diffraction efficiency of the reflectance grating under the grazing incidence condition is quite sensitive to the incidence angle. On the other hand, the diffraction efficiency under the normal incidence is not sensitive. However, the normal incidence condition in EUV region is only achieved by the use of transmission grating which is very difficult to fabricate. In this experiment, our object is to present a simple but precise method for the evaluation by using the compact transmission grating spectrometer (CTGS).

A CTGS is equipped with a quasi-free-standing transmission grating with groove density of 5882 l/mm made by electron-beam lithography and a nickel electroplating method. The collimated mono-chromatized light by both the 100 um aperture and a 100 um entrance slit is re-monochromatized by the transmission grating which is located just behind the entrance slit. The re-monochromatized light is detected by the silicon photodiode (SPD) which is mounted on the linear motion stage. This stage is apart 196.5 mm from the grating and is able to move along to the dispersion direction of the grating.

The present method has been first applied to the plane-grating monochromator beamline (BL5B). Figure 1 shows the typical spectrum observed by the CTGS. The incident light is monochromatized 17.8 nm by the G2-M22 configuration of BL5B. The peak at 17.8 nm is basically denoted as (1 - 1) peak, where the label is denoted as (diffraction order of the monochromatized light by PGM – diffraction order of the re-monochromatized light by CTGS). The peaks at 8.9 nm and 5.9 nm are labeled as (2 – 1) and (3 – 1) peaks, respectively. Fig. 1 also suggests that (4 – 1) peak is negligible small. In other word, 17.8 nm light under G2-M22 configuration has up to 3rd order contaminations. Then, 17.8 nm peak is definitely labeled as (1 – 1)+(2 – 2)+(3 – 3) peak, and 26.7 nm peak as (2 – 3) peak. By measuring spectral profile of EUV light from G2-M22 configuration at each wavelength using CTGS, higher diffraction- order light intensity in EUV light source, and dependence of CTGS efficiencies on wavelength, are determined self-consistently. The results assume only the detection efficiency of SPD (IRD Inc., AXUV-100). Figure 2 shows number of the photon ratio r_n of the n-th diffracted contamination to the 1st order light at the G2-M22 configuration of BL5B. Fig. 2 represents the purity of the monochromatized light under G2-M22 configuration is good at shorter wavelength side and is consistent with the optical design of BL5B.

.

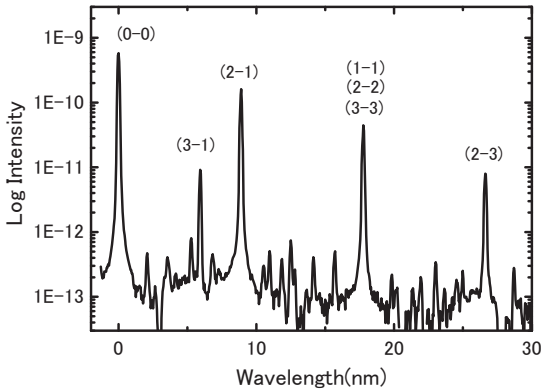

Fig. 1. Typical spectrum of the CTGS at 17.8 nm.

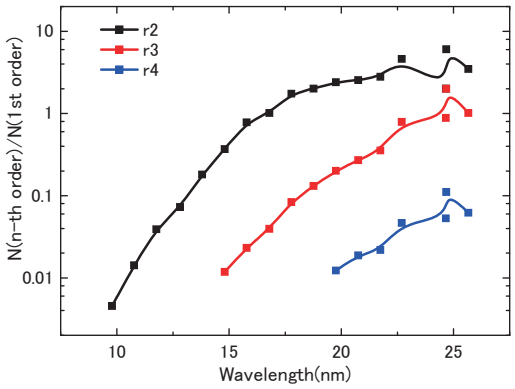

Fig. 2. Number of the photon ratio r_n of the n-th diffracted contamination to the 1st order light at the G2-M22 configuration of BL5B.

BL5B

Measurement of Absolute Efficiency for Micro Channel Plates by Using Pure-Calibrated EUV Beam

K. Yoshioka[1], G. Murakami[1], T. Toyota[1], G. Ogawa[1], A. Yamazaki[2], I. Yoshikawa[1]
[1]*Department of Earth and Planetary Science, Graduate School of Science, The University of Tokyo, Tokyo 113-0033 Japan*
[2]*Institute of Space and Astronautical Science, Japan Aerospace Exploration Agency, Sagamihara, Kanagawa 229-8510 Japan*

Introduction

We study the tenuous atmosphere of the planet Mercury thorough the optical observations. One of the main components of the atmosphere is helium. The atom has resonance scattering emission lines in the extreme ultraviolet (EUV) region, at 58.4nm. The intensity of the emission is proportional to column density of the scattered particle under the assumption of the optically thin condition. The information of the amount and the distribution of helium are crucial for discussing about the current environment and the evolution of the planet.

The Mercury Planetary Orbiter (MPO) in the BepiColombo mission will be launched in 2013 and put into the orbit around the Mercury after 6.5-year-long cruise. An ultraviolet Spectrometer, PHEBUS (Probing of Hermean Exosphere by Ultraviolet Spectroscopy) that is loaded onto the MPO will observe the atmosphere of Mercury in the EUV and FUV (far ultraviolet) region from the Mercury orbit. In our experiment, in order to calibrate the sensitivity of the PHEBUS, we measure the quantum efficiency of the micro channel plates (MCPs) which we use as the standard detector, at 58.4nm line.

Measurement and Result

We install a Sn (354.5nm) filter on the entrance of the SOR beam to eliminate the multi-order lines from the 58.4nm line with PGM35. At first, we investigate the purity of the 58.4nm line through the Sn filter. We judge the purity from the consistency between the wavelength characteristics of an Sn (173nm) filter for the particular lines at the EUV facilities of Institute of Space and Astronautical Science (ISAS) and those for the continuous lines at UVSOR. The former is measured for the emission lines of the helium gas with the discharge light source. Fig. 1 shows the transmittances of the filter measured at ISAS and UVSOR. It is clear that transmittances of the filter are consistent around the wavelength 58.4nm. We interpret from the result that the pure 58.4nm can be introduced through the Sn filter by using PGM35.

With the available pure 58.4nm line, then we measure the quantum efficiency of the MCPs. The quantum efficiency is calculated by the rate of the MCPs count to the electron yield of the photo diode which is absolutely calibrated. The result of the measurement shows that the quantum efficiency of the MCPs is 11.9±1.4% at 58.4nm line.

As the next step, in addition to the 58.4nm line, we plan to measure the quantum efficiency at the 73.4nm and 83.4nm lines, which are other observational objects of PHEBUS (73.4nm is the emission line of Neon and 83.4nm is that of the ionic oxygen). Then the purities of 73.4nm and 83.4nm lines are essential, and must be investigated for the next machine time.

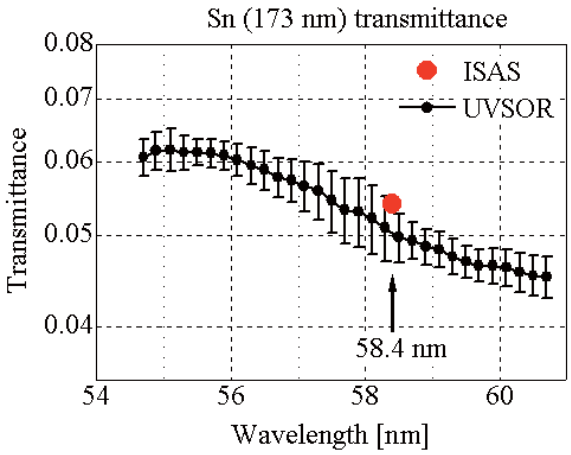

Fig. 1. The transmittances of a Sn (173nm) filter. The red dot shows the results of the measurements at the EUV facility of ISAS (the error is smaller than the dot size) and the solid line with dots shows that at UVSOR.

BL6U

Design of a New Monochromator for BL6U

E. Shigemasa[1], Y. Hikosaka[1], E. Nakamura[1], N. Kondo[1], T. Horigome[1], K. Amemiya[2]
[1]*UVSOR Facility, Institute for Molecular Science, Okazaki 444-8585 Japan*
[2]*Photon Factory, Institute of Materials Structure Science, Tsukuba 305-0801 Japan*

Various types of monochromators for synchrotron radiation have been proposed and constructed to realize vibrational spectroscopy in the soft x-ray range (100 ~ 1000 eV), which contains the *K*-shell thresholds of chemically important elements like C, N, and O, since the first successful observation for the vibrational structures of the π* resonance in the *K*-shell photoabsorption spectrum of nitrogen molecules [1]. Thanks to the high brilliance offered by undulator radiation, both high-resolution and high-flux are achievable simultaneously at a considerable high level. At the UVSOR, there is only one soft X-ray undulator beamline for high resolution spectroscopy, BL3U, in the photon energy region of interest.

Concerning the utilization of the first in-vacuum type undulator, which has been relocated from the long straight section U7 to the short one between B05 and B06, a new project for constructing the undulator beamline BL6U has been initiated. We have decided to choose the entrance slit-less configuration for the monochromator. A varied-line-spacing (VLS) plane grating monochromator (PGM) seems to be one of the most trustworthy ones to realizing high resolution in the soft x-ray range. In order to cover a wide photon energy region (30-500 eV) with one single grating, a variable-included-angle Monk-Gillieson mounting VLS-PGM [2], in which the grating is illuminated by converging soft X-rays, has been selected. Design study for the monochromator at BL6U has been completed, with the collaboration of KEK-PF. The monochromator designed will cover the photon energy ranging from 30 to 500 eV, with the resolving power higher than 10000 and the photon flux more than 10^{10} photons/sec.

Figure 1 shows a schematic layout of the optical elements of the present VLS-PGM. In front of all optical elements, there is an aperture S_0, located 5.0 m from the source position. The usual setting of this aperture is 2.0 mm^V × 2.0 mm^H, which limits the half acceptance angle to 0.4 $mrad^V$ × 0.4 $mrad^H$. The radiation is deflected horizontally by a toroidal mirror M_0 located 1.5 m downstream of the aperture. M_0 is one of the most important optical elements to realizing high resolution, which essentially focuses the radiation onto an exit slit S_1, and converging soft X-rays illuminate the VLS grating indicated by G. A plane mirror M_1 is located 1.5 m behind M_0. M_0, M_1, and G (Si substrates) are cooled from both sides by water-cooled copper alloy blocks. One laminar profile plane grating, which is ruled holographically, with the varied-line-spacing, is designed to cover the energy range from 30 eV to 700 eV. The groove density of the grating is 500 l/mm at its center position. The included angle of the grating should be changed from 167° to 176° in order to minimize the aberrations. A refocusing mirror M_2 has a toroidal shape, which focuses the monochromatized radiation at the sample position. All the grating and mirrors are coated with Au.

The resolution of the present monochromator was studied by ray-tracing simulation as well as analytical estimation. As a result, it is found that a resolving power E/ΔE of more than 10000 is achievable over the energy range from 30 to 500 eV with one single grating having the groove density of 500 l/mm. The throughput photon flux estimated ranges from 10^{10} to 10^{12} photons/sec for the ring current of 350 mA, with a resolving power of 10000. The practical construction of BL6U is expected to start from the summer of 2008.

[1] C. T. Chen, Y. Ma, F. Sette, Phys. Rev. A **40** (1989) 6737.
[2] K. Amemiya. T. Ohta, J. Synchrotron Rad., **11** (2004) 171.

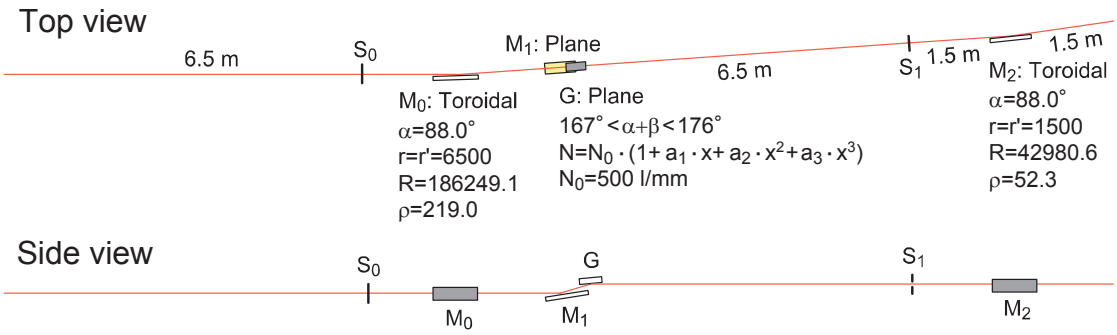

Fig. 1. Schematic layout of the monochromator designed for BL6U.

BL7U

Performance Test of High-Throughput Three-Dimensional Angle-Resolved Photoemission Spectroscopy at BL7U

T. Ito[1,2], S. Kimura[1,2], M. Sakai[1]

[1]*UVSOR Facility, Institute for Molecular Science, Okazaki 444-8585, Japan*

[2]*School of Physical Sciences, the Graduate University for Advanced Studies (SOKENDAI), Okazaki 444-8585, Japan*

In FY2006, we have constructed a new VUV beamline BL7U equipped with a three-dimensional angle-resolved photoemission (3D-ARPES) apparatus [1]. The aim of this beamline is to investigate the anisotropic interaction at the Fermi surface (FS) of inter-metallic compounds [1], namely "Fermiology", which is one of the most facilitated research fields in recent days, since the interactions among carriers, local spins, and lattice vibrations play a dominant role in the functionality of materials. After adjustment of the beamline and ARPES apparatus, we realize high-throughput 3D-ARPES beamline for the bulk-sensitive Fermiology of strongly correlated electron systems (SCES).

The BL7U equips an APPLE-II-type undulator for the VUV light source, a Wadsworth-type VUV monochromator, a multi-channel electron energy analyzer (MBScientific AB; 'Peter' A-1) and a liquid-helium flow-type cryostat with a 6-axis manipulation system (R-dec Co. Ltd.; i-Gonio). The light source and monochromator provide high-energy resolution ($E/\Delta E \geq 10^4$) with high photon flux ($\geq 10^{12}$ ph/s). The definition of the 6-axis of the manipulator are illustrated in Fig. 1.

Figure 2 shows a 3D-ARPES result on a strongly correlated 4f electron compound CeSb. With tuning sample tilting (θy) as well as photon energy (hν), we have successfully mapped out the 3D FS topology of cigar-shaped hole-like FS at the X point (image plot in Fig. 2), which is well reproduced by the band calculation (3D illustration in Fig. 2). It should be noted that the acquisition time of the present three dimensional (3D) FS image together with the 3D band structure is within 6 hours. The present high-throughput measurement can be realized by the wealth of the high-photon flux at BL7U as well as the 6-axis sample manipulation systems.

The present result clearly indicates that the VUV 3D-ARPES gives us a detective information of bulk 3D electronic structure which can be compared with band calculations. Furthermore, this method makes it possible to elucidate the origin of various functionalities through the direct observation of anisotropic interactions as quasi-particle band dispersions. In turn, it also derives a key for opening a new research field of *functionality design* by understanding the essential origin of various functionalities in the future.

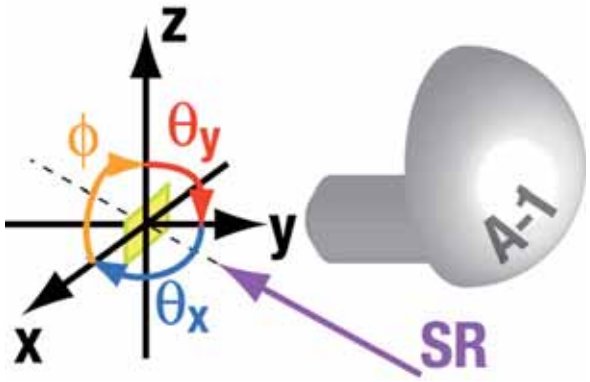

Fig. 1. The definition of 6-axis of the manipulator with respect to a sample (yellow square) together with the experimental layout of 3D-ARPES.

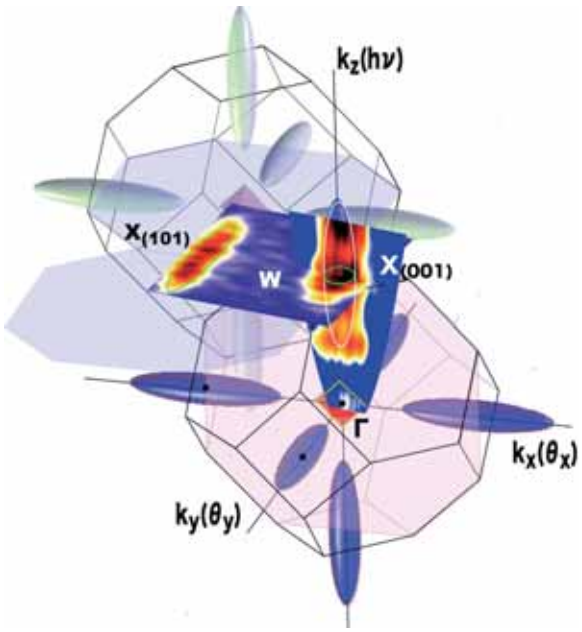

Fig. 2. 3D-FS image of CeSb obtained by mapped out the 3D-ARPES intensity at the Fermi level. 3D illustration of calculated FS is also depicted.

[1] S. Kimura *et al.*, AIP Conf. Proc. **879** (2007) 527.

BL8B1

Characterization of Mo/Si Multilayer Mirror for Time-Resolved Spectroscopy with Laser High Order Harmonic Pulses

M. Fushitani[1,2], A. Matsuda[1], A. Hishikawa[1,2,3]

[1]*Dept. of Photo-Molecular Science, Institute for Molecular Science, Okazaki 444-8585, Japan*

[2]*Dept. of Physical Sciences, The Graduate University for Advanced Studies (SOKENDAI), Okazaki 444-8585, Japan*

[3]*PRESTO, Japan Science and Technology Agency, Saitama 332-0012, Japan*

Recent advances in laser technology have allowed us to generate laser high-order harmonics (HH) in the soft X-ray region by focusing intense femtosecond infrared (IR) laser pulses to gaseous nonlinear media [1]. The laser HH pulses have characteristic features as 1) high photon energies extending up to the keV region, 2) ultrashort pulse duration on an attosecond timescale, 3) high photon flux comparable to synchrotron radiation, and 4) simple and precise synchronization of other laser light sources. Because of these aspects, the laser HH pulses are of great interest as a potential light source for time-resolved spectroscopy of ultrafast dynamics of electrons and nuclei that could not be elucidated in real time by conventional techniques.

To fully utilize the characteristics of laser high-order harmonics, appropriate optical components need to be employed. The laser HH pulses consist of odd order harmonics with different photon energies below the "cut-off" [1]. The harmonic-order (or wavelength) selection could be achieved by using a grating with large incident angles. In this case, however, the time resolution will be significantly reduced because of the pulse stretching due to large optical path differences. To keep pulse duration as short as possible, multi-layer coated mirrors are preferable. Among them, the molybdem/silicon (Mo/Si) multilayer has been widely used as a reflective coating for optical mirrors in the 13 nm (95 eV) region. In order to use one of the harmonics, Mo/Si multilayer mirrors with a narrow band width can be fabricated in such a way that only the selected harmonic pulse is reflected. In the present study, we characterize reflectance of Mo/Si multilayer mirrors at small incident angles.

The reflectance measurements of Mo/Si multilayer mirrors (NTT-AT Inc.) were performed at BL8B1. The synchrotron radiation, which was dispersed by the G3 grating (360 l/mm), was measured as reference light simultaneously by using gold (Au) mesh and Si photodiode (AXUV100, IRD Inc.) detectors in an energy range of 30~140 eV. The energy scale was calibrated with a sharp absorption edge of an aluminium (Al) filter (a thickness of 120 nm, Luxel Inc.) at 72.7 eV as well as that at 36.3 eV due to the second order light from the grating. From the transmission of the Al filter around the 90 eV region, the higher order light contribution was estimated to be less than 4 % of the total current of the Au and Si detectors. The light reflected by the Mo/Si multilayer mirror was detected at various incident angles of 5~27.5 degree by using the Si photodiode. The light before reflection was also monitored by the Au mesh, by which the intensity of incident light with respect to that of the original reference light is normalized at each wavelength.

Figure 1 shows reflectance of a Mo/Si multilayer mirror as a function of photon energy. The incident angle (θ) was varied from 5 to 27.5 degree with a step of 2.5 degree. The reflectance was determined to be 60 %, irrespective of the incident angle except for θ = 27.5°. The reflectance peak shifts toward the higher energy side while the band width becomes narrower as the incident angle increases. For θ = 5°, the peak position and the full width at half maximum of the reflectance were determined to be 89.6 eV and 2.8 eV, respectively. In this arrangement, the Mo/Si mirror selectively reflects the 59th harmonic (89.7eV) of an IR laser pulse at 815 nm (1.52 eV).

We are very grateful to the staff of the UVSOR facility.

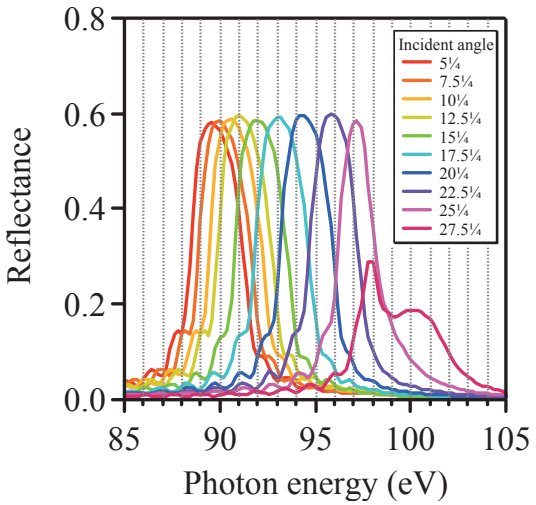

Fig. 1. Reflectance of Mo/Si multilayer mirror at incident angles between 5 and 27.5 degree.

[1] T. Brabec, F. Krausz, Rev. Mod. Phys. **72** (2000) 545.

BL2B

Performance Test of Z-Stack MCP Mounted in a TOF Mass Spectrometer

C. Huang[1], H. Katayanagi[1,2], Md. S. I. Prodhan[2], H. Yagi[1], B. P. Kafle[2], K. Mitsuke[1,2]
[1]*Institute for Molecular Science, Myodaiji, Okazaki 444-8585, Japan*
[2]*Graduate University for Advanced Studies, Myodaiji, Okazaki 444-8585, Japan*

The microchannel plates detector (MCP) is a kind of universal and traditional tool which is used for detection of photons and charged particles in a large variety of applications including imaging spectroscopy, electron spectroscopy, mass spectrometry, astronomy, molecular atomic collision studies, cluster physics and so on. The detection efficiency (η) of MCP is a very important parameter and is known to be a complicated function of the kinetic and internal energies and the mass to charge ratio (m/z) of impinging particles and the bias voltage. As for the conventional two-stage MCP, the η value decreases rapidly with the increase of m/z at m/z >150.[1] Compared with the two-stage MCP, the η of z-stack MCP (three-stage MCP) is much easier to be saturated.

Recently we have replaced the two-stage MCP in our TOF mass spectrometer by a three-stage MCP which includes three microchannel plates at the BL2B endstation of UVSOR. Some rare gases, i.e. helium, neon and krypton are utilized to test the performance of the new MCP. In the experiment, the output signal from the MCP was amplified with a preamplifier (EG&G, Ortec, 9301, gain=10) and an amplifier (EG&G, Ortec, 9302, gain=20), then discriminated by a constant fraction discriminator (EG&G, Ortec, 474). After the discrimination, the signal was processed by a time-to digital converter (FastComtec, 8867). Ion counts were normalized by photonflux and sample pressure to evaluate the relative η value.

Here we show the results of Kr as an example. In the experiment, the normalized signal counts of singly, doubly and triply charged ions of Kr were attained using several MCP bias voltage at $h\nu$=90eV. Fig 1 shows the dependence of normalized signal counts of Kr on the discriminator level when the MCP bias voltage is set to -2.7kV, -2.8kV, -2.9kV and -3.0kV.

In this figure, the normalized signal counts of individual Kr^{z+}(z=1-3) ions are almost the same when the discriminator level increases from 200 mV to 600 mV and the MCP bias voltage changed from -2.7kV to -3.0kV. At a given discriminator level, the count rate of Kr^{z+}(z=1-3) ion signal do not depend on the bias voltage. The same results were found in the helium and neon results. The ratios between multiply charged ions and singly charged ions of these rare gases were kept almost constant with the change of the discriminator level and bias voltage. Therefore, we concluded that η of z-stack MCP is made to operate in a saturate manner in the broad range of discriminator level and MCP bias voltage. Finally we determined the relative ion counts of C_{60}^{z+} (z=1-3) and their concomitant fragment ions. The η is saturated when the bias voltage is set to above 2.95 kV.

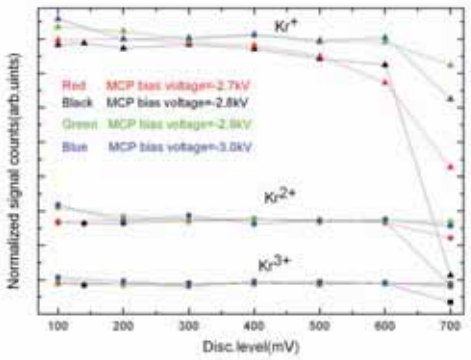

Fig. 1. The dependence of normalized signal counts on the discriminator level at different MCP bias voltages.

[1] K. Mitsuke *et al* J. Phys. Chem. A **111** (2007) 8336.

BL2B

Development of a New Momentum Imaging Spectrometer with the Use of Synchrotron Radiation Photoionization

C. Huang[1], H. Katayanagi[1,2], Md. S. I. Prodhan[2], H. Yagi[1], B. P. Kafle[2], K. Mitsuke[1,2]

[1]*Institute for Molecular Science, Myodaiji, Okazaki 444-8585, Japan*

[2]*Graduate University for Advanced Studies, Myodaiji, Okazaki 444-8585, Japan*

A novel momentum imaging spectrometer has been constructed to investigate dissociation mechanism of fullerenes molecules combining synchrotron radiation photoionization in the VUV in BL2B of UVSOR. The structure of the new apparatus is similar to the conventional velocity map imaging spectrometer developed by Eppink and Parker [1].

The performance of the spectrometer has been tested by using the He, Ne, Ar, Kr, SF_6 and CF_4. The best focusing condition was found to be

$$\frac{V_{ext} - V_{tub}}{V_{rep} - V_{tub}} = 0.7 .$$

Here V_{ext}, V_{rep} and V_{tub} correspond to voltages which applied to TOF extractor plate, TOF repeller plate and TOF tube respectively.

Figure 1 is the image of the Kr ions which was measured at the best focusing condition at $h\nu$=35eV. The inverse abel transform (IAT) [2] was applied to analyze all the image data. In the data processing, Welch window was used to suppress background noise. The velocity distribution of the projected ions was extracted from the raw data by using IAT method.

The Maxwell-Boltzman distribution of all of the rare gas ions has been calculated at the room temperature (300K). Comparing the velocity distribution of rare gas ions with the calculated Maxwell-Boltzman distribution, we found our experimental results agree with the calculated distribution Fig.2 shows the velocity distribution of Xe^{z+}(z=1-3).

Very recently, the first imaging data of the C_{60} ions have been achieved using the imaging setup in BL2B [3].

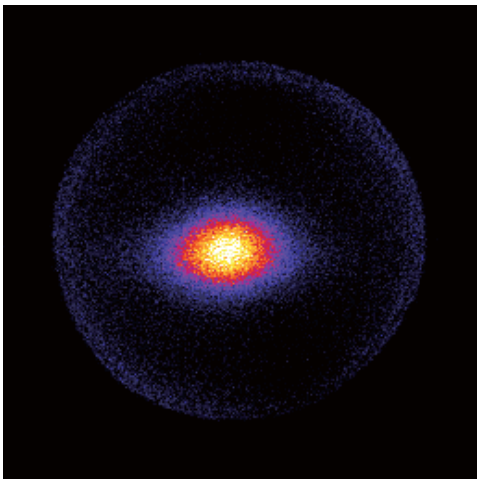

Fig. 1. The imaging of Kr ions which were measured at the best focusing condition at $h\nu$=35eV.

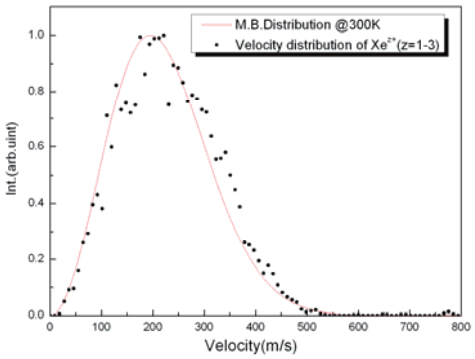

Fig. 2. The velocity distribution and the Maxwell-Boltzman distribution at 300K of Xe^{z+}(z=1-3).

[1] A. T. J. B. Eppink, D.H. Paker, Rev. Sci. Instrum. **69** (1997) 3477.

[2] A. J. R. Heck, D. W. Chandler, Annu. Rev. Phys. Chem., **46** (1995) 335.

[3] H. Katayagagi, *et al*, in preparation.

BL2B

Evaluation of the Optical Oscillator Strength of C_{60} in the Valence Region

B. P. Kafle[1], H. Katayanagi [1,2], S. I. Prodhan[1], H. Yagi [2], C. Huang [2], K. Mitsuke [1,2]

[1]*Graduate University for Advanced Studies, Okazaki 444-8585, Japan*

[2]*Department of Photo-Molecular Science, Institute for Molecular Science, Okazaki 444-8585, Japan*

We have reevaluated the absolute partial cross section $\sigma_{abs}(z+)$ for the formation of the ions in a charge state z from C_{60} [1], by applying essentially the same method as that employed in our previous studies for estimating $\sigma_{abs}(z+)$ (z = 1 - 3) at $h\nu$ = 25 to 120 eV ([2] and refs. therein). Specifically, the absolute partial cross section $\sigma(z+)$ for the formation of C_{60}^{z+} can be expressed as

$$\sigma_{\mathrm{abs}}(z+) = \frac{R(z+)}{\Phi n L F \tau} \cdot \frac{1}{\eta_{\mathrm{abs}}(z+)} . \quad (1)$$

Here, $R(z+)$ is the signal count rate of the photoions in a charge state z produced from C_{60}, Φ is the photon flux of synchrotron radiation, n is the number density of C_{60} in the ionization region, L is the length of the ionization volume along the light path, F is the repetition rate of the pulsed electric field, τ is the average residence time of the ions in the ionization volume under the field free condition. Open circles, triangles, and squares in Fig. 1 indicate, respectively, the absolute partial cross sections $\sigma(+)$, $\sigma(2+)$, and $\sigma(3+)$ for the formation of C_{60}^{+}, C_{60}^{2+}, and C_{60}^{3+} from C_{60}. Each partial cross section includes the contribution of not only the parent but also fragment ions produced by the sequential loss of a C_2 unit. Hence, it is equal to the cross section involving all the ionic species in a particular charge state.

In Fig. 2, open circles represent the sum of $\sigma_{abs}(+)$, $\sigma_{abs}(2+)$, and $\sigma_{abs}(3+)$ which is nearly equal to the total photoionization cross section $\sigma_{abs,I}$. In the $h\nu$ range from ~ 45 to 120 eV the present curve of $\sigma_{abs,I}$ is in fair agreement with the $\sigma_{abs,I}$ reported by Reinköster *et al.* [3] and absolute photoabsorption cross section curve $\sigma_{abs,A}$ by Colavita *et al.* [4]. This may prove the validity of our data analysis. Our $\sigma_{abs,I}$ of 401 Mb at $h\nu$ = 25.5 eV is a little smaller than $\sigma_{abs,A}$ determined by Jaensch and Kamke [5].

The oscillator strength f was calculated, by combining the present $\sigma_{abs,I}$ curve with the $\sigma_{abs,A}$ data given in Ref. [5] ($h\nu$ = 11.4–25 eV) and Yasumatsu *et al.* ($h\nu$ = 3.5–11.4 eV) [6]. The value integrated over the $h\nu$ range from 3.5 to 40.8 eV was 120.4 and that from 3.5 to 119 eV was 156.0. These values are significantly smaller than the corresponding oscillator strengths of 187.6 and 233.4 expected from the TKR sum rule and 60 times the total photoabsorption cross section of a C atom, $60\times\sigma$(C) [7]. The insufficiency of f is entirely predictable because the $\sigma_{abs,A}$ data points of Ref. [5] lie much lower than those compiled by Berkowitz [7]. Many authors have argued that the most dependable equilibrium vapor pressures of C_{60} were given by Piacente *et al.* in 1995 [8]. By using their vapor pressure data, we have reevaluated $\sigma_{abs,A}$ of Refs. [5] and [6]. As a result the f values were recomputed to be 178.5 and 230.5 for the $h\nu$ ranges, respectively, from 3.5 to 40.8 eV and from 3.5 to 119 eV. These values agree well with those expected from the TKR sum rule and $60\times\sigma$(C), namely 187.6 for the former range and 233.4 for the latter range.

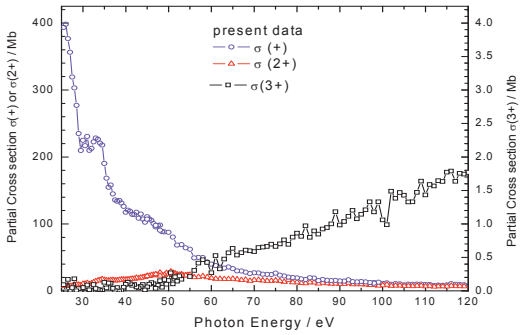

Fig. 1. Partial cross sections for single, double and triple photoionization of C_{60} determined from eq. (1).

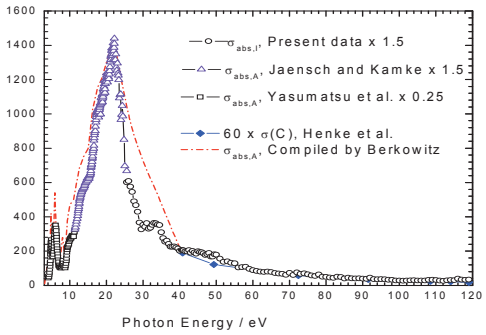

Fig. 2. Total photoionization and photoabsorption cross sections of C_{60} in the $h\nu$ range of 3.5–119 eV.

[1] B. P. Kafle *et al.*, J. Phys. Soc. Jpn. **77** (2008) 014302.
[2] K. Mitsuke *et al.*, J. Phys. Chem. A **111** (2007) 8336.
[3] A. Reinköster *et al.*, J. Phys. B **37** (2004) 2135.
[4] P. Colavita *et al.*, Phys. Chem. Chem. Phys. **3** (2001) 4481.
[5] R. Jaensch, W. Kamke, Mol. Mater. **13** (2000) 143.
[6] H. Yasumatsu *et al.*, J. Chem. Phys. **104** (1996) 899.
[7] J. Berkowitz, J. Chem. Phys. **111** (1999) 1446.
[8] V. Piacente *et al.*, J. Phys. Chem. **99** (1995) 14052.

BL2B

Velocity Map Imaging of C_{60} Molecular Beams

H. Katayanagi[1,2], C. Huang[1], S. I. Prodhan[2], H. Yagi[1], B. P. Kafle[2], K. Nakajima[3], K. Mitsuke[1,2]

[1]*Department of Photo-Molecular Science, Institute for Molecular Science, Okazaki 444-8585, Japan*

[2]*Graduate University for Advanced Studies, Okazaki 444-8585, Japan*

[3]*Faculty of Letters, Hosei University, Chiyoda-ku, Tokyo 102-8160, Japan*

The photoion images of fullerene (C_{60}) molecular beams were observed with the velocity map imaging technique [1]. The temperature of the beam was derived from the images and was consistent with that of the fullerene oven.

The design of our imaging setup was described elsewhere [2]; here we explain the experimental procedure briefly. The C_{60} sample was loaded in a cylindrical quartz cell and heated up by a heater around 700-800 K in vacuum. The C_{60} vapor passed through two apertures and reached the ionization region, where the C_{60} molecular beam intersected the monochromatized synchrotron radiation. Ions produced at the ionization region were extracted by a velocity map imaging electrode assembly and projected on to a position sensitive detector (PSD) of 25 mm in diameter and 375 mm away from the ionization region. No mass selection was made. We thus obtained two-dimensional (2D) projections of three-dimensional (3D) scattering distributions of the ions on the PSD. Focusing conditions of this electrode assembly were determined in advance using rare gases at room temperature as samples.

An image of the ions produced by photoionization of C_{60} at the photon energy of 70 eV is shown in Fig. 1a. The synchrotron radiation passes parallel to the abscissa and the C_{60} beam to the ordinate of the image. The image is parallel to the plane spanned by the synchrotron radiation and the C_{60} beam. Spatial distributions of C_{60}^+ directly reflect those of parent C_{60} in the beam. An acute vertical intense part is clearly observed at the center of the image. This part can be assigned to a projected shape of the C_{60} beam, or a 2D projection of 3D velocity and angular distribution of the beam, because the intensity of this part changed with changing the sublimation rate of C_{60} which can be controlled with the adjustment of the oven temperature. Around the "base" of the acute component, a subtle round component also exists. We considered that this component originated from ionized residual gases and, if any, fullerene vapor which stagnates around the ionization region. The acute component shows cylindrical symmetry around its major axis since the fullerene beam source mechanically has cylindrical symmetry.

We tried to derive the velocity distribution, or the temperature of the C_{60} beam from the present results. We measured a background image experimentally without fullerene evaporation and subtracted it from the image with fullerene evaporation. We regarded the major axis of the acute component as a cylindrically symmetric axis and applied the inverse Abel transform with which we can calculate a 2D section of the 3D distribution [3]. On the section, distance from an origin of the image is directly proportional to velocity. The origin and a coefficient to convert the distance into velocity were obtained from the ion images of Kr at room temperature. The velocity distribution of C_{60} beam is shown in Fig. 1b. Solid curve in Fig. 1b shows shifted Maxwell-Boltzmann (MB) distribution of which temperature was set to the same as that of the fullerene oven. The experimental distribution agreed well with the MB distribution with a small shift of 15 m/s.

As a result of the present experiment, we concluded that our imaging setup worked well even with fullerenes. We will observe photofragment ion images from fullerenes in order to investigate the dynamics of dissociative photoionization of fullerenes. In addition, an establishment of the present beam diagnostic method of evaporating fullerenes will allow us to design a new type of beam monitor for MBE or CVD experiments.

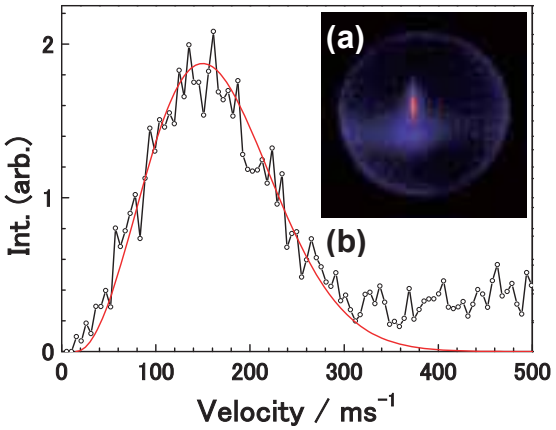

Fig. 1. (a) Ion image of C_{60} beam. (b) Velocity distribution of C_{60} beam. Black curve shows velocity distribution of C_{60} beam derived from (a), red curve shows MB distribution of 785 K with a shift of 15 m/s.

[1] A. T. J. B. Eppink, D. H. Parker, Rev Sci. Instrum. **68** (1997) 3477.

[2] B. P. Kafle *et al.* AIP Conf. Proc. **879** (2007) 1809.

[3] S. M. Candel et al. Comput. Phys. Commun. **23** (1981) 343.

BL2B

Total Electron Yield Spectroscopy and Electron-Signal-Triggered TOF Mass Spectrometry Developed for the Studies on Photodissociation Dynamics of Fullerens

H. Katayanagi[1,2], C. Huang[1], S. I. Prodhan[2], H. Yagi[1], B. P. Kafle[2], K. Nakajima[3], K. Mitsuke[1,2]

[1]*Department of Photo-Molecular Science, Institute for Molecular Science, Okazaki 444-8585, Japan*

[2]*Graduate University for Advanced Studies, Okazaki 444-8585, Japan*

[3]*Faculty of Letters, Hosei University, Chiyoda-ku, Tokyo 102-8160, Japan*

In order to detect all the photoelectrons from fullerenes, we modified a threshold electron analyzer [1] which could be attached easily at the opposite side of ion time-of-flight (TOF) and imaging spectrometers [2]. The performance of the modified electrodes as a total electron detector was inspected by measuring total electron yield (TEY) spectra and electron-signal-triggered ion TOF mass spectra of Kr.

We originally designed and produced the threshold electron analyzer to perform threshold electron photoion coincidence (TEPICO) experiments in order to clarify the dynamics of dissociative photoionization of fullerenes (C_{60}, C_{70}, etc.) [1]. The TEPICO experiments will allow us to determine the internal energies of parent ions uniquely. Meanwhile, we utilize the total electron detector for the following purposes: (1) supplying start triggers in the imaging experiments to select masses of ions imaged, (2) measuring the absolute photoionization cross sections of fullerenes from their TEY spectra. This method is more advantageous from the total ion yield (TIY) measurements, because the detection efficiency of a microchannel plate detector depends on the mass-to-charge ratios (m/z) of fullerene ions.

We have revised the former electron analyzer so as to make it applicable to the total electron detector by enlarging the diameters of the holes on lenses and applying higher voltage to the lenses and even to a stray electron shield covering the electrodes.

We measured TEY spectra of Kr in the photon energy range of 90-96 eV. The Kr sample was introduced to the chamber through a needle valve. A typical pressure in the chamber was 2×10^{-6} Torr. Figure 1 shows a typical TEY spectrum of Kr. This spectrum agrees very well with the TIY spectra measured at BL2B previously [3], except a small rise of the baseline because of stray electrons.

We also tried to measure TOF spectra of Kr^{z+} ions using the electron signal as a start trigger. Figure 2 shows a thus obtained TOF spectrum of Kr^{z+} at the photon energy of 55 eV. Peaks of singly and doubly charged Kr ions are clearly observed. The peaks have tails toward the longer flight time, which indicates a finer voltage adjustment is required. The peak area ratio of $(Kr^{2+})/(Kr^{+})$ is much larger than that we expected according to Ref. 4. This can be explained as a composite effect of the following reasons: doubly charged ions emit two electrons and thus double the probability of triggering, and the present electron detector has higher efficiency for the slower electrons produced by double ionization. The earlier peaks at flight times of 5.0 and 6.2 μs are probably due to residual water and nitrogen in the chamber. Although N_2 has almost the same m/z ratio as that of Kr^{3+}, the peak at 6.2 μs can be assigned to N_2^+ since the threshold for the triple ionization of Kr is 75 eV.

In summary, we concluded that this electron detector can be used to observe electrons from fullerenes of which number density is at most one order of magnitude smaller than those of rare gases, although further tuning of the detector will be needed.

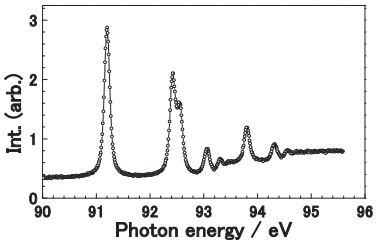

Fig. 1. Total electron yield spectra of Kr in the photon energy range of 90-95.6 eV. Peaks can be assigned to the $3d^{-1}{}_{5/2}$ and $3d^{-1}{}_{3/2}$ series.

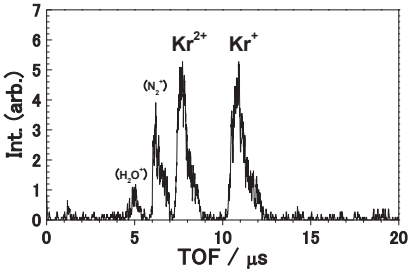

Fig. 2. Electron-signal-triggered TOF spectra of Kr^{z+} at the photon energy of 55 eV.

[1] H. Katayanagi *et al*., UVSOR Activity Report **33** (2006) 46.

[2] B. P. Kafle *et al*., AIP Conf. Proc. **879** (2007) 1809.

[3] M. Ono *et al*., Nucl. Instrum. Methods Phys. Res. A **467-468** (2001) 577.

[4] N. Saito, H. Suzuki, Int. J. Mass Spectrom. Ion Proc. **115** (1992) 157.

BL2B

Momentum Imaging of the Photofragments from C_{60} and Data Analysis of the Image

S. I. Prodhan[1], H. Katayanagi[1,2], B. P. Kafle[1], C. Huang[2], H. Yagi[2], K. Mitsuke[1,2]
[1]*The Graduate University for Advanced Studies Okazaki 444-8585, Japan*
[2]*The Institute for Molecular Science, Okazaki 444-8585, Japan*

We have developed a time-of-flight (TOF) based mass-selected momentum imaging spectrometer to observe the momentum distributions of the scattered fragments produced from dissociative photoionization of gaseous C_{60} at the BL2B in the UVSOR facility. We have adopted the Eppink-Parker type three-element velocity focusing lens system [1] (Repeller, Extractor, and Tube electrodes) to achieve the high kinetic energy (KE) resolution on the photofragment images. It is known that two possible mechanisms are proposed for the fragmentation processes [2,3], namely the sequential ejection of C_2 units as $C_{60}^+ \rightarrow C_{58}^+ + C_2$, $C_{58}^+ \rightarrow C_{56}^+ + C_2$, and the fission of C_{60}^+ to directly produce a final fragment as $C_{60}^+ \rightarrow C_{56}^+ + C_4$.

Several groups tried to distinguish the above two mechanisms by measuring the total average KE release in the decomposition of C_{60} into its fragments [4,5], though such efforts have met with failure because the two mechanisms give almost the same total average KE release. It is likely that expanding C_{56}^+ ion clouds arising from different reaction mechanisms give different shapes of image or different momentum distributions of C_{56}^+. We examined this statement by means of computer simulation and designed the momentum imaging apparatus [3] which is now installed in our experimental end station of BL2B.

In the momentum imaging technique the 3D momentum distributions of fullerene photofragment ions are projected on the 2D position sensitive detector (PSD). We performed the Monte Carlo simulation to generate the momentum images under the following conditions: TOF, 50μs; number of ions hitting at the surface of PSD, 8×10^5; temperature of the C_{60} molecular beam, 0K and 273K. The KE release in the C_2 or C_4 ejection takes a constant value of 0.4 eV, to a first approximation. Angular distribution is assumed to be isotropic and angles of ejection are selected randomly.

The simulated images of the fragment ion C_{56}^+ from C_{60} through the C_2 loss and C_4 loss mechanisms are depicted in Fig. 1. Obviously the two mechanisms are well distinguished at 0 K, but with increasing temperature they are hardly distinguishable. The experimental image of C_{56}^+ is a convolution of the momentum distribution of the parent C_{60} in the beam and that of C_{56}^+ produced by the reaction. We can observe the image of the parent C_{60}^+ (momentum distribution of C_{60} in the beam), as well as that of C_{56}^+. Thus, we are trying to deconvolute the effect of the initial C_{60} beam temperature by analyzing the image data.

We are carrying out experiments with C_{60} sample for checking the performance of the newly installed imaging spectrometer. The C_{60} and background images recently measured are shown in Fig. 2. The experimental conditions are given in the caption.

Fig. 1. Simulated 2D projections of the 3D scattering

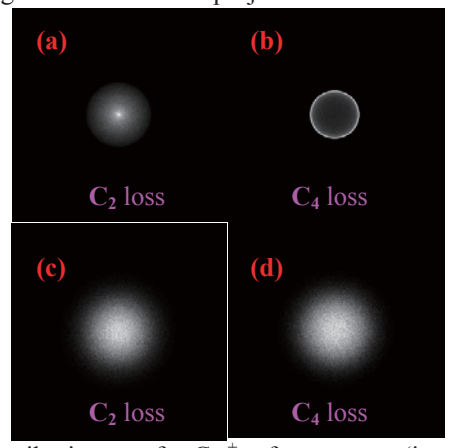

distributions of C_{56}^+ fragments (image size: 40×40mm). (a) and (c), sequential ejection of C_2 units; (b) and (d), fission of C_{60}^+. The beam temperature is 0K for (a) and (b) and 273K for (c) and (d).

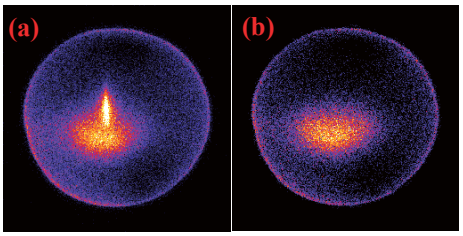

Fig. 2. (a) The experimental C_{60} image at beam temperature, 505.2°C (b) Background image at room temperature, 27°C. Photon energy,90eV; V_{MCP}, -2.2KV; V_{tube}, -350V; V_{rep}, 500V; V_{ext}, 250V; V_{deft}, 25V; data acquisition time, 60s.

[1] A.T. J. B. Eppink, D. H. Parker, Rev. Sci. Instrum. **68** (1997) 3477.
[2] K. Mitsuke *et al.*, AIP Conf. Proc. **811** (2006) 161.
[3] B. P. Kafle *et al.*, AIP Conf. Proc. **879** (2007) 1809.
[4] H. Gaber *et al.*, Z. Phys. D **24** (1992) 302.
[5] D. Muigg *et al.*, J. Chem.Phys. **108** (1998) 963.

BL3U

X-Ray Absorption Spectra of Small Kr Clusters: Mass-Selected Ion Yields with a TOF Spectrometer

M. Nagasaka, T. Horigome, T. Hatsui, N. Kosugi
Institute for Molecular Science, Myodaiji, Okazaki 444-8585, Japan

The cluster is an intermediate phase between isolated and condensed ones and has both properties of surface and bulk dependent on its size. Inner-shell spectroscopies such as X-ray absorption and photoelectron (XAS, XPS) are promising methods to investigate local, or site-selected, electronic structures [1, 2]. XAS and XPS of large clusters (average size N > 1000) show dominant bulk and surface features of clusters [1]. On the other hand, XPS of small clusters (N < 100) efficiently reveals several kinds of surface sites [2]. The site dependence in XAS of small clusters may be possible in neither total electron nor ion yield, because the amount of clusters is relatively low compared to monomers and dimers involved inherently in the adiabatic gas expansion. A component of small clusters should be extracted from the cluster/monomer/dimer mixture. In the present work, we have developed a compact time-of-flight (TOF) mass spectrometer to measure Kr_2^+ yields emitted from small clusters and then to obtain mass-selected ion yield spectra, which correspond to selective or enhanced XAS for small Kr clusters.

Kr clusters were produced by the adiabatic gas expansion. The gas was expanded through a 50 μm nozzle into vacuum with the stagnation pressure of 0.5 MPa, where the average size of Kr clusters was about 30. The Kr clusters were ionized or excited near the Kr $3d_{5/2}$ and $3d_{3/2}$ edges by using monochromatic soft x-rays from the high-resolution undulator beamline BL3U. In the present work, to get higher photon fluxes, photon energy band path was set to ~40 meV. To get XAS of small Kr clusters, the Kr_2^+ ions emitted from clusters after photoabsorption were collected as a function of photon energy by using a newly developed Wiley-McLaren type TOF mass spectrometer [3]. Figure 1 shows a schematic TOF mass spectrometer, where Kr_2^+ was triggered by pulsed voltage apparatus with the repetition ratio of 10 kHz, secondly accelerated, traveled in the drift tube, and collected by the MCP detector. The Kr_2^+ ions were extracted from the total signals by using delay-pulse generator and constant-fraction discriminator.

Figure 2 shows XAS of Kr clusters obtained in the present method. The spectra show contributions from both Kr atoms and Kr clusters. The peaks for Kr atoms also include contributions from Kr dimers, because the electronic state of dimers is close to that of atoms [2]. In the region of the lowest excitation $3d_{5/2}^{-1}5p$, the surface peak in the small clusters is clearly observed with 0.17 eV blueshift from the

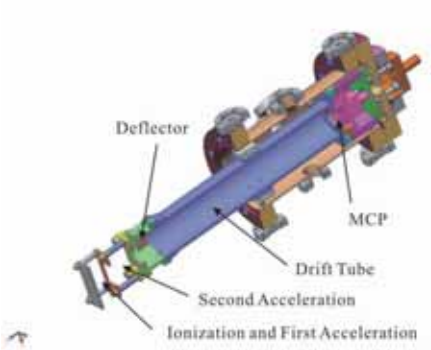

Fig. 1. Schematics of TOF mass spectrometer.

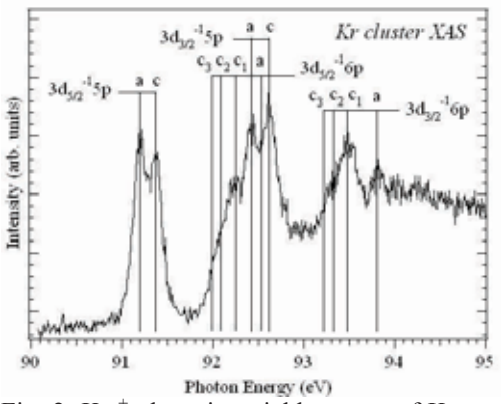

Fig. 2. Kr_2^+ photo-ion yield spectra of $Kr_{\sim 30}$ clusters, where a and c mean the Kr atoms/dimers and Kr clusters, respectively.

atomic/dimer peak. No bulk peak is observed. This blueshift is larger than the blueshift (0.13 eV) in large clusters (N ~ 4700) [1]. The cluster peaks in the $3d_{3/2}^{-1}5p$ region are also blue-shifted by 0.19 eV. On the other hand, the cluster peaks in the $3d_{5/2}^{-1}6p$ and $3d_{3/2}^{-1}6p$ regions are red-shifted by 0.29 eV and 0.32 eV, respectively, whereas 0.45 eV redshifts are reported in the $3d^{-1}6p$ peaks of large clusters [1].

The $3d^{-1}5p$ cluster peak (blue-shifted) widths are similar to the atomic/dimer ones, but the $3d^{-1}6p$ cluster peaks are broad with shoulder features c_1, c_2, and c_3 at the lower-energy part (red-shifted). In order to elucidate origin of these blue and red shifts, we are analyzing the present results by combining XPS, resonant XPS, and theoretical simulations.

[1] For example, M. Tchaplyguine *et al.*, J. Chem. Phys. **127** (2007) 124314.
[2] T. Hatsui *et al.*, J. Chem. Phys. **123** (2005) 154304.
[3] W. C. Wiley, I. H. McLaren, Rev. Sci. Instrum. **26** (1955) 1150.

BL3U

Resonant Auger Electron Spectra of Small Kr Clusters near the Kr 3d Thresholds

M. Nagasaka, T. Hatsui, N. Kosugi
Institute for Molecular Science, Myodaiji, Okazaki 444-8585, Japan

We have measured x-ray absorption spectra (XAS) of small krypton clusters (average size N ~ 30) by Kr_2^+ ion yields and successfully observed site-dependent surface $3d^{-1}np$ peaks [1]. In the present work, we applied resonant Auger electron spectroscopy (RAES) to the same small Kr clusters on the photoexcitation energies of $3d^{-1}5p$ and $3d^{-1}6p$ with distinct atom-surface energy shifts.

Kr clusters were produced by the adiabatic gas expansion through a 50 μm nozzle into vacuum with the stagnation pressure of 0.5 MPa, where the average size is estimated to be ~30, indicating only two or three bulk atoms and mostly surface atoms [1,2]. Kr clusters were excited by monochromatic soft x-rays from the undulator beamline BL3U. The photon energy band path was set to be 40 meV. RAES spectra were measured by using an electron energy analyzer, SES-200 combined with A-1 lens and detection system, with the pass energy of 100 eV [2].

Figures 1(a) and 1(b) show RAES spectra of small Kr clusters (with almost no bulk sites) by choosing the photoexcitation energies of cluster surface $3d_{5/2}^{-1}5p$ and $3d_{5/2}^{-1}6p$ transitions. In the clusters, difference between the $3d_{5/2}^{-1}5p$ and $3d_{5/2}^{-1}6p$ RAES spectra is relatively small. This may be mainly because the atomic 5p and 6p orbitals are strongly distorted and mixed in clusters. We could not remove atomic contributions in the cluster spectra.

The atomic RAES peaks are assigned according to the work of Jauhiainen *et al* [3]. We observed dominant *np* Rydberg series converging to ^{3}P, ^{1}D and ^{1}S $(4p)^4$ states, where the branching ratio is 16:53:31. This situation is also applicable to the cluster spectra; as compared with the atomic peaks, the $4p^45p$ cluster peaks are red-shifted by 0.6 eV and the $4p^46p$ cluster peaks are red-shifted by 2.1 eV. The stabilization energy in singly 3d ionized states is 0.5 eV in the same small clusters [1] and is 0.8 eV in the large clusters N = 4700 [4]. Thus, the stabilization energy of doubly 4p ionized states in the small cluster is 2.6 eV (2.1+0.5) and is 0.6 eV smaller than the corresponding atom-surface energy difference 3.2 eV in the large Kr clusters [4].

Similarly to the Kr 3d excitation spectra [1], Fig. 1 shows that the higher *np* Rydberg states (n > 6) are almost quenched in the $(4p)^4$ manifold in the cluster. Then, there may be n>>0 band-like features ("conduction band" [4]) around the single/double ionization thresholds. Normal Auger electrons from the single core hole state to doubly ionized states cannot be observed below the ionization threshold; however, resonant Auger spectra near the threshold sometimes show normal Auger-like features [4,5]. Although a 40.9 eV feature in Fig. 1(b) has not yet been successfully assigned, the peaks of 37.8 eV and 40.0 eV observed in Fig. 1(a) may be assigned to $(4p)^4np$ ^{1}D and ^{1}S with n >> 0 around the double ionization threshold. They are comparable to 37.0 and 39.3 eV double 4p ionization energies in the large cluster surface [4]. These discrepancies correspond to the difference in the stabilization energy of doubly 4p ionized states 0.6 eV as above discussed.

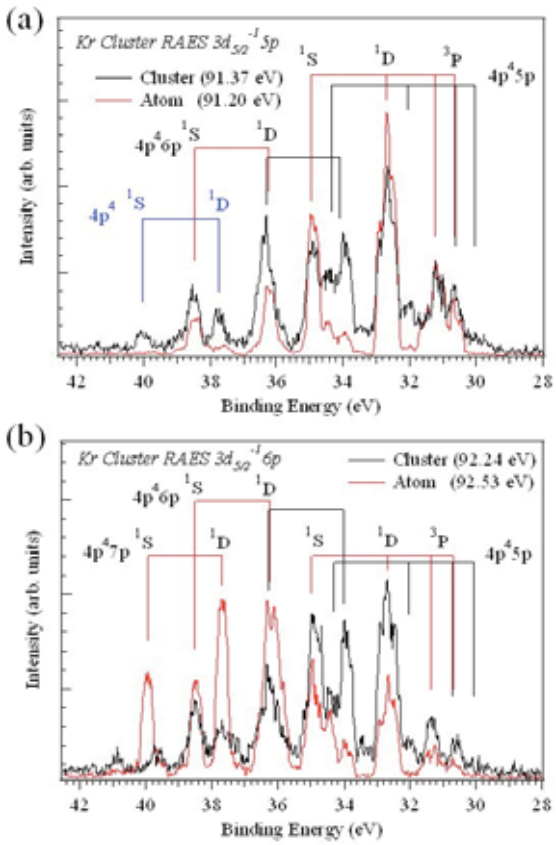

Fig. 1. RAES of Kr clusters (black line) following the (a) $3d_{5/2}^{-1}5p$ and (b) $3d_{5/2}^{-1}6p$ excitations in clusters [1], together with the atomic spectra (red line).

[1] M. Nagasaka *et al.*, in this volume.
[2] T. Hatsui *et al.*, J. Chem. Phys. **123** (2005) 154304.
[3] J. Jauhiainen *et al.*, J. Phys. B **29** (1996) 3385.
[4] M. Tchaplyguine *et al.*, J. Chem. Phys. **127** (2007) 124314.
[5] A. Kivimäki *et al.*, Phys. Rev. A **71** (2005) 033204.

BL4B

Formation of Metastable Carbonyl Sulfide (OCS) Dications Following Core-Hole Creation

M. Ito[1,2], K. Soejima[2], T. Kaneyasu[1], Y. Hikosaka[1], E. Shigemasa[1]
[1]*UVSOR Facility, Institute for Molecular Science, Okazaki 444-8585 Japan*
[2]*Graduate School of Science and Technology, Niigata University, Niigata 950-21 Japan*

While doubly charged molecular ions (or dications) are inherently unstable owing to the Coulomb repulsion between the nuclei, metastable molecular dications having lifetimes of at least μs order are known to exist from mass spectroscopic studies. In an inner-shell study of Carbonyl Sulfide (OCS), it has been reported that Auger decays of the S 2*p* core-hole states favorably populate metastable OCS^{2+}, in contrast to the case of the C 1*s* core-hole states [1]. In this study, we have used an Auger-electron-ion coincidence method to investigate formation mechanism of the metastable dications following the core-hole creations in OCS molecules.

The experiment was performed at BL4B, using the electron-ion coincidence spectrometer [2]. The electrons were analyzed in energy by a double toroidal electron analyzer, while ions were extracted from the interaction region into an ion momentum spectrometer by a pulsed electric field according to the detection of the electron. As an example, the time-of-flight (TOF) spectrum obtained in this way is shown in Fig. 1. To obtain sufficient Auger-electron counts, the coincidence data sets were recorded at three different photon energies as indicated in Fig. 1. The pass energy of the analyzer was set to E_{pass}=100 eV for the S 2*p* ionization, while for the C and O 1*s* ionization they were set to E_{pass}=240 eV. The resolving power of the energy analyzer was estimated to be better than $E_{pass}/\Delta E$=100.

Figure 2 shows the coincidence and conventional Auger spectra plotted in a binding energy scale. In order to obtain the coincidence spectra, the electron-ion coincidences are filtered by the time window corresponding to the flight time of the metastable OCS^{2+} (~3.5 μs). In this analysis, false coincidence signals due to uncorrelated particles were carefully subtracted from the raw data. The red curves depict conventional spectra while the blue curves represent the coincidence Auger spectra related to the metastable dications. The intensities are normalized to the conventional spectra, and thus the spectral intensities directly reflect the decay branching ratios.

The coincidence observation has revealed metastable character of the Auger final doubly charged states lying in the range 30 - 35 eV which are attributed to the valence two-hole $3\pi^{-2}$ states [3]. The metastable yields show dramatic increase in the S 2*p* core-hole creation. This intense production is qualitatively explained by considering the spatial distribution of the 3π orbital involved in the decay processes. Since the 3π valence orbital is mostly localized around the S atom in the OCS molecule [4], the 3π electron preferentially fills the S 2*p* core-hole due to a large overlap between the core and valence orbitals. Thus the Auger transition involving the 3π electrons is favored in the decay of the S 2*p* core-hole states rather than in those of the C and O core-hole states.

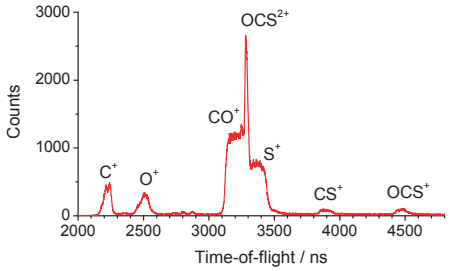

Fig. 1. TOF spectrum of ions measured in coincidence with sulfur LVV Auger electrons.

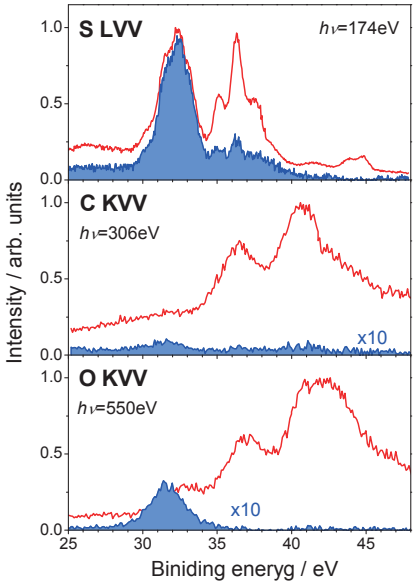

Fig. 2. Conventional (red curves) and coincidence (blue curves) Auger spectra of OCS. The coincidence spectra are extracted from the Auger-electron-ion coincidence data sets by filtering the Auger electron signals related to the formation of metastable OCS^{2+}.

[1] R. Feng *et al.*, Chem. Phys. **255** (2000) 353.
[2] T. Kaneyasu *et al.*, J. Electron Spectrosc. Relat. Phenom. **156-158** (2007) 279.
[3] T.X. Carroll *et al.*, J. Electron Spectrosc. Relat. Phenom. **51** (1990) 471.
[4] K.T. Leung, C.E. Brion, Chem. Phys. **96** (1985) 241.

BL4B

Stability and Dissociation of OCS^{2+} Formed via Auger Decays of S 2*p* Core-Hole States in OCS

T. Kaneyasu[1], M. Ito[1,2], Y. Hikosaka[1], E. Shigemasa[1]
[1]*UVSOR Facility, Institute for Molecular Science, Okazaki 444-8585 Japan*
[2]*Graduate School of Science and Technology, Niigata University, Niigata 950-21 Japan*

Auger decay is the main relaxation process following core ionization in molecules composed of light atoms. In the decay process, a valence electron fills the core-hole while another valence electron is ejected. Doubly charged molecules with two holes in the valence orbital, thus formed, often dissociate due to the Coulomb repulsion between the nuclear charges. The coincidence detection between the energy-selected Auger electrons and fragments ions is one of the most useful methods to gain a clear insight in the dissociation mechanism of the Auger final doubly charged states. We have developed an Auger-electron-ion coincidence spectrometer in which a toroidal electron energy analyzer and an ion momentum spectrometer are installed. In this report, we present a coincidence study on stability and dissociation of the Auger final states following the S 2*p* ionization of OCS.

The experiment was carried out on the beamline BL4B at the UVSOR facility. A detailed description of the spectrometer and data acquisition scheme were given in a previous paper [1]. An electron-ion coincidence data set was obtained for OCS at a photon energy of 174 eV corresponding to 2.15 eV above the S $2p_{1/2}$ threshold. Pass energy of the electron analyzer was set to E_{pass}=100 eV and the resolving power was evaluated to be better than $E_{pass}/\Delta E$ = 100. From the coincidence data set, we have extracted sulfur LVV Auger spectra for individual dissociation channels.

Figure 1(a) shows a conventional sulfur LVV Auger spectrum. Due to the spin-orbit splitting of the S 2*p* core-hole states (1.2 eV), the Auger spectrum is composed of two spectral components associated with individual core-hole states. The binding energy scale is calculated by subtracting the kinetic energy of Auger electrons from the ionization energy of the S $2p_{1/2}^{-1}$ core-hole state. Thus the scale is correct for the Auger lines related to the S $2p_{1/2}^{-1}$ state, but is shifted by 1.2 eV for those from the S $2p_{3/2}^{-1}$ state.

The spectrum shows band structures which are attributed to valence two-hole doubly charged states [2,3]. The assignment of the structures are denoted on the top of the spectrum. Auger electron spectra filtered by coincidences with OCS^{2+}, O^++CS^+ and $O+C^+$+S^+ are shown in Fig. 1(b)-1(d). The vertical bars in Figs. 1(c) and 1(d) indicate thermochemical thresholds for the ground states of the products. The intensities of the coincidence Auger spectra are normalized to that of the conventional spectrum, and thus the spectral intensity directly reflects the decay branching rations of the Auger final two-hole states. It is found that the $3\pi^{-2}$ states are mostly metastable, whose lifetimes should be much longer than the time-of-flight of OCS^{2+} (~3.5 μs) in the present spectrometer. The majority of the Auger final states around 36 eV corresponding to the $9\sigma^{-1}3\pi^{-1}$, $8\sigma^{-1}3\pi^{-1}$ and $2\pi^{-1}3\pi^{-1}$ states dissociates into CO^++S^+. The onset of this band structure exactly accords with the appearance potential (~34 eV) for the CO^++S^+ formation in valence double photoionization [4]. In the binding energy region above 40 eV, metastable OCS^{2+} can hardly be seen. The $9\sigma^{-1}2\pi^{-1}$ states in 40 - 43 eV predominantly dissociate into CO^++S^+. The high-lying states break apart into both the CO^++S^+ and $O+C^+$+S^+ fragments. The three-body dissociation arises only from the high-lying states.

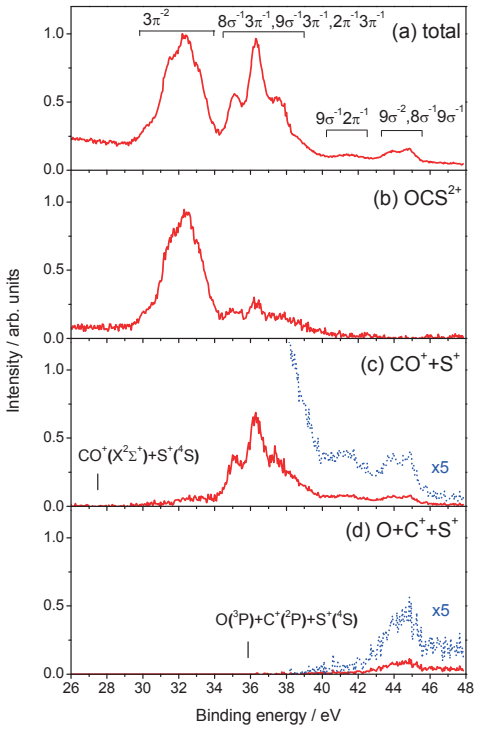

Fig. 1. (a) Conventional sulfur LVV Auger spectrum. Coincidence Auger spectra related to the formation of (b) metastable OCS^{2+}, (c) CO^++S^+ and (d) $O+C^+$+S^+.

[1] T. Kaneyasu *et al.*, J. Electron Spectrosc. Relat. Phenom. **156-158** (2007) 279.
[2] T. X. Carroll *et al.*, J. Electron Spectrosc. Relat. Phenom. **51** (1990) 471.
[3] D. Minneli *et al.*, J. Chem. Phys. **107** (1990) 6070.
[4] T. Masuoka, H. Doi, Phys. Rev. A **47** (1993) 278.

BL6B

Infrared Reflection-Absorption Spectroscopy of Alq_3 Thin Film on Silver Surface Using Synchrotron Radiation

Y. Sakurai[1], S. Kimura[1,2], K. Seki[3]

[1]*UVSOR Facility, Institute for Molecular Science, Okazaki 444-8585, Japan*

[2]*Department of Structural Molecular Science, The Graduate University for Advanced Studies, Okazaki 444-8585, Japan*

[3]*Department of Chemistry, Graduate School of Science, Nagoya University, Furo-cho, Chikusa-ku, Nagoya 464-8602, Japan*

Recently, organic semiconductors are attracting attention because of possible applications to electronic devices such as organic light emitting diodes (OLEDs). In OLEDs, tris(8-hydroxyquinoline) aluminum (Alq_3) is most widely used as the electron transport/light emitting material [1]. Alq_3 has two possible geometrical isomers of meridional (C_1 symmetry) and facial (C_3 symmetry) forms. In the meridional isomer, the three ligands around the central Al atom are not equivalent (Fig. 1(a)), while they are equivalent in the facial isomer (Fig. 1(b)). It has been reported that the meridional isomer is dominant in evaporated films [2]. However, in the case of Alq_3 molecules adsorbed directly on an Al surface, the facial isomer is predicted to be more stable than the meridional one by a theoretical investigation [3]. Since the facial isomer generally acts as an electron trap in amorphous film [4], this isomer may become an obstacle for the charge transport in the device [3,4]. Thus it is important to find whether facial isomer exists at the interface between the metal and the Alq_3 film or not.

Vibrational spectroscopy such as infrared (IR) spectroscopy is suitable technique for distinguishing these isomers. There is already an IR spectroscopic

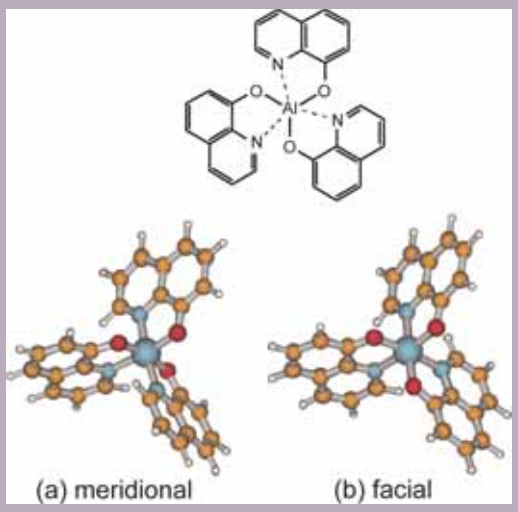

Fig. 1. The chemical structure and geometrical isomers of Alq_3.

study of the Alq_3 isomers by Cölle et al. using the facial isomer isolated in the pure form [5]. For the vibrational modes within the ligands observed in the wavenumber region above 700 cm^{-1}, the differences of the spectra between isomers appear only in the width of the absorption peaks. On the other hand, significant differences appear in the stretching modes around the central Al atom, namely, Al-N and Al-O stretching modes in the wavenumber region below 600 cm^{-1}. Therefore these modes become good probes to distinguish the isomers. In this study, we examined whether the facial isomer exists at the interface between the Ag and the Alq_3 film or not by infrared reflection-absorption spectroscopy (IRAS) using a synchrotron radiation (SR) light source. Use of highly brilliant infrared synchrotron radiation (IRSR) source enables us to obtain IRAS spectra in the low wavenumber region, which cannot be covered by conventional IRAS system using globar light source because of its low brilliance.

The SR-IRAS experiments were performed at an infrared-to-terahertz beamline BL6B of UVSOR-II. SR-IRAS system consists of an ultrahigh vacuum (UHV) chamber with evaporators (for Ag and Alq_3), focusing optics and a detector. Horizontally polarized parallel IRSR from a Michelson interferometer (Bruker IFS66v) is guided to an off-axis parabolic mirror with the focal length f of 152.4 mm to be focused on the sample surface with the incident angle of 80° relative to the surface normal. The reflected light is collected by the second off-axis parabolic mirror (f =152.4 mm) and guided to the third off-axis parabolic mirror (f =101.6 mm) to be focused on the detector. The UHV chamber is separated from the low vacuum of the focusing and collecting optics chambers by KRS-5 windows. The base pressure of the UHV chamber was below 5 x 10^{-7} Pa.

The Ag surface was prepared by vacuum evaporation on Si substrates (20 x 7 mm^2) using a Knudsen cell. Deposition of Alq_3, which was supplied by Nippon Steel Chemical Co., Ltd., was performed using a glass crucible coiled with a tungsten wire heater. The Ag surface was kept at room temperature during the deposition of Alq_3. The thickness of Alq_3 film was monitored using a

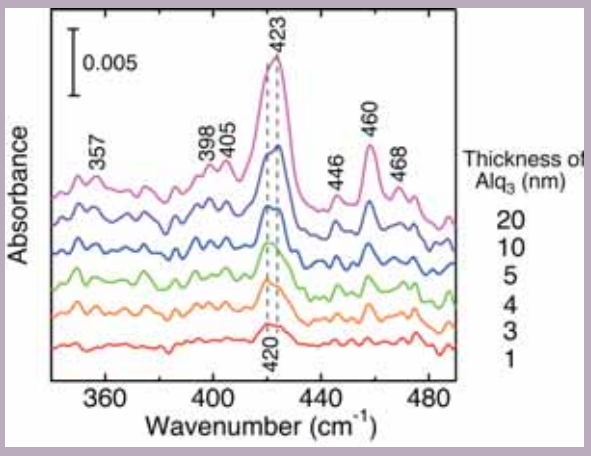

Fig. 2. The thickness dependence of the IRAS spectra of an Alq_3 film on Ag surface.

quartz microbalance. SR-IRAS spectra were accumulated with a 6μm-mylar beamsplitter in the Bruker system and a liquid-helium-cooled Si bolometer. Five (for 1 nm thick sample) or three (others) spectra of 100 scans each with a resolution of 2 cm^{-1} were averaged.

Figure 2 indicates the thickness dependence of the IRAS spectra of an Alq_3 film deposited on an Ag surface. In the spectrum of the film of 1 nm thickness, corresponding to nearly one monolayer, a peak at 420 cm^{-1} with a shoulder at 423 cm^{-1} is observed. With increasing thickness of Alq_3, peaks at 423 and 460 cm^{-1}, which are assigned to the Al-N stretching and pyramidalization modes of the nitrogen atoms [5], respectively, increase their intensity. There are also other Al-N stretching and pyramidalization modes with different phase relation among the ligands (for example, three Al-N bonds stretch in-phase or out of phase) from those mentioned above, and they appear as weak peaks at 398 and 405 cm^{-1} (Al-N stretching) and 446 and 468 cm^{-1} (pyramidalization) modes, respectively [5]. Considering the central AlO_3N_3 fragment, the meridional isomer has three Al-N stretching modes with different frequencies, while the frequencies of the corresponding modes in the facial isomer are split into two, with one of them doubly degenerated because of the C_3 symmetry [5]. All of them are infrared active. The observed spectra of the Alq_3 films, except for the one with 1 nm thickness, show three Al-N stretching modes at 398, 405 and 423 cm^{-1}. This indicates that the evaporated Alq_3 film predominantly consists of the meridional isomer as reported before [2]. In the IRAS spectra of the film of 1 nm thickness, two Al-N stretching modes at 397 and 405 cm^{-1} can not be observed. This can be understood if the molecules in the meridional form, since the estimated intensities of these peaks is only about 20% of that of the peak at 420 cm^{-1} [5], which is the same level as the noise. In the case of the facial isomer, on the other hand, the intensity of the peak around 398 cm^{-1} is expected to be almost half of that of the peak at 423 cm^{-1} [5], and this peak should be observed above the noise. In the spectrum of 1 nm thickness, however, no peak is observed at 398 cm^{-1}, and we can conclude that the meridional isomer is dominant even for the 1 nm thickness.

In the spectrum of the Alq_3 film of 1 nm thickness, the observed frequency of the Al-N stretching mode is slightly lower than that in the spectra of multilayer Alq_3. Similar "softening" of vibrational mode has been observed in the CH stretching mode of *n*-alkane adsorbed on metal surfaces, and it is ascribed to the small electron transfer from the metal to the molecule [6,7]. Moreover, DFT calculations by us show that the frequency of the Al-N stretching mode of Alq_3 anion is lower than that of Alq_3 molecule. Therefore the softening in the Alq_3/Ag system may originate from the small electron transfer from Ag to Alq_3 molecule. The observed much smaller frequency shift of the Al-N stretching mode of Alq_3 (3 cm^{-1}) than that of the CH stretching of *n*-alkanes (~100 cm^{-1}) might be understood by the larger distance between the central part of the Alq_3 and the Ag surface than that between the CH bond of flat-lying *n*-alkane molecule and the metal surface.

To summarize, thin Alq_3 films deposited on an Ag surface were investigated by IRAS using a synchrotron radiation light source. The observed IRAS spectra indicate that the Alq_3 film predominantly consists of meridional isomer including the first monolayer adsorbed on the Ag surface. In the spectrum of monolayer Alq_3, Al-N stretching mode slightly shifts to the lower wavenumber side than that of multilayer Alq_3, possibly due to the charge transfer between the Alq_3 and Ag surface.

[1] C. W. Tang and S. A. VanSlyke, Appl. Phys. Lett. **51** (1987) 913.
[2] M. Brinkmann *et al.*, J. Am. Chem. Soc. **122** (2000) 5147.
[3] S. Yanagisawa and Y. Morikawa, Chem. Phys. Lett. **420** (2006) 523.
[4] A. Curioni, M. Boero, and W. Andreoni, Chem. Phys. Lett. **294** (1998) 263.
[5] M. Cölle *et al.*, Phys. Chem. Chem. Phys. **5** (2003) 2958.
[6] M. Yamamoto *et al.*, J. Phys. Chem. B **104** (2000) 7363.
[7] Y. Hosoi *et al.*, Surf. Sci. **515** (2002) 157.

BL1B

Vacuum Ultraviolet Spectroscopy of Heavily Boron-Doped Diamonds

O. Arimoto[1], D. Gotoh[2], T. Katagiri[3], T. Aoki[3], D. Iri[3], M. Itoh[3]

[1]*Department of Physics, Kyoto Pharmaceutical University, Kyoto 607-8412, Japan*

[2]*Graduate School of Natural Science and Technology, Okayama University, Okayama 700-8530, Japan*

[3]*Department of Electrical and Electronic Engineering, Shinshu University, Nagano 380-8553, Japan*

Diamond is known as a band insulator of indirect type with a wide band gap of 5.5 eV [1,2]. By the slight doping of boron, it becomes a p-type semiconductor, making a shallow acceptor level above the top of the valence band with an activation energy of ~0.37 eV. With increasing boron concentration beyond the critical value $n_c \sim 2 \times 10^{20}$ cm^{-3} for the metal-insulator (MI) transition, the boron-doped diamond shows metallic character. Recently, Ekimov and coworkers have found superconductivity in the heavily boron-doped diamond synthesized by high-pressure high-temperature (HPHT) method [3]. Subsequently, studies on the superconductivity using films made by a microwave plasma-assisted chemical vapor deposition (MPCVD) method confirmed reproducibility of the superconductivity [4]. The MPCVD method is a useful technique to control the boron density in a wide range. In order to understand the electronic structure and the mechanism of the superconductivity in heavily boron-doped diamond, various theoretical proposals and experiments such as angle-resolved photoemission spectroscopy [5] have been performed. However, systematic measurement of the fundamental optical spectra has not been done so far.

In the present study, we have performed measurements of vacuum ultraviolet reflection spectra of pure and heavily boron-doped diamonds. The top of valence band and the bottom of conduction band of pure diamond locates at the Γ point and the X point in the Brillouin zone, respectively [1,2]. The reflection spectrum is characterized by the reflection peaks at 7.4 eV and 12.6 eV. The former corresponds to the direct transition at the Γ point, while the latter to the direct transition at the X point [1,2] .

All the samples used in the present study were supplied from the Kawarada's laboratory, Waseda University. Heavily boron-doped epitaxial diamond films were grown on the type Ib diamond substrates by using the MPCVD method. Figure 1 shows reflection spectra of pure and heavily boron-doped diamonds around the direct transition at the X point. Measurements were done at room temperature. The spectra (a) and (b) are for the single crystals of pure diamond (type IIa) and type Ib diamond, respectively, grown by HTPT synthesis. The spectra (c) to (e) are for the heavily doped samples. Boron concentrations of the samples B65, B67, B63 and B69 are 6.2×10^{19}cm^{-3}, 2.8×10^{20}cm^{-3}, 1.8×10^{21}cm^{-3}, and 8.1×10^{21}cm^{-3},

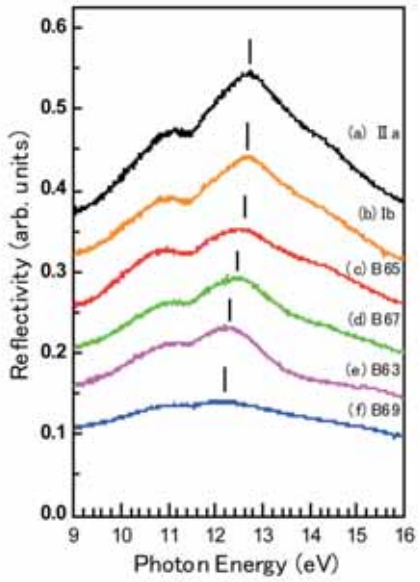

Fig. 1. Reflection spectra of pure and heavily boron-doped diamonds in the energy region of the direct transition at the X point. See text for details.

respectively. The sample B65 is insulating (semiconducting) and the sample B67 is metallic, while the samples B63 and B69 are superconducting with T_c of 2.5 K and 7.2 K, respectively. Vertical bars in the figure show the reflection peak originating from the direct transition at the X point, which locates at 12.6 eV for the pure diamond. As seen in the figure, the reflection peak shows low energy shift with increase of the boron concentration. This fact indicates that an optical energy gap at the X point becomes narrow with increase of the boron concentration. It is noteworthy that any evident energy shift was not confirmed for the reflection peak at 7.4 eV due to the direct transition at the Γ point.

[1] W. C. Walker *et al*., Phys. Rev. **134** (1964) A153.
[2] W. Saslow *et al*., Phys. Rev. Lett. **16** (1966) 354.
[3] E. A. Ekimov *et al*., Nature **428** (2004) 542.
[4] Y. Takano *et al*., Appl. Phys. Lett. **85** (2004) 2851.
[5] T. Yokoya *et al*., Nature **438** (2005) 647.

BL1B

Photoionization of Perylene on Ionic Liquid Surfaces

N. Inoue, T. Ishioka, A. Harata

Department of Molecular and Material Sciences, Kyushu University, Kasugakoen 6-1, Kasuga-shi, Fukuoka 816-8680, Japan

Ionic liquids are rapidly expanding topics of research because of their favorable properties such as high ionic conductivity and controllable hydrophobicity. Much effort has focused on the physical properties of ionic liquids. The dielectric environment is a key factor for modeling solvent behavior because many approaches rely on dielectric continuum models for the solvent. Interfacial dielectric properties can be different from those of bulk liquids, which may distort analysis of interfacial behavior such as calculation of solvation energies of molecules across the interface. Photoionization is a suitable technique studying for interfacial process, and ionization threshold measured by this method directly reflects dielectric environment. In this report ionization threshold energies of perylene on ionic liquid were measured, and interfacial dielectric properties of ionic liquids were studied.

Ionic liquids : 1-butyl-3-methylimidazolium tetra fluoroborate, hexafluorophosphate, bistrifluoro methane sulfonylimide ([bmim][BF_4], [bmim][PF_6], and [bmim][Tf_2N]), ethylammonium nitrate ([EtA][NO_3]), and protonated betaine bistrifluoro methane sulfonylimide ([Hbet][Tf_2N]) were prepared as described elsewhere. In a typical experiment, the light was emitted from the chamber to a He-purged cell through an MgF_2 window. Light energy is in 4-8eV. The emitted light was reflected with an Al mirror and vertically irradiated on the sample surface. Applied voltage was 400V (interval length of mesh electrode and solution is 5mm). Hexane solution of perylene at 1×10^{-4}M was added dropwise by 250μl onto each ionic liquid in a Pt cell of 2.5cm in diameter. After evaporation of hexane the photoinduced current (～1pA) was measured by a picoammeter (Keithly model 428).

Measured photoionization spectra were analyzed and threshold values were determined by fitting the spectra to the empirical formula of $I = (E\text{-}E_{th})^{2.5}$. Table1 shows the measured photoionization threshold of perylene on ionic liquids. In the case of [bmim][Tf_2N], current signal was below the detection limit in a vacuum. The threshold energy lies higher in a vacuum than in any other solvent because polarization energy is always exothermic and current by photoionization should have been detected within the measured range of wavelength if the perylene molecule is present at the surface of ionic liquids. It is considered that perylene molecule lies enough deep to keep photoinduced electron within [bmim][Tf_2N]. The energy required to photoionize a solute in a solu-

Table 1. Measured photoionization thresholds of perylene on ionic liquids and the relative dielectric constant of ionic liquids.

Compound	Threshold Energy / eV	Dielectric constant
[bmim][BF_4]	6.45 ± 0.11	11.7 ± 0.6[2]
[bmim][PF_6]	6.67 ± 0.15	11.4 ± 0.6[2]
[bmim][Tf_2N]	-	12.3 ± 0.3[3]
[Hbet][Tf_2N]	5.12 ± 0.17	43.7 ± 0.9[4]
[EtA][NO_3]	5.97 ± 0.22	26.2[5]
Water*	5.9 ± 0.1[1]	80.4

*Reference

-tion satisfy $E = I_p + V_o + P_+$, where I_p stands for ionization potential of solute in vacuum, V_o conduction band energy of solvent, and P_+ polarization energy of solvent. In this experiment, V_o equals zero because electron is emitted from surface. Photoionization threshold of imidazolium based ionic liquids is lower than that in a vacuum (6.960eV). This result is consistent with that of water surface. However, P_+ is much smaller than water. It is suggested that solvation by imidazolium based ionic liquid is weak. With respect to dielectric constant, [bmim][BF_4] is larger than [bmim][PF_6], but in polarization energy, the order is in inverse. This may relate to the character that [bmim][BF_4] is more hydrophilic than [bmim][PF_6]. Some kind of attractive interaction between [bmim][BF_4] and polar species formed by photoionization or trace impurity of water may explain the results. Photoionization threshold of [EtA][NO_3] is close with that of water. It is reasonable because the dielectric constant of [EtA][NO_3] is higher than that of imidazolium based ionic liquids. Photoionization threshold of [Hbet][Tf_2N] was quite lowered. [Hbet][Tf_2N] is an ionic liquid with the ability to coordinate metal ion. This property may cause that anomalous behavior.

Dielectric environment of perylene on ionic liquids are largely influenced by the composition of ionic liquids. It is not clear that which property of ionic liquid contributes the solvation energy of perylene. Further research is in pregress to clarify interfacial dielectric property of ionic liquids.

[1] Inoue *et al*., Chem. Lett. (1998) 609.
[2] Wakai *et al*., J. Phys. Chem. B **109** (2005) 17028.
[3] Krossing *et al*., J. Am. Chem. Soc. **128** (2006) 13427.
[4] N.Inoue, unpublished results
[5] Weingartner *et al*., J. Phys. Chem. A **105** (2001) 8646.

BL1B

Photoluminescence in $LaAlO_3$ Single Crystals

K. Kanai, E. Hirata, Y. Ohki

Dept. Electrical Engineering and Bioscience, Waseda University, Shinjuku 169-8555 Japan

Lanthanum aluminate ($LaAlO_3$) has been attracting much attention as a promising candidate for a gate insulator in advanced metal-oxide-semiconductor devices. By analyzing photoluminescence (PL) properties of $LaAlO_3$, we have been examining the localized states present in the band gap that are assumed to cause leakage current.

Experimental

The samples examined are Czochralski-grown $LaAlO_3$ (100) single crystals, about 0.5 mm thick with both sides polished. Using synchrotron radiation under multibunch operation at the BL1B line of UVSOR Facility as a photon source, PL, PL excitation (PLE), and absorption spectra were measured at 10 K.

Results and Discussion

Figure 1 shows PL spectra of $LaAlO_3$ excited at 5.1 eV. Three sharp PL peaks are observed at around 1.60, 1.64, and 1.675 eV, while a broad PL peak is observed at around 2.8 eV. Figure 2 shows the PLE spectra of $LaAlO_3$ for each PL. Note that the PLE spectra are normalized to respective maximum intensities. The PLE spectrum detected at 2.8 eV begins to rise at around 4.5 eV, and decreases sharply at around 5.7 eV. On the other hand, the PLE spectra of the other three PLs show an abrupt rise at around 5.7 eV.

The absorption spectrum shown in Fig. 3 shows a steep rise at around 5.7 eV, namely at the energy in good agreement with the band gap energy of 5.6 eV [1]. Furthermore, the energy of 5.7 eV corresponds to the energy at which the PLE spectrum detected at 2.8 eV shows a steep decrease and to the energy at which the PLE spectra detected at 1.60, 1.64, and 1.675 eV show an abrupt increase in Fig. 2. In addition, it seems that the gradual absorption increase in the range from 4.7 to 5.7 eV corresponds to the broad peak appearing in the PLE spectrum detected at 2.8 eV. From these results, the 2.8-eV PL is assumed to be caused by electrons excited to localized states in the band gap. In contrast, the other three PLs at around 1.60, 1.64, and 1.675 eV are assumed to be caused by de-excitation of electrons excited to the conduction band.

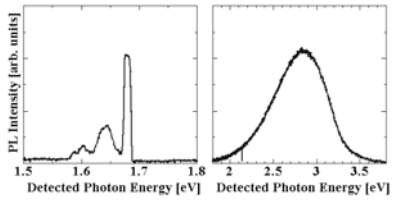

Fig. 1. PL spectra of $LaAlO_3$ excited at 5.1 eV.

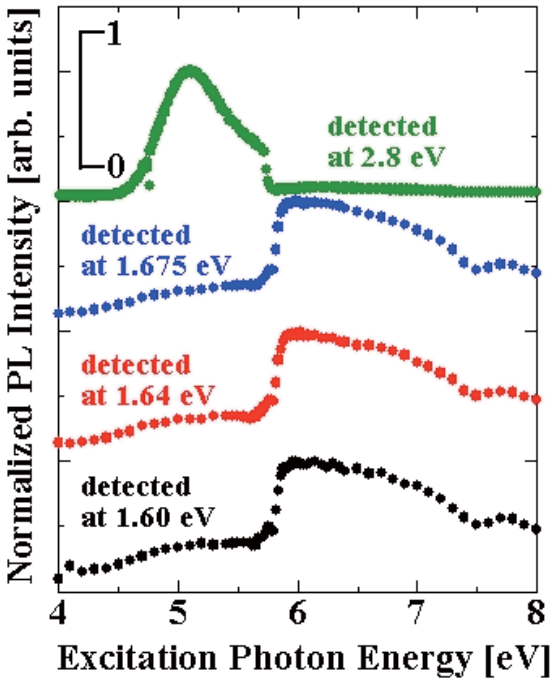

Fig. 2. PLE spectra of $LaAlO_3$ detected at 1.60, 1.64, 1.675, and 2.8 eV.

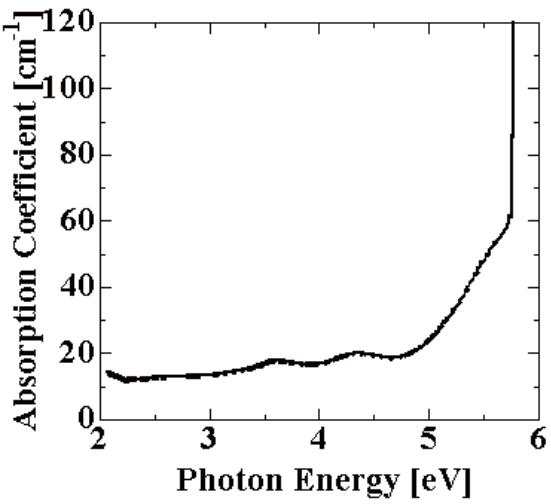

Fig. 3. Absorption spectrum of $LaAlO_3$.

[1] S. G. Lim *et al.*, J. Appl. Phys. **91** (2002) 4500.

BL1B

Luminescence Properties of $Bi_{12}GeO_{20}$ (BGO) Crystals

T. Katagiri[1], D. Iri[1], T. Aoki[1], M. Itoh[1], M. Fujita[2], Y. Usuki[3]
[1]*Department of Electrical and Electronic Engineering, Shinshu University, Nagano 380-8553*
[2]*Japan Coast Guard Academy, Kure 737-8512*
[3]*Furukawa Co. Kannondai, Tsukuba 305-0856*

Introduction

Bismuth germanium oxide, $Bi_{12}GeO_{20}$ (BGO), is a very efficient photoconductor and has both high sensitivity and quick response as a photorefractive crystal. However, little is known about its optical properties, as compared to another BGO ($Bi_4Ge_3O_{12}$) that is widely used as a scintillation material. In the present study, we have investigated reflection spectra, emission-excitation spectra, and luminescence decay kinetics of $Bi_{12}GeO_{20}$ crystals.

Experiment

Crystals of $Bi_{12}GeO_{20}$ were obtained from Furukawa Co. Reflection spectra were measured on the cleaved surfaces. Emission spectra were examined using a grating monochromator equipped with a LN/CCD camera in the temperature range T = 5–300 K. Luminescence decay kinetics was detected by an MCP with use of a time-correlated single-photon counting technique under the single-bunch operation of the storage ring (time duration: 1.3 ns; pulse interval: 177.6 ns).

Results and Discussion

The reflection spectra measured at T = 5 K showed a sharp peak at the fundamental absorption edge. This peak locating at 3.65 eV (340 nm) is naturally assigned to the excitonic transition of $Bi_{12}GeO_{20}$.

Figure 1 shows the emission spectra measured under the excitation with 150-nm photons at verious temperatures in the range of T = 5–45 K. A strong band peaking at 452 nm is observed together with a very weak band around 650 nm. The intensity of the 452 nm band decreases rapidly with increasing T.

The excitation threshold of the 452 nm emission was around 3.44 eV (360 nm), which coincides with the low-energy tail region of the exciton band. This fact suggests that the 452 nm luminescence is intrinsic to $Bi_{12}GeO_{20}$, and arises from the radiative annihilation of the excitons that have self-trapped by inducing lattice deformation around themselves. The self-trap site could be either Bi^{3+} or O^{2-}.

In Fig. 2 are shown the decay behaviors of the 452 nm luminescence measured in the range of T = 5–45 K. One may see two decay components: a fast one with a lifetime of nanoseconds and a slow one with a lifetime of more than 1 μs. The latter is seen as a piled-up component. As T is increased, the lifetime of the slow component becomes shorter, resulting in reduction of the piled-up component. This result is consistent with the temperature dependence of the emission intensity in Fig. 1.

The present work is the first observation of the intrinsic luminescence of $Bi_{12}GeO_{20}$.

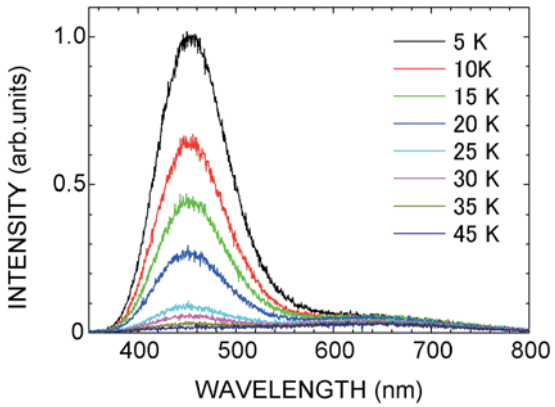

Fig. 1. Emission spectra of $Bi_{12}GeO_{20}$ excited at 150 nm in the temperature range T = 5–45 K.

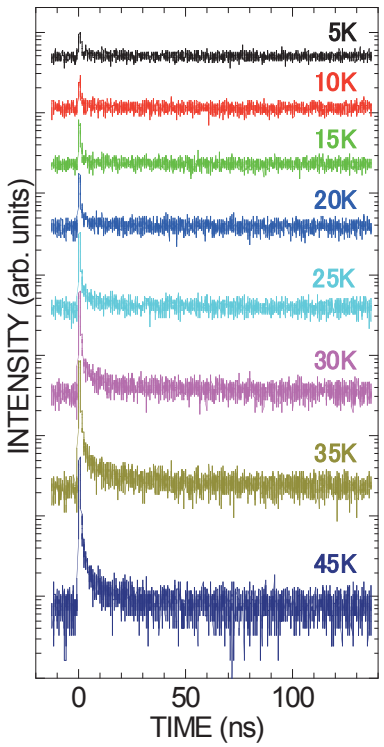

Fig. 2. Decay behaviors of the 452 nm luminescence of $Bi_{12}GeO_{20}$ excited at 150 nm at T = 5–45 K.

BL1B

Optical Studies of Hydrogen-Bonded Dielectrics TlH_2PO_4

T. Kawai[1], N. Ohno[2]
[1]*Graduate School of Science, Osaka Prefecture University, Sakai 599-8531, Japan*
[2]*Graduate School of Engineering, Osaka Electro-Communication University, Neyagawa 572-8530, Japan*

Thallium dihydrogen phosphate TlH_2PO_4 (TDP) is closely related to the KH_2PO_4(KDP) -type crystals, which are interesting hydrogen- bonded materials undergoing structural phase transitions accompanied by ferroelectricity and antiferroelectricity. In these compounds, short hydrogen bonds link PO_4 groups in three-dimensional (KDP) or two-dimensional (TDP) networks. The TDP crystal undergoes the antiferroelectric phase transition from the monoclinic $P2_{1/a}$ symmetry to the triclinic $C1$ symmetry at 230 K [1]. Though a number of studies on crystal structure and dielectric properties of TDP have been made above and below the phase transition temperature [1-4], optical properties and the electronic states are comparatively less studied.

In the present study, we have investigated the optical properties of TDP for the first time in UV and VUV regions at the BL-1B beam line of UVSOR. The TDP compound was synthesized by mixing stoichiometric amounts of Tl_2CO_3 and H_3PO_4. After several times of recrystallization, crystals of TDP were grown by an ordinary evaporation method from the saturated aqueous solution.

Figure 1 shows the reflection (red curve) and absorption (blue) spectra of TDP measured at 10 K. The dip structure at 5.26 eV in the reflection spectrum is due to the reflection from the back surface of the crystal, because the energy position corresponds to that where the absorption spectrum exhibits a sharp increase. A sharp peak with dispersive structure is observed at 5.70 eV above the rise of the absorption spectrum. In the higher-energy region, several broad structures are also observed. Most of the KDP-type crystals exhibits no obvious dispersion-like structure due to the exciton transition in the reflection spectra and broad structures are observed in the energy region from 7.0 to 8.2 eV [5,6]. The broad structures of KDP have been ascribed to the transition related with the energy levels in $H_2PO_4^-$ complex anions. The distinguished sharp peak with dispersive structure at 5.70 eV in TDP would be the first exciton transition. It is well-known that the Tl^+ impurity centers doped in the KDP-type crystals exhibit the absorption band due to the intra-cationic transition in the Tl^+ ion at 5.8 eV [7,8]. Therefore, the sharp dispersion-like structure of TDP at 5.8 eV should be attributed to the exciton transition based on cationic excitation in the Tl^+ ions.

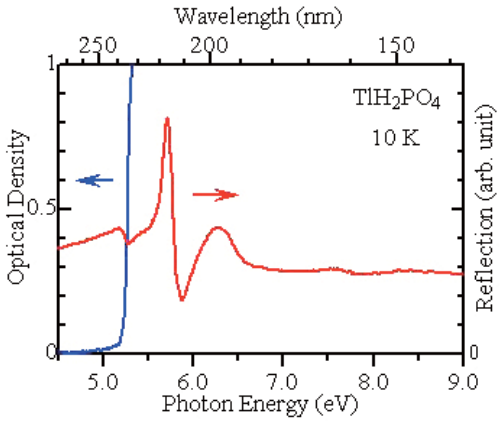

Fig. 1. Reflection spectrum (red) and absorption spectrum (blue) of TlH_2PO_4 at 10 K.

[1] I. H. Oh *et al.*, Acta Cryst. B **62** (2006) 719.
[2] N. Yasuda, S. Fujimoto, T. Asano, Physics Lett. **76A** (1980) 174.
[3] H. Yoshida *et al.*, J. Phys. Soc. Jpn. **53** (1984) 910.
[4] E. Alvarez-Otero *et al.*, Acta Cryst. B **58** (2002) 750.
[5] S. Saito, R. Onaka, Ferroelectrics **21** (1978) 553.
[6] S. Matsumoto, M. Fujisawa, S. Suga, J. Electron. Spectrosc. Relat. Phenom. **79** (1996) 51.
[7] I. Fujita, J. Phys. Soc. Jpn. **66** (1997) 2893.
[8] K. Ichimura *et al.*, Phys. Status Solidi (c) **3** (2006) 3607.

BL1B

Vacuum-Ultra Violet Reflectance Spectroscopy of Orbital-Ordered Bilayer Manganites

Y. S. Lee[1], Y. Tokunaga[2], T. Arima[3], Y. Tokura[2,4,5]

[1]*Department of Physics, Soongsil University, Seoul 156-743, Korea*

[2]*ERATO (Multi-Ferroics), Japan Science and Technology Agency (JST) Tsukuba 305-8562*

[3]*Tohoku University*

[4]*Correlated Electron Research Center (CERC) National Institute of Advance Industrial Science and Technology (AIST), Tsukuba 305-8562Japan*

[5]*Department of Applied Physics, University of Tokyo, Tokyo 113-8656 Japan*

Recent studies on strongly correlated electronic systems have revealed many unexpected phenomena due to the interplay among the spin, charge, and orbital degrees of freedom. Especially, the nanoscale self-organization and the associated complexity of electronic systems are issues of current interest. One of the representative phenomena is the concomitant charge and orbital orderings in manganites, which is involved in the metal-insulator transition with magnetic field and other various control parameters. At the lowest temperatures, the charges are ordered in a checkerboard type, forming alternating Mn^{3+}/Mn^{4+} sites, and simultaneously, the e_g orbitals in Mn^{3+} sites are aligned in zigzag chain type. The direction of e_g orbital lobes defines the orbital chain and stripe. This well-organized charge, spin, or orbital ordering occurs in the ab plane for a variety of manganites including layered compounds.

In this beamtime, we have measured the reflectivity spectra of the bilayer manganites, $Pr(Sr_{1-x}Ca_x)_2Mn_2O_7$ (PSCMO), for $0 \le x \le 1$ in a photon energy range of 4 – 30 eV at room temperature using the beam line BL1B. We connected the measured spectra to the low energy ones below 5 eV, and calculated the optical conductivity spectra through the Kramers-Kronig transformation.

The bilayer PSCMO compounds exhibit an peculiar phase diagram spanning from the A-type 2D metallic phase to the charge-orbital ordered phase with the increasing x from $x = 0$. The boundary between two phases is located around $x = 0.4$. Notably, the PSCMO compounds with the ground state of the charge-orbital ordering experiences the spontaneous rotation of orbital stripe by 90° with the variation of temperature. Two successive charge-orbital ordering transitions were studied in details at a particular concentration x = 0.9 by performing a combination of various experimental measurements such as Dc resistivity, magnetization, optics, x-ray scattering measurements, and so on. It is noted that the ground charge-orbital ordering states turn out to be a charge polarized state due to the coincidence in the stacking patterns of the distorted bilayer Mn-O network and the charge ordering along the c axis.

Figure 1 shows the optical conductivity spectra for the x = 0.2 and 0.9 PSCMO. The dominant structures observed in optical conductivity spectra are labeled as A, B, C, and D, from the lowest energy sequence. The lowest energy of the A structure, mainly responsible for the transport, is associated with the electron hopping from Mn^{3+} to Mn^{4+} e_g bands. This structure is located at much lower energy for the x = 0.2 compound with the 2D metallic character than that for the x = 0.9 compound with the insulating charge-orbital ordering. The B structure is assigned as the charge transfer energy from O 2p to Mn e_g bands. On the other hand, it is difficult to assign structures above 5 eV as transitions with a single character, because the valence bands of four elements (Pr, Sr, Ca, and Mn) should be involved in a complicated manner. While the C structure is associated with the transitions from O 2p to Pr 3d, Ca 4s, and Sr 5s bands, the occupied Pr 5p, Ca 3p, and Sr 4p may be involved in the formation of the D structure. In this case, the strong difference in the intensity of the D structure between x = 0.2 and x = 0.9 compounds implies that the Ca 3p band should be located in much deeper than the Sr 4p band.

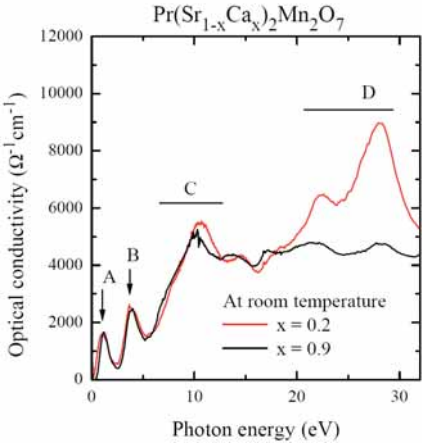

Fig. 1. Optical conductivity spectra of the x=0.2 (red line) and x = 0.9 (black line) $Pr(Sr_{1-x}Ca_x)_2Mn_2O_7$ compounds.

[1] Y. Tokura, Rep. Prog. Phys. **69** (2006) 797.

[2] Y. Tokunaga *et al*., Nature Materials **5** (2006) 937.

BL1B

Optical Properties of Sm^{2+} in KY_3F_{10}

T. Nakamura, T. Ishikawa, M. Satoh, N. Kashiwagura, M. Yamaga
Department of Mathematical and Design Engineering, Faculty of Engineering, Gifu University, Gifu 501-1193 Japan

Introduction

Rare earth ion-doped materials have been extensively studied for use in important applications such as laser, scintillator [1], and optical memory. Persistent spectral hole burning (PSHB) is applied to frequency domain optical memories. The hole burning of Sm^{2+} in disordered crystals and glasses was reported. Temperature dependence of the Sm^{2+} emission in KY_3F_{10} crystals excited by vacuum ultraviolet (VUV) and ultraviolet (UV) lights was measured, in order to examine dynamic processes of the $4f^6$ and $4f^55d^1$ excited states of Sm^{2+} in the crystal.

Experimental

Sm^{2+} doped KY_3F_{10} crystals were grown using the Bridgeman method. The optical absorption, emission and excitation spectra of Sm^{2+} in the crystal were measured using the BL1B beam line in the UVSOR. The measurement temperatures were in the range of 17-300 K.

Results and Discussion

Figure 1 shows the optical absorption, emission and excitation spectra observed in Sm^{2+}-doped KY_3F_{10} at 10 K. The absorption spectrum is composed of many bands in the wavelength range of 100-400 nm. The 160-nm excitation produces a broadband with a peak of 450 nm and three intense line groups around 560, 600, and 650 nm due to residual Sm^{3+} ions in the crystal. The 195-nm excitation produces only the 450-nm broadband. On the other hand, the emission spectrum excited at 300 nm is different from that excited at 160 nm. The emission lines around 550 and 700 nm are due to the transition from the higher energy levels of $^5D_3$ and $^5D_0$ to the lower energy levels of ^7F_J (J=0-3) of Sm^{2+}. The excitation spectra for the emission wavelengths at 500, 510, and 690 nm have the band structure in the range of 180-420 nm, being almost similar to the absorption spectrum.

Figure 2 shows the temperature dependence of the emission spectra excited at 280 nm. The 450-nm broadband and sharp lines in the range of 500-660 nm are drastically decreased above 150 K, while the sharp lines in the range 690-800 nm are almost constant up to 300 K. This result suggests that the excited states of ^5D_J (J=3,2,1) deexcite nonradiatively to the ground state with the increase of temperatures. The temperatures corresponding to the decrease of the intensities of the emission from the ^5D_J (J=3,2,1,0) excited states increase with the decrease of the number of J, that is, the emission from the the $^5D_0$ excited state is stable up to 300 K.

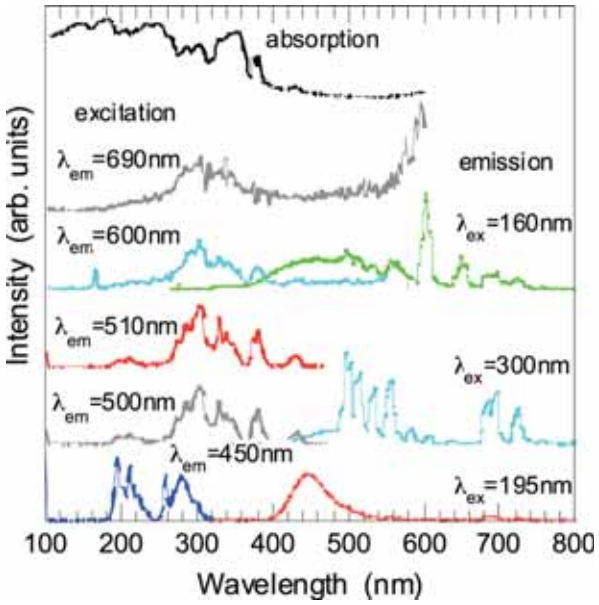

Fig. 1. Absoprtion, emission and excitation spectra of Sm^{2+} in KY_3F_{10} at 14 K

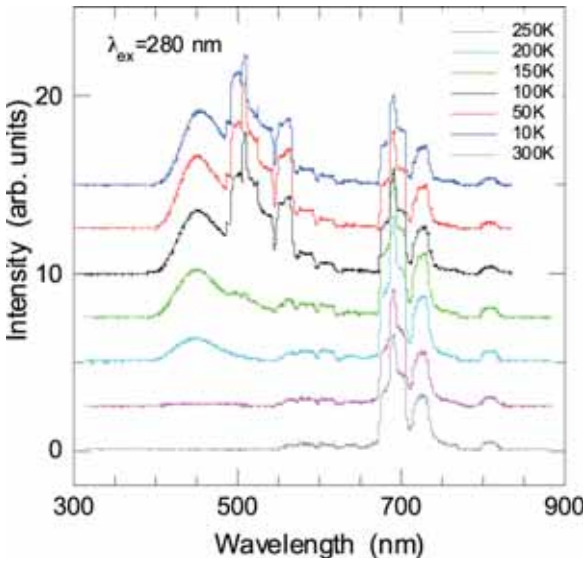

Fig. 2. Temperature dependence of the emission spectra of Sm^{2+} in KY_3F_{10}excited at 280 nm.

[1] M. Yamaga *et al.*, J. Materials Science: Materials in Electronics (2008) *in press*.

BL1B

Luminescence Properties of $YBO_3:Bi^{3+}$ and $YBO_3:Sb^{3+}$

N. Ohno, K. Kohmoto

Division of Electronics and Applied Physics, Graduate School of Engineering, Osaka Electro-Communication University, Neyagawa, Osaka 572-8530, Japan

Xe dimer (Xe_2) discharge fluorescent lamp is one of the candidates for alternative lighting sources to a conventional Hg discharge fluorescent lamp. New phosphors suitable for the conversion of vacuum ultraviolet (VUV) light into visible light are quite desired at present. In the Xe_2 discharge florescent lamps, phosphors are excited by VUV light of 7.2 and 8.4 eV. Most phosphate and borate hosts are transparent up to ~ 10 eV, so that the VUV light can directly excite impurity activators in these hosts. The strong absorption due to the impurity ions would give efficient conversion of the VUV light.

In the present study, luminescence properties of trivalent Tl^+-type centers in yttrium borate have been studied in the UV and VUV region. The $YBO_3:Bi^{3+}$ and $YBO_3:Sb^{3+}$ phosphors were prepared by amounts of the appropriate starting compound powders of YBO_3 adding Bi_2O_3 or Sb_2O_3 (1 mol %), mixing and firing in a carbon crucible at 1100ºC in air or nitrogen atmosphere [1]. Impurity Bi^{3+} and Sb^{3+} ions would be expected to be substituted for Y^{3+} ions in the host lattices.

Figure 1 shows luminescence (blue curve) and photo-excitation (red curve) spectra of $YBO_3:Bi^{3+}$ measured at room temperature. Luminescence peaks located at 3.8 eV and a small hump at 2.8 eV are observed for the excitation of VUV light. The 3.8 eV luminescence is excited with photons of 4.7 eV and 6-8 eV of Xe discharge energies. These excitation peaks are located at lower energies than the absorption edge of the host YBO_4 (~ 10 eV). Therefore, the observed luminescence bands of $YBO_3:Bi^{3+}$ would be responsible for intra-ionic transitions in impurity Bi^{3+} ions.

Figure 2 shows luminescence (blue curve) and photo-excitation (red curve) spectra of $YBO_3:Sb^{3+}$ at room temperature. There appear luminescence peaks at 3.6 eV and 2.9 eV for the excitation of VUV light. The 3.6 eV luminescence band is stimulated with photons of 4.7 eV and 6-8 eV. These luminescence and excitation peak energies are found to be quite similar to those of $YBO_3:Bi^{3+}$.

Tl^+-type ions doped in alkali-halide crystals with a high symmetry crystal structure exhibit three characteristic absorption bands arising from the $s^2 \rightarrow sp$ transitions, namely, A, B and C bands [2]. These absorption bands have been attributed to the optical transition from the $^1S_0$ ground state to $^3P_1$, $^3P_2$, and $^1P_1$ excited states, respectively. The present study has shown that the excitation band at 4.7 eV in $YBO_3:Bi^{3+}$ and $YBO_3:Sb^{3+}$ could be tentatively assigned as the A band nature due to $^1S_0 \rightarrow {}^3P_1$ transition in Bi^{3+} and Sb^{3+} impurity ions. The excitation bands at 6–8 eV show composite structures, which is a common feature of the C band of Tl^+-type ions. Therefore, these structures in the VUV region are ascribed to the C band originated from $^1S_0 \rightarrow {}^1P_1$ transitions in Bi^{3+} and Sb^{3+} ions.

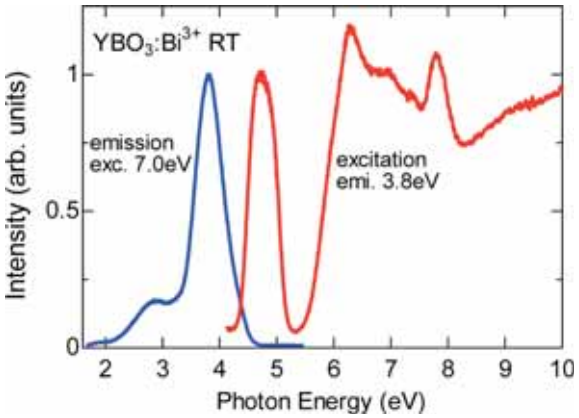

Fig. 1. Luminescence (blue curve) and excitation (red curve) spectra of $YBO_3:Bi^{3+}$ at room temperature.

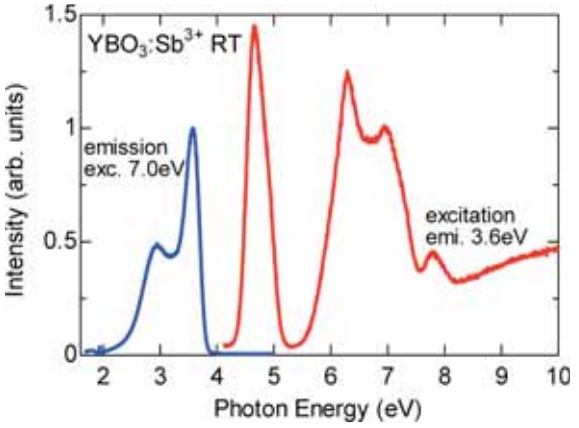

Fig. 2. Luminescence (blue curve) and excitation (red curve) spectra of $YBO_3:Sb^{3+}$ at room temperature.

[1] X. Z. Zeng *et al.*, J. Lumin. **121** (2006) 1.
[2] W. B. Fowler, *Physics of Color Centers,* Academic Press Inc., New York, 1968.

BL1B

Photoluminescence of Hydroxyapatite Irradiated by Ultraviolet Synchrotron Orbital Radiation Light (4)

M. Ohta

Department of Material Science and Technology, Faculty of Engineering, Niigata University, 8050 Ikarashi 2-no-cho, Niigata 950-2181, Japan

It was known that rare earth ions dosed for oral administration to mouse and rat are transferred to blood vessel through the ileum and deposited its teeth and bone, which mainly consists of hydroxyapatite ($Ca_{10}(PO_4)_6(OH)_2$) [1-2]. Recently, rare earth is also useful as a contrast medium for magnetic resonance imaging, restriction enzyme, biocatalyst, and so on in fields of biochemistry, physiology, medicine, etc. However, the behavior of rare earth in the living body system remains an open question until now. We have found that Eu ion substituted Ba ion in Eu doped $Ba_{10}(PO_4)_6Cl_2$ phosphor, which matrix is apatite structure [3]. The Eu ions or Gd ions are also found to substitute easily for calcium ions in hydroxyapatite which is soaked in $EuCl_3$ or $GdCl_3$ aqueous solution, and to play on emission center.

In this study, hydroxyapatite samples doped with $YbCl_3$ aqueous solution were prepared in order to apply to phosphor. Their characteristics were investigated by photoluminescent property of Yb ion-doped hydoxyapatite samples excited by ultraviolet synchrotron orbital radiation light.

Yb-doped hydroxyapatite samples were prepared as follows: hydroxyapatite was soaked in $YbCl_3$ aqueous solution. After 72 hr, Yb-doped hydroxyapatite was separated from $YbCl_3$ aqueous solution by filtation and then dried by using with infrared ray.

The photoluminescent property of each sample exited by ultraviolet synchrotron orbital radiation light (BL-1B) was observed by using with a multi-channel analyzer.

Figure 1 shows photoluminescence spectra of Yb ion-doped hydroxyapatite samples excited by BL-1B. The photoluminescence spectra have the peak due to $^5D_{5/2} \rightarrow {}^5F_{7/2}$ (about 980 nm), regardless of excitation wave length from120 to 420 nm. The peak intensity is higher at 150 and 210 nm of excitation wave length. The peak intensity increases with the concentration of $YbCl_3$ aqueous solution and is held constant at from 1 to 10 mM. This fact is different from the results of Eu-doped and Gd-doped samples, reported previously [4].

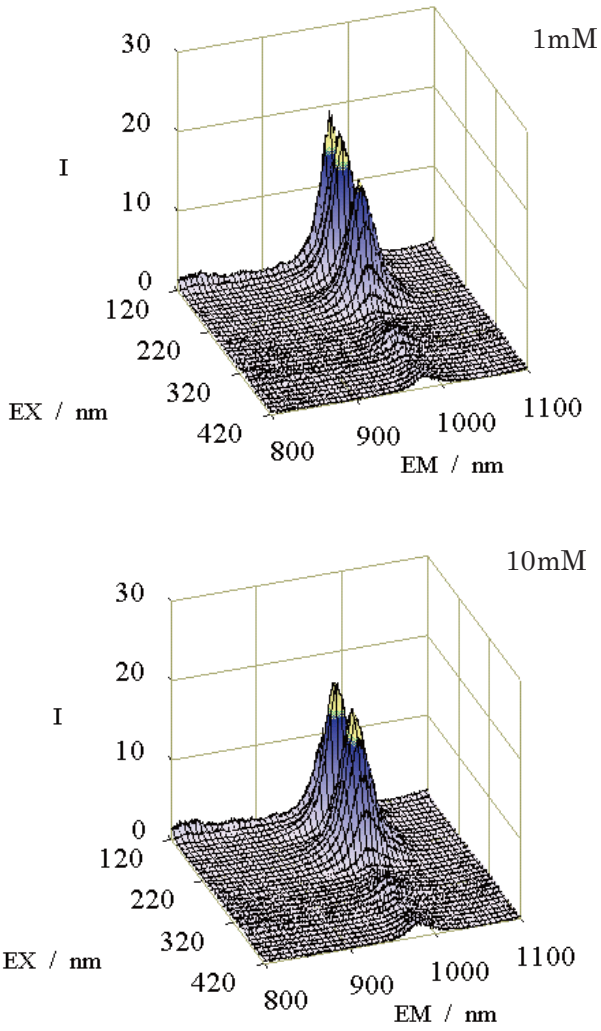

Fig. 1. Photoluminescent spectra of Yb ion-doped hydroxyapatite samples excited by ultraviolet synchrotron orbital radiation light.

[1] S. Hirano, K. T. Suzuki, Environ. Health Perspect. **104** (Supplement 1) (1996) 85.
[2] K. Kostial, B. Kargacin, M. Lendeka, Int. J. Radiat. Biol. Relat. Stud. Phys. Chem. Med. **51** (1987) 139.
[3] M. Sato, T. Tanaka, M. Ohta, J. Electrochem. Soc. **141** (1994) 1851.
[4] M. Ohta, UVSOR Activity Report 2006 (2007) 75.

BL1B

Effects of Curing and Filler Dispersion Methods on Dielectric Properties of Epoxy Nanocomposites

M. Okada[1], N. Hirai[1], T. Tanaka[2], Y. Ohki[1], T. Imai[3], M. Harada[4], M. Ochi[4]
[1] *Department of EEBS, Waseda University, Shinjuku 169-8555, Japan*
[2] *Graduate School of IPS, Waseda University, Kita-Kyushu 808-0135, Japan*
[3] *Power and Industrial Systems R&D Center, Toshiba Corp., Kawasaki 212-8582, Japan*
[4] *Department of Applied Chemistry, Kansai University, Suita 564-8680, Japan*

The effects of the differences in the curing and filler dispersion methods on the dielectric properties were examined for epoxy/clay nanocomposites.

The base epoxy resin is diglycidyl either of bisphenol A cured with acid anhydride or with amine, while the clay added is montmorillonite modified by either a solubilization method or an organo method. The clay content was constant at 5 wt% throughout all the samples [1]. Table 1 shows the sample codes.

The electric conductivity was calculated by measuring the absorption current for 1000 s after the application of electric field of 10 kV/mm, while the permittivity was measured in the range of 10^{-1}-10^{7} Hz. All the above measurements were carried out at room temperature.

Using synchrotron radiation (SR) under multi-bunch operation at the BL1B line of UVSOR Facility (beam energy: 750 MeV) as a photon source, the ultraviolet (UV) photon absorbance, photoluminescence (PL) and PL excitation (PLE) spectra from the samples were measured at 10 K.

Irrespective of the filler dispersion method, both the electric conductivity and permittivity are higher in the amine-cured samples than in the acid anhydride-cured samples as shown in Figs. 1 and 2.

Furthermore, UV photon absorption becomes significantly larger at photon energies higher than 3.4 eV in the amine-cured samples and at energies higher than 4.0 eV in the acid anhydride-cured samples, irrespective of the filler dispersion method, as shown in Fig. 3. A PL band, which shows an emission peak at the energy where the UV absorption begins to increase, was found to appear in all the samples as shown in Fig. 4. From these results, the PL is due to electronic transition across the band gap, which is smaller in the amine-cured samples than in the acid anhydride-cured samples.

In most materials, the permittivity and conductivity become higher if the band gap is smaller. The present results agree with this general tendency.

Table 1. Sample codes.

	Unmodified epoxy	Solubilization Method	Organo Method
Acid anhydride curing agent	E(U)AH	C(S)AH	C(O)AH
Amine curing agent	E(U)AM	C(S)AM	C(O)AM

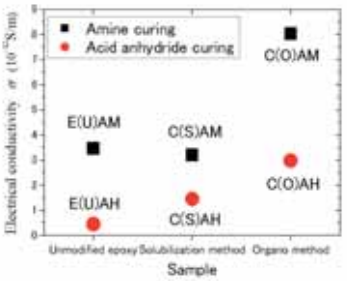

Fig. 1. Electrical conductivity (1000 [s] after voltage application).

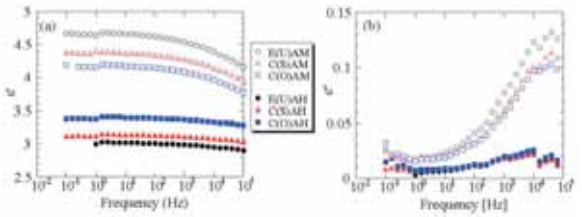

Fig. 2 Dielectric constant (a) and dielectric loss factor (b) of each sample

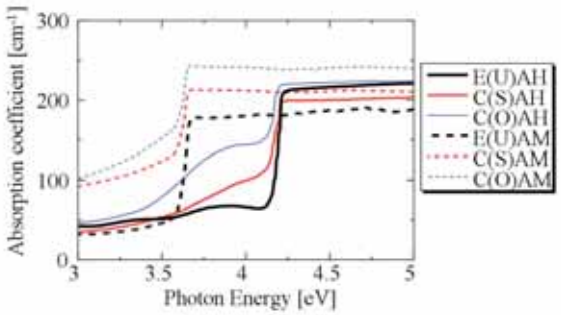

Fig. 3. Ultraviolet absorption spectra.

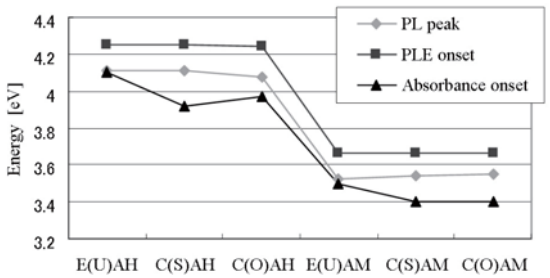

Fig. 4. PL peak, PLE onset, and absorbance onset energies.

[1] M. Harada *et al.*, Network Polymer Symposium Japan (2006) 105 (in Japanese).

BL1B

The Temperature Dependence of Absorption Spectra for Heavy Lanthanides in $LiYF_4$ and its First-Principles Analysis

S. Watanabe[1], H.Yoshida[1], K. Ogasawara[1], M. Yoshino[2]
[1]*Department of Chemistry, Kwansei Gakuin University, 2-1 Gakuen, Sanda 669-1337 Japan*
[2]*Department of Materials, Physics and Engineering, Nagoya University, Furo-cho, Chikusa-ku, Nagoya, 464-8603, Japan*

The divalent or trivalent lanthanide ions in wide band gap host crystals or glasses have drawn attentions due to their application for luminescent materials in UV and VUV regions such as solid-state lasers or phosphors. In those materials, the trivalent lanthanide ions (Ln^{3+}) in $LiYF_4$ crystal have been well known as exquisite luminescence centers.

In this work, we have investigated the temperature dependence of $4f^{n}$-$4f^{n-1}5d^{1}$ absorption spectra for heavy lanthanides in $LiYF_4$ host crystal. As the luminescence centers, we adopted the three heavy lanthanide ions, which are Terbium (Tb^{3+}), Dysprosium (Dy^{3+}) and Erbium (Er^{3+}). And we also analyzed the spectra based on the first-principles calculation for multiplet energy and absorption spectrum using the 4-component relativistic configuration interaction (CI) method [1]. This calculation method has been successfully applied to calculation of the multiplet energy levels and optical absorption spectrum between multiples for impurity ions in host crystals [2]. By measurements of the absorption spectrum at low temperature, we could directly compare the theoretical absorption spectrum to that obtained by the first-principles calculation. Therefore, the combination of measurements of the absorption spectrum at low temperature and first-principles calculations is very effective procedure for analysis of optical properties.

The $LiYF_4$ single crystal doped with Ln^{3+} (Ln^{3+}=Tb^{3+}, Dy^{3+}, Er^{3+}) were grown by Bridgman-Stockbarger method. The concentration of Ln^{3+} in the sample was 0.3 mol%.

Fig. 1 shows the temperature dependence of experimental absorption spectra and the theoretical absorption spectrum for Dy^{3+} in $LiYF_4$.

The $4f^{9}$-$4f^{8}5d^{1}$ absorption spectrum for Dy^{3+} in $LiYF_4$ is observed by using the SR source for the first time. The experimental absorption spectra were very complicated and did not strongly depend on temperature except for the peak D, E. These results indicate that the configuration interaction of each multiplet is very strong. In addition to Dy^{3+} impurity absorption, the absorption of $LiYF_4$ host crystal was observed above about 10.8 eV.

The theoretical spectrum is in good agreement with experimental one. Though the absolute mutiplet energy levels are not reproduced exactly, the relative peak position and shapes of absorption spectrum are reproduced fairly well without any empirical parameters.

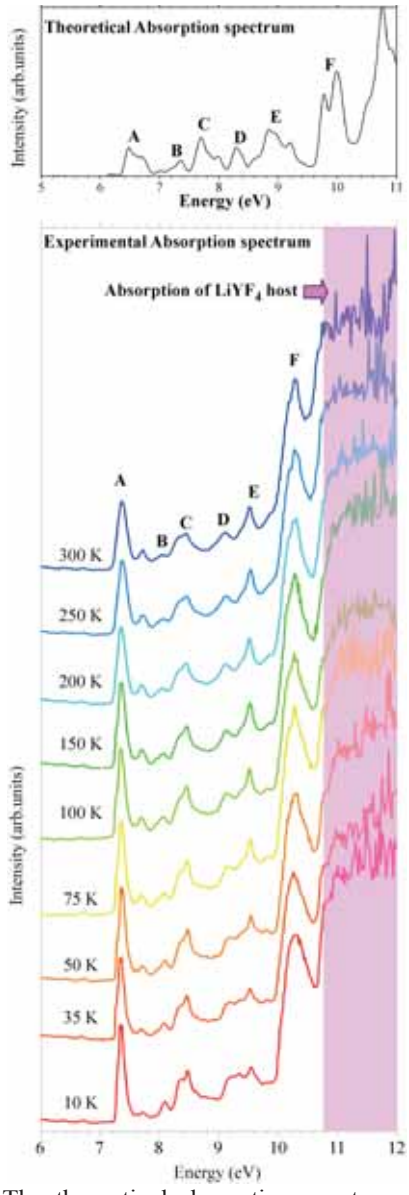

Fig. 1. The theoretical absorption spectrum and the temperature dependence of experimental absorption spectra for Dy^{3+} in $LiYF_4$.

[1] K. Ogasawara *et al.*, Phys. Rev. B **64** (2001) 143.
[2] K. Ogasawara *et al.*, J. Solid Statate Chem. **178** (2005) 412.

BL1B

Excitation Spectra for Lanthanides in YAG and its First-Principles Analysis

M. Yoshino[1], S. Watanabe[2], H. Yoshida[2], K. Ogasawara[2]

[1]*Department of Materials, Physics and Energy Engineering, Nagoya University, Nagoya 464-8603, Japan*

[2]*Department of Chemistry, Kwansei Gakuin University, Sanda 669-1337, Japan*

The trivalent lanthanide ions (e.g. Nd^{3+}, Er^{3+}, Yb^{3+}) in $Y_3Al_5O_{12}$ (YAG) crystals have drawn attentions due to their application for luminescent materials in NIR to UV regions such as solid-state lasers or phosphors. And, Pr^{3+} and Tb^{3+} have also attracted attentions as luminescence centers. In this work, the $4f^n$-$4f^{n-1}5d^1$ excitation spectra and emission spectra for lanthanides in YAG crystal have been measured. As the luminescence centers, Pr^{3+} and Tb^{3+} are used. The lanthanides ion doped YAG samples are produced by solid state reactions. The concentration of Ln^{3+} in the samples are 3 mol%. And the spectra are analyzed based on the first-principles calculation for multiplet energy and absorption spectrum using the relativistic configuration interaction (CI) method [1]. This calculation method has been successfully applied to calculation of the multiplet energy levels and optical absorption spectrum for impurity ions in hosts [2]. Fig. 1 shows the experimental excitation spectrum for Pr^{3+} in YAG. The two peaks exist around 4-6 eV correspond to the $4f^2$-$4f^1 5d^1$ absorption. And the spectrum above about 6.5 eV relates to absorption of YAG host. And this sample shows strong emission in VIS region as shown in Fig. 2. Fig. 3 shows the theoretical absorption spectrum for Pr^{3+} in YAG. Though the absolute multiplet energy levels are not reproduced, the shapes and distribution of peak position in excitation spectrum are roughly reproduced without any empirical parameters. The experiments and calculation are also examined about Tb^{3+} in YAG (Fig. 4).

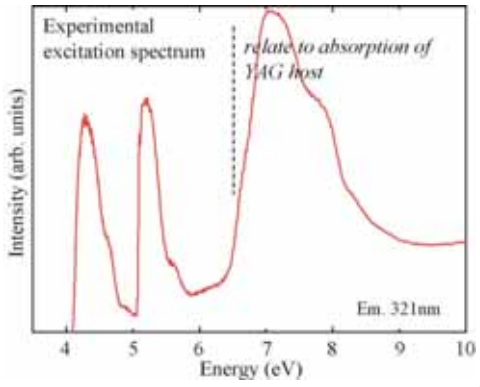

Fig. 1. Experimental excitation spectrum for Pr^{3+} in YAG.

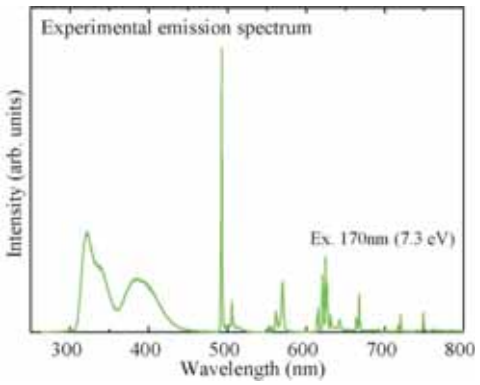

Fig. 2. Experimental emission spectrum for Pr^{3+} in YAG.

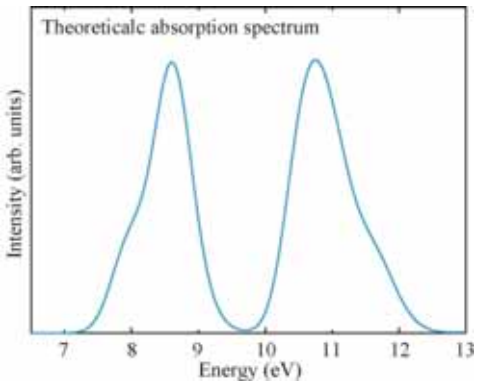

Fig. 3. Theoretical absorption spectrum for Pr^{3+} in YAG.

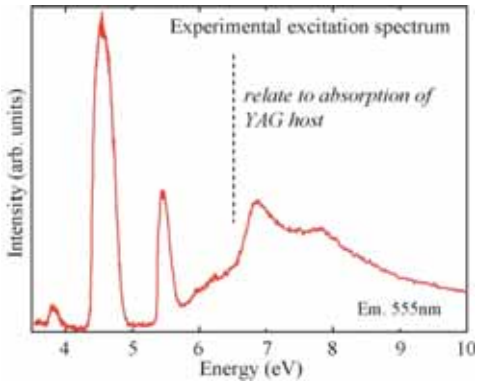

Fig. 4. Experimental excitation spectrum for Tb^{3+} in YAG.

[1] K. Ogasawara *et al.*, Phys. Rev. B **64** (2001) 143.
[2] K. Ogasawara et al., J. Solid State Chem. **178** (2005) 412.

BL5B

Absorption Spectra of Dilute Magnetic Semiconductor GaCrN in VUV Region

S. Emura, S. Kimura, Y. Hiromura, H. Asahi
ISIR, Osaka University, Mihoga-oka 8-1, Ibaraki, Osaka 567-0047

In present society, infrastructures of communication are demanded to expand in the speed and the quantity. One of future devices in this field is a spin-related device. Several candidates are considered and a part of those starts in fundamental research. Theoretical study also reveals the possibility of dilute magnetic semiconductor that exhibits ferromagnetism at room temperature and predicted that GaN-based dilute magnetic semiconductors, especially Cr-doped GaN, are highly potential candidates for those materials. This material, Cr doped wide gap semiconductor, shows ferromagnetic properties even at 400K experimentally. This is one of highest Curie temperatures at present in dilute magnetic semiconductors. Furthermore, GaCrN substance emits luminescence at the energy of near the band gap of Ga. We have, thus, three independent characters for GaCrN, semiconductor nature, ferromagnetism, and optical feature.

The origin of the magnetic behaviors of dilute magnetic semiconductors based on nitride is still open in discussion, though several first-principles calculations, as described above, appeal to the public. It seems that their predictions do not clearly explain magnetic characteristics such as the dependence of the magnetic strength on the magnetic dopant concentration, peculiar form of M – H curve, and the weak hysteresis.

The growth of cubic-GaN:Cr layers was performed on MgO (001) substrates by radio frequency (RF) plasma-assisted molecular beam epitaxy techniques. Sources used here were elemental Ga and Cr and plasma-excited nitrogen. After thermally cleaning of MgO substrate surfaces, several monolayer of GaN were grown at low substrate temperature (540˚C) and then 50 nm of cubic-GaN buffer layer was grown at 700˚C. On the cubic-GaN buffer layer, cubic-GaCrN layer with approximately 100 - 200 nm in the thickness was grown as a function of Cr cell temperature (T_{Cr} = 810 - 1030˚C). The fixed nitrogen flow rate (1.5 SCCM) with the fixed plasma power (180 W) was supplied during growth for all of the cubic-GaN:Cr layers. Growth rate and slightly N-rich condition of V-III ratio were kept constant for all the samples grown at different substrate temperatures. Therefore, the Ga flux of 1.9, 1.6 and 1.3×10^{-7} Torr was used for the substrate temperature of 700, 540 and 350˚C respectively because evaporation of Ga atoms is suppressed on the grown surface at lower temperature. Finally, GaN layer with 10 nm in the thickness was deposited to avoid the oxidation of GaN:Cr layer surfaces.

In consideration of the electronic state of Cr in GaN matrix to survey the origin of the ferromagnetism of GaCrN, the molecular orbital schema of CrN_4 is important. The molecular orbitals of $(CrN_4)^{-9}$ are resolved in tetrahedral symmetry by group theory as follows,

N-*2p*: $a_1 + e + t_1 + 2t_2$ (a_1 and t_2 are σ orbitals) (1)
N-*2s*: $a_1 + t_2$ (2)
Cr-*3d*: $e + t_2$ (3)

The schematic semi-quantitative diagram is shown in Fig.1. The quantitative parts in the figure are deduced from the combination of 1s core absorption spectra and VUV absorption spectra observed. The three electrons belonging to the magnetic dopant Cr atom occupy with a manner of two kinds, so-called, low spin state and high spin state. The present problem is which state is preferable. It strongly affects the ferromagnetism of this system GaCrN. The VUV dichronic and ESR measurements are necessary to confirm whether the Cr state takes low or high spin state.

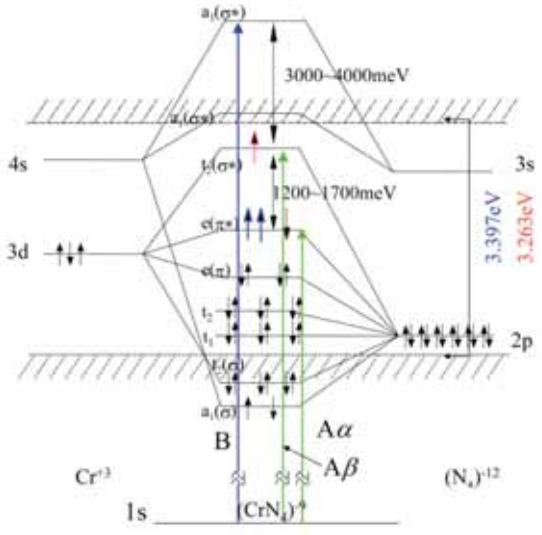

Fig. 1. Schematic energy diagram of the $(CrN_4)^{-9}$ molecular.

BL5B

Photostructural Changes in Amorphous Chalcogenide Materials

K. Hayashi

Department of Electrical and Electronic Engineering, Gifu University, Gifu 501-1193, Japan

Introduction

It is well-known that amorphous chalcogenide materials exhibit a variety of photoinduced phenomena by irradiation of light with energy corresponding to the optical band gap [1]. Photoinduced changes observed in amorphous chalcogenide materials are classified into two types, irreversible and reversible changes. Reversible changes can be induced optically in amorphous bulk materials and well-annealed evaporated thin films, in which the changes can be removed by annealing to the glass-transition temperature. The reversible photodarkening arising from the red-shift of the optical absorption edge is a typical reversible photoinduced phenomenon. Irreversible changes are induced in as-deposited evaporated thin films. The irreversible photodarkening in as-deposited amorphous films is an irreversible change, it is believed that it occurred by photo-polymerization. The irreversible changes observed in EXAFS [2-3] and IR [4] are interpreted by rearrangement of bonding configurations of molecular species within as-deposited evaporated films.

To our knowledge, little attention has been given to photoinduced changes at the vacuum ultra-violet (VUV) absorption spectrum. In this report, we investigate photoinduced changes at the VUV transmission spectra on as-deposited evaporated films and well-annealed evaporated films.

Experimental

Thin films of amorphous chalcogenide semiconductor (a-As_2S_3 and a-As_2Se_3) were prepared onto ultrathin collodion films by conventional evaporation technique. A typical thickness of an amorphous film was around 200nm. The ultrathin collodion films were prepared onto stainless steel metal plates in which two pinholes of the 1.0mm diameter opened. A xenon arc lamp with IR-cut-off filter was used as a light source. Before the measurement of the VUV transmission spectrum, the unilateral of the sample was irradiated with the light in a vacuum to the degree in which the sample sufficiently produced the photodarkening. The measurement of the VUV transmission spectra were carried out at room temperature at the BL5B beam line of the UVSOR facility of the Institute for Molecular Science. And the spectrum was measured by using the silicon photodiode as a detector. To eliminate the higher order light from the monochromator, an aluminum thin film was inserted between the monochromator and sample. We also monitored the spectrum of the light source by measuring the total photoyield of a gold mesh.

Results and Discussion

Figure 1 shows the VUV transmission spectrum of an as-deposited a-As_2Se_3 film at room temperature in the photon energy region between 40 and 65eV. Two main absorption peaks were observed in this energy region. One absorption peak around 44eV corresponds to the 3d core level of As atom. Another absorption peak around 57eV corresponds to the 3d core level of Se atom. As shown in the Fig. 1, the spectral line width of that absorption is very broad and multiple shoulders are observed. A similar spectrum is observed in the as-deposited a-As_2S_3 film. It can be attributed to the spin-orbit splitting of the 3d core level of each atom as observed by XPS. As for the origins of the shoulders, it is not clear. I think that these shoulders are related to the local structures of the amorphous network. The detailed experiments and analysis will be done in the next step.

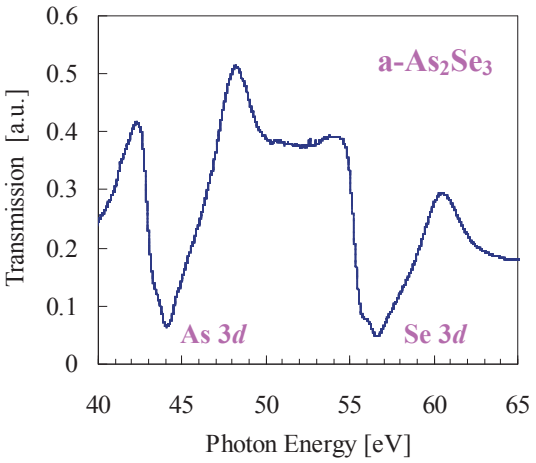

Fig. 1. The VUV transmission spectrum of an as-deposited a-As_2Se_3 film.

Acknowledgements

This work was partly supported by Research Foundation for the Electrotechnology of Chubu.

[1] Ke. Tanaka, Rev. Solid State Sci. **4** (1990) 641.
[2] J.P. De Neuvile, S.C. Moss, and S.R. Ovsinsky, J. Non-Cryst. Solids, **13** (1973/1974) 191.
[3] A.J. Lowe, S.R. Elliot, and G.N. Greaves, Philos. Mag. B **54** (1986) 483.
[4] S. Onari, K. Asai, and T.Arai, J. Non-Cryst. Solids **77&78** (1985) 1215.

BL5B, BL7B

Optical Oscillator Strength Distribution of Amino Acids from 3 to 250 eV and Examination of the Thomas-Reiche-Kuhn Sum Rule[1]

M. Kamohara, Y. Izumi, M. Tanaka, K. Okamoto, K. Nakagawa*
Graduate school of Human Development and Environment, Kobe University, Tsurukabuto, Nada-ku,Kobe 657-8501, Japan

Absorption spectra of amino acid films were measured in the photon energy range of vacuum ultraviolet (VUV) and soft X-ray region in an attempt to examine the validity of the Thomas-Reiche-Kuhn oscillator strength sum rule.

Thin films of glycine (Gly), alanine (Ala), phenylalanine (Phe), and methionine (Met) were prepared by the vacuum sublimation technique on the collodion substrates.

Absorption spectra were measured at the beamline 5B and 7B of the synchrotron radiation facility UVSOR in the Institute of Molecular Science, Okazaki, Japan. Values of optical absorption cross section $\sigma(E)$ at photon energy E were translated into the optical oscillator strength distribution df /dE . An example of obtained results for Met films is shown in Fig. 1, in which large peak from 10 eV to 70eV is due to transitions between valence levels and small peak from 170 eV to 250 eV was due to transitions from 2s and 2p levels of sulfur atom of Met.

According to the Thomas-Reiche-Kuhn oscillator strength sum rule, integrated value ftotal of df /dE should be equal to the number of electrons Ne associated to the optical transition within the energy range of integration. After careful examinations, we obtained values of ftotal and Ne to be 27.3 and 30 for Gly, 31.0 and 36 for Ala, 63.2 and 64 for Phe, and 60.1 and 62 for Met, respectively. We concluded that the T-R-K sum rule meets in a good manner for amino acid molecules.

This work was done thorough the joint programs of the Institute for Molecular Science, 18-515 and 18-534.

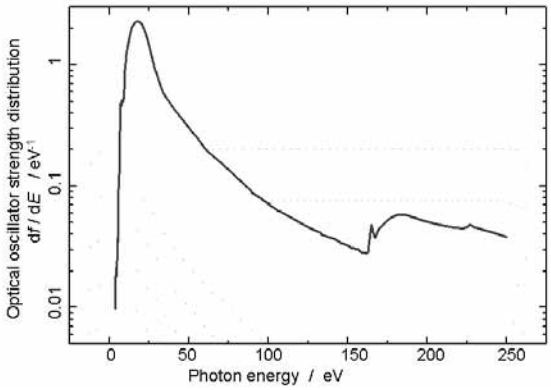

Fig. 1. Optical oscillator strength distribution of methionine thin film.

*Corresponding author: nakagawa@kobe-u.ac.jp

[1] M. Kamohara *et al.*, J. Rad. Phys Chem. (2008) *in press*.

BL6B

Far-Infrared and Millimeter Wave Spectroscopy of Superionic Copper Conductors

T. Awano

Department of Electronic Engineering, Tohoku Gakuin University, Tagajo 985-8537, Japan

Superionic conductors have high ionic conductivity as liquid or electrolyte solution. Far-infrared and millimeter wave region corresponds to the frequency boundary between translation and vibration movement of conduction ion. Spectroscopic study of this frequency region, therefore, seems to make characteristic dynamics of mobile ions in superionic conductors, such as correlative collective movement of mobile ions clear.

$RbCu_4Cl_{3+x}I_{2-x}$ crystals have the highest ionic conductivity at room temperature and have the same structure as $RbAg_4I_5$. Therefore this is a suitable system to compare dynamics of mobile ions.

Fig. 1 shows absorption spectra of $RbCu_4Cl_{3.25}I_{1.75}$ crystal obtained by K-K analysis from reflectivity spectra. Broad absorption peak was observed around 40, 80 and 110-200cm^{-1} at room temperature. These bands have doublet structure at low temperature. This seems to be due to difference of local structure by chlorine and iodine ion. The number of couples of cations and chlorine or iodine ions is comparable and absorption intensity seems to be almost equal.

The 110-200 cm^{-1} bands seems to be symmetric breathing modes of CuX_4 (X= Cl or I) tetrahedron. In CuI, TO phonon frequency is 130 cm^{-1} and 170 cm^{-1} in CuCl. These bands were observed around 100-120 cm^{-1} in $RbAg_4I_5$. This frequency shift coincides with the inverse of square root of the mass ratio of conduction ions.

The 80 cm^{-1} band seems to be Rb-X vibration in RbX_6 octahedron. In RbI, the frequency of TO phonon is 80cm^{-1}.

The 40 cm^{-1} band seems to be the attempt mode which is an outward motion of the mobile ion in halogen cage. In silver conductors, the attempt mode is observed around 20 cm^{-1}[1]. This frequency shift coincides with the inverse of square root of the mass ratio of conduction ions.

Reflectivity at low energy side increased at room temperature. This is due to translational movement of conduction ion. Correlation of ionic movement by coulomb repulsion seems to occur because the number of available site for conduction ion is not so many and the distance between them is not so large. Such a collective movement in phase is able to be regarded as "ionic plasmon". Plasmon fitting by Drude model in energy loss function spectra of $RbCu_4Cl_{3.125}I_{1.875}$ is shown in fig. 2. Energy loss function, Im(1/ε), is proportional to absorption intensity by transverse wave. The dotted line shows calculated one from the Drude model. The fitting curve well coincides with the energy loss function spectrum of the spectral region below the attempt mode, i.e. below 35cm^{-1}, at 298 K. The plasma frequency, 45 cm^{-1}, in the fitting parameters is proportional to the inverse of square root of mass ratio of silver and copper ion, comparing with those in MAg_4I_5[1] i.e. 26-27cm^{-1}. The plasmon fitting was impossible for the spectra at low temperatures. This means that such a movement in phase needs kinetic energy of the conduction ion much larger than the activation energy of the ionic conduction.

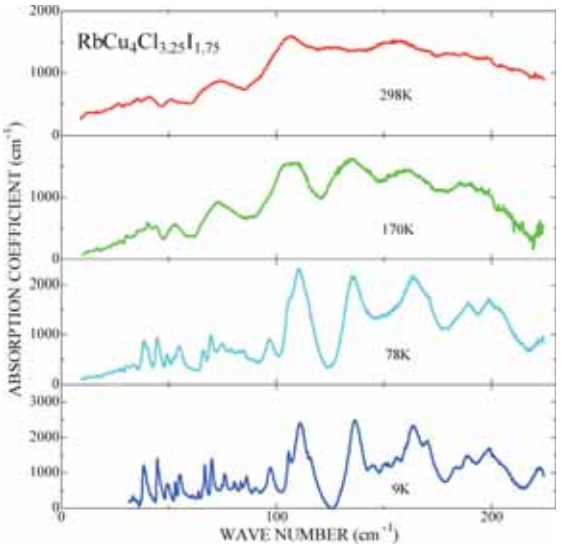

Fig. 1. Absorption spectra of $RbCu_4Cl_{3.25}I_{1.75}$.

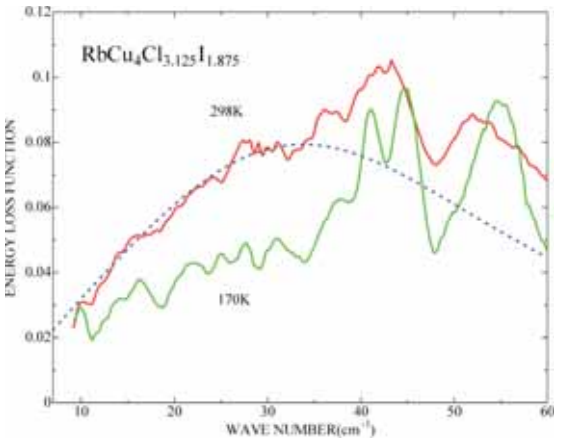

Fig. 2. Energy loss function spectra of $RbCu_4Cl_{3.125}I_{1.875}$.

[1] T. Awano, T. Nanba, M. Ikezawa, Solid State Ionics **53-56** (1992) 1269.

BL6B

Infrared Spectroscopy on $CeIn_3$ under Pressure

T. Iizuka[1], T. Mizuno[1], K. E. Lee[2], H. J. Im[2, 3], Y. S. Kwon[2], S. Kimura[3, 1]

[1]*School of Physical Sciences, The Graduate University for Advanced Studies (SOKENDAI), Okazaki 444-8585, Japan*

[2]*Department of Physics, Sungkyunkwan University, Suwon 440-746, Korea*

[3]*UVSOR Facility, Institute for Molecular Science, Okazaki 444-8585, Japan*

Introduction

In recent years, some compounds called "heavy fermion" (HF) attract attention because of their various physical properties. The physical properties originate from the hybridization between itinerant conduction electrons and local 4*f* electrons. One of the characteristic physical properties is superconductivity due to the HF, which appears near a quantum critical point (QCP) located in between the local and itinerant characters of 4*f* electrons. There are many experimental and theoretical studies to clarify the origin of the various physical properties at QCP. The various physical properties originate from electronic structure near the Fermi level. To investigate the electronic state at QCP and the translation process from local to itinerant character of 4*f* electrons, we measured reflectivity spectra of $CeIn_3$ that is an $AuCu_3$-type cubic intermetallic HF compound with a magnetic ground state resulting from the competition between long ranged antiferromagnetism(T_N=11K), which is produced by RKKY interaction, and the Kondo effect. With applying pressure, the ground state changes from antiferromagnetic to nonmagnetic HF state via the QCP [1]. Therefore this material is suitable to investigate the electronic structure around the QCP.

Experimental

The single crystalline $CeIn_3$ sample was synthesized by an arc melting under argon atmosphere, and then annealed at 600 ℃ for three weeks inside an evacuated quartz tube. The THz reflection spectroscopy under pressure was performed at the THz micro-spectroscopy end station of UVSOR-II BL6B. A diamond anvil cell was employed to produce high pressure. KBr was used as a pressure medium and a gold film as a reference. The pressure was calibrated by a ruby fluorescence method.

Results and Discussion

We obtained pressure-dependent reflectivity spectra [$R(\omega,P)$] of $CeIn_3$ at 300K in the pressure region from 0.7 to 5.6 GPa as shown in Fig. 1. The spectra were divided by that at 0.7 GPa to emphasize the pressure dependence. With increasing pressure, the $R(\omega,P)$ intensity around 0.75 eV was enhanced.

To explain the pressure-dependent of $R(\omega,P)$, an interpretation using the periodic Anderson model (PAM) has been employed by Hancock *et. al.* [2] and Okamura *et. al.* [3], previously. In their interpretation, the reflectivity peak in the middle infrared region originates from the optical transition in between the bonding and antibonding states of the hybridization band of the conduction and local 4*f* electrons predicted with PAM. Due to the PAM, the $R(\omega,P)$ peak must shift to the higher energy side. However, in this study, the $R(\omega,P)$ peak does not shift with increasing pressure. The result is not consistent with the prediction of PAM. This result suggests that the interpretation by usual PAM is insufficient. Recent theoretical study on $YbAl_3$ indicates that the infrared peak originates from the band structure including the hybridization between the conduction and 4*f* electrons [4]. Our result is consistent with the theoretical work.

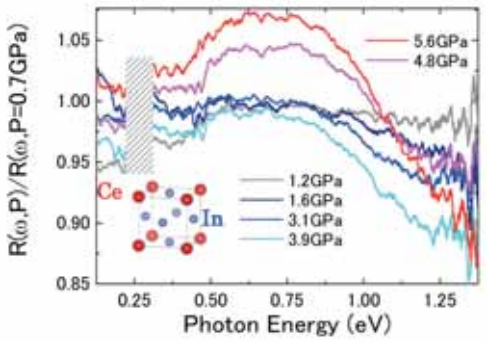

Fig. 1. Reflectivity spectra [$R(\omega,P)$] of $CeIn_3$ with $AuCu_3$-type cubic crystal structure (inset) under pressure at 300K divided by that at 0.7 GPa. The hatched area is that $R(\omega,P)$ cannot be measured because of an absorption of the diamond.

[1] S. Kawasaki *et al.*, J. Phys. Soc. Jpn. **73** (2004) 1647.

[2] J. N. Hancock *et al.*, Phys. Rev. Lett. **92** (2004) 186405.

[3] H. Okamura *et al.*, J. Phys. Soc. Jpn. **76** (2007) 023703.

[4] H. Kuroiwa *et al.*, J. Phys. Soc. Jpn. **76** (2007) 124704.

BL6B

Phonon-Polariton of Superconducting InN Observed by Far-Infrared Synchrotron Radiation

T. Inushima[1], Y. Ota[1], T. Yanagawa[2], K. Fukui[2]
[1]*Department of Electronics, Tokai University, Hiratsuka, 259-1292 Japan*
[2]*Department of Electronics and Electrical Engineering, University of Fukui, Fukui 910-8507 Japan*

Temperature dependence of the reflectivity of superconducting InN with a carrier concentration of 3.5~4.7×10^{17}cm^3 is investigated from 50 to 750 cm^{-1} using infrared synchrotron radiation. E_1 phonon is observed separately from plasma oscillation, and in the energy range below E_1(TO), phonon-polariton is observed up to 10^4 cm^{-1}. The lifetime of the E_1(TO) phonon is directly determined by the reflectivity measurements. From the temperature dependence of the lifetime, it is concluded that the E_1(TO) phonon decays primarily into phonons with a renormalized frequency of 177 cm^{-1}. From the plasma edge position the electron effective mass is estimated to be m_e=0.076m_0 for the intrinsic InN.

All of the InN films investigated had a hexagonal structure and their c-axes were perpendicular to the sapphire (0001) planes. Therefore, one E_1 optical phonon was observed in this configuration. Figure 1 shows the reflectivity spectrum of GS1586 (n_e=3.5×10^{17}cm^3). In the spectrum there is a clear Reststrahren band around 500 cm^{-1}, which is due to the E_1 optical phonon. A reflection edge due to the plasma oscillation is observed at 200 cm^{-1}. The reflectivity spectrum is analysed using a following dielectric function,

$$\varepsilon(\omega) = \varepsilon_0 + \frac{\omega_p^2}{\omega^2 - i\omega\gamma} + \frac{\omega_{TO}^2 - \omega^2}{\omega^2 - \omega_{TO}^2 + i\omega\Gamma}. \qquad (1)$$

Using Eq. 1, the reflectivity spectrum is well reproduced and fitting parameters are obtained.

As is seen in Fig.1, the oscillations below E_1(TO) are due to the interference of the penetrating light in the InN film. In this case, the light with momentum k is expressed by polariton and is expressed using ε(ω) of InN as follows,

$$\frac{c^2 k(\omega)^2}{\omega^2} = \varepsilon(\omega); \quad k(\omega) = \frac{N\omega\lambda}{2cd} \quad . \qquad (2)$$

The observed phonon-polariton dispersion is shown in Fig. 2. In this experiment, the phonon-polariton is observed up to 1.2 eV (10^4 cm^{-1}).

The ratio of Γ/ω_{TO} is the energy dissipation rate for the E_1 vibration. When we regard this as an unharmonic factor of the crystal, InN has 3.3×10^{-3}, which is comparable to those of III-V compounds, indicating that the crystal growth technology of InN has attained the level of major III-V compounds. Nevertheless, the InN investigated here shows superconductivity. Once it was proposed that the In-In nano-structure spread in the *a-b* plane was the cause of the occurrence of the superconductivity[1]. The results presented here show that there is no such structure in InN. At present we have to conclude that InN has strong electron-phonon and electron-electron interactions and the superconductivity is induced by this effect.

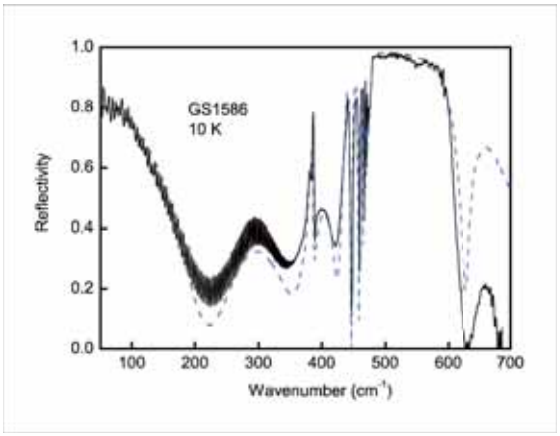

Fig. 1. Reflection spectrum of GS1586 at 10 K. The fitted line (blue line) is drawn using Eq. 1. The fitting parameters are; ω_p=0.03 eV, ω_{TO}= 0.0594 eV, ε_0=10.3, Γ=0.0002 eV, γ=0.008 eV, ε_∞=6.7, d=4.2 μm.

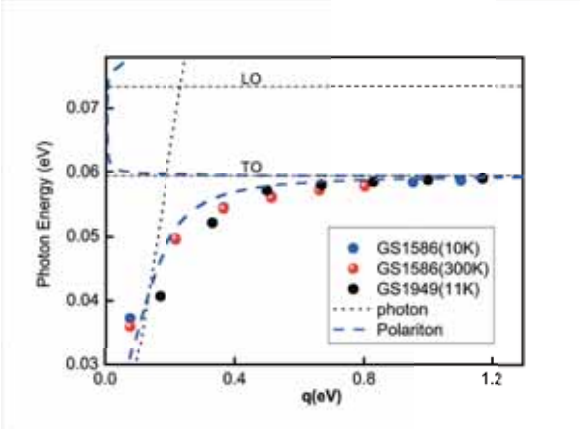

Fig. 2. Phonon-polariton wavenumber q=ħck is plotted against photon energy ħω. The data points are obtained at the peak positions shown in Fig. 1, where the order starts at the peak at 300 cm^{-1}, where N=0.5. The dashed line is drawn using ε(ω) given in Eq. 2, and the dotted line is the dispersion of the light.

[1] T. Inushima, Phys. Stat. Sol. (c) **4** (2007) 660.

BL6B

Solid State Spectroscopy of Proteins in Terahertz Region

X. Jin[1], S. Kimura[2], H. Kihara[1]

[1]*Department of Physics, Kansai Medical University, 18-89 Uyama-Higashi, Hirakata 573-1136, Japan*

[2]*UVSOR, Institute for Molecule Science, and School of Physical Sciences, The Graduate University for Advanced Studies (SOKENDAI), Myodaiji, Okazaki 444-8585, Japan*

The terahertz (THz) region of the electromagnetic spectrum has energies of approximately 1 - 10 meV, which corresponds approximately to the frequency range of the transition between rotational states of molecules. Due to the strong frequency-dependent attenuation of water, dry, or partially hydrated samples should be used in the THz study. THz spectroscopy has been used to studying the dynamics of DNA, polypeptide and proteins. [1.2] In order to investigate effects of secondary structures on THz spectra of proteins, we measured the THz spectra of representative proteins having various secondary structures, myoglobin (α-helix-rich), lysozyme (α/β protein), β-lactoglobulin (β-sheet-rich) and α-synuclein (unfolded).

All experiments were done at THz beam line BL6B at UVSOR-II. The thickness of the samples was around 0.5 mm. The lyophilized samples were tightly pressed to form a tablet. The measurements were done at the wavenumber range of 10-200 cm^{-1} at room temperature. Each spectrum was accumulated 500 times. The final spectra were divided by the cell spectrum in order to subtract absorbance of the cell. All measurements were repeated three times to get good consistency. When the wavenumber is above 100 cm^{-1}, absorbance of the protein become very high and noisy.

Figures 1-4 show these protein absorbance spectra. The red lines are smoothed ones. Figures 1 (myoglobin) and 2 (lysozyme) show a broad peak around 20-25 cm^{-1}, respectively, while Figures 3 (β-lactoglobulin) and 4 (α-synuclein) do not show specific peaks at the corresponding region. These results seem to imply that proteins are classified into two different groups, with and without α-helix. It would be more related to the over-all concerted motion of the proteins.

[1] B. Brooks and M. Karplus, Proc. Natl. Acad. Sci. **80** (1983) 6571.

[2] F. P. David *et al.*, Chem. Phys. Chem. **8** (2007) 2412.

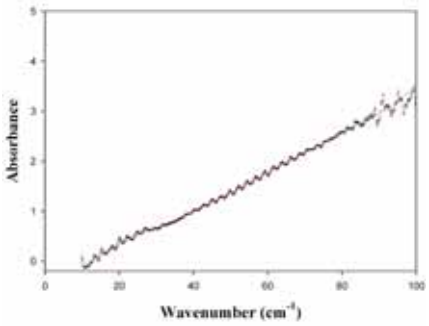

Fig. 1. Absorbance spectrum of myoglobin.

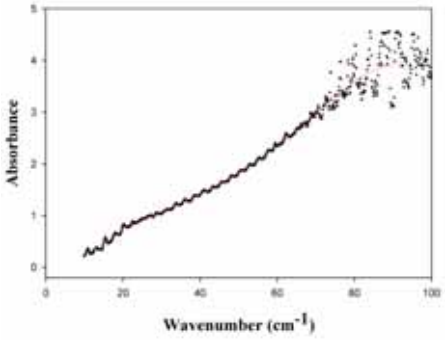

Fig. 2. Absorbance spectrum of lysozyme.

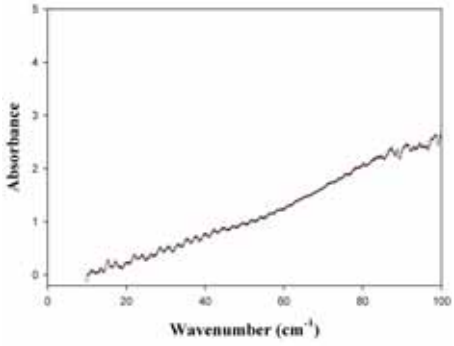

Fig. 3. Absorbance spectrum of β-lactoglobulin.

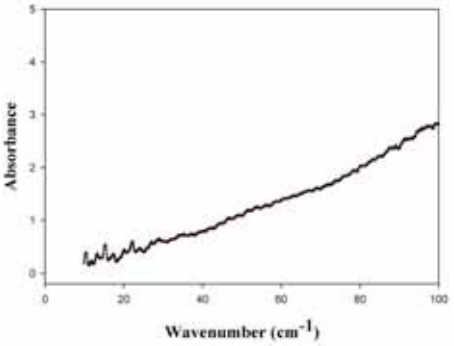

Fig. 4. Absorbance spectrum of α-synuclein

BL6B

Temperature Dependence of Electron Mobility of InN

R. Ueda, K.Kurihara, T. Yanagawa, K. Fukui, A. Yamamoto
Dept. Elec. Elec. Engi., Univ. of Fukui, Fukui, 910-8507, Japan

III-V nitride semiconductors and there mixed crystal semiconductors are used for promising high intensity light emitting diodes (LED) and laser diodes (LD). Especially, InN has a matched band gap for the fiber communication wavelength, and it also has small effective mass and high electron mobility which are required for high speed electronic devices. Since, it is difficult to grow bulk InN crystals, the high quality crystalline InN thin films have been fabricated by the MBE or MOCVD methods. However, there is considerable lattice mismatch between InN layer and the substrate (normally Al_2O_3). Then, the electric properties of the InN sample are sometime affected by this interface layer and it is difficult to separate the electric properties of InN crystalline layer from those of the interface layer. Then, the infrared (IR) reflectance measurements have been investigated as one of the complementary measurement methods for obtaining the carrier concentration of the InN crystalline layer. In this method, since the dielectric constant is described by the phonons and plasmon which are characterized by each layer, the reflectance spectra are analyzed by the fitting calculations based on the appropriate layer model [1]. In this report, we extend the aim of those analyses to the electron mobility and demonstrate that the temperature dependence of the electron mobility can be discussed using the infrared reflectance spectra analyses.

Figure 1 shows the typical reflectance spectrum of the InN thin film at 300K and the fitting curve. The carrier concentration measured by Van der Pauw method is 9.8×10^{18} cm^{-3}. The fitted curve shown in Fig. 1 is based on the two layers model which means no consideration of the interface layer in the optical point of view and in agreement with the observed spectrum. The fitting parameters are $\varepsilon_\infty = 8.3$, $\omega_L = 581$ cm^{-1}, $\omega_T = 478$ cm^{-1}, $\omega_P = 836$ cm^{-1}, $\gamma = 265$, $\Gamma = 2$ and h (thickness of crystalline InN layer) = 200 nm. Since the effective mass is still unknown for InN, we suppose it is $0.1m_0 \sim 0.15m_0$ according to the theoretical prediction, where m_0 is the static mass of the electron. The carrier concentration derived from IR reflectance spectrum is estimated to $6.5 \sim 9.7 \times 10^{18}$ cm^{-3}, which is a little smaller than Van der Pauw result. However, from this result, it is concluded that the electric properties of this InN sample are not affected by those of the interface layer.

The γ are described by Eq. (1),

$$\gamma = \frac{e}{m^* \mu} \quad (1)$$

where m^*, n and μ are effective mass, carrier concentration, and electron mobility of the carriers, respectively. From Eq. (1), the electron mobility can be derived from the IR reflectance measurement by using the damping factor γ of the plasmon which is one of the parameters of the spectrum fitting and the effective mass m^*. Figure 2 shows the electron mobility of the InN crystalline layer derived from the IR reflectance measurements as a function of the temperature. The electron mobility of InN is almost constant in the whole temperature range, and is in agreement with the results of the Hall effect measurement. Therefore, the infrared reflectance spectra analyses can be used for the electron mobility estimation of InN thin films.

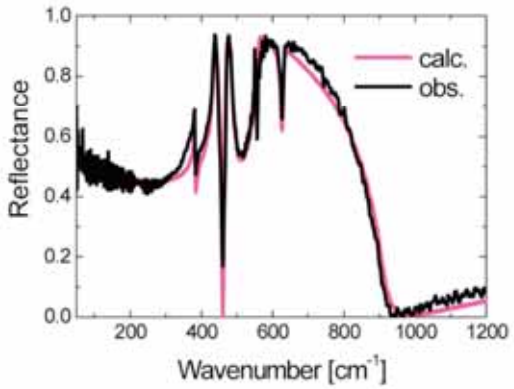

Fig. 1. Reflection spectrum and the fitting result of the InN film in 300K.

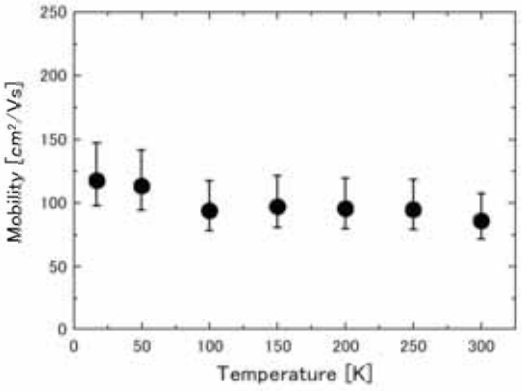

Fig. 2. The electron mobility of the InN crystalline layer at each temperature.

[1] Y. Ishitani *et al.*, phys. stat. sol. (c) **0** (2003) 2838.

BL7B

Comparative Study of Photoluminescence Properties between $ScPO_4:Zr^{4+},Mn^{2+}$ and $YPO_4:Zr^{4+},Mn^{2+}$ Phosphors

Y. Inada[1], M. Kitaura[2], K. Fukui[1]

[1]*Dep. of Elec. Elec. Eng., Univ. of Fukui, Fukui, 910-8507*

[2]*Fukui National College Technology, Sabae, 916-8507*

Photoluminescence (PL) properties of divalent manganese ions are sensitive for the structure of host crystals. An adjustment of the environment around Mn^{2+} ions by the choice of host materials leads to the improvement of PL properties; the diversification of emission color and the increase in PL intensity. It is thus expected that Mn^{2+} activated phosphors have the potential controlling PL properties artificially on demand. In the present study, we have synthesized the phosphor of $ScPO_4:Zr^{4+},Mn^{2+}$, and the PL and PL excitation (PLE) spectra of it have been measured using vacuum ultraviolet photons.

Samples of $ScPO_4:Zr^{4+},Mn^{2+}$ were synthesized by the solid state reaction with the regent of Sc_2O_3, $(NH_4)_2HPO_4$, ZrO_2, and MnC_2O_4. The concentration of Mn^{2+} and Zr^{4+} ions were adjusted to be 2.5 mol% in preparation. The powders were mixed by a ball mill, and then fired at 800 °C in air for 5 hours. The powders thus obtained were sintered at 1200 °C in nitrogen atmosphere for 3 hours.

The PL spectrum of $ScPO_4:Zr^{4+},Mn^{2+}$ at 14 K is shown in Fig. 1. In this figure, the PL spectrum of $YPO_4:Zr^{4+},Mn^{2+}$ at 14 K was also shown as a reference. These spectra were obtained under excitation with 6.5 eV photons. The PL spectra of $ScPO_4:Zr^{4+},Mn^{2+}$ and $YPO_4:Zr^{4+},Mn^{2+}$ are dominated by the 2.34 eV (green) band and the 2.53 eV (blue-green) bands, respectively. The PL intensity of the G band is about twice as large as the intensity of the BG band. The PLE spectra for the G and BG bands at 14 K are shown in Figs. 2(a) and 2(b), respectively. The lowest energy peak is located at 3.08 eV in $ScPO_4:Zr^{4+},Mn^{2+}$ and at 3.15 eV in $YPO_4:Zr^{4+},Mn^{2+}$. The peak energy is lower in $ScPO_4:Zr^{4+},Mn^{2+}$ than in $YPO_4:Zr^{4+},Mn^{2+}$.

In the PL and PLE spectra, the G band of $ScPO_4:Zr^{4+},Mn^{2+}$ is similar to the BG band of $YPO_4:Zr^{4+},Mn^{2+}$. As generally accepted, the PL band of Mn^{2+} originates from the transition from the $^6A_1$ (^6S) ground state to the $^4T_1$ (^4G) excited state. The energies of the lowest PLE peaks in Figs.2(a) and 2(b) are close to the energy difference between the ^6S and ^4G states [1]. This indicates that the G and BG bands originate from the intra-3*d* transition of Mn^{2+} ions.

As the host material is changed from YPO_4 to $ScPO_4$, the lowest PLE peak slightly shifts into low-energy side. Since the $^6A_1 \rightarrow {}^4A_1 + {}^4E$ transition is scarcely influenced by the crystal field potential [2], the peak shift is not due to the change in crystal field strength at the Mn^{2+} site. One plausible effect for the peak shift is the change in electrostatic interaction of 3d electrons in Mn^{2+} ions. In fact, the results in electron spin resonance (ESR) measurement has revealed that the 3*d* wave function of Mn^{2+} spreads out in $ScPO_4$ lattice more than in YPO_4 lattice.

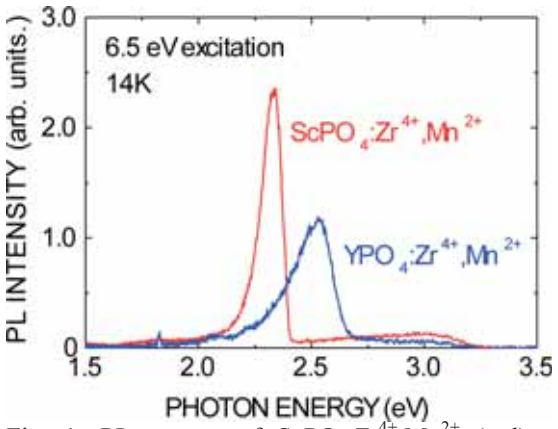

Fig. 1. PL spectra of $ScPO_4:Zr^{4+},Mn^{2+}$ (red) and $YPO_4:Zr^{4+},Mn^{2+}$ (blue) at 14K under excitation with photons at 6.5eV.

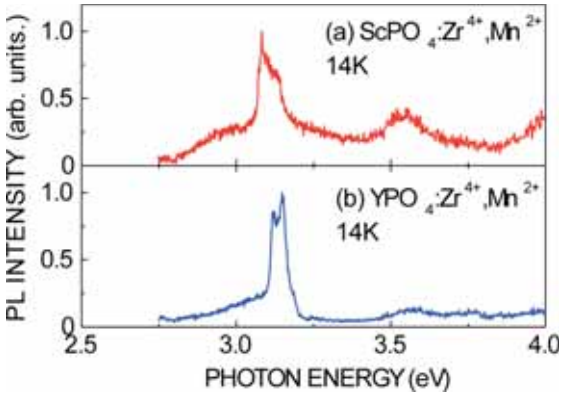

Fig. 2. PLE spectra for the G band in $ScPO_4:Zr^{4+},Mn^{2+}$(a) and the BG band in $YPO_4:Zr^{4+},Mn^{2+}$(b) at 14K.. The intensities are normalized to unity at their maxima.

[1] J. W. Stout, J. Chem. Phys. **31** (1959) 709.

[2] H. Kamimura, S. Sugano, Y. Tanabe, *Haiishiba Riron to Sono Oyo* (Ligand Field Theory and its Applications) (Shokabo, Tokyo, 1990) 10th ed., 224 (in Japanese).

BL7B

VUV Reflection Spectroscopy of PdO and PtO Thin Films

Y. Iwai, K. Nakagawa, T. Mizunuma, K. Nakatsuru, K. Chijiwa, K. Ohba, S. Matsumoto, H. Matsumoto

School of Science & Technology, Meiji University, Kawasaki 214-8571 Japan

Both PdO and PtO have the tetragonal cooperite structure (space group D^9_{4h}) and extremely near lattice constants. Extensive experimental and theoretical studies have been performed on the electronic structures of PdO [1, 2]. On the other hand, there are a few reports of PtO in experimental data obtained by electric and optical measurements. To discuss the electronic structures, researchers have tried calculation and referred them [3]. However, because of restricted experimental data, there are unresolved problems such as a behavior like a p-type semiconductor with high conductivity, and an absence of optical band gap.

The purpose of this work was to achieve optical responses of PdO and PtO thin films in wide-range photon energy, and investigate electronic structures by comparing experiment data and theoretical calculation.

Thin films of PdO and PtO were deposited by RF reactive sputtering on fused quartz, at a temperature of 573 °C. Metal palladium and platinum plate were used as the target, and the sputtering was carried out in argon and oxygen mixture gases. The film thickness was about 150 nm. Composition ratio, chemical bonding states and crystallinity of the films were investigated by RBS, XPS and XRD.

Reflection spectra of the films were measured in the vacuum ultraviolet region up to 30 eV with the 3-m normal incident monochromator (grating: G1 and G2) at BL-7B of UVSOR-II. And a silicon photodiode sensor was used as a detector for the reflection light.

According to the analyses, both palladium and platinum oxide thin films are composed of polycrystalline PdO or PtO.

Figure 1 shows the reflection spectra of PdO and PtO thin films at room temperature. Similar characters are involved in each spectrum: a dip named dip-A in the figure located at about 11 eV, a band named band-B at about 6-8 eV in lower energy side of the dip-A, and a broad band with some features above the dip-A. However, these are at different position in energy.

To analyze the differences, DV-Xα molecular orbital calculation was performed. Figure 2 shows energy level diagrams of $[M_{13}O_{28}]^{-30}$ (M=Pd, Pt) clusters embedded in Madelung potential represented by formal charges. Band gap arises from the splitting off in the d orbital slightly hybridized with O2p. In each oxide, lower side of d band and O2p band construct the valence band. The reason that the lower side of valence band lies slightly lower in PtO is considered stronger d-O2p hybridization due to the larger radius of Pt. And now, energy position of the dip-A observed in reflection spectra is higher in PtO thin film. If there is no large difference in unoccupied levels as final states between PdO and PtO, it is consistent with the widths of valence bands and the energy positions of the dips. And on the same assumption, it can be thought that the fact that the band-B is observed at higher energy on PtO originates the downward diffusing of O2p orbital compared to that of PdO.

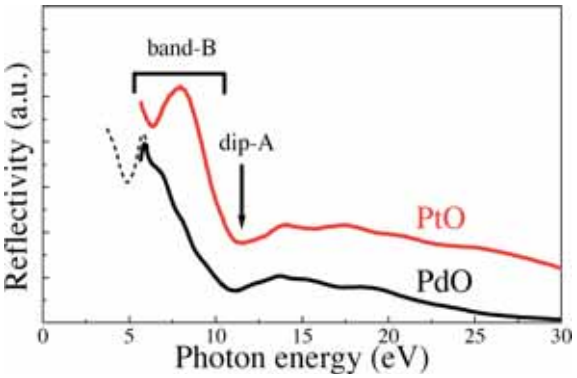

Fig. 1. Reflection spectra of PdO and PtO thin films. The solid line is the data obtained at UVSOR, and the dotted line represents the data obtained elsewhere.

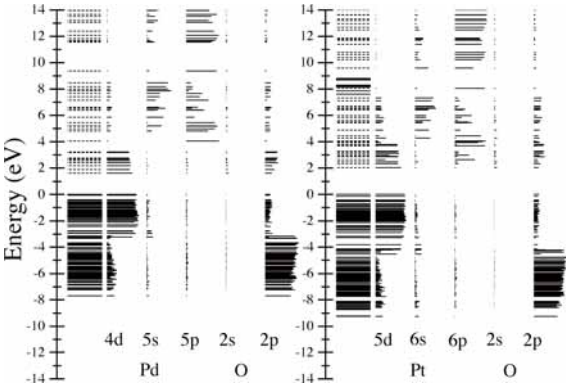

Fig. 2. Energy level diagrams of $[M_{13}O_{28}]^{-30}$ cluster (M=Pd, Pt). The energy is referred to the top of the valence band. The broken lines represent unoccupied levels.

[1] H. A. E. Hagelin *et al.*, J. Electron. Spectrosc. Relat. Phenom. **124** (2002) 1.
[2] R. Ahuja *et al.*, Phys. Rev. B **50** (1994) 2128.
[3] J. Uddin *et al.*, Phys. Rev. B **71** (2005) 155112.

BL7B

Angle Dependence of Polarized Excitation Spectra in AlGaN

M. Kishida[1], F. Suzuki[1], K. Fukui[1], H. Miyake[2], K. Hiramatsu[2]
[1]*Dept. Elec. Elec. Engi., Univ. of Fukui, Fukui 910-8507, Japan*
[2]*Dept. Elec. Elec. Engi. Mie Univ., Mie 514-8507, Japan*

AlGaN alloys are becoming important optical materials which have the UV emission bands with the variable photon energies from 3.4 to 6.28 eV, therefore the studies of mechanisms of UV emissions require wide energy range of the excitation photons, and the SR is well-suited.

The band structures of both AlN and GaN are shown in Figure 1. The valence band at the Γ point is splitting into three bands by the crystal field effect (Δ_{cr}) and the spin orbit interaction (Δ_{so}). The three bands are called as crystal field split off hole (CH) band, heavy hole (HH) band, and light hole (LH) band, respectively, and the transitions from CH, HH and LH bands to the conduction band are labeled as A, B and C transitions, respectively. Furthermore, since these bands have the anisotropy, the A transition is allowed under ***E***//*c* condition, and both B and C are ***E*** ⊥ *c*, where ***E*** and *c* represent the electric field vector of the excited light and the crystal axis, respectively. Usually, the AlGaN (including GaN and AlN) crystalline thin films become wurtzite structure, and *c*-axis is perpendicular to the surface. Therefore the minimum band gap excitation is allowed in the case of GaN (B transition), but is not in the case of AlN (A transition). These conditions directly affect to the optical properties, and the experimental research of finding the band inversion Al fraction is important. Then, we have been measured the angle dependence polarized photoluminescence excitation spectra.

$Al_xGa_{1-x}N$ (x = 0.46, 0.54, 0.65, 0.74, 0.763) samples were grown on the sapphire substrates via 1μm AlN single crystal films by MOVPE method at Mie University. The thicknesses of AlGaN thin films are about 1μm. All measurements were performed at about 20K.

Figure 2 shows the excitation spectra of $Al_{0.763}Ga_{0.237}N$ at 0 degree of the incidence angle (***E*** ⊥ *c*) and 60 degree. The ***E*** // *c* spectra is calculated using these two spectra. The intensity of the ***E*** // *c* spectrum is higher than that of the ***E*** ⊥ *c*, and the red shift of the peak energy is observed in the ***E*** ⊥ *c* spectrum. These results represent that the A transition is allowed at x = 0.763, Δ_{so} is not clear (small), and the shift represents Δ_{cr}.

Figure 3 shows the Al fraction dependence of Δ_{cr}. The Δ_{cr}s at x = 0 and 1 are taken from ref. 1. Fig. 3 results shows the band inversion is occurred at around x = 0.5. Fig. 3 also indicates that there is the negative bowing which is similar to the x dependence of the band gap itself, though the bowing parameters are different with each other.

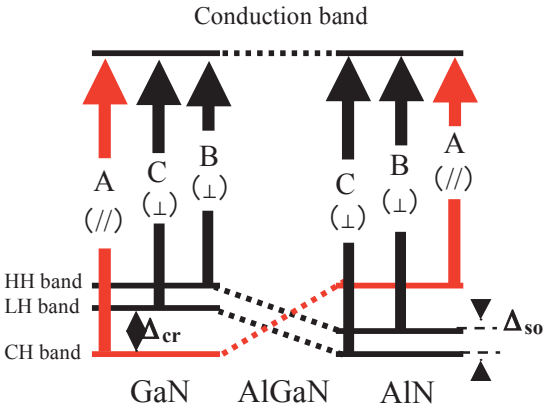

Fig. 1. Band structures of AlN, GaN and AlGaN.

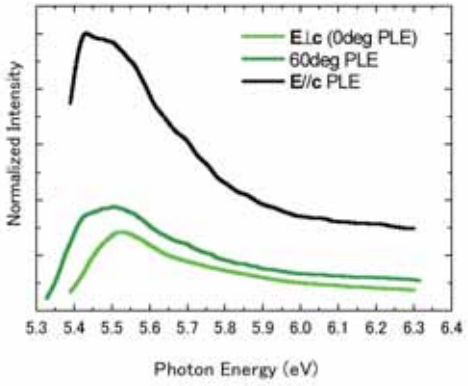

Fig. 2. Angle dependence of the polarized photoluminescence exciton spectra (PLE) of $Al_{0.763}Ga_{0.237}N$.

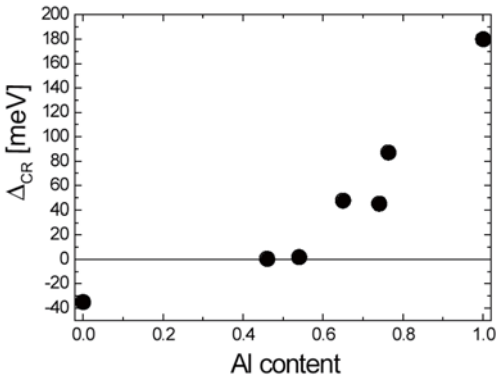

Fig. 3. Al fraction dependence of Δ_{cr}.

[1] A. Shikanai *et al.*, J. Appl. Phys, **81** (1997) 417.

BL7B

Temperature Dependence of the Photoluminescence of the SrScCuOS Layered Oxysulfide

T. Nakazato[1], Y. Furukawa[1], H. Ogino[2], S. Saito[1], S. Ono[3], N. Sarukura[1], K. Kishio[2]

[1]*Institute of Laser Engineering, Osaka University, Osaka 565-0871 Japan*

[2]*Department of Applied Chemistry,University of Tokyo, Tokyo 113-8656, Japan*

[3]*Faculty of Engineering, Nagoya Institute of Technology, Nagoya 466-8555, Japan*

The development and engineering of the wide gap semiconductors are important for optoelectronics. Electrical and optical properties of various III-V or II-V compounds have become clear that the photoabsorption and the emission near the band gap are dominated by excitons. It is said that the excitons enhance emission efficiency because of their large oscillator strengths and room temperature excitonic emission is crucial for light emitting diode operation. Unfortunately, excitons are usually only experimentally observed in high quality crystals and at low temperatures. Ueda *et al*.[1], investigated the temperature dependence of the photoluminescence (PL) spectra of LaCuOS and found that the emission from excitons can be observed at room temperature. They also mentioned that the Cu-S bonding in Cu-S layer defines the electronic structures near band gap. We are interested in SrScCuOS because it has Cu-S layer as LaCuOS. This suggests that it could also be a potential UV material. In the present study, we have measured the temperature dependence of the PL spectra of SrScCuOS to evaluate the optical properties.

We have measured the PL spectra of 3 SrScCuOS crystals, labeled sample A, B, C and E at the BL7B port of the UVSOR. The excitation wavelength was 340 nm. In order to investigate the temperature dependence of PL spectra, these measurements have been carried out at 24-120 K and room temperature.

Figure 1 shows the temperature dependence of the PL spectra. The peaks exist at about 370 nm in all samples. The peak intensities become stronger with lower temperature. These spectra have interesting temperature dependence as will be discussed below. In the case of sample A and E, only one broad peak was found for each temperature setting. A blue shift is observed and the width becomes narrower at lower temperature. Samples B and C showed not only a narrowing of the peak width but a splitting was observed, as well. A temperature dependent relative blue shift between the two peaks could not be observed due to limitations in the spectral resolution. The shorter wavelength peak relatively becomes stronger as compared with the longer wavelength feature as temperature is increased in both samples, B and C. At present, we cannot conclude whether these peaks in each sample are excitonic in nature. Nonetheless, the prospects are interesting because excitonic emission in oxides has not been reported so often. The differences in the PL spectra of A, B, C and E might originate from anisotropy in the defects, impurities, or structures of the Cu-S layers.

We have measured the temperature dependence of the PL spectra of SrScCuOS to evaluate the optical properties. An intensive temperature-dependent PL and absorption study is necessary to confirm the excitonic nature of the observed UV emission.

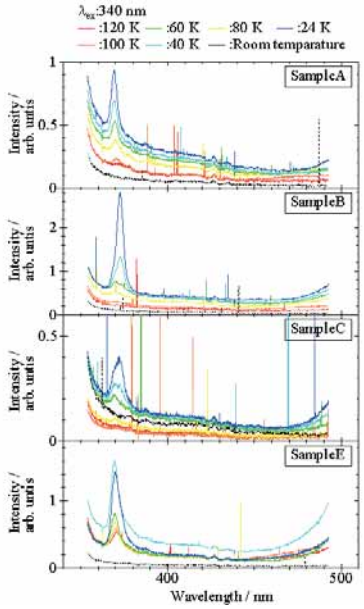

Fig. 1. PL spectra of the SrScCuOS at 20-120 K and room temperature. The excitation wavelength is 340 nm.

[1] Ueda *et al*., Appl. Phys. Lett. **78** (2001) 2333.

BL7B

Energy and Temperature Dependences of Time Resolved Decay Curves in AlGaN Alloys

T. Sakai[1], M. Suzuki[1], T. Kondo[1], K. Fukui[1], S. Naoe[2], H. Miyake[3], K. Hiramatsu[3]

[1]*Dept. Elec. Elec. Engi., Univ. of Fukui, Fukui 910-8507, Japan*

[2]*Dept. Mech. Sys. Engi., Kanazawa Univ., Kakuma, Kanazawa 920-1192, Japan*

[3]*Dept. Elec. Elec. Engi., Mie Univ., Mie 514-8507, Japan*

The ternary AlGaN alloys are promising materials for ultraviolet (UV) optical devices. They are known as the wide band gap semiconductors with the features of the high melting point and the high hardness. The mechanisms of the near band edge photoluminescence (PL) are not clarified enough though the qualitative improvements of the AlGaN emission devices are remarkable. We have been measuring PL, PL excitation (PLE) and time resolved decay (TRD) curves. These results suggest that the near band edge emission band consists of three adjacent emission components (bands) which interact with each other, especially lower two components show the highly efficient energy transfer between them. In this experiment, we have been carried out both the energy and temperature dependence TRD curves of the various Al fraction samples to confirm this model.

$Al_xGa_{1-x}N$ (x=0.37～0.85) samples were made by the MOVPE method at Mie University. The thicknesses of AlGaN thin films are about 1μm on 1μm AlN single crystal films with Al_2O_3 substrates. The TRD measurements were performed at single bunch operation modes. A conventional 30cm VIS-UV monochromator with liquid N_2 cooled CCD detector is used for PL measurements of all samples. The time region of our TRD measurements using TAC method (time correlated single photon counting method) is 0~178 ns and the resolution is about 1 ns.

Figure 1 shows PL spectra of the three adjacent components and the total of various Al fraction samples at ~ 10K. Three components are called as the slow (in the order of 100 ns or less), middle (10 ns order), and fast (less than 1 ns : under the time resolution of our TAC system). The total spectrum represents the sum spectrum of these three components, and it must be in good agreement with the normal (time integrated) PL spectra, conversely, the agreements between the total spectra in Fig. 1 and the normal PL spectra of the various Al fraction samples are good validation checks of our model. In fig.1, it is quite obvious that the slow component become dominant with increasing Al fraction. This behavior is similar to the Al fraction dependence of the PL band width. Since the PL band width corresponds to the classical alloy broadening, the compositional inhomogeneity is increasing with increasing Al fraction up to x = 0.85 and probably introduces some kinds of defects.

Figure 2 shows the temperature dependences of three components of $Al_{0.54}Ga_{0.46}N$. The hot colors represent the high intensity regions. The intensity alternation from slow component to middle one with increasing temperature is clearly seen at the low temperature, and similar behavior is also seen between middle to fast at higher temperature side. The intensity alternation between slow and middle components reveals that there is the energy transfer path between them and the thermal energy makes the excited electrons at the energy level corresponded to the slow component move to that corresponded to the middle component. These kinds of the intensity alternations are seen in all Al fraction samples, and we think we can confirm our model at the various Al fraction samples.

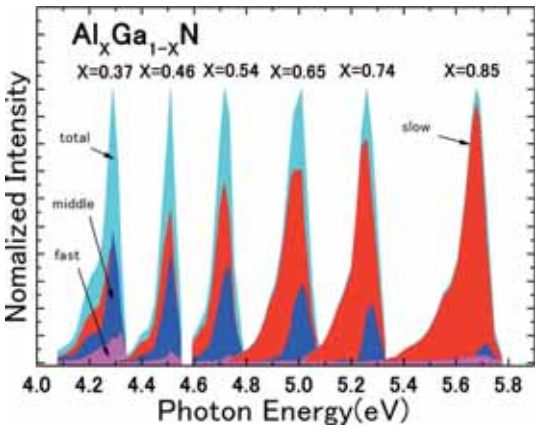

Fig. 1. PL spectra of each element in all samples.

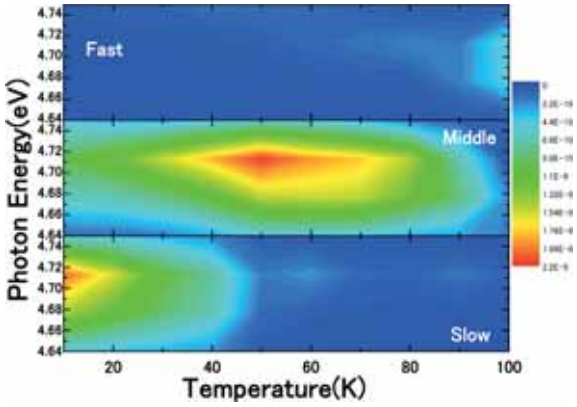

Fig. 2. Temperature dependence of time resolved PL spectra of $Al_{0.54}Ga_{0.46}N$.

BL7B Photoabsorption Cross Section of C_{60} Thin Film from 1.3 to 42 eV

H. Yagi[1], K. Nakajima[2], K. R. Koswattage[3], K. Nakagawa[3], C. Huang[1], Md. S. I. Prodhan[1], B. P. Kafle[1], H. Katayanagi[1], K. Mitsuke[1]

[1]*Department of Photo-molecular Science, and Grad. Univ. Adv. Studies, Institute for Molecular Science,Okazaki 444-8585, Japan*

[2]*Science Research Center, Hosei University, Chiyoda-ku, Tokyo 102-8160, Japan*

[3]*Faculty of Human Development, Kobe University, Nada-ku, Kobe 657-8501, Japan*

Since the discovery of the method for bulk synthesis of C_{60} [1], optical properties of solid C_{60} have been studied by various techniques. But most of the studies were restricted to photon energies below 7 eV. Above 11 eV, only EELS measurements were carried out. In the present study, we have measured absorption spectra of C_{60} thin films from 1.3 eV to 42 eV.

C_{60} films were prepared by vacuum deposition on collodion thin film substrates. The deposition rate and the amount of deposited C_{60} were estimated from the readings of the crystal-oscillator surface thickness monitor (Inficon, XTM/2). Collodion substrates and the thickness monitor were located 90 mm above the sample holder and at symmetrical positions with respect to the molecular beam axis. We prepared three samples with the thickness d = 11, 28, and 57 nm. The deposition rate was 0.16-0.29 Å/s. Optical absorption measurements were carried out at BL7B of the UVSOR facility. The photoabsorption cross section of C_{60} film was estimated by using the Lambert-Beer law

$$I=I_0\exp(-\sigma Nd). \quad (1)$$

Here, σ is the photoabsorption cross section, N is the number density of C_{60} molecules and calculated from the mass density 1.65 g/cm^3 [2], d is the C_{60} film thickness, I_0 is the light intensity after passing through a substrate, and I is the light intensity after passing through a C_{60} film and a substrate. I_0 and I were measured succesively and normalized by the ring current in the storage ring.

The σ values obtained from the results of 28 and 57 nm thick films show good agreement at hν ≤ 12.5 eV. In the energy range 12.5-27.5 eV, I was so small for the 57 nm thick film that we could not estimate correct σ values. The σ from the results of 11 nm thick film also shows good agreement with those of the other films if multiplied by a factor of 0.85. This is probably due to the uncertainty of the film thickness of 11nm thick film. Figure 1 shows thus estimated photoabsorption cross section of C_{60} thin film (black curve) in comparison with that calculated from EELS spectra of C_{60} thin film (green curve) [3]. The two curves are almost consistent with each other. Photoabsorption cross section of gaseous C_{60} is also shown in Fig. 1 (red curve) [4]. The positions of the peaks and shoulders on the σ curve for the C_{60} thin film agree well above 10 eV with those for gaseous C_{60}. This agreement, however, becomes worse below 7 eV and the width of the peak at 22 eV is much larger in the solid phase.

Smith has shown that absorption spectra of C_{60} in the gas phase and solution resemble each other [5] by introducing the Chako factor [6]

$$\alpha_s/\alpha_g = (n^2+2)^2/9n. \quad (2)$$

Here, α_s and α_g are the absorption coefficient in solution and in the gas phase, respectively, and n is the refractive index of the solution. Linder shows that when the solvent is not transparent, Chako factor should be replaced by [7]

$$\alpha_s/\alpha_g = [(n^2+2-k^2)^2+(2nk)^2]/9n. \quad (3)$$

Here, k is the extinction coefficient of the solution. These factors are derived by considering the effect of van der Waals interaction and Lorentz local field. Solid C_{60} is a molecular solid which is bonded by weak van der Waals forces with a cubic structure. Therefore this relation is probably applicable to the solid C_{60}. Present data multiplied by the the Linder factor is shown in Fig. 1 (blue curve). Here, n and k are calculated from the EELS spectra [3]. After the correction of the Linder factor, the present data agrees very well with σ in the gas phase except in the energy range 24-34 eV.

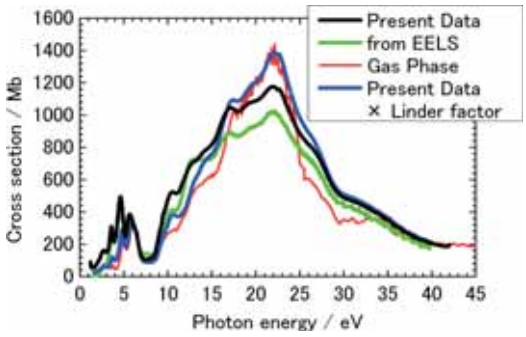

Fig. 1. Photoabsorption cross section of C_{60}.

[1] W. Kratschmer *et al.*, Nature **347** (1990) 354.
[2] K. Prassides, H. W. Kroto, Phys. World **5** (1992) 44.
[3] E. Sohmen *et al.*, Z. Phys. B Condens. Matter **86** (1992) 87.
[4] B. P. Kafle *et al.*, J. Phys. Soc. Jpn **77** (2008) 014302.
[5] A. L. Smith, J. Phys. B **29** (1996) 4975.
[6] N. Q. Chako, J. Chem. Phys. **2** (1934) 644.
[7] B. Linder and S. Abdulnur, J. Chem. Phys. **54** (1971) 1807.

BL7B Photoabsorption Cross Section of C_{70} Thin Film from 1.3 to 39 eV

H. Yagi[1], K. Nakajima[2], K. R. Koswattage[3], K. Nakagawa[3], C. Huang[1], Md. S. I. Prodhan[1], B. P. Kafle[1], H. Katayanagi[1], K. Mitsuke[1]

[1]*Department of Photo-molecular Science, and Grad. Univ. Adv. Studies, Institute for Molecular Science,Okazaki 444-8585, Japan*

[2]*Science Research Center, Hosei University, Chiyoda-ku, Tokyo 102-8160, Japan*

[3]*Faculty of Human Development, Kobe University, Nada-ku, Kobe 657-8501, Japan*

The optical properties of solid C_{70}, the second most stable and abundant fullerene, have been studied by a variety of techniques, though most of the studies were restricted to photon energies below 6 eV. Even in this energy range, the values of the photoabsorption cross section of solid C_{70} differ between different literature. In the present study, we have measured the absorption spectra of C_{70} thin films from hν = 1.3 eV to 39 eV.

In the vacuum, C_{70} films were deposited on collodion thin film substrates. The details of sample preparation are described elsewhere [1]. We prepared three samples with the thicknesses of d = 11, 29, and 57 nm. The deposition rate ranges between 0.19-0.26 Å/s. Optical absorption measurements were carried out at BL7B of the UVSOR facility. The photoabsorption cross section of the C_{70} film was estimated by using the Lambert-Beer law

$$I = I_0 \exp(-\sigma N d). \quad (1)$$

Here, σ is the photoabsorption cross section, N is the number density of C_{70} molecules and calculated from the mass density 1.64 g/cm^3 [2], d is the thickness of the C_{70} film, I_0 and I are the intensities of the light measured with a photodiode by inserting, respectively, the film of neat collodion and that of collodion covered with C_{70} across the photon beam axis. The intensity was measured successively at wavelength intervals of 1 nm and normalized by the storage-ring current.

Figure 1 shows the photoabsorption cross section of the three C_{70} samples with different thicknesses. Their σ values do not agree with each other. Figure 1 also contains the σ curve calculated from the reported EELS spectra of C_{70} thin film with the thickness of 200 nm (green curve) [3]. Our σ curve for the 29 nm C_{70} film and that calculated from EELS show good agreement at hν ≥ 25 eV. Figure 2 shows the expanded spectra of Fig. 1 at hν ≤ 6 eV. The σ values determined from EELS [3], ellipsometry [4], and optical absorption spectroscopy [5] are also plotted. These results and our present data are not consistent with each other. This is possibly due to the difference of the crystal structure. At room temperature, solid C_{70} adopts face-centered cubic (fcc) or hexagonal close packed (hcp) structures depending on the history of its formation [2]. A number of effects determine the relative abundances of hcp and fcc phases. In the present study, the conditions of sample preparation were almost the same for all the samples. Therefore, the thickness of the C_{70} film may affect the crystal structure, or there may be other reason for the disagreement between the three σ curves.

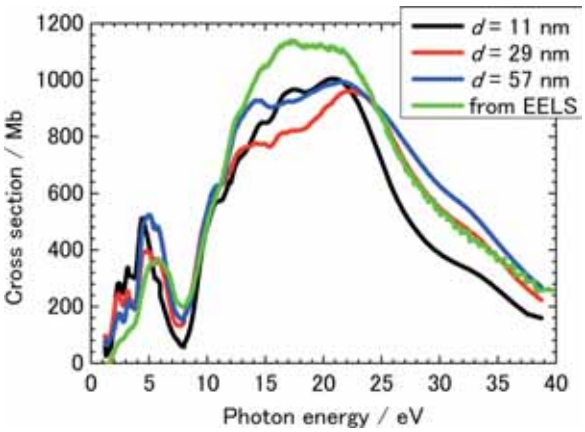

Fig. 1. Photoabsorption cross sections of C_{70} thin films from 1.3 to 39 eV.

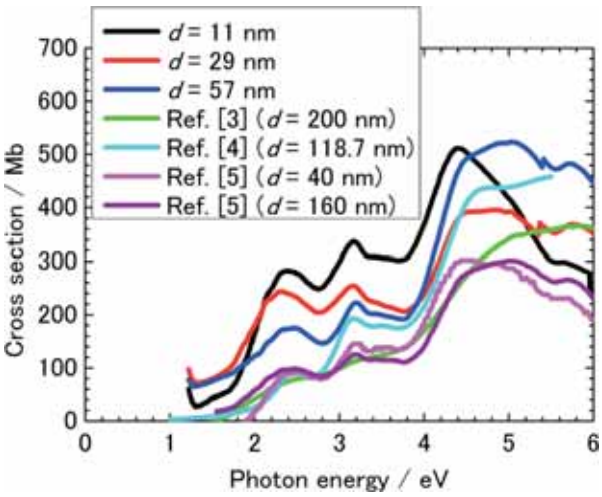

Fig. 2. Photoabsorption cross section of C_{70} thin films below 6 eV in comparison with those of other studies [3-5].

[1] H. Yagi *et al.*, UVSOR Activity Report 2007 (2008).
[2] G. B. M. Vaughan *et al.*, Science **254** (1991) 1350.
[3] E. Sohmen *et al.*, Z. Phys. B Condens. Matter **86** (1992) 87.
[4] Ren *et al.*, Appl. Phys. Lett. **61** (1992) 124.
[5] Zhou *et al.*, J. Appl. Phys. **80** (1996) 459.

FEL

Pumped Wavelength-Dependence of Ce:LuLiF$_4$ as Fast Scintillator Using Storage Ring Free-Electron Lasers

Y. Furukawa[1], T. Nakazato[1], M. Cadatal[2], M. Pham[2], T. Tatsumi[1], A. Saiki[1], Y. Arikawa[1], S. Saito[1], N. Sarukura[1], H. Nishimura[1], H. Azechi[1], K. Mima[1], T. Fukuda[3], M. Hosaka[4], M. Katoh[4], N. Kosugi[4]

[1]*Osaka university, Yamadaoka2-6, Suita, Osaka565-0871, Japan*

[2]*The Graduated University for Advanced Studies, Hayama, Kanagawa 240-0193, Japan*

[3]*Tohoku University, 2-1-1 Katahira, Aoba-ku, Sendai 980-8577, Japan*

[4]*Institute for Molecular Science, Myodaiji, Okazaki, Aichi 444-8585, Japan*

There is an emerging demand for the development of fast neutron scintillator for laser confined nuclear fusion with a fast ignition scheme [1]. For the precise measurement of ignition timing, a scintillator with a fast response time to the high-energy neutron while providing sufficient contrast to the gamma ray is still under investigation. Li 6 is known to have a large cross section for high-energy neutrons. Therefore, lithium-rich compounds with high quantum efficiency light emitting ion are the prominent candidates. From this aspects, we have considered Ce:LuLiF$_4$.

For the development of such scintillation devices, the characterization of the response time for different neutron or photon excitation energies is extremely important for the optimum design of the material and doping concentration.

For this purpose, free electron lasers (FEL) are attractive for their flexible tunability. Among such FELs, storage ring free-electron lasers (SRFEL) should be the appropriate choice because of their adequately high repetition rate [2].

In this presentation, Ce:LuLiF$_4$ as a fast scintillator is evaluated using a SRFEL operated in deep UV region. The response time is found to remarkably shorten for the excitation of the lower level of the absorption band.

The SRFEL at the UVSOR facility in the Institute for Molecular Science, Japan was used as the excitation light source. The excitation wavelengths used are 216 nm and 243 nm. The repetition rate of FEL is 11.3 MHz. The SRFEL was focused on the sample. The fluorescence spectrum and the fluorescence lifetime of the Ce:LuLiF$_4$ sample are measured using the spectrograph coupled to a streak camera. The two peaks in streak camera image as shown in Fig. 1 are attributed to the 11.3 MHz laser repetition rate. Fig. 2 shows that the fluorescence decay time for excitation wavelengths of 290 nm, 243 nm, and 216 nm are 43 ns, 32 ns, and 35 ns, respectively.

In conclusion, the response time is found to be remarkably shortened for the excitation of lower-level of the absorption band of Ce:LuLiF$_4$ as fast scintillator. This response time is already acceptable for the scintillator for the diagonastic device for the laser fusion with fast ignition scheme. The SRFEL operated in deep UV region is shown to be powerful tool for the material survey of neutron scintillation devices.

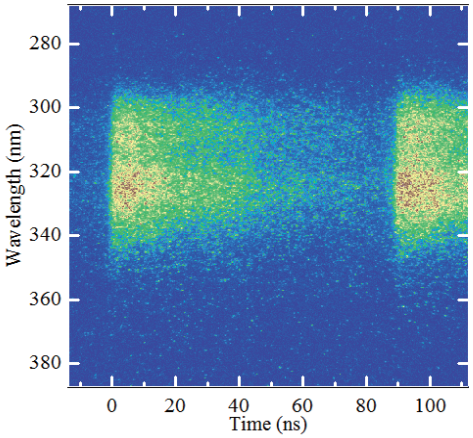

Fig. 1. Streak camera images of Ce:LuLiF$_4$ emission when excited with 216 nm.

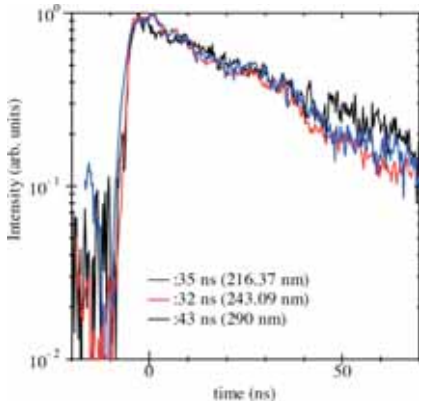

Fig. 2. Fluorescence lifetimes for 290 nm, 243 nm, and 216 nm excitation.

[1] R. Kodama *et al.*, Nature **432** (2004) 1005.

[2] M. Hosaka *et al.*, Nucl. Inst. Methods in Phys. Res. A **483** (2002) 146.

BL1A, BL8B1

Electronic Structure Change of $LiNi_{1/2}Mn_{1/2}O_2$ Cathode Materials for Lithium-Ion Secondary Batteries from Metal L-Edge and Oxygen K-Edge Spectroscopy

Y. Arachi[1], H. Kobayashi[2], H. Maeda[1], T. Asai[1]
[1]*Faculty of Engineering, Kansai University, Osaka 564-8680, Japan*
[2]*Research Institute for Ubiquitous Energy Devices, AIST, Ikeda, Osaka, 563-8577 Japan*

In order to establish the materials design for the Lithium ion batteries, we have employed the variety of measurement techniques and specifically, examined the crystal structure and electronic structure using X-ray, neutron diffraction and XAFS measurements. The absorption peaks of transition metal $L_{2,3}$ edges can directly obtain the information of unoccupied 3*d* states. Because the quadrupole transitions from 1*s* to 3*d* (K edge) are much weaker than dipole from 2*p* to 3*d*. In addition, O K edge spectra provide bonding interactions between metal and oxygen due to the overlapping between 3*d* of metal and 2*p* orbital of oxygen. In our field, the alternatives to conventional $LiCoO_2$ cathode material have been extensively searched due to small natural deposits of Co and its toxicity. $LiNi_{0.5}Mn_{0.5}O_2$ with layered-NaCl type structure proposed as one of a promising material manifests fascinated character such as a good cycleability and reversible capacity of 150 mAh/g within the voltage range of 3.0 to 4.3 V, which corresponds to one-half of theoretical capacity (280mAh/g). Recently, we have synthesized the material by using ion exchange reaction, which showed the suppression of Li/Ni disordering in the layered structure. In this study, the electronic structural changes were observed by XANES spectra of Ni, Mn L-edges and O K-edge respectively and the charging behavior was examined.

$LiNi_{1/2}Mn_{1/2}O_2$ was prepared by ion exchange reaction of $NaNi_{1/2}Mn_{1/2}O_2$ as a precoursor. $NaNO_3$ and precipitates of Ni, Mn hydroxides were mixed and then calcinated at 600°C for 12h. The obtained powders were pressed and sintered at 900°C for 12h in air. The ion exchange reaction was carried out in Li molten salt(LiCl: $LiNO_3$=1:1 (mol), eutectic point = 244°C) at 280-450°C for 0.1 to 10 h. and de-lithiated samples were electrochemically and chemically prepared. The former was used by coin-type cells with Li/1M $LiPF_6$ in EC:DEC(1:1)/samples and the latter was by the chemical oxidants, ammonium persulfate as the following reaction:

$$S_2O_8^{2-} + 2e^- \rightarrow 2\ SO_4^{2-}$$

$$LiNi_{1/2}Mn_{1/2}O_2 \rightarrow Li_{1-x}\ Ni_{1/2}Mn_{1/2}O_2 + xLi^+ + xe^-.$$

X-ray absorption measurements at the Ni, Mn L-edges and O K-edge by total electron yield were performed on BL1A, BL8B1 and occasionally BL4B.

$LiNi_{1/2}Mn_{1/2}O_2$ showed a single phase adopted the a-$NaFeO_2$ structure like as $LiCoO_2$. Neutron diffraction measurements demonstrated that the lattice parameters are a = 2.8922(0) Å and c = 14.31(5) Å and Ni occupancy at Li site, g_{Ni} is 0.028. The chemical composition can be expressed as $[Li_{0.97}Ni_{0.03}]_{3a}[Li_{0.03}Ni_{0.47}Ni_{0.50}]_{3b}O_2$, referring to the Wyckoff positions 3*a* and 3*b* with space group *R*3m. The structure depended on the ion-exchange reaction temperature and time. As increased the reaction temperature and time, the Li/Ni disorder became remarkable. The irreversible capacity was improved by the ion-exchange. Figure 1 shows the selected XANES spectra of O K-edge for chemically oxidized $Li_{1-x}Ni_{0.5}Mn_{0.5}O_2$. The notation from deLi1 to deLi4 corresponds to the reaction time of 0.1 to 1.0 h at various steps. These peaks indicate transition metals 4*sp*. A peak of **A** slightly shifted towards lower energy, while maintaining the peak position of **B**. As the sample oxidized, the orbital of O 2*p* introduced a hole. On the other hands, the results of Ni L-edge showed a slightly higher shift and that of Mn L-edges showed no chemical shifts for all the samples. On the basis of these results, we are constructing the band structure and investigating the charging mechanism for this material.

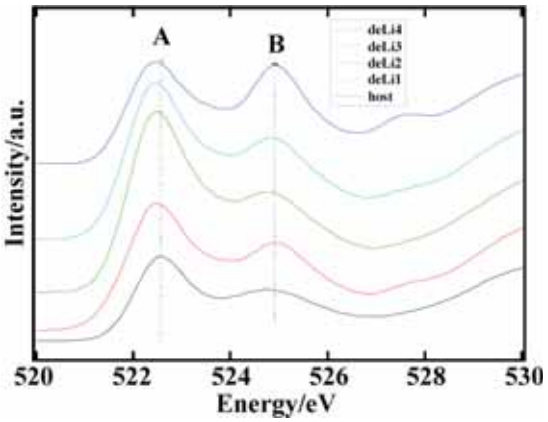

Fig. 1. O K-edge XANES spectra of chemically oxidized $Li_{1-x}Ni_{1/2}Mn_{1/2}O_2$.

BL1A

Mo L_{III}-Edge XANES Study of Catalytically Active Mo Sites on H-MFI for Methane Dehydriaromatization with Hydrogen

H. Aritani[1], H. Shibasaki[1], N. Naijo[1], K. Takanashi[1], K. Nagashima[1], A. Nakahira[2]
[1]*Faculty of Engineering, Saitama Institute of Technology, Fukaya 369-0293, Japan*
[2]*Graduate School of Engineering, Osaka Prefecture University, Sakai 599-8531, Japan*

Introduction

Mo-modified H-MFI catalysts show high activity for dehydroaromatization of methane in absence of oxygen. In this reaction, reduction of Mo species is brought about in contact with methane in initial step, and reduced Mo ions react methane to form carbide and/or oxycarbide species in next step. It has been accepted that the carbide and/or oxycarbide species are the active center for dehydroaromatization of methane. However, deactivation cannot be avoided by carbon deposition. Hydrogen co-feed with methane is effective for suppression of coking. On the other hand, excess hydrogen may affect a reduction of Mo species during the reaction, and decrease of active Mo-oxycarbide species may give low reactivity. Thus the effect of hydrogen with methane is very important to give an effect on Mo states. This study addresses the effects of hydrogen co-feed on methane dehydroaromatization over Mo/H-MFI catalysts. Mo L_{III}-edge XANES studies were introduced to characterize the active Mo species on H-MFI before/after the methane dehydroaromatization in the absence/presence of hydrogen.

Experimental

Catalysts were prepared by impregnation of H-MFI support with $MoO_2(acac)_2$–$CHCl_3$ solution, and followed by drying overnight and calcination at 773 K. H-MFI supports were synthesized hydrothermally at 413 K for a week, and followed by ion-exchange and calcination at 873 K. Mo L_{III}-edge XANES spectra were measured in BL1A of UVSOR-IMS in a total-electron yield mode. Photon energy was calibrated by using Mo metal-foil at Mo L_{III}-edge, and normalized XANES spectra and their second derivatives were obtained. Catalytic activity was evaluated in a fixed bed flow reactor. Each catalyst (0.25 g) was placed in a quartz-tube reactor, and pretreated in He–H_2(0-1%) flow (30 mL min^{-1}) at 973 K for 1 h. Then CH_4(20%)–H_2(0-3%)–He reactant gas was fed at 973 K (30 mL min^{-1}: SV = 7.2 L g^{-1} h^{-1}). Products were analyzed by online GC. Amount of coking carbon was evaluated by thermogravimetry.

Results and Discussion

For the dehydroaromatization in our study, 5.0

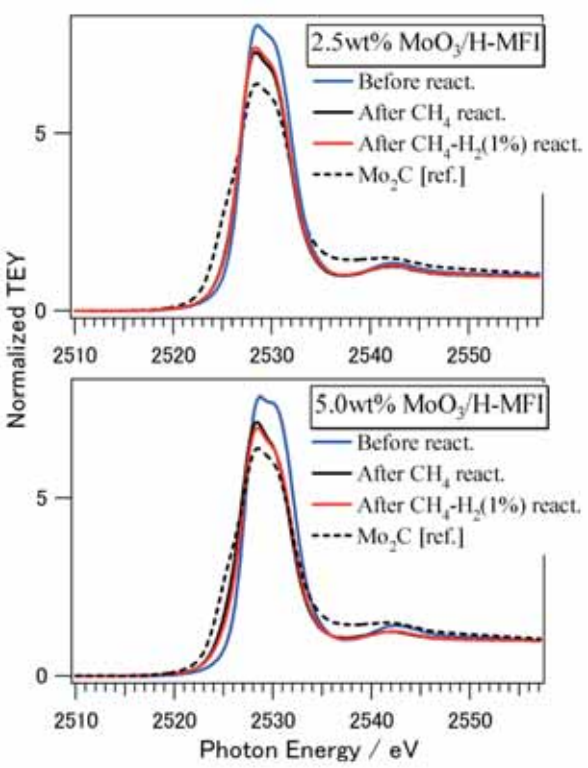

Fig. 1. Mo L_{III}-edge XANES of Mo/H-MFI before/after methane dehydroaromatization.

Mo-loading on H-MFI (Si/Al_2=72) showed a maximum C_6H_6 yield under no additives with CH_4(20%) reactant. H_2(1%) co-feed with CH_4 gave low deactivation, indicating the suppression of coking. But excess H_2 (in 1.5 %) enhanced the deactivation. H_2 pretreatment brought about low activity in the initial step. These results suggest that both inhibition of excessive Mo reduction and suppression of coking on H-MFI relate to the highly catalytic activity for methane dehydroaromatization. The results of L_{III}-XANES (Fig. 1) and their 2nd derivatives suggests the coexistence of Mo^{2+} and oxidized ions after the reaction with CH_4 or CH_4-H_2(1%). On the other hand, Mo^{2+} is dominant after H_2(1%)-He pretreatment. These results indicate that H_2 co-feed with CH_4 does not affect the reduction of active Mo sites, and H_2 pretreatment (without CH_4) brings about the reduction to form Mo^{2+} species in major. And thus, it is concluded that active Mo species consist of Mo^{2+}-oxycarbide species on H-MFI support.

BL1A

Local Structure Analysis of Composite Oxide Electrodes of Dye-Sensitized Solar Cells by XAFS Method

S. Iwamoto[1], Y. Sazanami[1], T. Kadata[1], H. Ozaki[1], W. Hong[1], H. Kanai[1], M. Inoue[1], T. Inoue[2], T. Hoshi[2], K. Shigaki[2], M. Kaneko[2]

[1]*Graduate School of Engineering, Kyoto University, Katsura, Kyoto 615-8510, Japan*

[2]*Nippon Kayaku Co.Ltd., 31-12, Shimo 3-chome, Kita-ku, Tokyo 115-8588, Japan*

Dye-sensitized solar cells (DSSCs) attract great attention because of their high photovoltaic conversion efficiency, simple fabrication process, and low material and production costs [1]. In the last two decades, noticeable improvement in short-current density (J_{sc}) and fill factor (*ff*) has been attained; however, only a slight increase has been accomplished with regard to open-circuit voltage (V_{oc}). In usual DSSCs, titanium oxide and iodide-based solution are used as the electrode and electrolyte, respectively. As the maximum V_{oc} is determined by the difference between the Fermi level of the electrode under illumination and the redox potential of the electrolyte, using these two components, Voc is definitely limited to ca. 0.9 V. Recently, we found that a DSSC consisting of a conjugated acid organic sensitizer and a nanocrystalline Mg-containing TiO_2 generated quite a high V_{oc} of 1 V [2]. In this study, Mg K-edge XANES of various Mg-containing samples were measured to elucidate the local structure of the Mg-modified titanias.

Mg-modified titanias (Mg(x)-TiO_2, where x is Mg/Ti charged ratio) were prepared by the thermal reaction of mixtures of titanium tetraisopropoxide and magnesium acetate tetrahydrate in 1,4-butanediol at 300 ºC (Glycothermal method) [3]. X-ray diffraction (XRD) analysis shows that the obtained products of $x \leq 0.2$ were nanocrystals with the anatase structure. The unit cell parameters of these Mg-modified titanias were increased with increasing the amount of the Mg addition, indicating that Mg^{2+} ions were incorporated in the anatase structure. In Fig. 1, Mg K-edge XANES of various samples are shown. The spectra of Mg-modified TiO_2 samples prepared by an impregnation method (designated as Mg(x)-TiO_2(imp)) suggested the presence of MgO phase. On the contrary, the spectra of Mg(x)-TiO_2 samples preapered by the glycothermal method show peaks at 1310 and 1314 eV, which are similar to that of $MgTi_2O_5$, suggesting that of Mg^{2+} ions are incorporated in octahedral sites in titania matrix. In the UV-vis absorption spectra of Mg(x)-TiO_2, the absorption edges were gradually shifted to the lower wavelength side as the amount of Mg modification increased. This result indicates the shifts of the flat band potentials of the Mg(x)-TiO_2, which contribute to the enhancement of the V_{oc}.

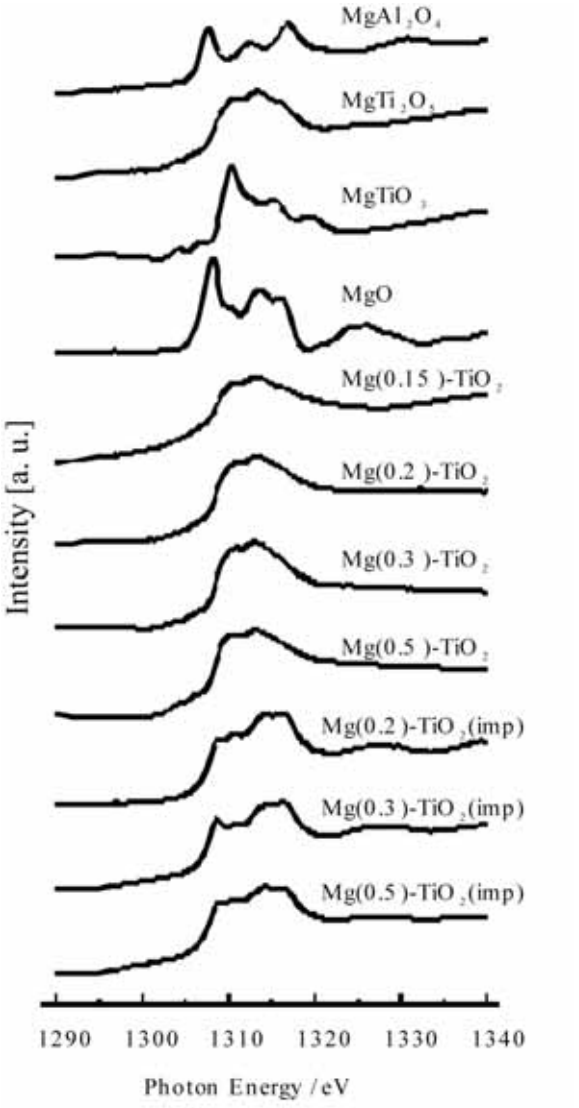

Fig. 1. Mg K-edge XANES of various Mg-containing samples.

[1] M. Grätzel, Nature **414** (2001) 338.
[2] S. Iwamoto *et al.*, ChemSusChem, in press.
[3] M. Inoue, J. Phys.: Condens. Mater **16** (2004) S1291.

BL1A

Local Environment Analysis of Mg Ions in β-Tricalcium Phosphate

K. Kawabata[1], H. Sato[1], T. Yamamoto[2]

[1]*Institute for Sports and Health Science, Kwansei Gakuin University, 662-8501 Japan*

[2]*Faculty of Science and Engineering, Waseda University, 169-8555, Japan*

Introduction

Bioactive ceramic materials, such as hydroxyapatite and β-tricalcium phosphate (β-TCP), have been widely studied and already applied in dentistry and orthopedics to repair bone defects and substitution. As it is well known that the natural bone contains many kinds of trace elements, such as Mg, Na, K, Zn, Fe, Mn etc. To understand the basic properties of natural human bone, it is very important to know the effects of these trace elements. In the present study, the local environment analysis of Mg ions in β-TCP is carried out by the near-edge X-ray absorption fine structure (NEXAFS) technique, which was successfully applied for Mn-doped β-TCP [1].

Experiments

β-TCP samples doped with Mg ions, $Ca_{2.7}Mg_{0.3}(PO_4)_2$, are synthesized by the conventional solid-state reaction method. High purity powders of $CaHPO_4$, $CaCO_3$ and $Mg(OH)_2$ were mixed and grinded in an agate mortar for an hour and the resulting powder was calcined in an air at 1273 K for 6 hours. NEXAFS measurements were carried out at BL1A in UVSOR by the total electron yield method. Powder samples were put on the carbon adhesive tape. The incident photon beams were monochromatized using double-crystal of KTP (110).

Results

Prior to the NEXAFS measurements, the sample powder was examined by using the X-ray diffraction (XRD) technique, in which no extra diffraction peaks due to the precipitates was seen in the XRD pattern. Observed NEXAFS spectrum of Mg-doped β-TCP is compared with those of the reference materials (MgO and $Mg(OH)_2$) in Fig. 1. Significant difference between these three NEXAFS spectra were clearly seen, which indicate the local environment of Mg ions in these three materials is quite different. The first principles calculations within the density functional theory (DFT) were also performed for the theoretical estimation of the NEXAFS spectra with the all-electron linearized augmented plane wave package, WIEN2k [2]. Calculated NEXAFS spectra of Mg-doped β-TCP and MgO at Mg K-edge are compared with the experimental ones in Fig. 2. Good comparison of NEXAFS spectra between observed and calculated ones can be obtained. From the results of the XRD, the NEXAFS and the first principles calculations, we could conclude that Mg ions in β-TCP are substituted on Ca^{2+} site in β-TCP. This type of combinational analysis with the NEXAFS and the first principles calculations must be applied for the analysis of local environment of other trace elements in the bioceramic materials.

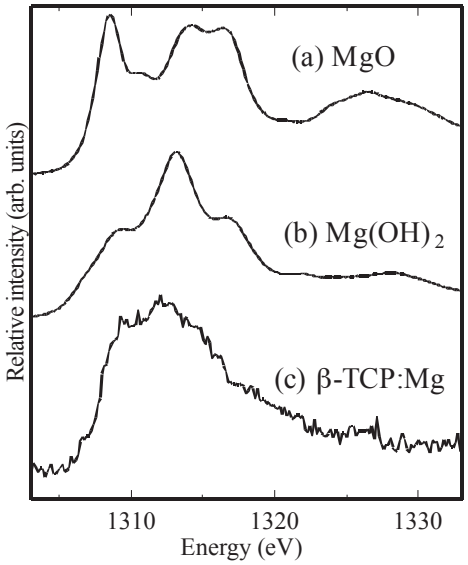

Fig. 1. Observed Mg K-edge NEXAFS spectra of (a) MgO, (b) $Mg(OH)_2$ and (c) Mg doped β-TCP.

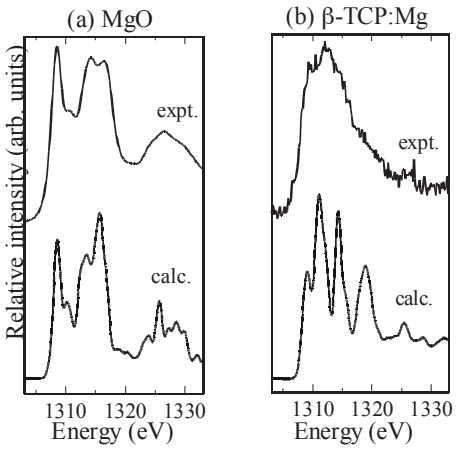

Fig. 2. Comparison between observed and calculated NEXAFS spectra at Mg K-edge of (a) MgO and (b) Mg-doped β-TCP.

[1] K. Kawabata *et al.*, J. Ceram. Soc. Jpn. **116** (2008) 108.

[2] P. Blaha *et al.*, http://www.wien2k.at.

BL1A, BL8B1

Study on the Surface Structures of the $LiNi_{0.8}Co_{0.15}Al_{0.05}O_2$ Electrode after the Preservation Tests for Li-Ion Battery Cells (II)

H. Kobayashi, M. Shikano, D. Mori

Research Institute for Ubiquitous Energy Devices, AIST, Ikeda, Osaka, 563-8577 Japan

Introduction

Several of the requirements of rechargeable batteries for hybrid electric vehicles (HEVs) are quite different to those of portable electronic devices. In particular, high specific power and long calendar life are very important requirements of HEV applications. Much effort has been applied to understanding the mechanisms that limit the calendar life of high power Li-ion cells. Until now, although the deterioration in the power performance of currently available lithium batteries is thought to result from problems with the positive electrodes, the mechanism of deterioration of the electrodes is still poorly understood. Detailed information on the changes taking place in both the cathode and anode is essential in order to determine the origin of the degradation of power performance. In this study, $LiNi_{0.8}Co_{0.15}Al_{0.05}O_2$ positive electrodes from cells that had undergone power fading through preservation tests were examined by XANES analysis to obtain information on their surfaces. The relationship between power fade and the surface state of the positive electrode was studied.

Experimental

We made 18650-type cylindrical battery cells with a capacity of about 400 mAh, which were designed to have a rate capability of more than 10 C. The positive and negative electrode was comprised of $LiNi_{0.8}Co_{0.15}Al_{0.05}O_2$ and hard carbon, respectively. Each cell was characterized using the standard battery test procedure given in the partnership for a new generation of vehicles (PNGV) Battery Test Manual. The changes in both capacity and power were checked every few weeks. After completion of the degradation test, the SOC of the cell was adjusted to 50% immediately before disassembling it, since the chemical and physical properties of the active materials are influenced by the SOC. After disassembly of the SOC-adjusted cell, the surface of the positive electrode was examined by XANES in order to study the surface film or phase transitions in particles of the active material. The Li K-edge and P-K edge XANES spectra of the samples were measured on the BL8B1 and BL1A beamline of the UVSOR Facility. Data were obtained in the total electron yield (TEY) modes.

Results

Table 1 summarizes the relative capacity and power after preservation tests. The relative capacity and power decreased on increasing the test temperature from 40 ºC to 60 ºC. Figure 1 shows the Li K-edge XANES spectra of 50% SOC samples before and after preservation tests. In TEY mode on the BL8B1, Li K-edge XANES spectra provide information on the surface structure. The spectrum measured before preservation tests contained peak A, corresponding to LiF. After the preservation tests, the intensity of peak A clearly decreased at 60 ºC after 96 weeks and the shape of peak A was close to that of the Li_2CO_3 spectrum (data not shown). These results indicate that a part of the layered structure at the surface of the positive electrode was covered with Li_2CO_3 at 60 ºC after 96 weeks. In TEY mode on the BL1A, P K-edge XANES spectra also provide information on the surface structure. The P K-edge spectrum measured before and after preservation tests showed the existence of P-containing surface films (data not shown). The relationship between power fade and the surface state of the positive electrode will be studied in detail.

Table 1. Summary of preservation test results.

Temp.	Preservation Period (Weeks)	Relative Capacity	Relative Power
40C°	96	0.918	0.868
60C°	96	0.716	0.571

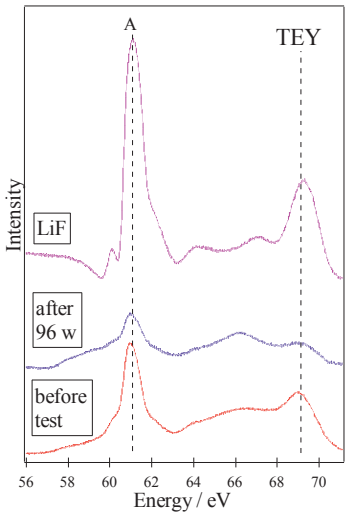

Fig. 1. Li K-edge XANES spectra for the positive electrode before and after preservation tests at 60 ºC.

BL1A

Characterization of Aluminum Naphthalocyanine Complexes by X-ray Absorption Spectra at Cl and Al K-Edges

T. Kurisaki[1], D. Tanaka[1], Y. Sakogawa[1], H. Wakita[1,2]

[1]*Department of Chemistry, Faculty of Science, Fukuoka University, Nanakuma, Jonan-ku, Fukuoka 814-0180, Japan*

[2]*Advanced Materials Institute, Fukuoka University, Nanakuma, Jonan-ku, Fukuoka 814-0180, Japan*

Naphthalocycnine (NPC) has p-conjugated system bigger than that of phthalocycnine (PC). Therefore, the metal complexes of NPC is expected a very interesting property. However, the electronic structure of naphthalocycnine is not well known. In the previous work, we studied the electronic structure of aluminum phtalocycnine by the X-ray absorption spectroscopy [1, 2]. This result suggested that there is correlation between the shape of XANES spectrum and the local structure

In this work, we applied the x-ray absorption near edge structure (XANES) spectroscopy to aluminum compounds combined with oxygen atoms. The results of the measurement indicate unoccupied and occupied electronic structure of aluminum compounds. The X-ray absorption spectra were measured at BL1A of the UVSOR in the Institute of Molecular Science, Okazaki [3]. The ring energy of the UVSOR storage ring was 750MeV and the stored current was 110-230 mA. Al K-edge absorption spectra were recorded in the regions of 1620-1750eV by use of two KTP(011) crystals. The absorption was monitored by the total electron yield using a photomultiplier. The samples were spread into the carbon tape on the first photodynode made of CuBe of the photomultiplier.

The Al K-edge XANES spectra for the aluminum naphthalocycnine and aluminum phthalocycnine are shown in Fig. 1. A change of the spectral patterns was not clearly observed between the aluminum naphthalocycnine and aluminum phthalocycnine. This result showed that the electronic structures of the aluminum ion in these complexes are about the same. We are going to try to analyze the Cl K edge XANES spectra.

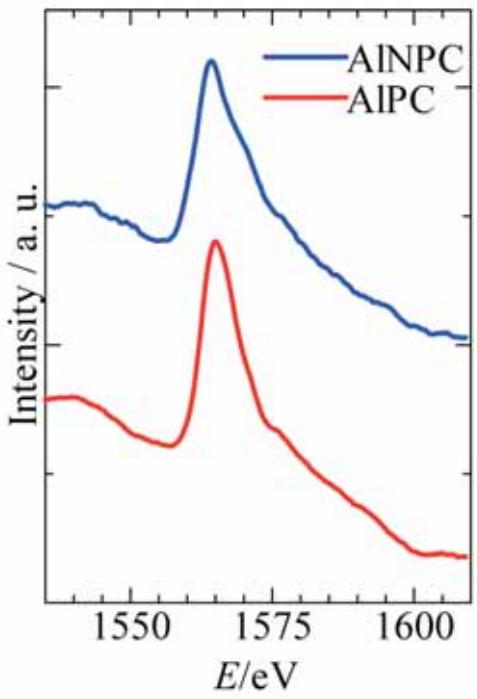

Fig. 1. Observed Al K-edge XANES spectra of aluminum naphthalocycnine and aluminum phthalocycnine

[1] H. Ichihashi *et al.*, Jpn. J. Appl. Phys. **38** *(suppl.)* (1999) 101.

[2] S. Matsuo *et al.*, Adv. Quan. Chem. **42** (2002) 407.

[3] S. Murata *et al.*, *Rev. Sci. Instrum*. **63** (1992) 1309.

BL1A

Study of Al K-Edge of Local Structure in Mesoporous Alumina Bulk Prepared by Hydrothermal Hot-Pressing

A. Nakahira, H. Nishimoto, H. Nagata, Y. Hamada, T. Kubo
Osaka Prefecture University, Gakuen-cho, Sakai 599-8531, Japan

Mesoporous alumina has attracted much attention because of their possible uses as supports for catalysts and adsorption. However, the application of mesoporous alumina was restricted because it was obtained as a powder only. Solidification of mesoporous alumina will improve handleability and expand application. Nakahira et al reported that densified bulky mesoporous silica was successfully synthesized using hydrothermal hot-pressing (HHP) method [1]. Therefore, we attemped to synthesize mesoporous alumina bulk by this HHP method and exmine the local structure around Al by XANES spectra.

Mesoporous alumina powder was prepared as a starting material [2]. Mixture of powder and water was heated at 110 °C with the uniaxial pressing under 40MPa and kept constant for 2 hours. Obtained bulks were identified by XRD. Al K-edge XANES spectra were obtained in a total electron yield mode at room temperature using a KTP double–crystal monochrometer at BL01A of the UVSOR. The spectra were collected in the photon energy range from 1520 to 1600 eV atintervals of 0.05 eV with a dwell time of 1 s.

XRD patterns showed that mesoporous alumina HHP bulk was also retained the mesoporous structure after HHP. Figure 1 shows the results of Al K-edge XANES of mesoporous alumina HHP bulk (a), starting mesoporous alumina powder (b), and γ-alumina (c) as reference materials of amorphs-like γ-alumina. The spectrum of HHP bulks was significantly similar to those of starting mesoporous alumina powder and γ-alumina. Hence, there is no apparent change in the relative intensity nor the width of these spectra. These results of XANES revealed that there is not large difference for local structure around Al between bulks prepare by HHP and ones before HHP treatment.

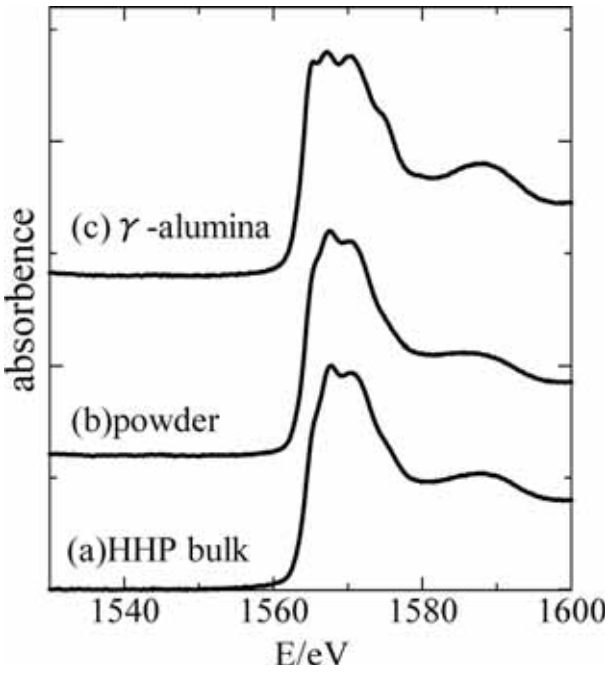

Fig. 1. Al K-edge XANES spectra of mesoporous alumina bulk prepared by HHP.

[1] H. Nagata *et al.*, Materials Transactions **47** (8) (2006) 2103.
[2] F. Vaudry, S. Khodabandeh, M. E. Davis, American Chemical Society **8** (1996) 1451.

BL1A

Structure Charactarization of Poly(vinyl butyral)-Silica Organic-Inorganic Nano-Hybrid by X-Ray Absorption Spectrum

H. Nameki[1], T. Yoshida[2], S. Yoshimoto[1], K. Yamada[1], H. Fukaya[1]

[1]*Indusrial Research Institute, Aichi Prefecture, nishi-shinwari, Kariya 448-0003, Japan*

[2]*Department of Materials, Physics and Energy Engineering, Nagoya University, Furo-cho, Chikusaku, Nagoya 464-8603, Japan*

Introduction

The organic-inorganic nano hybrids are expected as a new material that has the properties of both the inorganic materials and the organic materials. In general, flexibility and hardness are the trade-off relation, and then materials which have both the flexibility and the hardness have been difficult to prepare in past technology. By nano-level hybridization of poly(vinyl butyral) as the organic material and silica(SiO_2) as the inorganic material, we developed a novel material that has both flexibility(impact resistance) and hardness simultaneously[1]. To consider the appearance mechanism of this peculiar property, we examined the structure of the hybrid by X-ray absorption spectroscopy.

Experimental

Alkoxides(tetraethoxysilane and 3-glycidoxy-propyltrimethoxysilane) were added into 5% 2-propanol solution of PVB, and HCl or NH_4OH was added into the mixture as catalyst(the amount of the catalyst is 0.05mol per 1 mol of total alkoxides). In a part of these sample, water(10mol per 1mol of total alkoxides) was added to reacting solution. Thus, sample preparation was done by four methods(shown in table1). The reacted solution was stirred for 2 hours further, and then this was coated into a brass substrate. The coated substrate was preserved in a desiccator for 16 hours, and then heated first at 333K for 2h, next at 363K for 2h. Structure characterization of these sample was done by measuring Si-K edge X-ray absorption spectra at BL1A in UVSOR.

Results and Discussion

Figure 1 shows X-ray absorption spectra of samples and a silica glass as standard material. In all spectra, peak of strong intensity was observed at 1845eV, which was assigned to Si-K edge absorption. Above the energy of the peak, oscillation pattern due to the structure around Si atom was observed.

The oscillation pattern of sample #2 and that of sample #4 were quite similar to each other, on the other hand, these were different from that of sample #1 or #3. Sample #2 and 4 were prepared through H_2O addition, then hydrolysis of alkoxides was occurred and alkoxides was polymerized to form silica(SiO_2 multi-units). The oscillation pattern of spectra was considered to reflect the structure of multi-units silica.

In the sample #1 or #3, alkoxides was mainly reacted with hydroxyl group of PVB, not with each other, because of no addition of H_2O. Then in sample #1 and #3, silica was dispersed as SiO_2 mono unit in the hybrid. This means the arrangement of atoms(oxygen) around Si is irregular in bond distance in sample #1 or #3. Especially, spectrum of the sample #1 was quite similar to the silica glass, which has amorphous structure.

The sample #1 is superior in the properties of transparency, flexibility and impact resistance to the sample #2,#3,#4. The structural difference showed in X-ray absorption spectra is considered to be concerned with the difference in these properties, and that may contributes the appearance of the peculiar property of sample #1.

Table 1. Sample preparation conditions.

No.	Catalyst	H_2O addition	Remarks
#1	HCl	none	showing excellent properties
#2	HCl	added	
#3	NH_4OH	none	not homogeneous sample(opaque)
#4	NH_4OH	added	not homogeneous sample(opaque)

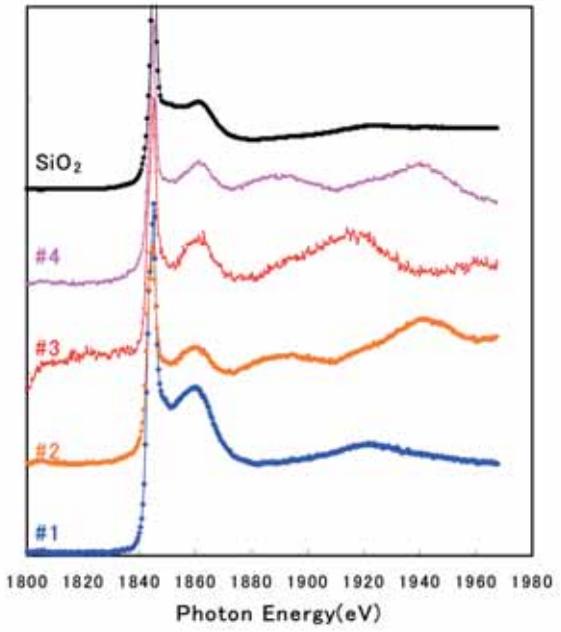

Fig. 1. X-ray absorption spectra of the hybrid samples.

[1] Japan Patent, 2007-119635.

BL1A

In-Situ Measurement of X-Ray Excited Optical Luminescence from a Silica

T. Yoshida[1], T. Tanabe[2], S. Muto[1], H. Yoshida[3]

[1]*Department of Materials, Physics and Energy Engineering, Nagoya University, Furo-cho, Chikusa-ku, Nagoya 464-8603*

[2]*Department of Advanced Energy Engineering Science, Interdisciplinary Graduate School of Engineering Science,Kyushu University6-10-1, Hakozaki, Higashi-ku, Fukuoka 812-8581*

[3]*EcoTopia Science Institute, Nagoya University, Furo-cho, Chikusa-ku, Nagoya 464-8603*

Degradation of optical properties of silica glass by ionizing radiation is one of the main concerns for their use in fusion and fission environments. Although the radiation damage of silica glass has been extensively studied, the detailed damaging processes and/or radiation effects are not yet fully understood. This is partly because most of the studies have been done by post-irradiation tests, which cannot give information on the "processes" but only "traces" or "results" since the relaxation time of excited electrons is usually very short.

Recently, we have tried *in situ* measurement of X-ray excited optical luminescence (XEOL) from a silica glass. The *in situ* measurements were very effective for observing the dynamic changes in their electrical properties by ionizing radiations. In the present study, we examined the changes in XEOL of a silica glass with respect to excitation X-ray energy near the threshold of the Si *K*-edge, irradiation time and temperature.

The sample used in this study was a low-OH fused silica glass (T-2030) disc produced by Toshiba Ceramics, Japan. The diameter and thickness of the sample were 13 mm and 2 mm, respectively. XEOL of the silica glass by X-ray energy between 1.8 and 1.9 keV was measured between 50 K and 300 K on the beam line 1A at UVSOR-II, Institute for Molecular Science. The luminescence was collected and guided by a lens in a UHV chamber to the monochromator (CP-200, JOBIN YVON) and detected by a multi-channel analyser (OMAIII, EG&G PRINCETON APPLIED RESEARCH), which covers the photon energies from ca. 1.5 eV to 4 eV.

We selected three excitation X-ray energies of 1834 eV (just below the Si *K*-edge), 1848 eV (on the white line) and 1858 eV (well above the threshold). In the measurement of XEOL at room temperature, an intense emission band peaked around 3.1 eV is observed in each spectrum. The previous studies assigned the origin of the 3.1 eV band to the intrinsic $B_{2\beta}$ center [1,2]. We also measured XEOL at lower temperatures, and found the broadening of the emission band below 100 K. Fig. 1(a) shows XEOL of the same sample measured at 50 K. A peak position is shifted to the lower energy side, because an additional emission band appears around 2.6 eV, revealed by the peak fit, as shown in Fig.1.

Figs. 1(b) shows the time evolutions of the XEOL intensities at 50 K for the three excitation energies. The intensity value of each point was evaluated by the total area of the emission band in Fig. 1(a). The luminescence intensity is monotonically decreased with the irradiation time at the excitation energy of 1848 eV, whereas at 1834 eV and 1858 eV, the intensities are nearly constant with the irradiation time. A difference spectrum (not shown) between the spectra after irradiated for 300 and 5000 seconds at 1848 eV was dominated by the component peaked at 2.6 eV, indicating that the observed intensity reduction is mainly ascribed to the reduction of this component. These results above suggest that a specific type of point defects in the sample is preferentially decomposed by a specific electronic transition excitation. In other words, a selective electronic excitation can control formation and/or annihilation of a specific type of defects.

In the present case, the transition induced by 1848 eV X-ray corresponds to that from the Si 1*s* occupied state to the 3*p* antibonding orbitals relating to the Si–O bonds. The high-density electron excitation will break the Si–O bonds and also excite the electrons trapped at the luminescent centers of the 2.6 eV band, which could effectively contribute to the decomposition of the centers.

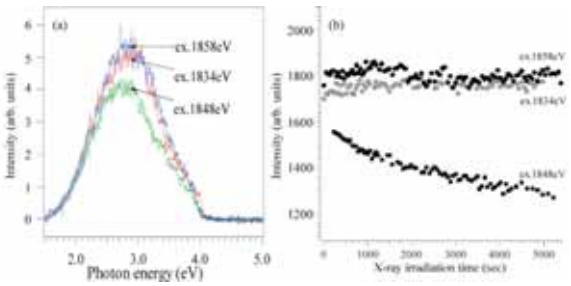

Fig. 1. (a) Optical luminescence spectra of a fused silica glass excited by X-rays with the energies of 1834, 1848 and 1858 eV at 50K. (b) Irradiation time dependence of XEOL intensities at 50 K.

[1] R. Tohmon *et al.*, Phys. Rev. B **55** (1989) 1337.
[2] S. Agnello *et al.*, J. Non-cryst. Solids **232-234** (1998) 323.

BL3U

Direct Observation of Electronic States at Inner Pentacene Thin Films Beneath Au Electrodes

H. S. Kato[1], F. Yamaguchi[1,2], M. Kawai[1,2], T. Hatsui[3], M. Nagasaka[3], N. Kosugi[3]
[1]*RIKEN (The Institute of Physical and Chemical Research), Wako 351-0198, Japan*
[2]*Department of Advanced Materials Science, University of Tokyo, Kashiwa 277-8501, Japan*
[3]*UVSOR Facility, Institute for Molecular Science, Okazaki 444-8585, Japan*

Introduction

In order to extend new functionality of electronic devices, the molecular devices have recently been investigated with great efforts. The organic field effect transistor (OFET) is a typical molecular device that controls electric conductivity by injection of carriers into the organic thin film under the applied electric field. The conductive mechanism has generally been understood with a scheme of band bending of electronic states, based on the knowledge of inorganic semiconductor transistors. However, the energy diagram might be not exactly the same between organic and inorganic materials, because of more localized orbitals of the organics. Moreover, it is also important to elucidate the difference of electronic states for future advanced devices utilizing the noble characters of organic materials. Therefore, the direct observation of electronic states in the organic thin films under operation conditions has been required.

In this study, we aim to establish a new experimental method that elucidates the electronic state change in organic thin films of OFET under the electric field. The fluorescence-yield X-ray absorption spectroscopy (FY-XAS) should be a promising method for detection of inner electronic states of organic devices, because the fluoresced X-ray has a long mean free path more than several 10 nm in most of materials even for soft X-ray excitation. In addition, the X-ray is not disturbed by applied electric field, besides emitted electrons. Thus, we have attempted to utilize FY-XAS for investigation of inner electronic states of OFETs.

Experimental

To investigate the electronic states of OFET, pentacene (Pn) thin films on the SiO_2-covered Si substrates were fabricated using a molecular beam deposition system at RIKEN. The quality of their morphology and crystallinity was high enough in comparison with those in previous reports. The performance for FETs of the fabricated Pn thin films was also confirmed with additive deposition of Au electrodes on the films. By the same preparation, the fully Au-covered Pn thin-film samples were made to evaluate the field effects obtained from uniform electric fields in the films.

The FY-XAS measurements were performed at the BL3U beamline of UVSOR facility in IMS. The samples were set in a BL3U end-station through sample-entry system. The fluorescence intensities were measured using a retarding field detector consisting of MCP plates.

Results and Discussion

Figure 1 shows the incidence angle dependence of fluorescence-yield C K-edge XA spectra of the Pn films (t = 20 nm), in which the spectra of a non Au-covered Pn film and a fully Au-covered Pn film are compared. In both cases, the relative intensities of π^* components at photon energies of ≈ 285 eV decrease with increasing incidence angle of excitation X-ray, while the broad σ^* components above 300 eV increase with increasing incidence angle. These results are consistent with the structure of crystallized Pn thin films on SiO_2 substrates; the molecular axis is towards surface normal with a small tilting angle in each monolayer. The small difference between the non Au-covered and fully Au-covered Pn films would be due to a perturbation at the Au deposition form a thermal evaporation source. However, the similarity in the incidence angle dependence of the spectra evidences that the perturbation is not significant for the whole Pn thin film. As above, the FY-XAS measurements have enough potential to characterize the inner organic thin films even beneath electrodes.

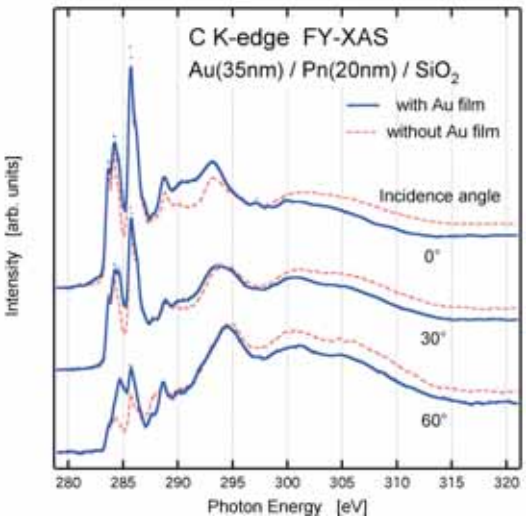

Fig. 1. Incidence angle dependence of fluorescence yield C K-edge XA spectra of pentacene thin films on SiO_2-covered Si substrate, in which the spectra of a non Au-covered Pn film (red broken lines) and a fully Au-covered Pn film (blue solid lines) are compared. The incidence angle is defined from surface normal.

BL4B

Study on the Surface Structures of the $LiNi_{0.8}Co_{0.15}Al_{0.05}O_2$ Electrode after the Preservation Tests for Li-Ion Battery Cells (I)

H. Kobayashi, M. Shikano

Research Institute for Ubiquitous Energy Devices, AIST, Ikeda, Osaka, 563-8577 Japan

Several of the requirements of rechargeable batteries for hybrid electric vehicles (HEVs) are quite different to those of portable electronic devices. In particular, high specific power and long calendar life are very important requirements of HEV applications. Much effort has been applied to understanding the mechanisms that limit the calendar life of high power Li-ion cells. Until now, although the deterioration in the power performance of currently available lithium batteries is thought to result from problems with the positive electrodes, the mechanism of deterioration of the electrodes is still poorly understood. Detailed information on the changes taking place in both the cathode and anode is essential in order to determine the origin of the degradation of power performance. In this study, $LiNi_{0.8}Co_{0.15}Al_{0.05}O_2$ positive electrodes from cells that had undergone power fading through preservation tests were examined by XANES analysis to obtain information on their surfaces. The relationship between power fade and the surface state of the positive electrode was studied.

Experimental

We made 18650-type cylindrical battery cells with a capacity of about 400 mAh, which were designed to have a rate capability of more than 10 C. The positive and negative electrode was comprised of $LiNi_{0.8}Co_{0.15}Al_{0.05}O_2$ and hard carbon, respectively. Each cell was characterized using the standard battery test procedure given in the partnership for a new generation of vehicles (PNGV) Battery Test Manual. The changes in both capacity and power were checked every few weeks. After completion of the degradation test, the SOC of the cell was adjusted to 50% immediately before disassembling it, since the chemical and physical properties of the active materials are influenced by the SOC. After disassembly of the SOC-adjusted cell, the surface of the positive electrode was examined by XANES in order to study the surface film or phase transitions in particles of the active material. The O K-edge XANES spectra of the samples were measured on the BL4B beamline of the UVSOR Facility. Data were obtained in the total electron yield (TEY) mode.

Results

Figure 1 shows the preservation period vs. relative capacity and power. The relative capacity and power decreased on increasing the test temperature from 40 ºC to 60 ºC. Figure 2 shows the O K-edge XANES spectra of 50% SOC samples before and after preservation tests. In TEY mode, O K-edge XANES spectra provide information on the surface structure. The spectrum measured before preservation tests contained peak A, corresponding to oxygen originating from the layered structure, and peaks B and C. After the preservation tests, the intensity of peak A clearly decreased at 60 ºC after 96 weeks, while the intensities of peaks B and C increased. The position of peak B was close to that of the NiO spectrum, indicating the existence of a cubic phase on the surface, and the position of peak C was close to that of Li_2CO_3, or to conductive materials such as AB (data not shown). These results indicate that a part of the layered structure at the surface of the positive electrode was transformed to a cubic structure at 60 ºC after 96 weeks.

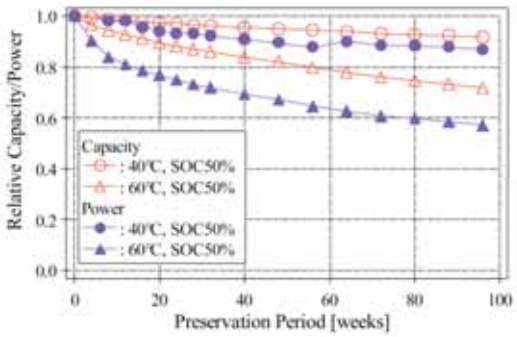

Fig. 1. Preservation period vs. relative capacity and power.

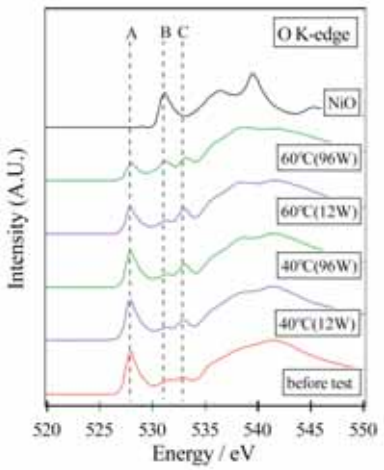

Fig. 2. O K-edge XANES spectra for the positive electrode after preservation tests at 40 ºC and 60 ºC.

BL4B

Magnetic Properties of C_{60} and Co Nanocomposite Films

Y. Matsumoto[1], S. Sakai[1], T. Takagi[2], T. Nakagawa[2], T. Yokoyama[2]

[1]*Advanced Science Research Center, Japan Atomic Energy Agency (JAEA), Tokai Naka-gun, Ibaraki 319-1195 Japan*

[2]*Department of Materials Molecular Science, Institute of Molecular Science (IMS), Okazaki, Aichi 444-8585, Japan*

Recently, we have found that fullerene (C_{60}) and cobalt (Co) nanocomposite films show large tunnel magnetoresistance (TMR) effects at low temperature [1]. As shown schematically in a figure 1, these films consist of a matrix of C_{60}-Co compounds and dispersed Co nano particles [2]. However, observed TMR effects cannot be explained only by a spin transport among the Co particles even if they are completely spin polarized. Therefore, in the present work, we have investigated local magnetic properties of C_{60}-Co films by X-ray magnetic circular dichroism (XMCD) spectroscopy.

MCD measurements were performed at beam line 4B with a super conducting magnet. The details of this MCD system are described elsewhere [3]. Different Co content films of $C_{60}Co_x$ (x: the number of Co atoms per a C_{60} molecule) were prepared by a co-deposition method [1] under the UHV condition ($<10^{-7}$Pa) and then transferred into the experimental chamber without breaking the vacuum. The Co $L_{III,II}$-edge MCD spectra were taken with the polarization factor of ~0.85. Total energy resolution of 0.75eV was applied in the present work.

Figure 2(a) and 2(b) show XAS spectra at the Co 3d←2p excitation, and MCD spectra of different contents of $C_{60}Co_x$ and pure-Co films measured at 5T and 4.9K, respectively. In the case of Co dense films (x>10), peak profiles of MCD spectra are similar to those of the pure Co film. This result indicates that Co particles dispersed into the film have a same magnetic property as a Co metal. On the other hand, in the case of Co dilute films (x<10), MCD signal are different to pure-Co film (see inset, Fig. 2(b)). According to our previous works of Raman spectroscopy [2], the matrix of C_{60}-Co compounds is dominant in this composition domain. In fact, XAS spectrum of $C_{60}Co_{4.3}$ has several fine structures as shown in Fig. 2(a) in contrast to the Co film. Though the derails of such structures which show MCD responses are not clearly right now, it is expected that they are connected to the hybrid molecular orbitals (MOs) of Co 3d band and C_{60} π^* orbital from XPS and C K-edge NEAXFS measurements. In addition, it has been also observed that MCD signal of Co dilute films indicate the strongly temperature dependence (not shown in figures here). Especially, MCD signal of $C_{60}Co_{4.3}$ film was vanished at 77K. These findings indicate that there are hybrid MOs which show paramagnetic properties in the C_{60}-Co compounds. It is speculated that these states act as a spin-filter in spin transport processes.

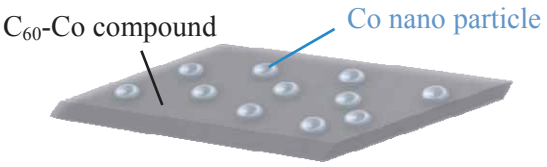

Fig. 1. Schematically illustration of the C_{60} and Co nanocomposite film.

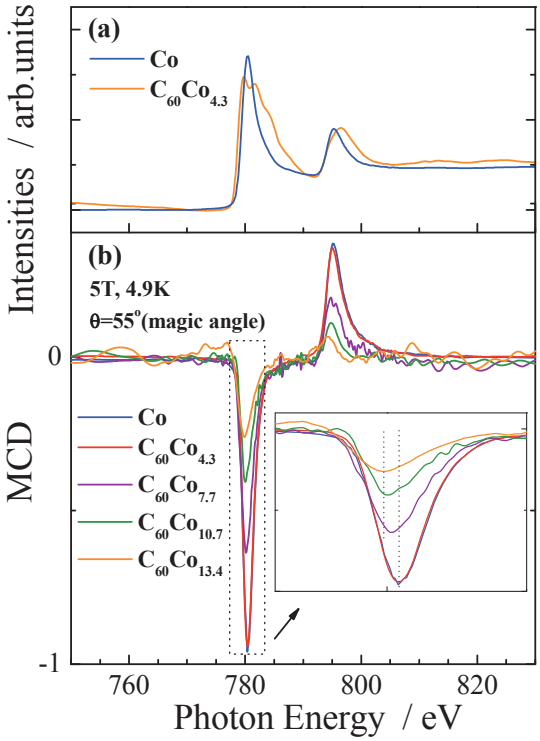

Fig. 2. Co L-edge XAS spectra (a), and MCD spectra of different Co contents of $C_{60}Co_x$ and the pure Co -film measured at 5T and 4.9K (b).

[1] S. Sakai, I. Sugai, S. Mitani, K. Takanashi, Y. Matsumoto, H. Naramoto, P. V. Avramov, S. Okayasu, Y. Maeda, Appl. Phys. Lett. **91** (2007) 242104.

[2] S. Sakai, H. Naramoto, V. Lavrentiev, K. Narumi, M. Maekawa, A. Kawasuso, T. Yaita, Y. Baba, Mater. Trans. **46** (2005) 765.

[3] T. Nakagawa, T. Takagi, Y. Matsumoto, T. Yokoyama, Jpn. J. Appl. Phys. *in press*.

BL5U

Valence Band Spectra of Fe/Si Interfaces Changing Probing-Depth

T. Ejima, T. Goto, T. Jinno

Institute for Multidisciplinary Research for Advanced Materials, Tohoku University, Sendai 980-8577 Japan

Node and antinode positions of standing waves can easily move in uppermost layers of the multilayer, therefore photoelectrons excited in the uppermost layers can be effectively scanned through the interface of the layers [1]. Recently, these positions can be determined by total electron yield (TEY) spectra measured simultaneously with reflection spectra [2].

Magnetic coupling between Fe layers in Fe/Si multilayers exhibits initially ferromagnetic one, then antiferromagnetic, and finally ferromagnetic or no coupling with an increase of the sandwiched Si layer thickness [3]. When the thickness of the Si layer is 2.0 – 2.5 nm, the coupling changes from antiferromagnetic one to ferromagnetic or non-magnetic one. The origin of this inter-layer coupling is controversial, and is roughly classified into either a metallic model as Fe-Si compound or a semiconductor model as amorphous Si [4, 5]

In this study, electronic structures of Fe/Si interfaces of Fe/Si/Fe trilayers deposited on a Mo/Si reflection multilayer are investigated using photoelectron spectroscopy changing the probing depth, which is caused by the phase changes according to the changes of the thicknesses of the uppermost trilayers and of incident wavelength. The phase changes are observed in situ by both TEY and reflection spectra.

Nominal layer structure of the Fe/Si/Fe trilayer estimated from the experimental deposition rates is represented in Fig. 1. Magnetic behavior of this trilayer estimated from the VSM measurement was ferromagnetic one. The photoelectron spectra were measured with TEY spectra. Probing depth estimated from the TEY and reflection spectra is represented in Fig. 1 concerning with the Ar^+ etching time and obtained UPS spectra [2].

Obtained UPS spectra represented in Fig. 2 can be classified into 3 groups: first is a Fe-Si compound structure (spectra b – d), second is an amorphous Si structure (spectra e – f), and the last is a Fe structure (spectra h & i). This classification of the electronic structures suggests that inter-diffusion layer between Fe/Si layers is formed when a Fe layer is deposited onto a Si layer, and not formed when a Si layer is deposited onto a Fe layer. The second Si-like electronic structures observed between the Fe layers suggest that the origin of the coupling is well explained by the semiconductor model, if the ferromagnetic behavior is caused by the inter-layer coupling.

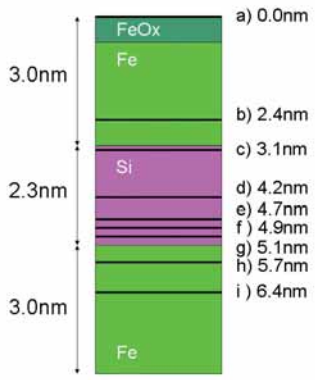

Fig. 1. Nominal layer structure of Fe/Si/Fe trilayer with estimated probing depth.

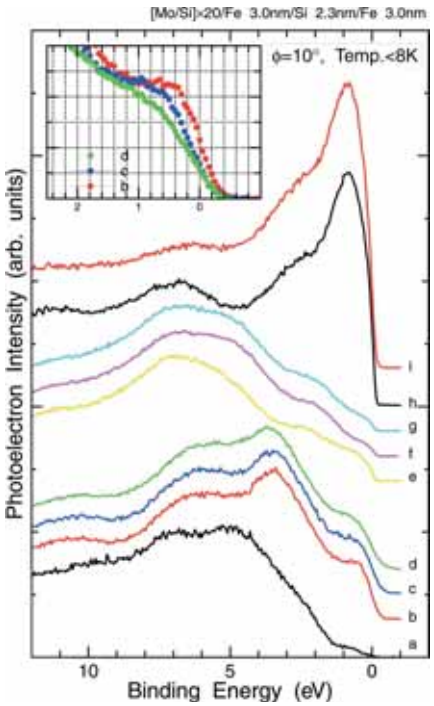

Fig. 2. Valence band spectra of Fe/Si interfaces changing the probing depth. Characters represent the probing depths that are designated in Fig. 1.

[1] S. –H. Yang *et al.*, J. Phys., Condens. Matter **14** (2002) L407.
[2] T. Ejima *et al.*, Appl. Phys. Lett. **89** (2006) 021914.
[3] E. E. Fullerton *et al.*, J. Magn. Magn. Mater. **117** (1992) L301.
[4] For example, P. Bruno, C. Chappert, Phys. Rev. Lett. **67** (1991) 1602.
[5] For example, D. M. Edwards *et al.*, Phys. Rev. Lett. **67** (1991) 493.

BL5U

Fermi Surface Mapping of 8 ML Fe/Cu(001) by Angle-Resolved Ultraviolet Photoemission Spectroscopy

X. Gao[1], H. Miyazaki[2,3], S. Chen[1], A. T. S. Wee[1], T. Ito[3], S. Kimura[3], J. Yuhara[2], K. Soda[2,3]

[1]*Department of Physics, National University of Singapore, Singapore 117542*

[2]*Graduate School of Engineering, Nagoya University, Nagoya 464-8603, Japan*

[3]*UVSOR Facility, Institute for Molecular Science, Okazaki 444-8585, Japan*

Introduction

Despite many years' research efforts in Fe/Cu(001) system, it remains one of the most complicated magnetic thin film systems. It is generally believed that there are three thickness range of the Fe film with different magnetic properties and structures [1]: below 3 monolayers (ML), Fe film has so-called face center distorted (fct) structure and is ferromagnetic; from 4 ML to about 10 ML, the film has a ferromagnetic fct top layer with the rest layers either anti-ferromagnetic or paramagnetic with fcc structure depending on the temperature; above 11 ML, the whole film changes to bcc structure and is ferromagnetic. Non-uniform reduced magnetic response in the second thickness range than in the other two ranges are still full of mysteries and there are still disputes about its nature. Fermi surface mapping by ultraviolet photoemission spectroscopy (UPS) is a powerful technique to study electronic structure in k space. Although there have been Fermi surface mapping studies of Co and Ni grown on Cu(001) and many studies of valence band using UPS for Fe/Cu(001), no Fermi surface mapping has been reported so far for Fe/Cu(001).

Experimental

Cu(001) surfaces were prepared by cycles of Ar^+ ion bombardment at 1 keV and annealing at 800 K in an ultrahigh vacuum system. The (1x1) pattern was clearly observed on the clean Cu (001) surface by low energy electron diffraction. 8 ML Fe film was *in situ* evaporated onto the Cu(001) surface at room temperature, which was cooled down to 5 K for UPS. The thickness was monitored by a quartz oscillator and calibrated using XPS. Angle-resolved photoelectron spectra were recorded under 2.7 x 10^{-8} Pa with a high-resolution energy analyzer at BL5U. The total energy resolution was 14 meV with the excitation photon energy of 90 eV at 5 K.

Results and Discussion

Figure 1 shows the photoemission intensity of 8 ML Fe/Cu(001) along [001] direction recorded at a photon energy of 90 eV. Dispersions of both Fe 3*d* at the Fermi surface and Cu 3*d* at the binding energy of about 2 eV can be clearly observed.

Figure 2 shows Fermi surface mapping for 8 ML Fe/Cu(001) at 5 K obtained from angle-resolved UPS using the photon energy of 90 eV. The energy slice for the mapping is set at the binding energy of 0.4 eV. Further study of the Fermi surface mapping using different photon energies at various temperatures to compare with theoretical calculation should help to understand the nature of the fcc Fe films on Cu(001).

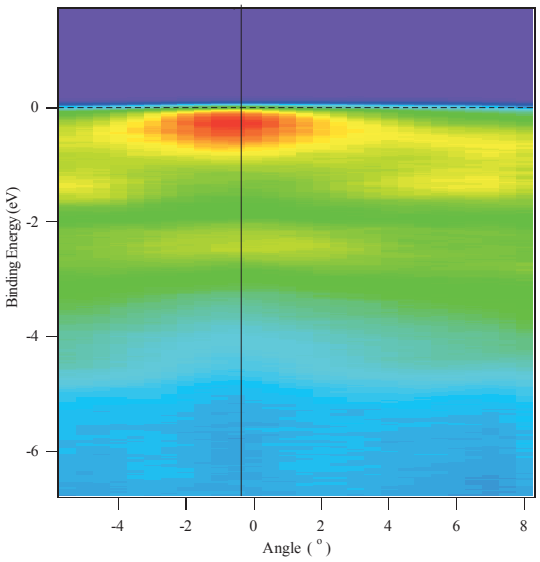

Fig. 1. Photoemission intensity of 8 ML Fe/Cu(001) around [001] direction (indicated by the dark solid line).

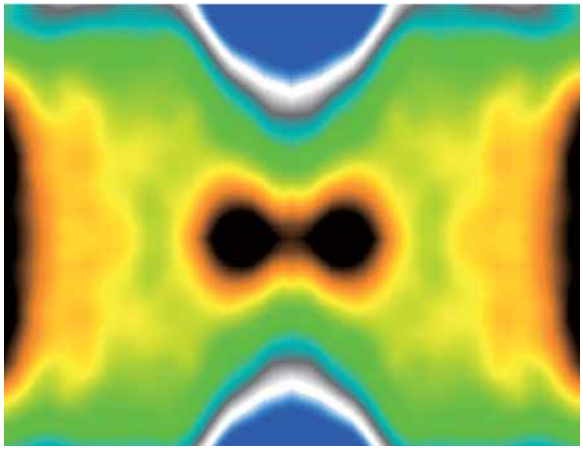

Fig. 2. Fermi surface mapping for 8 ML Fe/Cu(001) at 5 K using photon energy of 90 eV.

[1] D. Li *et al.*, Phys. Rev. Lett. **72** (1994) 3112; D. Li *et al.*, Appl. Phys. **76** (1994) 6425.

BL5U

Ce and Gd 4d-4f Resonant Photoemission Studies of $Ce_{1-x}Gd_xCoSi_3$

H.J. Im[1,2], H. Miyazaki[3,2], T. Ito[2,4], S. Kimura[2,4], J.B. Hong[1], Y.S. Kwon[1]
[1]*Department of Physics, Sungkyunkwan University, Suwon 440-746, Korea*
[2]*UVSOR Facility, Institute for Molecular Science, Okazaki 444-8585, Japan*
[3]*Graduate School of Engineering, Nagoya University, Nagoya 464-8603, Japan*
[4]*School of Physical Sciences, The Graduate University for Advanced Studies, Okazaki 444-8585, Japan*

We have performed Ce and Ge 4d-4f resonant photoemission spectroscopy (RPES) on $Ce_{1-x}Gd_xCoSi_3$ systems in order to understand the origin of quantum criticality in view of electronic structure. As Gd is replaced by Ce, the ground state changes from the antiferromagnetic (x = 1.0, 0.8, 0,6) to non-magnetic heavy fermion (x = 0, 0.2) via the quantum critical point (QCP, x = 0.4) [1,2]. This is considered as a new type of QCP since the antiferro-magnetism and non-magnetism originate from the different kinds of f-electrons belonging to Gd and Ce ions, respectively, and seem to compete each other causing the QCP. Therefore, the studies of the electronic structure of both Gd and Ce 4f states are essential to understand the new QCP [1,2].

RPES measurements for polycrystalline samples $Ce_{1-x}Gd_xCoSi_3$ (x = 0, 0.2, 0.4, 0.6, 1) were carried out at BL5U. The used photon energies are 120 (on) and 113 eV (off) for Ce 4d-4f RPES, and 146.5 (on) and 134.8 eV (off) for Gd 4d-4f RPES. Total energy resolutions are about 65 and 95 meV for the photon energies of 120 and 146.5 eV, respectively. Measurement temperature is 10 K. Sample surfaces were prepared by *in situ* fracturing under 2×10^{-8} Pa. Sample cleanliness is checked by the absence of oxidization peak around 6 and 10 eV.

Figure 1 displays Gd 4d-4f on-RPES spectra for x = 0.2, 0.4, 0.6, and 1. All spectra are subtracted by Shirley background, and then are normalized to the intensity of Gd $4f^6$ final-state peaks around -8.4 eV according to the Gd composition ratio. In the regime of from -3.5 to -2 eV, the broad peaks, which are overlap of both Ce $4f^0$ final state and non-f-states, are observed. Particularly, the Ce $4f^1$ final-states, the so-called tail of Kondo resonance, show some variation. For the meaningful comparison of Kondo resonance peaks, Ce 4f spectra should be extracted, precisely.

Figure 2 shows the Ce 4f spectra for x = 0, 0.2, 0.4, and 0.6, which are obtained by the subtraction of off-spectra from on-spectra in Ce 4d-4f RPES. We clearly observe the well-defined Ce $4f^0$ and Ce $4f^1$ final states around -2.5 eV and at the Fermi level, respectively. It should be noted that the sharp tail of Kondo resonance (Ce $4f^1$-state near E_F) persists from non-magnetic (x = 0, 0.2) to magnetic (x = 0.6) regime via the QCP (x = 0). This indicates that the new kind of QCP in this system does not come from the change of Ce 4f electronic structures unlike a local quantum critical scenario [5].

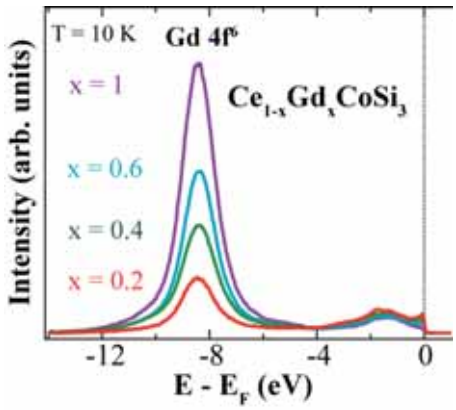

Fig. 1. Gd 4d-4f on-RPES spectra of $Ce_{1-x}Gd_xCoSi_3$.

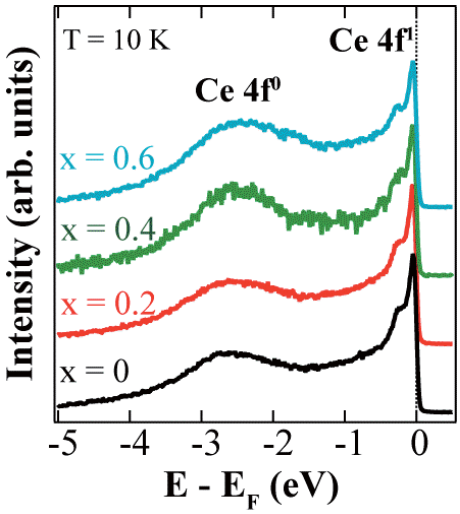

Fig. 2. Ce 4f spectra of $Ce_{1-x}Gd_xCoSi_3$ obtained in Ce 4d-4f RPES measurements.

[1] J.B. Hong *et al.*, J. Magn. Magn. Mater. **310** (2007) 292.
[2] J.B. Hong *et al.*, Physica B **403** (2008) 911.
[3] D. Eom *et al.*, J. Phys. Soc. Jpn. **67** (1998) 2495.
[4] H.J. Im *et al.*, Phys. Rev. B **72** (2005) 220405.
[5] Q. Si *et al.*, Nature **413** (2001) 804.

BL5U

Photoemission Studies on Quantum-Well States of Pb-Covered Ag Films on Si(111)

H. Ke, H. Narita, I. Matsuda
Institute for Solid State Physics (ISSP), University of Tokyo, 5-1-5 Kashiwanoha, Chiba 277-8581, Japan

Spin controls in utrathin metal films have been important topics in developing (nanometer-scale) spintronics and studying modern solid state physics. When thickness of metal film reduces to electron wavelength, electron energy is quantized by quantum size effect, resulting in formation of quantum-well states (QWS's). In contrast to isolated metal thin films, those on solid substrates have shown new intriguing spin properties through boundary conditions between films and substrates.[1] Spin-polarization of quantum Ag film has been reported when the film was grown on Fe substrate (*e.g.* Fe).[2] The polarization originates from spin-polarized bulk bands of the ferromagnetic metal substrate, which induces spin-dependent reflection phase shift at the film/substrate interface for electrons confined in the film. While varieties of spin properties have been reported in nanometer-thick metal film on metal substrates, there has been little report for those on the semiconductor substrates.

In the present research, we have challenged to realize spin-split bands in a nonmagnetic metal (Ag) film on a semiconductor (Si) substrate by ultilizing the strong Rashba effect at a surface atomic layer induced by heavy metal deposition. Up to now, we have succeeded in demonstrating spin-splitting of QWS subbands for Bi-covered quantum Ag film on Si(111).[3] Then, we move on to Pb-covered Ag film on Si(111). In contrast to the former case, the latter one is expected show spin-split Fermi surfaces, which induce exotic macroscopic properties.

The experiment was performed at the undulator beamline of BL-5U at UVSOR. With a high-resolution analyzer of MBS-Toyama 'Peter' A-1, angle-resolved photoemission spectroscopy measurements were performed at photon energy of 21 ~ 29 eV.

Figure (a) shows experimental band dispersion of thin Ag film (~30 ML) deposited on Si(111)7x7. We observed clear Fermi-edge and a broad spectra feature around 2 eV. On the other hand, after 1 ML-Pb adsorption on the Ag film, we detected subbands of QWS as shown in Fig. (b). This drastic spectral change is likely due to change of the film morphology. The Pb adatoms seemed to induce formation of continuous Ag film from rough Ag islands on Si(111). Analyses of the band parameters are underway.

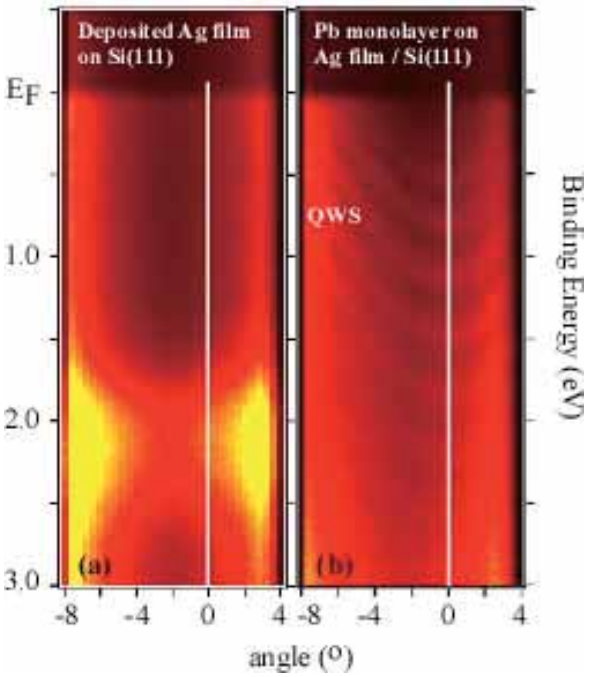

Fig. 1. Experimental band dispersion diagrams for (a) ~30 ML-Ag film deposited on Si(111)7x7 and (b) that is subsequently covered with Pb monolayer.

[1]*(A review paper)* I. Matsuda *et al.*, e-J. of Surf. Sci. and Nanotechnology **2** (2004) 169.
[2] N. V. Smith *et al.*, Phys. Rev. B **49** (1994) 332.
[3] H. Ke *et al.*, submitted to Phys. Rev. Lett.

BL5U

Temperature-Dependent Angle-Resolved Photoemission Spectra on Ferromagnetic EuO Thin Films

H. Miyazaki[1,2], T. Ito[2,3], S. Ota[1,2], H. J. Im[4], S. Yagi[1], M. Kato[1], K. Soda[1,2], S. Kimura[2,3]

[1]*Graduate School of Engineering, Nagoya University, Nagoya 464-8603, Japan*

[2]*UVSOR Facility, Institute for Molecular Science, Okazaki 444-8585, Japan*

[3]*School of Physical Sciences, The Graduate University for Advanced Studies, Okazaki 444-8585, Japan*

[4]*Department of Physics, Sungkyunkwan University, Suwon 440-746, Korea*

Europium monoxide (EuO) is a ferromagnetic semiconductor with the Curié temperature (T_C) at around 70 K [1, 2]. In the electron doping case by the Eu excess or substitute Gd^{3+} or La^{3+} from Eu^{2+} ion, the T_C increases up to 150 K and the electrical resistivity drops twelve-order of magnitude below the T_C originating in a metal-insulator transition (MIT) [2, 3]. To reveal the origin of these physical properties of EuO, it is important to clarify the electronic structure. Three dimensional angle-resolved photoemission spectroscopy (3D-ARPES) using a synchrotron radiation source is the most powerful technique to directly determine the electronic band structure. Using this technique we observed the change in the Eu 4*f* and O 2*p* states across T_C.

Single-crystalline EuO thin films with a thickness of about 50 nm were fabricated by the molecular beam epitaxy (MBE). Epitaxial growth of the single-crystalline EuO thin films with the 1 x 1 EuO (100) patterns was confirmed with low energy electron diffraction (LEED) and reflection high energy electron diffraction (RHEED) methods. The T_C measured with a superconducting quantum interference device (SQUID) magnetometer was 71 K. The 3D-ARPES measurements were performed at the beam line 5U of UVSOR-II combined with the MBE system. The total energy and momentum resolutions for the ARPES measurement were set 123 meV and 0.020 $Å^{-1}$ at the Γ point and 45 meV and 0.014 $Å^{-1}$ at the X point, respectively.

Figure 1 shows temperature dependent 3D-ARPES spectra obtained for EuO (100) at the Γ (a) and X (b) points. ARPES peaks at binding energies E_B of 1.0 – 3.0 eV and of 4.0 – 7.0 eV are attributed to the Eu 4*f* and O 2*p* states, respectively, based on a band structure calculation as well as the photoionization cross section [4, 5]. In the ferromagnetic phase below 71 K, every peaks shift to the lower binding energy side by about 0.2 eV than that in the paramagnetic phase. These energy shifts originate from the band splitting of the Eu 5*d* state due to the ferromagnetic transition. In addition, the top of the Eu 4*f* states at the Γ and X points is shifted away from the main 4*f* states and also the intensity increases. In contrast, the O 2*p* state is spitted into two bands below T_C. The bands at the higher and lower binding energies are attributed to the majority and minority spin states, respectively. Since the Eu 4*f* state is fully polarized, the 4*f* state mainly hybridizes with the majority spin state of O 2*p*. Therefore, the bonding and antibonding states of the Eu 4*f* and O 2*p* states are shifted to the higher and lower binding energy side, respectively. This result indicates that the origin of the ferromagnetic transition is strong hybridization between the Eu 4*f* and O 2*p* states.

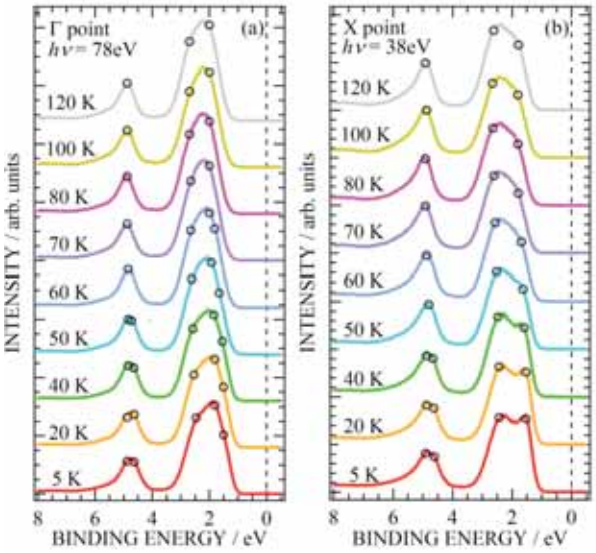

Fig. 1. Temperature dependence of the photoemission spectra of an EuO (100) thin film at the Γ (a) and X (b) points. The open circles indicate the peaks position evaluated from the second-derivative curveof each spectrum.

[1] N. Tsuda *et al.*, Electronic Conduction in Oxides (Springers College) (1976).
[2] A. Mauger *et al.*, J. Phys. (paris) **39** (1978) 1125.
[3] Y. Shapira, S. Foner, and T. B. Reed, Phys. Rev. B **8** (1973) 2299; Phys. Rev. B **8** (1973) 2316.
[4] H. Miyazaki *et al.*, Physica B **403** (2008) 917.
[5] J. J. Yeh and I. Lindau, At. Data Nucl. Data Tables **32** (1985) 1.

BL5U

Angle-Resolved Ultra-Violet Photoemission Study of $Fe_{2-x}V_{1+x}Al$

K. Soda[1,2], K. Nakamura[3], H. Miyazaki[1,2], M. Inukai[1], F. Ishikawa[4], Y. Yamada[4]
[1]*Graduate School of Engineering, Nagoya University, Nagoya 464-8603 Japan*
[2]*UVSOR Facility, Institute for Molecular Science, Okazaki 444-8585 Japan*
[3]*School of Engineering, Nagoya University, Nagoya 464-8603 Japan*
[4]*Faculty of Science, Niigata University, Niigata 950-2181, Japan*

Introduction

Heusler-type intermetallic compound Fe_2VAl shows unusual transport properties, which are reminiscent of the heavy fermion system [1]. The off-stoichiometric alloys $Fe_{2-x}V_{1+x}Al$ also reveal the remarkable enhancement in the thermoelectric power, which cannot be explained in terms of a rigid band model [2]. Theoretical studies suggest that the unusual properties may be induced by magnetic clusters around anti-site defects, whose *d* states appear within a sharp pseudogap across the Fermi energy E_F in its semimetallic electronic structure [3,4]. Thus, we have investigated the electronic structures of $Fe_{2-x}V_{1+x}Al$ using angle-resolved photoemission spectroscopy (ARUPS) in order to clarify the origins of the unique transport and thermoelectric properties.

Experimental

The ARUPS measurements were performed at BL-5U using linearly polarized synchrotron light as an excitation light source. Single crystalline specimens of $Fe_{2-x}V_{1+x}Al$ were prepared by the Czochralski pulling method in a tetra-arc furnace [2] and their clean (001) surfaces were obtained by *in situ* fracturing them at low temperatures.

Results and Discussion

Figure 1 shows ARUPS spectra of the $Fe_{2.05}V_{0.95}Al$ (001) surface recorded with the (010)-polarized 65 eV excitation light at various polar angles θ along the (100) axis, which elucidates the electronic structure along the Γ-X line. There are at least two prominent bands and three weak bands, whose peak positions are indicated by black solid circles in Fig.2, the image plot of the second derivative of the ARUPS spectra versus the wave vector. The band structure of Fe_2VAl calculated by a code Wien2k is also shown by white curves in the figure. In spite of the expected increase in the valence electron concentration for $Fe_{2.05}V_{0.95}Al$, no electron pockets are clearly observed at the X point. This might be caused by the small enrichment of Al in the growth of the single crystals and result in the observed positive thermoelectric power [2].

Detailed analysis near E_F around the Γ and X points will be reported elsewhere.

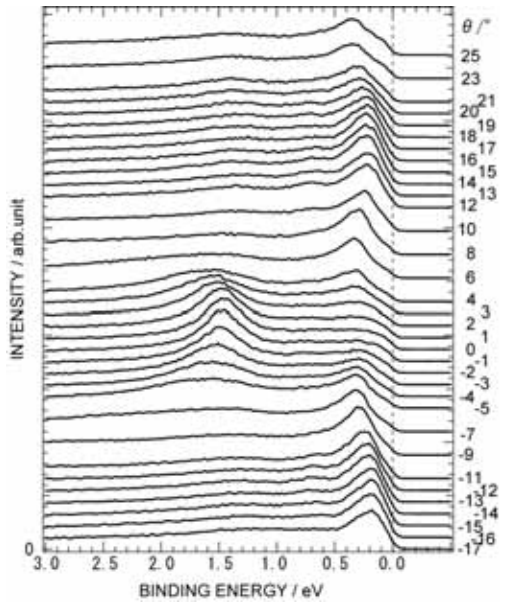

Fig. 1. Angle-resolved photoemission spectra of $Fe_{2.05}V_{0.95}Al$.

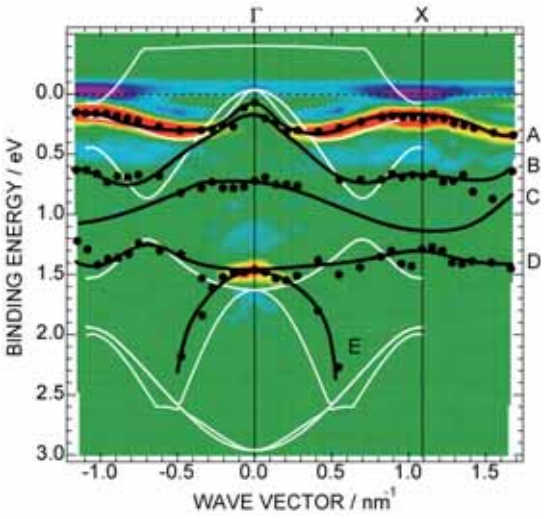

Fig. 2. Energy dispersion relation along the Γ-X line of $Fe_{2.05}V_{0.95}Al$.

[1] Y. Nishono *et al.*, Phys. Rev. Lett. **79** (1997) 1909.
[2] F. Ishikawa *et al.*, J. Magn. Magn. Mater. **310** (2007) e616.
[3] J. Deniszczyk, Acta Phys. Pol. B **32** (2001) 529.
[4] S. Fujii *et al.*, J. Phys. Soc. Jpn. **72** (2003) 698.

BL5U

Surface Chemistry of Alkyl-Passivated Si Nanoparticles Studied by Photoelectron Spectroscopy

A. Tanaka, N. Takashima, M. Imamura, T. Kitagawa, Y. Murase
Department of Mechanical Engineering, Graduate School of Engineering, Kobe University, Kobe 657-8501, Japan

Introduction

Numerous works focused on the optical properties of Si nanoparticles prepared by various methods have been reported to date. However, these optical properties in the literatures are ascribed to various sources, and this discrepancy is considered to originate that the physical properties of nanoparticles are greatly influenced by surface chemistry due to increase of surface area to volume ratio by reducing the size to the nanometer scale. In this paper, we have compared the valence-band photoemission spectra of fully *n*-butyl-passivated Si nanoparticles and those with oxygen contaminants in order to investigate their surface chemistry.

Experiment

Synthesis procedure of *n*-butyl-passivated Si nanoparticles used in this work is described elsewhere [1]. Photoemission measurements were performed at BL-5U of UVSOR II Facility for as-synthesized (fresh) *n*-butyl-passivated Si nanoparticles with mean diameter of d_c=1.1 nm and those exposed to ambient air for 10 minutes.

Results and Discussion

Figure 1 shows the valence-band photoemission spectra of as-prepared *n*-butyl-passivated Si nanoparticles with d_c=1.1 nm and those exposed to ambient air for 10 minutes, on the HOPG substrate at room temperature with photon energy of 195 eV. Spectral features in the photoemission spectrum of as-prepared *n*-butyl-passivated Si nanoparticles originate from the C *2sp*- and Si 3*sp*-derived valence electronic states. The valence-band maximum energy (HOMO) energy is estimated to about 2.2 eV below the Fermi level as shown by thin arrow on lower spectrum in Fig. 1. If the Fermi level is considered to be located in the middle of HOMO-LUMO gap, HOMO-LUMO gap of the present *n*-butyl-passivated Si nanoparticles with d_c=1.1 nm can be estimated to about 4.4 eV. This result agrees with the recent quantum Monte Carlo (QMC) calculation by Putzer *et al.* [2]. On the other hand, it is confirmed from the FT-IR spectrum that the exposure to ambient air of the present *n*-butyl-passivated Si nanoparticles induce the removal of surface-passivants of alkyl groups and subsequent passivation of oxygen. As shown in Fig. 1, the valence-band spectrum of Si nanoparticles with oxygen contaminants exhibits an additional feature centered around 2.6 eV in binding energy (as shown by thick arrow in Fig. 1). Putzer *et al.* have also reported the QMC HOMO-LUMO gaps of surface-passivated Si nanoparticles with and without oxygen contaminants, and have shown a significant decrease of HOMO-LUMO gap due to the oxygen contaminations [2]. Moreover, they have also calculated the density of states (DOS) in surface-passivated Si nanoparticles with various contaminants by means of local density approximation (LDA). When a double bonded contaminant such as oxygen and sulfur is added to Si nanoparticle, Si sp^3 network is considerably distorted and HOMO and LUMO change their nature significantly. As a result, HOMO and LUMO states localized in the vicinity of the Si=O double bond, and the modified DOS originated from the HOMO and LUMO appears near the Fermi level as the additional features. From the comparison with this theoretical LDA DOS, it is considered that the additional feature in the present photoemission spectrum of Si nanoparticles with oxygen contaminants is ascribed to the modified HOMO states by oxygen contaminations.

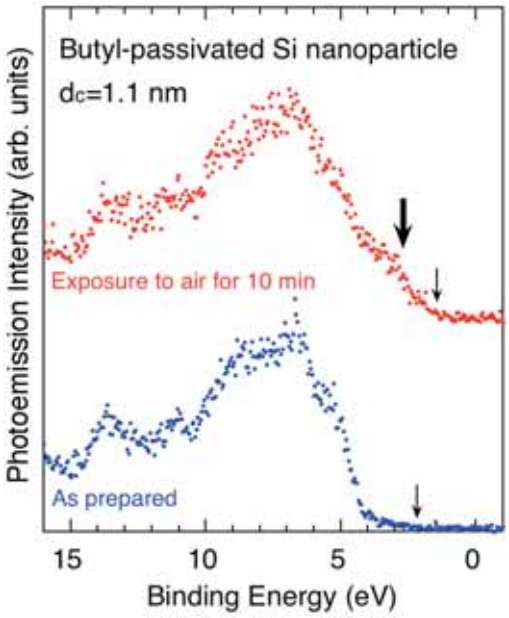

Fig. 1. Valence-band photoemission spectra of as-synthesized *n*-butyl-passivated Si nanoparticles with d_c=1.1 nm (blue) and those exposed to ambient air for 10 minutes (red).

[1] A. Tanaka *et al.*, Solid State Commun. **140** (2006) 400.
[2] A. Puzder *et al.*, Phys. Rev. Lett. **88** (2002) 097401.

BL7U

Momentum-Dependent Kondo Resonance Peaks in a Low-Energy Angle-Resolved Photoemission Spectroscopy

H.J. Im[1,2], T. Ito[2,3], H. Miyazaki[4,2], S. Kimura[2,3], C.I. Lee[1], K.E. Lee[1], Y.S. Kwon[1]

[1]*Department of Physics, Sungkyunkwan University, Suwon 440-746, Korea*

[2]*UVSOR Facility, Institute for Molecular Science, Okazaki 444-8585, Japan*

[3]*School of Physical Sciences, The Graduate University for Advanced Studies, Okazaki 444-8585, Japan*

[4]*Graduate School of Engineering, Nagoya University, Nagoya 464-8603, Japan*

For investigation of the electronic structure of strongly correlated electrons system, bulk-sensitive high-resolution angle-resolved photoemission spectroscopy (ARPES) with utilizing tunable photons has been a great challenge issue to physicists. In the case of cuprate superconductors, for instance, their electronic structures have been well surveyed with high energy resolution regardless of the bulk- or surface-states because of the two-dimensional electronic structure of CuO_2 layers which governs their physical properties [1]. On the other hand, the precise understanding of heavy-fermion systems requires the three-dimensional bulk electronic structure with high resolution [2]. This can be realized in a low energy photoemission using the synchrotron radiation source. Recently, the high resolution ARPES apparatus has been equipped in BL7U of UVSOR-II with photon energies from 6 to 40 eV [3].

Therefore, we have performed ARPES on $CeCoGe_{1.2}Si_{0.8}$, where the c-f hybridization bands were firstly observed in Ce 4d-4f resonant ARPES [4], as a target sample. The used photon energy is 15 eV, where the measured momentum spaces include Γ-point in normal emission. Total energy resolution is about 15 meV. Measurement temperature is 20 K which is very low compared to the Kondo temperature of $CeCoGe_{1.2}Si_{0.8}$ (T_K ~ 350 K). Sample surfaces were prepared by *in situ* cleaving under ultra high vacuum. Sample cleanliness is checked by the variation of spectral shape of valence which becomes broad due to surface contamination.

Figure 1 is the spectrum of valence band obtained in angle-integrated mode. We observed the two prominent spectral weights around -1.2 and -2.5 eV, and the tail of Kondo resonance peak at the Fermi-level. This indicates that Kondo resonance peaks composed of mainly f-state is well observed although the cross section of f-state is smaller than one of non-f-states (spd-state) in a low kinetic energy of photoelectrons.

Figure 2(a) is an intensity plot of ARPES spectra which represents a band dispersion. It is observed that a conduction band crosses the Fermi level at k = 0.2 $Å^{-1}$, where the evidence of c-f hybridization must appear as in Ce 4d-4f resonant ARPES [4]. Figure 2(b) shows the energy distribution curves at k = 0.07 and 0.2 $Å^{-1}$. The tail of Kondo resonance peak at the Fermi-vector (k = 0.2 $Å^{-1}$), while the corresponding feature is absent at k = 0.07 $Å^{-1}$. This indicates that Kondo resonance peak has the momentum dependence in agreement with a periodic Anderson model [4].

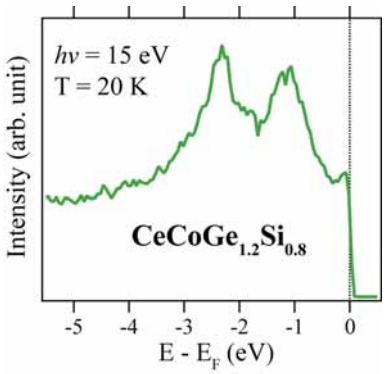

Fig. 1. Angle-integrated PES spectrum of $CeCoGe_{1.2}Si_{0.8}$ in valence band regime.

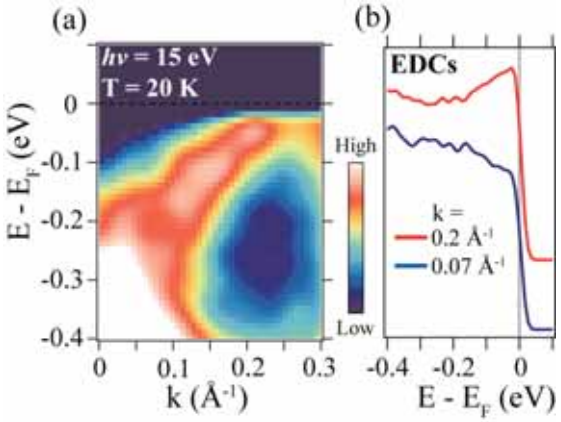

Fig. 2. (a) ARPES intensity plot of $CeCoGe_{1.2}Si_{0.8}$ at $h\nu$ = 15 eV. (b) Energy distribution curves at k = 0.2 and 0.07 $Å^{-1}$.

[1] A. Damascelli *et al.*, Rev. Mod. Phys. **75** (2003) 473.

[2] D. Malterre *et al.*, Adv. Phys. **45** (1996) 299.

[3] T. Ito *et al.*, AIP Conference Proceedings **879** (2007) 587.

[4] H.J. Im *et al.*, Phys. Rev. Lett. **100** (2008) 176402.

BL7U

Evidence of Three-Dimensional CDW Formation on $CeTe_2$: VUV Three-Dimensional Angle-Resolved Photoemission Study

T. Ito[1,2], H. J. Im[3], S. Kimura[1,2], Y. S. Kwon[3]

[1]*UVSOR Facility, Institute for Molecular Science, Okazaki 444-8585, Japan*

[2]*School of Physical Sciences, the Graduate University for Advanced Studies (SOKENDAI), Okazaki 444-8585, Japan*

[3]*Department of Physics, Sungkyunkwan University, Suwon 440-749, Korea*

Low-dimensional electronic structure is believed to be an important essence to understand the anomalous physical properties, such as a charge/spin density wave formation, high-*T*c superconductivity, etc., originating from the anisotropic electronic/magnetic structure. In turn, the investigation of the three-dimensional effect in the electronic structure is essentially important to understand the anomalous physical properties of low-dimensional compounds. To demonstrate the importance of three-dimensionality to insight into the anomalous physical properties, we have performed three-dimensional angle-resolved photoemission spectroscopy (3D-ARPES) on quasi-two-dimensional charge-density-wave (CDW) compound $CeTe_2$ [1] where the existence of three-dimensional anomaly at the Fermi surface (FS) has been reported [2].

The 3D-ARPES was performed at the beamline 7U of UVSOR-II, the Institute for Molecular Science, which has been developed in 2007 for bulk-sensitive ARPES on strongly correlated electron systems in the VUV region [3]. Taking account of the inner potential of $V \sim 16.4$ eV [2], we set the measurement axis along (110) plane of Te 5*p* hole-like FS (see hatched blue area in Fig. 1).

Figure 2 shows the evolutions of the hole-pocket around the MR line as a function of photon energy $h\nu$, in other word, of the k_z line in the Brillouin zone. We clearly observe that the Te 5*p* band (solid line) folds at the E_F crossing point (dashed line) at $h\nu = 19$ eV (ΓM line), *i.e.*, the Fermi surface of the Te 5*p* band is nested due to the CDW formation. Furthermore, with decreasing photon energy, the separation between the Te 5*p* band and the folded band gradually increases. This result suggests that the nesting condition becomes imperfect from the ΓM to ZR lines gradually. The observed change of the folded band certainly indicates the existence of the unexpected three-dimensional CDW vector in quasi-two-dimensional $CeTe_2$.

The origin of the observed three-dimensional CDW vector is not clear at present, since there are few examples of three-dimensional study of electronic structure so far, especially for the quasi-two dimensional materials. Present observation of three-dimensional interactions on quasi-two dimensional $CeTe_2$ clearly indicates that 3D-ARPES will shed light on understanding the effect of anisotropic interactions originating in the various functionalities.

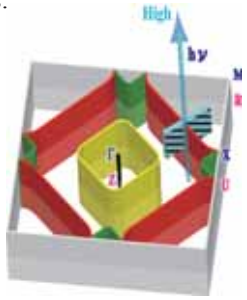

Fig. 1. Schematic Fermi surface of $CeTe_2$.

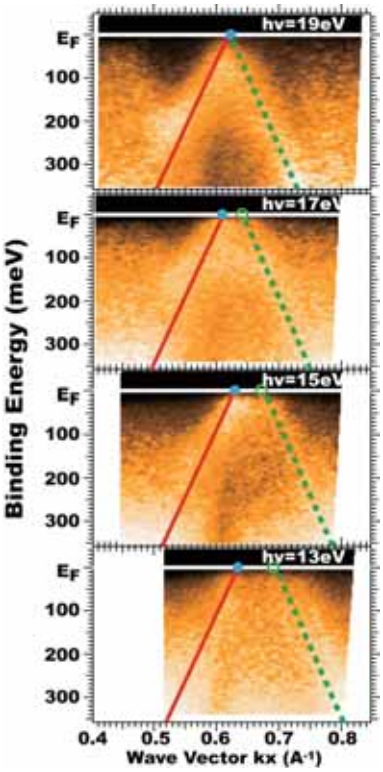

Fig. 2. $h\nu$-dependent experimental band structure of $CeTe_2$ The images of $h\nu = 19$ and 13 eV correspond to the band structure in the ΓM and ZR lines, respectively. See the text for details.

[1] M. H. Jung *et al.*, J.Phys.Soc.Jpn **69** (2000) 937.
[2] T. Ito *et al.*, J. Mag. Magn. Mater. **310** (2007) 431; Physica B **378-380** (2006) 767.
[3] S. Kimura *et al.*, AIP conf. Proc. **879** (2007) 527.

BL7U

Temperature-Dependent Extremely Low-Energy Photoemission Spectroscopy of a Fe-Based "Kondo Semiconductor"

A. Sekiyama[1], G. Funabashi[1], S. Komori[1], M. Kimura[1], M. Tsunekawa[1], H. Sugiyama[1], T. Uyama[1], H. Nakamura[2], T. Ito[3], S. Kimura[3], S. Imada[1], S. Suga[1]

[1]*Graduate School of Engineering Science, Osaka University, Toyonaka, Osaka 560-8531, Japan*

[2]*Graduate School of Engineering, Kyoto University, Kyoto 606-8501, Japan*

[3]*UVSOR Facility, Institute for Molecular Science, Okazaki 444-8585 Japan*

Introduction

Kondo semiconductor or Kondo insulator, which shows nonmagnetic semiconducting behavior at low temperatures with a formation of the (pesudo-)gap while it is rather metallic at high-temperature, is one of intriguing subjects in strongly correlated electron systems. $FeSb_2$ [1,2] is recognized as a candidate for the Kondo semiconductor, whose macroscopic properties are similar to those for already known 4f-based Kondo semiconductors. From previous photoemission studies [3], it has been known that the surface of the Kondo semiconductor is often metallic. Therefore, bulk-sensitive photoemission is very important to clarify their intrinsic electronic states. Recently, extremely low-energy photoemission (ELEPES, $h\nu < 10$ eV) has been thought as another possible technique [4] as bulk-sensitive photoemission, being complementary to high excitation-energy photoemission. We have performed ELEPES for $FeSb_2$ in order to examine the bulk electronic state.

Experimental

ELEPES was performed at BL7U by using a photoelectron spectrometer of MB Scientific A1 analyzer. In order to obtain clean surfaces, the bulk $FeSb_2$ samples were fractured *in situ*. We have measured both surface-sensitive and bulk-sensitive photoemission spectra by controlling excitation photon energies from 6.5 to 30 eV. The energy resolution was set to ~5 meV.

Results and Discussions

Figure 1 shows the temperature dependence of the ELEPES spectra measured at $h\nu = 6.5$ eV for $FeSb_2$. The spectra have been normalized by the spectral weight above the binding energy of 200 meV. At all measuring temperatures, the intensity monotonously decreased from the binding energy of 200 meV toward the Fermi level (E_F). In this energy region, the spectral weight is clearly reduced with lowering temperature. This indicates that the density of states near E_F decreases from 200 K in the metallic phase to 20 K in the semiconducting phase in the energy scale of 200 meV. Such temperature dependence is not seen in normal metals, suggesting that the electronic structure changes intrinsically with temperature. On the other hand, a clear Fermi cut-off is seen at 20 K. If it is assumed that the surface contribution in these ELEPES spectra is negligible, we can conclude that $FeSb_2$ is semimetallic at low temperatures, in other words, a Kondo semiconductor with the negative indirect gap.

There is a broad peak at the binding energy of about 200 meV in all photoemission spectra at $h\nu$ = 6.5, 10, 21 and 30 eV (not shown here) which we have measured at 20 K in the so-called semiconductong phase. When we normalized the spectra by the intensity of the broad peak, the Fermi cut-off intensity decreases rather discontinuously from $h\nu = 21$ eV to 10 eV whereas it is comparable between $h\nu = 30$ eV and 21 eV, and between $h\nu = 10$ eV and 6.5 eV, respectively. This discontinuous reduction of the cut-off might be ascribed to the higher bulk sensitivity of the photoemission at $h\nu \leq 10$ eV than that at $h\nu > 20$ eV.

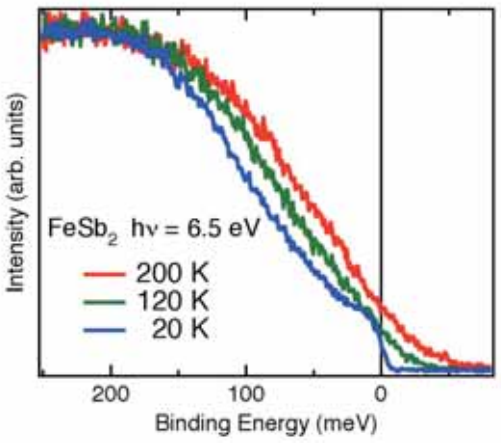

Fig. 1. Temperature-dependent extremely low-energy photoemission spectra of $FeSb_2$.

[1] C. Petrovic *et al.*, Phys. Rev. B **67** (2003) 155205.
[2] C. Petrovic *et al.*, Phys. Rev. B **72** (2005) 045103.
[3] For example, K. Breuer *et al.*, Phys. Rev. B **56** (1997) R7061.
[4] T. Kiss *et al.*, Phys. Rev. Lett. **94** (2005) 057001.

BL7U

Electronic Structure and Thermoelectric Power of $La_{2-x}Sr_xCuO_4$

T. Takeuchi[1,2], H. Komoto[2], T. Ito[3], S. Kimura[3]

[1]*EcoTopia Science Institute, Nagoya University, Nagoya 464-8603 Japan*

[2]*Department of Crystalline Materials Science, Nagoya University, Nagoya 464-8603 Japan*

[3]*UVSOR Facility, Institute for Molecular Science, Okazaki 444-8585 Japan*

Thermoelectric power of the cuprate superconductors is widely known to possess unusual behaviors such as the non-linear temperature dependence and the positive to negative sign-reversal with increasing hole-concentration. These behaviors are not generally observable for metallic compounds. Strong electron correlation is considered as one of the possible origins inducing such unusual behaviors in thermoelectric power.

By using the angle resolved photoemission spectroscopy (ARPES) and the semi-classical Bloch-Boltzmann theory, we revealed for the $Bi_2Sr_2CuO_{6+\delta}$ (Bi2201) and $Bi_2Sr_2CaCu_2O_{8+\delta}$ (Bi2212) superconductors that the unusual behaviors of the thermoelectric power, especially its large magnitude with positive sign in underdoped samples, are caused by the strong scattering of the conduction electrons at the anti-ferromagnetic zone boundary (AFZB). [1,2] Note here that the AFZB is essentially caused by the anti-ferromagnetic ordering of the conduction electrons, that is not fully observable in the superconductors but in the Mott-Insulator as a consequence of the carrier localization caused by the strong on-site coulomb interaction. Therefore, it is safely argued that the thermoelectric power of the cuprate superconductor is indeed characterized by the strong electron correlation.

One may wonder that the effects of the electron correlation on the thermoelectric power, that is caused strong scattering at the AFZB, could be closely related with the stability or instability of superconducting phase. To gain deeper insight into the relation between the strong scattering at the AFZB and superconducting transition temperature, we determined the development of the AFZB scattering of conduction electrons as a function of carrier concentration by analyzing thermoelectric power of the $La_{2-x}Sr_xCuO_4$ (LSCO) superconductors as we did for the Bi2201 and Bi2212 in our previous works. [1,2]

The single grained $La_{2-x}Sr_xCuO_4$ samples of $0.06 \leq x \leq 0.25$ were prepared by the floating-zone method. The superconducting transition temperature was determined by the magnetization measurement with the SQUID magnetometer. We also measured electrical resistivity and thermoelectric power with the Thermal Transport Option of the Physical Property Measurement System assembled by Quantum Design Inc. High resolution ARPES was performed at the BL05U of UVSOR, Okazaki Japan. The energy resolution employed in this study was ~20meV, which was defined by the energy with of intensity reduction from 90 % to 10 % at the Fermi level of reference gold electrically contacted with samples. The ARPES measurements were performed at 50K with the incident photon energy of 30.0 eV.

Figure 1 shows a typical example of the observed ARPES images together with the energy distribution curves and the momentum distribution curves which were cut from the image. The band dispersion is clearly observed, and we safely determined $\varepsilon(\mathbf{k})$ with employing the tight-binding function fitting of four different transfer integrals. Once $\varepsilon(\mathbf{k})$ is determined, spectral conductivity $\sigma(\varepsilon)$ can be calculated from $\varepsilon(\mathbf{k})$ under an assumption of constant mean free path as we assumed in our previous analysis on the Bi2201 and Bi2212. By taking the effect of the AFZB scattering into account, we calculated thermoelectric power of LSCO from the experimentally determined $\sigma(\varepsilon)$. Figure 2 shows calculated and measured thermoelectric power. The calculated thermoelectric power quantitatively reproduced the measured one even in their carrier concentration dependence. As a result of this calculation, we realized that the LSCO is more strongly affected by the AFZB scattering than the Bi2201 and Bi2212. This tendency must be caused by the smaller carrier concentration of LSCO than that of Bi2201 and Bi2212.

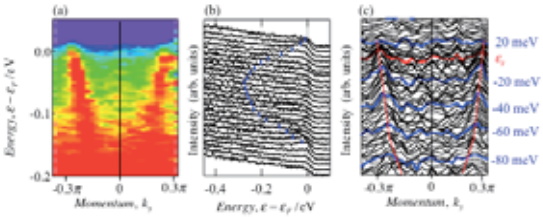

Fig. 1. (a) an ARPES intensity image near the (π, 0) point of $La_{1.75}Sr_{0.25}CuO_4$ accumulated at 50K. (b) Energy distribution curves and (c) momentum distribution curves cut from the ARPES image. A band crossing the Fermi level is clearly observed.

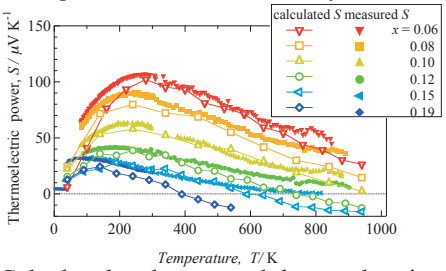

Fig. 2. Calculated and measured thermoelectric power of $La_{2-x}Sr_xCuO_4$. The measured value is quantitatively reproduced by the calculation.

[1] T. Kondo *et al.*, *Phys. Rev. B* **72** (2005) 024533.
[2] T. Takeuchi *et al.*, *J. Elec. Spec. Relat. Phenom.* **156-158** (2007) 452-456.

BL8B1

Graphitization of Thin Films Formed by Focused-Ion-Beam Chemical-Vapor-Deposition

K. Kanda, J. Igaki, N. Yamada, R. Kometani, S. Matsui
Laboratory of Advanced Science and Technology for Industry, University of Hyogo, Kamigori, Hyogo, 678-1205 Japan

Focused-ion-beam chemical-vapor deposition (FIB-CVD) method is developed as an effective technique for producing of three-dimensional nano-structures, which formed complex shape with overhung, hollow and bridging structure. In this method, scanning of focused Ga ion beam under the phenanthrene gas atmosphere using as a source gas leads to deposition of carbon material at arbitrary nano-scale area. The fundamental structure of carbon material formed by FIB–CVD is diamond-like carbon (DLC) from the measurement of Raman spectrum [1]. It was known that pillars grown by FIB–CVD had a Ga-rich core and these residual Ga departed from the FIB–CVD DLC by the annealing at 700°C. In the other hand, the pillar was reported to graphitize by the transfer of Ga using flash discharge [2].

The coordination of the carbon atoms has been principally determined by near-edge x-ray absorption fine structure spectroscopy (NEXAFS). The movement of Ga in the FIB-CVD DLC thin film by annealing was observed in the NEXAFS study [3], but the graphitization was not obviously confirmed. In the present study, FIB-CVD DLC films of ≈200 nm thickness were prepared by annealing at 1 hour in the temperature range from room temperature to 750°C. Fig. 1 shows the C K-edge NEXAFS spectra of FIB-CVD DLC films, (a) as deposition and (b) after 1 h annealing at 750°C with that of (c) graphite as a reference. The intensity of a peak at 285.4 eV, corrsponding to 1s→π* trangition increased by the annealing. This increase indicated that sp^2/sp^3 ratio increased in the film. In the 290-320 nm of σ* resonance region, the several bands characteristic to FIB-CVD DLC thin film changed by the annealing to the strctural bands characteristic to the graphite. These changes indicated that FIB-CVD DLC films graphitized by the 1 h annealing at 750°C.

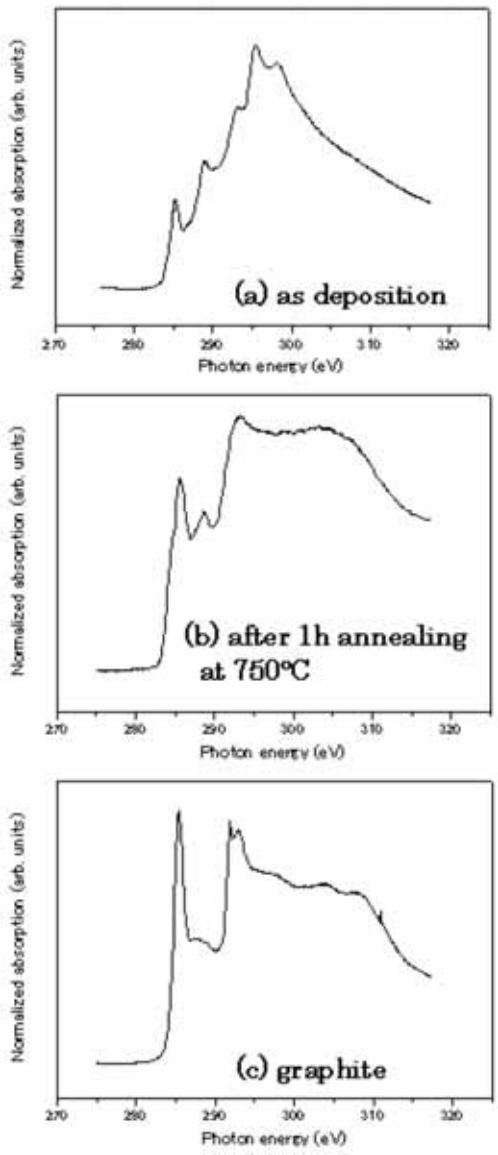

Fig. 1. C K-edge NEXAFS spectra of FIB-CVD DLC thin films and graphite.

[1] S. Matsui *et al.*, J. Vac. Sci. Tech. B **18** (2000) 3181.
[2] J. Fujita *et al.*, Appl. Phys. Lett. **88** (2006) 83109.
[3] A. Saikubo *et al.*, Jpn J. Appl. Phys. **46** (2007) 7512.

BL8B1

Characterization of Various Lithium Compounds by an XAFS Method

T. Kurisaki[1], Y. Sakogawa[1], D. Tanaka[1], H. Wakita[1,2]

[1]*Department of Chemistry, Faculty of Science, Fukuoka University, Nanakuma, Jonan-ku, Fukuoka 814-0180, Japan*

[2]*Advanced Materials Institute, Fukuoka University, Nanakuma, Jonan-ku, Fukuoka 814-0180, Japan*

Lithium compounds are used in industrial and commercial applications such as lithium ion batteries, lithium glasses, and medicines of a manic-depressive illness. The XAFS method has not been widely used to estimation the characteristic of these materials owing to the low energy (below about 70eV) of Li K edge. However, there are a few reports about Li-K XANES spectra [1].

In this work, we applied the X-ray absorption near edge structure (XANES) spectroscopy to lithium compounds. X-ray absorption spectra of near Li K absorption edges were (XAFS) measured at BL8B1 of the UV-SOR in the Institute of Molecular Science, Okazaki [4]. The energy of the UVSOR storage ring was 750MeV and the stored current was 110-230 mA. The absorption was monitored by the total electron yield using a photomultiplier. We employed the discrete variational (DV)-Xα molecular orbital (MO) method to obtain calculated spectra, and compared observed spectra with the calculated spectra.

The Li *K* XANES spectra for various lithium compounds are shown in Fig. 1. The energy was not calibrated by standard samples. The energy position of each first peak should not depend on the charge of anion. However, the peak shapes are different by the anions. This result showed that the two aluminum compounds have different electronic state. We are going to try to calculate the spectra by DV-Xα molecular orbital calculations

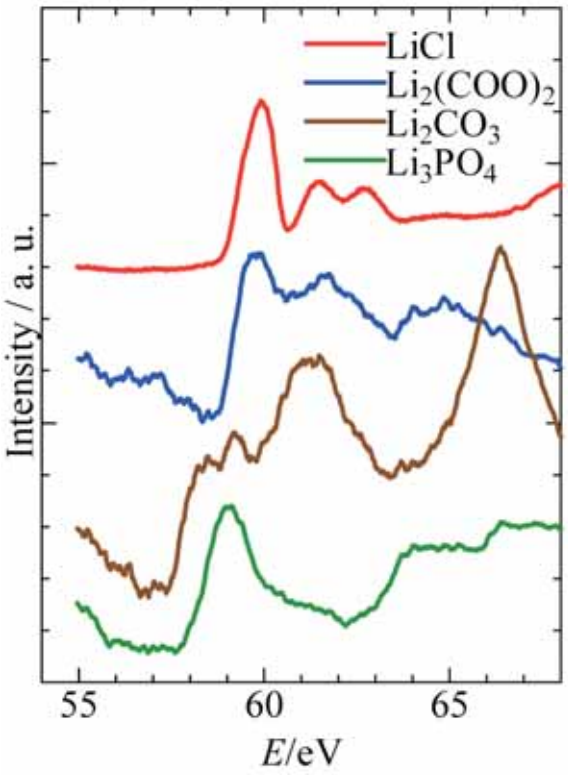

Fig. 1. Li K-edge XANES spectra of lithium compounds.

[1] J. Tsuji *et al.*, Adv. X-ray Chem. Anal. Jpn. **31** (2000) 149.
[2] J. Tsuji *et al.*, J. Synchrotron Radiat. **8** (2001) 554.
[3] J. Tsuji *et al.*, X-Ray Spectrom. **31** (2002) 319.
[4] S. Murata *et al.*, Rev. Sci. Instrum. **63** (1992) 1309.

BL8B1

N K-Edge XANES Analysis of Nitrogen Implanted in TiO_2

T. Yoshida[1], S. Muto[1], H. Yoshida[2]

[1]*Department of Materials, Physics and Energy Engineering, Nagoya University, Furo-cho, Chikusa-ku, Nagoya 464-8603*

[2]*EcoTopia Science Institute, Nagoya University, Furo-cho, Chikusa-ku, Nagoya 464-8603*

Photocatalytic reactions at the surface of titanium dioxide (TiO_2) under UV light irradiation have been attracting much attention due to their practical applications such as environmental cleaning. Recently, Asahi *et al.* reported that substitutional doping of nitrogen into TiO_2 contributed to narrowing of the band gap, thus providing a visible-light response [1]. Furthermore, previous investigations demonstrated that nitrogen doping generated new optical absorption bands in the visible-light region and the absorbance evolved with increasing nitrogen. On the other hand, absorbance may not be linearly proportional to the photocatalytic activity, and it is thus important to understand the chemical environment of N in TiO_2. In the present investigation, structural analysis was performed for N^+-implanted TiO_2 catalysts by means of X-ray absorption spectroscopy (XAFS).

The samples used in this study were TiO_2 (1 0 0) single crystals (5 x 5 x 0.5 mm^3), supplied by Furuuchi Kagaku, Japan. Mass analyzed 100 keV N_2^+ ions (50 keV/ N^+ ion) were injected into the samples at room temperature, perpendicular to the sample surface. The N^+ fluence ranged from 1 to 5 x 10^{21} m^{-2}. After the ion implantation, parts of the samples were heat-treated at 573 K for 2 hours in air.

A typical photocatalytic experiment consisted of placing the N^+-implanted sample in 0.5 ml of aqueous methylene-blue (MB) solution (9.8 μmol/L) and subsequent exposure to visible-light using a 15 W Xe lamp with a cut filter for $\lambda > 430$ nm. The light absorbance at $\lambda = 664$ nm after exposure for 2 hours was measured to estimate the photocatalytic activity of the samples.

N K-edge XANES spectra of the N^+-implanted TiO_2 samples were measured at the BL-8B1 station of UVSOR-II at the Institute for Molecular Science, Okazaki, Japan. Data were recorded at room temperature in total electron yield mode, and the X-ray energy dependence of the N Auger electron yield was monitored [2]. Considering the escape depth of the Auger electrons, the spectra probe the sample from the surface up to a few nanometers in depth.

The photocatalytic activity reached its maximum at a fluence of 3 x 10^{21} m^{-2} and then decreased with the fluence. The sample implanted at a fluence of 5 x 10^{21} m^{-2} followed by heat-treatment at 573 K was almost photocatalytically- inactive under visible-light irradiation.

Fig.1 shows the N K-edge XANES spectra of the N^+-implanted TiO_2 samples and a TiN powder. Similar XANES features for (a) and (b) suggest that N in the sample implanted by 3 x 10^{21} m^{-2} (highest active photocatalyst) is in a chemical environment similar to that in TiN. More thorough observation suggested that double-peak around 400 eV in (b) shifted to the lower energy side compared with that of TiN, which was well reproduced by the theoretical prediction using FEFF code [3] when N occupies one of the O sites of TiO_2, as suggested in ref.[1]. On the other hand, the XANES spectrum of the sample implanted with the N^+ fluence of 5 x 10^{21} m^{-2} followed by heat-treatment (almost inactive to visible-light) shows a distinct single peak at around 401 eV (Fig. 1c). This peak was attributed to formation of N̄O and/or N̄N bonds near the surface [3], which significantly suppresses the photocatalytic activity.

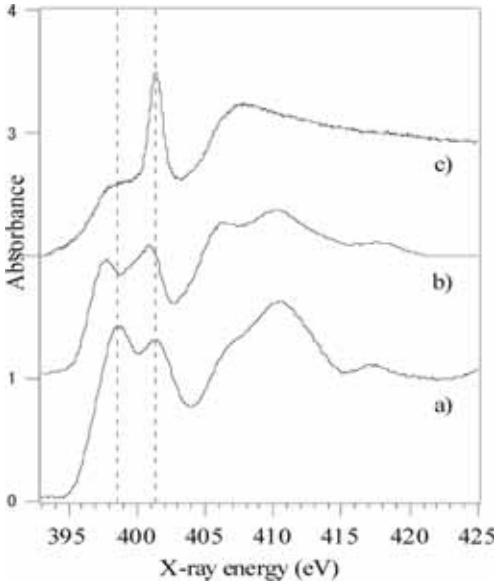

Fig. 1. N K-edge XANES spectra of a TiN(a), N^+-implanted at 3 x 10^{21} m^{-2}(b) and 5 x 10^{21} m^{-2} followed by heating at 573 K for 2 h(c).

[1] R. Asahi *et al.*, Science **293** (2001) 269.
[2] A. Erbil *et al.*, Phys. Rev. B **37** (1988) 2450.
[3] A. L. Ankudinov *et al.*, Phys. Rev. B **58** (1998) 7565; J. Stöhr, R. Jaeger, Phys. Rev. B **26** (1982) 4111.
[4] J.-H. Wang *et al.*, Anal. Chim. Acta **476** (2003) 93.

BL8B2

Electronic Structure at Highly Ordered Organic/Metal Interfaces

H. Yamane*, K. Kanai, K. Seki

Department of Chemistry, Nagoya University, Nagoya 464-8602, Japan

The electronic structure at the interface formed between an organic semiconductor film and a metal electrode plays a crucial role in the performance of electronic devices using organic semiconductors such as electroluminescent displays, field-effect transistors, and photovoltaic cells. In particular, the energetics of the molecular energy levels near the Fermi level (E_F) of metals, *i.e.*, the energy level alignment at organic/metal interfaces, are of fundamental importance in discussing various charge phenomena related to organic devices such as the barrier heights for the charge injection and separation at the interface [1]. In the field of organic/metal interfaces, one of the important issues is the elucidation and control of the *interface state*, which may dominate the energy level alignment at organic/metal interfaces. However, it is generally not easy to discuss the interfacial electronic structure precisely since the energetics at organic/metal interfaces is easily modified by the presence of the interface-specific electrical and geometrical phenomena. To fully clarify the possibly complicated electrical and geometrical phenomena at the interface, a more pertinent experimental approach to this issue would be to use a well-characterized system, *e.g.*, epitaxially grown organic thin film on atomically flat and clean metal single crystal surfaces, in quantitative electron spectroscopic measurements.

From the above point of view, by using angle-resolved UV photoemission spectroscopy (ARUPS), we have studied the electronic structure of well-ordered thin films of metal-phthalocyanines (M-Pc), perylene-tetracarboxylic dianhydride (PTCDA), and pentacene (Pn) prepared on metal single crystal surfaces. Among these, it was reported that Pn molecules on Cu(110) in the monolayer regime form a highly ordered film structure with planar adsorption geometry, where the molecular long axis is parallel to the [1$\bar{1}$0] substrate direction [2].

Figure 1(a) and (b) shows the observed energy versus momentum [$E(\boldsymbol{k}_{\parallel})$] relation for the flat-lying Pn monolayer film on Cu(110) along (a) $\phi = 0°$ (the [1 $\bar{1}$ 0] substrate direction) and (b) $\phi = 28°$. The abscissa is the parallel momentum component ($\boldsymbol{k}_{\parallel}$), and ordinate is the binding energy (E_b) relative to the E_F of the substrate. In order to map out the $E(\boldsymbol{k}_{\parallel})$ relation, we took the second derivative of the raw ARUPS spectra [$-d^2I(E_b)/dE_b^2$] at $h\nu$ = 20 eV after smoothing for specifying the energies of the spectral features. Open and filled circles indicate the peak position of the Pn-derived peaks A–C in the raw ARUPS spectra measured at $h\nu$ = 20 and 30 eV, respectively. The selected raw ARUPS spectra of the valence levels and the secondary-electron cutoff are shown in Fig. 1(c) and (d), respectively. We found that (i) the change in the work function (*i.e.*, vacuum level shift Δ) upon the adsorption of the flat-lying Pn monolayer film is $\Delta = -0.9$ eV [Fig. 1(d)] due to the formation of the interfacial dipole layer [1], and that (ii) peaks A–C are the interface-specific states. The latter finding (ii) was concluded since the energy positions and the orbital symmetries of peaks A–C cannot be explained by the UPS spectrum of the gas-phase Pn [3] and its orbital symmetries [4]. These interface states A–C may originate from the molecular energy levels split due to the hybridization with the wave function of the substrate, which can modify the energies and the orbital symmetries, as in the case of the Pn/Cu(119) interface reported by Ferretti *et al* [5]. According to their theoretical calculation in Ref 5 based on the density-functional theory, the density-of-states just below E_F and peak A in Fig. 1 can be ascribed to the resultant split levels of the former lowest unoccupied molecular orbital (LUMO) level, and peaks B and C in Fig. 1 can be ascribed to the resultant split levels of the former highest occupied molecular orbital (HOMO) level.

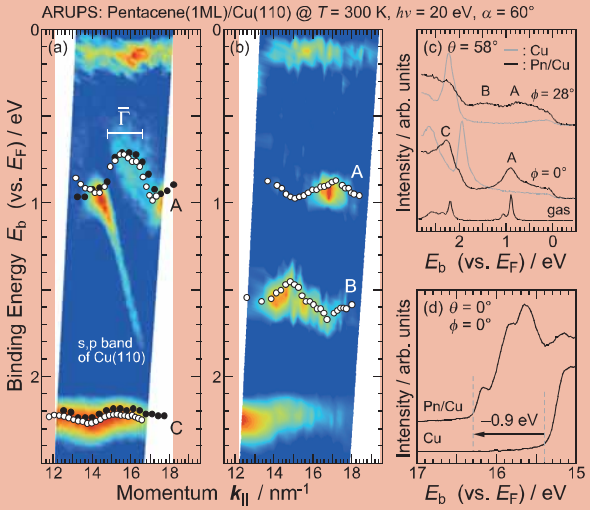

Fig. 1. (a,b) $E(\boldsymbol{k}_{\parallel})$ relation for the highly ordered flat-lying Pn monolayer film on Cu(110) at ϕ = (a) 0° and (b) 28°. The abscissa is the parallel component of the momentum ($\boldsymbol{k}_{\parallel}$), and ordinate is the binding energy (E_b) relative to the Fermi level (E_F) of the substrate. Open and filled circles indicate the position of the Pn-derived peaks measured at $h\nu$ = 20 and 30 eV, respectively. (c,d) Selected ARUPS spectra of the Pn monolayer film and the bare substrate for the regions of (c) valence levels and (d) secondary-electron cutoff.

It is interesting to note that, as seen in Fig. 1(a) and (b), the interface states A–C show dispersive behavior. At ϕ = 0° [Fig. 1(a)], the $E(\boldsymbol{k}_{\parallel})$ curve of peak A measured at $h\nu$ = 20 eV corresponds well with that measured at $h\nu$ = 30 eV, and the $E(\boldsymbol{k}_{\parallel})$ curve of peak C has turning points at the same $\boldsymbol{k}_{\parallel}$ as that for peak A. At ϕ = 28° [Fig. 1(b)], the turning points for peak B appears at the same $\boldsymbol{k}_{\parallel}$ as that for peak A, and the phase of the $E(\boldsymbol{k}_{\parallel})$ curve for peak B is opposite to that for peak A. Furthermore, the experimentally observed $\bar{\Gamma}$ point ($\bar{\Gamma}_{exp}$) exists around $\boldsymbol{k}_{\parallel}$ = 15.7±0.9 nm^{-1} at ϕ = 0°, which is the center of the fifth Brillouin zone. From the $E(\boldsymbol{k}_{\parallel})$ curves of peaks A and C, we can estimate the lattice constant (λ) along the [1$\bar{1}$0] substrate direction using the relation $\lambda = 2\pi/K$, where K is the size of the Brillouin zone, under the assumption of a tight-binding model. The deduced value of λ is 1.6 nm, which agrees well with the lattice constant of the flat-lying Pn monolayer film along the [1$\bar{1}$0] substrate direction [2]. Thus, the observed dispersive behavior can be ascribed to the intermolecular band dispersion in the flat-lying Pn monolayer film on Cu(110) with a large bandwidth of 0.25 eV for the uppermost valence band A, which seems to form a free-electron-like parabolic dispersion. Thus, the effective mass of the hole (m_h^*) can be calculated from

$$\frac{1}{m_h^*} = \frac{1}{\hbar^2}\frac{d^2E(\boldsymbol{k})}{d\boldsymbol{k}^2}.$$

Using this equation, we estimated m_h^* to be 0.24m_0 at 300 K within the tight-binding approximation. In the case of usual π-conjugated flat-lying organic monolayers, the intermolecular interaction is mainly dominated by the weak intermolecular σ-σ interaction, which gives small bandwidth of less than 0.05 eV. The observed band dispersion with rather small m_h^* may originate from the intermolecular interaction *via* the substrate due to the hybridization between the molecular orbitals and the free-electron-like Cu bands. On the other hand, Temirov *et al.* reported the inplane intermolecular band dispersion for the unoccupied state in a PTCDA monolayer on Ag(111) with an effective mass of electron m_e^* of 0.47m_0 by using the high-resolution scanning tunneling microscopy and spectroscopy [6]. The observed dispersion in Ref 6 is far larger than expected for the PTCDA monolayer alone [7], and they suggest that the dispersion might be related to the surface state since the effective mass is similar to that of the Ag(111) surface. However, in the case of pentacene/Cu(110), there is no known surface state along the [1$\bar{1}$0] substrate direction on the Cu(110) surface within the observed energy window. It must therefore be concluded that the mechanisms of interfacial dispersion of π-conjugated molecules are not yet fully understood. For further consideration about this issue, a joint experimental and theoretical study is now in progress.

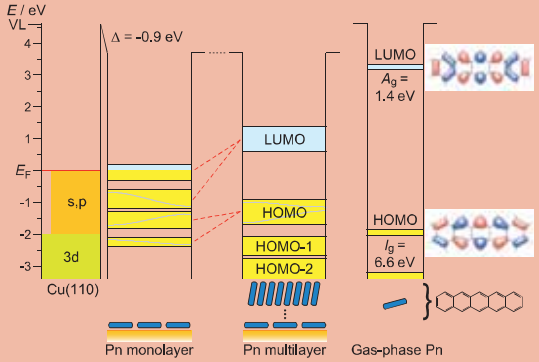

Fig. 2. Energy level diagrams for the Pn/Cu(110) system and the gas phase Pn. The LUMO energy for the Pn multilayer was estimated from Ref 8. The ionization energy for gas phase Pn (I_g) is 6.6 eV [3], and the intermolecular polarization energy for holes can be estimated to be 1.7 eV. If the intermolecular polarization energy for electrons is equal to that for holes, the electron affinity for gas phase Pn (A_g) can be estimated to be 1.4 eV.

In summary, the energy level diagram for the Pn/Cu(110) system is presented in Fig. 2. From the UPS spectra in Fig. 1, the work function of the clean Cu(110) surface is 4.6 eV and its change (Δ) by the Pn adsorption is –0.9 eV. For the flat-lying monolayer film, we clearly observed the electronic structure characteristic of the interface with the following findings: (i) formation of the interface states with possible modification of the orbital symmetry and the energy position, and (ii) two-dimensional intermolecular band dispersion of these interface states with m_h^* for the upper branch being 0.24 m_0 at 300 K. These interface states can be deduced to originate from the hybridization of the molecular orbitals such as the HOMO and the LUMO levels with the wave function of the substrate, which may also lead to the observed band dispersion by the intermolecular interaction through the substrate. Further studies on the correlation between the electronic and the film structures would lead to a breakthrough for the understanding of charge phenomena in organic solids.

*Present address: Institute for Molecular Science
E-mail: yamane@ims.ac.jp

[1] H. Ishii *et al.*, Adv. Mater **11** (1999) 605.
[2] S. Lukas *et al.*, Phys. Rev. Lett. **88** (2001) 028301; S. Söhnchen *et al.*, J. Chem. Phys. **121** (2004) 525.
[3] V. Coropceanu *et al.*, Phys. Rev. Lett. **89** (2002) 275503.
[4] H. Yamane *et al.*, Phys. Rev. B, **76** (2007) 165436; Phys. Stat. Sol. (b), **245** (2008) 793.
[5] A. Ferretti *et al.*, Phys. Rev. Lett., **99** (2007) 046802.
[6] R. Temirov *et al.*, Nature, **444** (2006) 350.
[7] H. Yamane *et al.*, Phys. Rev. B, **68** (2003) 033102.
[8] F. Amy *et al.*, Org. Electron. **6** (2005) 85.

BL4A

Synchrotron Radiation Stimulated Etching of Polydimethylsiloxane with XeF_2

T.Y. Chiang[1], T. Makimura[2], C. S. Wang[3], T. Urisu[1,4]

[1]*Institute for Molecular Science, Okazaki 444-8585 Japan*

[2]*Tsukuba University, 1-1-1Tennoudai Tsukuba, Ibaraki 305-8573 Japan*

[3]*Shanghai Jiao Tong University, 1954 Hua Shan Rd. Shanghai 200030 P. R. China*

[4]*The Groduate University for Advanced Studies, Okazaki 444-8585 Japan*

The synchrotron radiation (SR) stimulated etching of silicon elastomer polydimethylsiloxane (PDMS) has been demonstrated with XeF_2 as the etching gas. An etching system with a differential pump and paraboloid mirror was constructed to perform the etching. The PDMS was found to be effectively etched under the SR irradiation with flowing XeF_2, and the etching process was area-selective and anisotropic. An etching rate of about 45μm・150mA^{-1}・min^{-1} was obtained at a XeF_2 atmosphere of 0.5 Torr in etching chamber.

Fig. 1. Schematic view of the beam line 4 A. DP_i: differential pumpimg chamber. TMP: turbo molecular pump, IP: ion pump, EC: etching chamber. FM: focusing mirror.

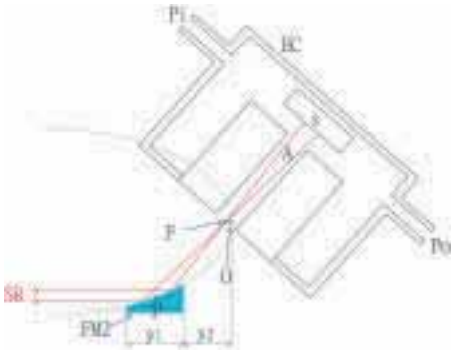

Fig. 2. Beam trace in focusing mirror chamber and etching chamber. S: specimen, A: aperture EC: etching chamber FM: focusing mirror.

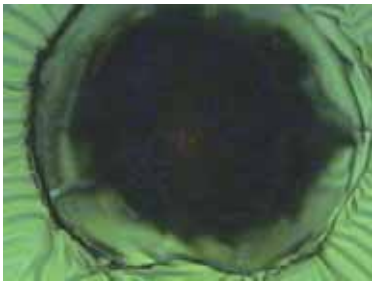

Fig. 3. Top view of the etched pattern on PDMS by SR etching using XeF_2 gas.

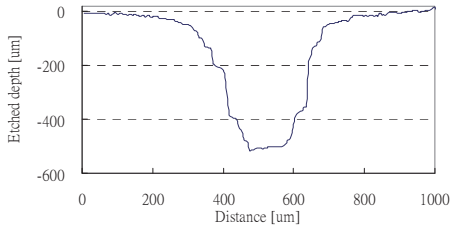

Fig. 4. Depth profile of the etched pattern shown in Fig. 3.

BL4B

Characterization of Self-Assembled Co Nanorods Grown on Cu(001)-(2×3)N Studied by XMCD

X. D. Ma[1, 2], T. Nakagawa[1, 3], Y. Takagi[1, 3], M. Przybylski[2], J. Kirschner[2], T. Yokoyama[1,3]

[1]*Department of Structural Molecular Science, The Graduate University for Advanced Studies (Sokendai), Myodaiji-cho, Okazaki, Aichi 444-8585, Japan*

[2]*Max-Planck-Institut f˙ur Mikrostrukturphysik, Weinberg 2, 06120 Halle, Germany*

[3]*Institute for Molecular Science, Myodaiji-cho, Okazaki, Aichi 444-8585, Japan*

Introduction

Recently, York and Leibsle [1] discovered self-assembled growth of well extended Co nanorods on Cu(110)-(2×3)N. The Co nanorods are well isolated from each other up to as much as ~2.0 monolayer (ML) Co coverage with six times intervals along the [001] direction. We have here investigated XMCD of 0.8 ML Co/Cu(110)-(2×3)N substrates.

Experimental

A Cu(110) single crystal was dosed with N by mild N_2^+ bombardment and subsequent annealing at ~473 K to yield (2×3)N surfaces. Co was deposited on these surfaces at ambient temperature using a commercial evaporator. The angle-dependent Co *L*-edge XMCD measurements were performed with a total electron yield mode using a UHV-compatible superconducting magnet (7 T) XMCD system with a liq. He cryostat (the sample temperature of 4.9 K).

Results and Discussion

Figure 1 depicts the magnetization curves recorded with the electron yield at the L_{III} peak top energy. The magnetizations are found to be almost saturated at H=±5 T for all the axes ([001] is the easy axis). The curves were simulated using a simple second-order magnetic anisotropy model to deduce the macroscopic magnetic anisotropy constants. The two magnetic anisotropy constants K_P and K_A respectively caused by the planar (film origin) and axial (rod origin) anisotropies and the size of the spin block N were assumed. The parameters were determined as K_P=1.2×10^{-4} (eV/atom), K_A=2.0×10^{-5} (eV/atom), and N=15 (atom). The planar magnetic anisotropy K_P that makes the surface normal the hardest axis is found to be much larger than that of the rod axial anisotropy K_A.

The angle dependence of the XMCD spectra shown in Fig. 2 was analyzed. The results are m^x_{orb}=0.23 μ_B, m^y_{orb}=0.19 μ_B, m^z_{orb}=0.16 μ_B, m^x_T=–0.005 μ_B, m^y_T= 0.011 μ_B, m^z_T=–0.006 μ_B, and m_{spin}=1.01 μ_B, where m_T is the magnetic dipole moment. The orbital magnetic moment decreases in the sequence of x ([001]), y ([1-10]), and z ([110]), which is consistent with the above magnetic anisotropy constants. This consequently implies that the magnetic anisotropy originates from the difference in the spin-orbit interaction. Note that the spin magnetic moment obtained is significantly smaller than that of the bulk *hcp* Co, because the small spin magnetic moment in Co may originate from the strong covalent bonds with N in the present nanorods.

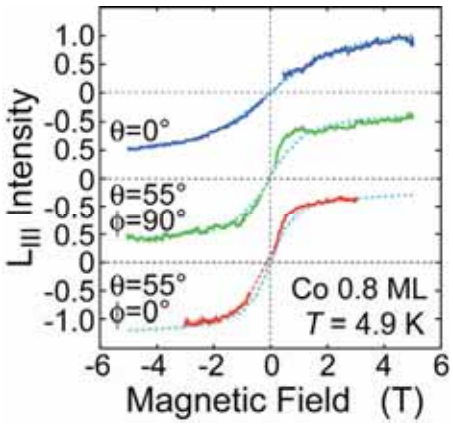

Fig. 1. Magnetization curves at T=4.9 K recorded with the intensity at the L_{III} peak energy. The simulated magnetization curves using a simple magnetic anisotropy model are also shown.

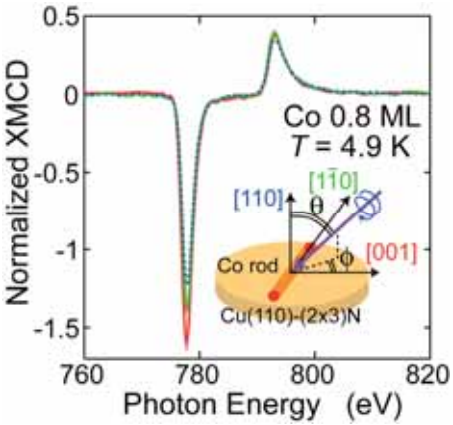

Fig. 2. Co *L*-edge XMCD spectra of 0.8 ML Co on Cu(110)-(2×3)N at T=4.9 K and H=±5.0 T for θ_{in}=0° (blue) and (θ_{in},φ_{in})=(55°,90°) (green) and H=±3.0 T for (θ_{in},φ_{in})=(55°,0°) (red).

[1] S. M. York, F. M. Leibsle, Phys. Rev. B **64** (2001) 033411.

BL4B

Enhancements of Spin and Orbital Magnetic Moments of Submonolayer Co on Cu(001) Studied by XMCD

T. Nakagawa[1], Y. Takagi[1], T. Yokoyama[1]
[1]*Institute for Molecular Science, Okazaki 444-8585, Japan*

Introduction

Enhancements of the magnetic moments of ultra-thin films have extensively been investigated both theoretically and experimentally because of their importance in fundamental physics as well as technological applications to magnetic recording media. In the present work, we have investigated the enhancements of spin and orbital magnetic moments for submonolayer Co/Cu(001) by means of XMCD using a UHV-compatible XMCD system with a 7 T superconducting magnet and a liquid He cryostat [1].

Experimental

A submonolayer Co film was deposited on a clean Cu(001) surface from a commercial evaporator. The thickness of the film investigated was estimated to be 0.4 ML from the Co *L*-edge absorption intensity. Co $L_{III,II}$-edge circularly polarized X-ray absorption spectra were recorded at the X-ray incidence polar angles θ_{in} of 60° (grazing incidence) and 0° (normal incidence). The spectra were taken at 6.0 K by switching the magnetic field.

Results and Discussion

Figure 1 shows the magnetization curve of 0.4 ML Co at 6.0 K along the surface normal [001] direction, which is the magnetically hardest axis. The data were scaled using the area of the Co L_{III} peak. The XMCD intensity is found to increase linearly up to H=±2.5 T, while the values at H=±5.0 T are apparently weaker than the ones expected from the extrapolated linear line. By fitting the experimentally obtained data points with a second-order magnetic anisotropy model, the lowest magnetic field for saturation is estimated to be ~3.4 T. The magnetic fields of ±5 T are thus confirmed to saturate the magnetization even along the magnetically hardest [001] axis.

Figure 2 depicts the Co $L_{III,II}$-edge XMCD spectra for θ_M=90° and 0°, where θ_M denotes the polar angle of magnetization. Although the two XMCD spectra are not very different from each other, small dissimilarities can clearly be seen around the $L_{III,II}$-edge peaks, indicating small anisotropic features in the present submonolayer film.

Using the sum rules and the formulas of XMCD angle dependence, the magnetic dipole terms were obtained to be $m_T^{//}$=0.010±0.05 μ_B and $m_T^{\perp}$=−0.020 ±0.05 μ_B. Consequently, the spin magnetic moment was given as 1.79±0.10 μ_B, which is larger than that of bulk *hcp* Co (1.55 μ_B), and the orbital magnetic moments of $m_{orb}^{//}$=0.29±0.05 μ_B and $m_{orb}^{\perp}$=0.23±0.05 μ_B are much more significantly greater than the bulk value of 0.15 μ_B. Theoretical estimations for the spin and orbital magnetic moment of monolayer Co/Cu(001) were reported as m_{spin}=1.85 μ_B and m_{orb}=0.261 μ_B [2], which are consistent with the present results. Enhancements of the magnetic moments compared with the corresponding bulk values were thus clearly elucidated: ~12% for the spin magnetic moment and ~96 and ~53% for the orbital magnetic moments along the surface parallel and normal directions, respectively.

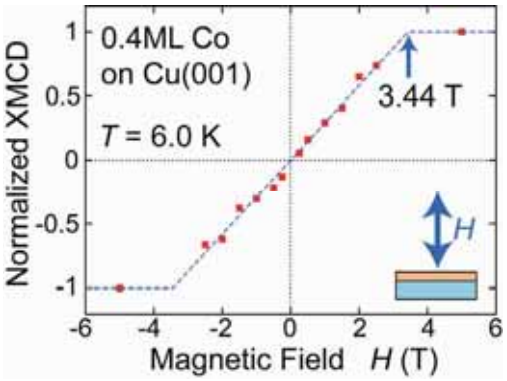

Fig. 1. Magnetization curve of 0.4 ML Co/Cu(001) at 6.0 K along the [001] direction, recorded as a normalized Co L_{III} XMCD intensity. The red points are the experimental data, and the blue dashed line is the fitted result.

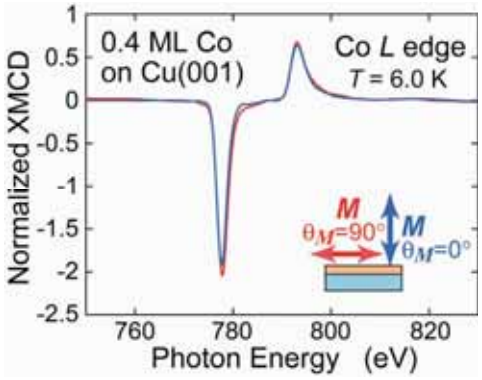

Fig. 2. Co $L_{III,II}$-edge XMCD spectra of 0.4 ML Co on Cu(001) at 6.0 K for the magnetization parallel (θ_M=90°) and perpendicular (θ_M=0°) to the surface.

[1] T. Nakagawa, Y. Takagi, Y. Matsumoto, T. Yokoyama, this volume & also Jpn. J. Appl. Phys., *in press*.
[2] O. Hjortstam, J. Trygg, J. M. Wills, B. Johansson, O. Eriksson, Phys. Rev. B **53** (1996) 9204.

BL4B

Variation of Magnetic Anisotropy upon Adsorption of NO on Co/Cu(001) Studied by XMCD

T. Nakagawa[1], Y. Takagi[1], T. Yokoyama[1]
[1]*Institute for Molecular Science, Okazaki 444-8585, Japan*

Introduction

Adsorption of atoms and molecules on magnetic thin films is an attractive surface scientific subject since it .is known to change drastically magnetic anisotropy and to induce sometimes spin reorientation transitions. In the present work, we have investigated NO adsorption on submonolayer Co/Cu(001) by means of XMCD using a UHV-compatible XMCD system with a 7 T super- conducting magnet and a liquid He cryostat [1].

Experimental

A 0.8 monolayer (ML) Co film was deposited on a clean Cu(001) surface from a commercial evaporator at room temperature and was subsequently dosed with NO at ~100 K. Co $L_{III,II}$-edge circularly polarized X-ray absorption spectra were recorded at T=5.0 K and H=5.0 T with the X-ray incidence polar angles θ_{in} of 55° (grazing incidence) and 0° (normal incidence).

Results and Discussion

Figure 1 depicts the magnetization curves of 0.8 ML Co on Cu(001), recorded as Co L_{III} XMCD intensity at the peak top energy. Unfortunately, the curve along the hard axis of θ_{in}=0° is not saturated. Using the θ_{in}=0° data, the second-order magnetic anisotropy constants including demagnetization energies are obtained as K_2=−370 (μeV/atom) for clean Co and −130 (μeV/atom) for NO adsorbed Co. This indicates significant suppression of the in-plane magnetic anisotropy upon NO adsorption.

Figure 2 depicts the Co $L_{III,II}$-edge XMCD spectra for θ_{in}=55° and 0°. NO adsorption induces the shift of the peak energies and the suppression of the XMCD intensity. Using the sum rules, the spin and orbital magnetic moments are derived. Although the magnetization for clean Co (θ_{in}=0°) is not saturated, the ratio m_{orb}/m_{spin} was assumed to be invariant to yield the orbital magnetic moment. In the case of NO adsorption, both the magnetizations were assumed to be saturated and this allows us to evaluate magnetic dipole terms appropriately and hence the intrinsic spin magnetic moments.

The d-hole number is found to increase significantly from d_h=2.56±0.13 (clean) to 2.92±0.15 (NO-ads.), implying the oxidation of Co upon NO adsorption. The spin magnetic moment noticeably decreases from m_{spin}=1.780±0.18 μ_B (clean) to 0.89 ±0.05 μ_B (NO-ads.). This indicates strong interaction between an unpaired electron of NO and exchange-split Co 3d levels. The anisotropic orbital magnetic moments show the most prominent difference. For clean Co, the analysis yields $m_{orb}^{//}$=0.299±0.02 μ_B and $m_{orb}^{\perp}$=0.228±0.02 μ_B, while the NO-adsorbed Co gives $m_{orb}^{//}$=0.106±0.01 μ_B and $m_{orb}^{\perp}$=0.111±0.01 μ_B. These results clarifies that the strong in-plane magnetic anisotropy in clean Co is derived from much larger in-plane spin-orbit interaction than the perpendicular one and that NO adsorption leads to the loss of anisotropy in the spin-orbit interaction. The weak in-plane magnetic anisotropy for NO adsorbed Co may originate from the demagnetization energy (shape anisotropy).

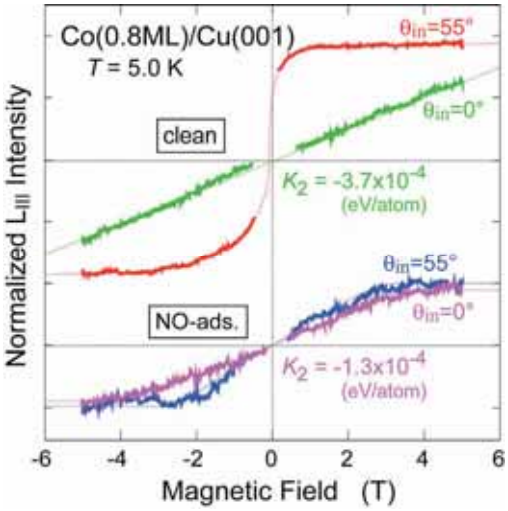

Fig. 1. Magnetization curves of 0.8 ML Co on Cu(001) at T=5.0 K before and after NO adsorption.

Fig. 2. Angle dependent Co $L_{III,II}$-edge XMCD spectra of 0.8 ML Co on Cu(001) at T=5.0 K before and after NO adsorption.

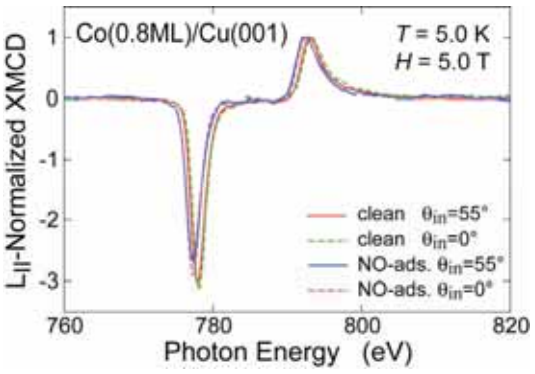

[1] T. Nakagawa, Y. Takagi, Y. Matsumoto, T. Yokoyama, this volume & also Jpn. J. Appl. Phys., *in press*.

BL8B2

Photoelectron Angular Distribution of Mn-Phthalocyanine Monolayer on Ag(111)

T. Aoki[1], S. Hosoumi[1], C. Karino[1], R. Sumii[2], S. Nagamatsu[1], N. Ueno[1], S. Kera[1]

[1]*Graduate School of Advanced Integration Science, Chiba University, Chiba 263-8522 Japan*

[2]*Graduate School of Science, Nagoya University, Nagoya 464-8602 Japan*

Origins of the energy position and the shape of HOMO bands are keys to understand interface properties of organic films. The electronic structure of the adsorbed monolayer on a metal substrate is generally modified much by a strong electronic coupling. In this study changes in the electronic structure due to different spin configuration and/or change in the ligand field upon adsorption were investigated for Mn-phthalocyanene (MnPc) on Ag(111). Angle-resolved UPS (ARUPS) using synchrotron radiation is a powerful tool to study the geometrical structure of the ultrathin films of organic molecules as well as the electronic structure. In the previous work we have succeeded to analyze the emission (θ) and azimuthal (ϕ) angle dependences of ARUPS of thin films of large organic molecules using single scattering approximations [1].

In this report, we show the observed θ and ϕ dependences of 2p- and 3d-orbital derived bands in ARUPS spectra for well-ordered MnPc monolayer (ML) on the Ag(111) substrate.

Experimental

θ and ϕ dependences of ARUPS spectra were recorded at photon incidence angle α=45°, hν=28 eV, and T=295 K. The purified MnPc molecules were carefully evaporated onto a clean Ag(111) substrate. We confirmed 6-hold molecular domains (2 domains in each crystal axis) from LEED results.

Results and Discussion

Figure 1 shows a typical HeI UPS spectrum of annealed-MnPc (ML)/Ag(111) at θ =0°. The results obtained for MnPc (ML) /HOPG are also shown [2]. For MnPc/Ag(111), feature A appearing at 0.35 eV, which is located at lower energy position than MnPc/HOPG, can be ascribed to HOMO band of MnPc. Feature B, HOMO-1, which is located at similar energy position as for MnPc/HOPG, might be assigned to a single π MO as observed in other various Pcs. The shift of A and small satellites (s) might come from interface states formed upon orbital hybridization.

Figure 2 shows the observed θ (a) and ϕ (b) dependences of the band A (HOMO) and band B (HOMO-1) intensities, respectively. The θ pattern from B is rather similar to that of MnPc/HOPG, indicating the HOMO-1 is assigned to 2p-derived orbital (a_{1u}) as seen in other Pc/HOPG systems. We found that the deformation of the MO upon adsorption is surely occurring but not significant. The θ pattern for A (HOMO), however, is completely different from that of MnPc/HOPG, indicating that the 3d-derived MO has changed. The electronic structure, especially 3d-derived MOs, of MnPc may be rearranged due to different spin configuration and/or change in the ligand field upon absorption. Now we are trying to obtain the angular dependences by using the multiple-scattering theory combined with MO calculation [3] under various spin configulations and MOs.

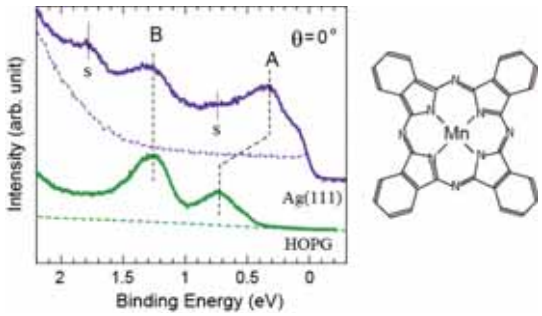

Fig. 1. HeI UPS of 1-ML-MnPc on Ag(111) and HOPG. Both dashed curves are UPS from a clean substrate.

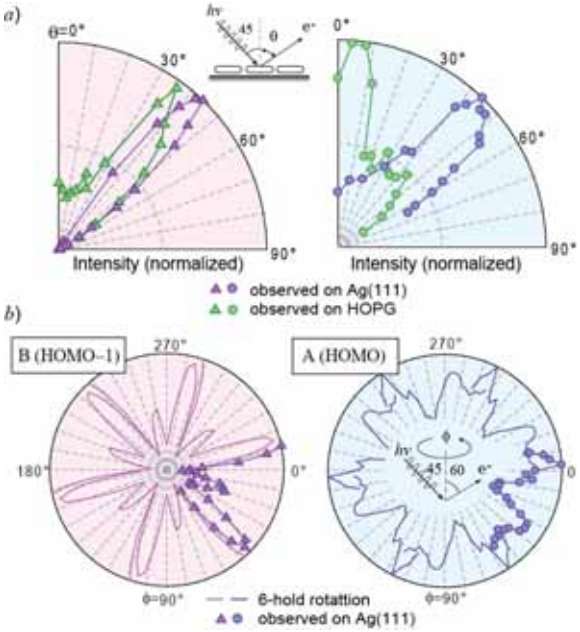

Fig. 2. (a) Observed θ patterns of band A (right) and B (left) obtained at α=45°, ϕ=0°. (b) Observed ϕ patterns of band A and B for MnPc/Ag(111) obtained at α=45°, θ=60°.

[1] N. Ueno *et al*, J. Chem. Phys. **107** (1997) 2079.

[2] S. Kera *et al*, UVSOR Activity Report 2006 (2007) 113.

[3] S. Nagamatsu *et al*, e-J. Surf. Sci. Nanotech, **3** (2005) 461.

BL8B2

Interaction between Entrapped Atoms and C_{78} Fullerene Cage

S. Hino [1], M. Kato[2], D. Yoshimura[3, 4], H. Moribe[5], H. Umemoto[5], Y. Ito[5], T. Sugai[5], H. Shinohara[5], M. Otani[6], Y. Yoshimoto[6], S. Okada[7]

[1]*Graduate School of Materials Sci. & Biotech., Ehime Univ., Matsuyama 790-8577 Japan*
[2]*Graduate School of Sci. & Technology, Chiba Univ., Chiba 263-8522, Japan*
[3]*UVSOR, Institute for Molecular Science, Okazaki 444-8585, Japan*
[4]*Research Center of Material Science, Nagoya Univ., Nagoya 464-8602, Japan*
[5]*Graduate School of Science, Nagoya Univ., 464-8602, Japan*
[6]*Institute for Solid State Physics, Univ. of Tokyo, Kashiwa 277-8581, Japan*
[7]*Center for Computational Sciences, Univ. of Tsukuba, 305-8571 Tsukuba Japan*

Ultraviolet photoelectron spectra (UPS) of metallofullerene, $La_2@C_{78}$ that has D3h cage symmetry were measured using a synchrotron radiation light source [1]. The UPS are shown in Fig. 1. Its spectral onset energy was 0.70 eV below the Fermi level, indicating the semiconductive nature of this metallofullerene. The UPS consisted of numerous crests and troughs. Further, a change in intensity upon tuning the excitation energy was observed; however, the intensity of the change was not as large as those observed for other fullerenes. Previously measured UPS of $Ti_2C_2@C_{78}$ are also shown in Fig. 1 [2]. When the UPS of $Ti_2C_2@C_{78}$ were reported, it was thought that it was the mixture of two $Ti_2@C_{80}$ isomers, and it has been questioned that it is not the mixture but actually $Ti_2C_2@C_{78}$. Further it has been proposed that the cage symmetry of $Ti_2C_2@C_{78}$ is D_{3h}.

There are two so-called Isolated Pentagon Rule satisfying D3h cage structure in C_{78} fullerene family. The UPS of $La_2@C_{78}$ differ considerably from those of $Ti_2C_2@C_{78}$, so that, at first, it was thought that these two metallofullerenes have different D_{3h} cage.

In order to examine this assumption, DFT calculation has been carried out in both cages with La_2 or Ti_2C_2 entrapped cages. Calculated DOS is shown in Fig. 1. Comparison revealed that both metallofullerenes have the same cage symmetry classified as D_{3h} (78:5) according to Fowler and Manolopoulos [3]. In most UPS of fullerenes, the UPS of the fullerenes having the same cage are analogous. Present results are rather extraordinary. Thus distribution of wave functions (DWF) in metallofullerenes is examined. Figure 2 shows the wave function distribution of HOMO and HOMO-1 orbitals of these two metallofullerenes.

DWF of the HOMO of both fullerenes is almost the same, but that of the HOMO-1 differs considerably: while HOMO-1 of $La_2@C_{78}$ distributes on the fullerene cage, that of $Ti_2C_2@C_{78}$ penetrates into the cage and tries to make hybridized bond with Ti atoms. Titanium has a tendency to form carbide. Possibly there might strong interaction between Ti atoms and cage constructing carbon atoms, and this is the reason why the same cage symmetry having $La_2@C_{78}$ and $Ti_2C_2@C_{78}$ give completely different UPS.

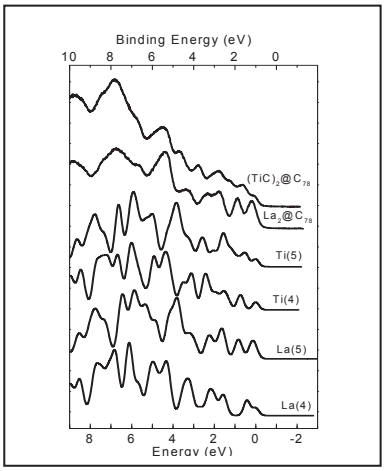

Fig. 1. UPS of $La_2@C_{78}$ and $Ti_2C_2@C_{78}$. Calculated DOS assuming La_2 or Ti_2C_2 species entrapped D_{3h} C_{78} is also shown.

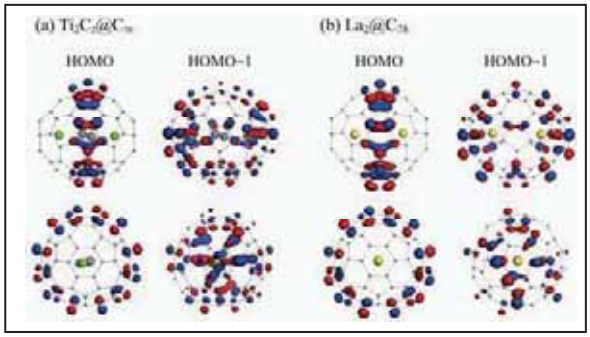

Fig. 2. Distribution of HOMO and HOMO-1 wave functions. Green circles indicate Ti, Yellow circles La, and grey circles C. Large grey circle indicate entrapped carbon atom.

[1] S. Hino *et al.*, Phys. Rev. B **75** (2007) 125418.
[2] K. Iwasaki *et al.*, Chem. Phys. Lett. **397** (2004) 169.
[3] P. W. Fowler, D. E. Manolopoulos, "An Atlas of Fullerenes", Oxford University Press, Oxford, 1995.

BL8B2

Energy Level Alignment at PTCDA / Metal Interfaces

E. Kawabe[1], H. Yamane[1], R. Sumii[2,3], K. Koizumi[1], K. Kanai[2], Y. Ouchi[1], K. Seki[1]

[1]*Graduate School of Science, Nagoya University, Furo-cho, Chikusa-ku, Nagoya 464-8602 Japan*

[2]*Research Center for Materials Science, Nagoya University,*

[3] *Present address: Photon Factory, Institute of Materials Structure Science, High Energy Acceleration Research Organization, Oho 1-1, Tsukuba, 305-0801 Japan*

Recently extensive research has been carried out for applying organic materials to electronic devices. It is important to understand how the energy levels align at organic / metal (O / M) interfaces for improving their performance. However, the detailed mechanism of the energy level alignment at O / M interface is still unclear. Vázquez *et al*. proposed the induced density of interface states (IDIS) model [1] to theoretically explain the vacuum level (VL) shift at O / M interface [2, 3]. They made several assumptions to simplify the calculation, i.e. (1) the energy levels of the highest occupied molecular orbital (HOMO) and the lowest unoccupied molecular orbital (LUMO) are broadened to form continuous levels, which is called the IDIS by the interaction with the metal state, (2) only the s-state is taken into account as the metal state. Although this model well explains the observed Δ at organic / Au interfaces, it has been still unclear whether this model can be generally applied to various metal substrates. Thus we investigated the energy level alignment at the interfaces between perylene-3, 4, 9, 10-tetracarboxylic dianhydride (PTCDA, Fig. 1) and metals (Au, Ag and Cu) by ultraviolet photoelectron spectroscopy (UPS).

The plot of the observed Δ as a function of the metal work function (Φ_M) is shown in Fig. 1. In the IDIS model, it is expected that Δ and Φ_M show a linear relation. However, we cannot see such relation. The UPS spectra of monomolecular layer (1 ML) PTCDA film on Au(111), Ag(111) and Cu(111) are shown in Fig. 2. The interface states are observed for Ag and Cu interfaces, and they are not the broadened states but the split states. These results indicate that the IDIS model cannot be applied to these interfaces, and that the interaction with the metal d-band states cannot be neglected.

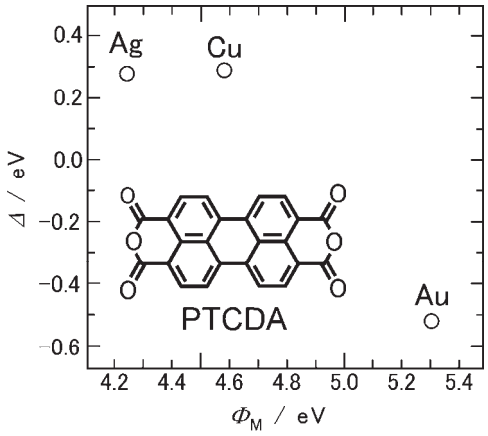

Fig. 1. Plot of Δ as a function of Φ_M. Inset: Molecular structure of PTCDA.

Then we estimate the interface interaction by taking into account the metal d-band states. We expect that [5] the magnitude of the attractive interaction depends on the inverse of the energy separation between the LUMO of PTCDA and the centroid of the metal d-band ($\varepsilon_{d\text{-}LUMO}$), and that the magnitude of the repulsive interaction depends on the coupling matrix element (V) between the adsorbate state and the metal d-band state. The value of $\varepsilon_{d\text{-}LUMO}$ for the PTCDA / Cu interface is the smallest. The value of V for the PTCDA / Au interface is the largest, since V increases with the principal quantum number. From these results, it is found that the interaction for the Au interface is very weak (physisorption), and those for the Ag and Cu interfaces are strong (chemisorption). These results indicate that the observed VL shift for the Au interface is due to the rearrangement of the surface electron cloud at the Au surface by the push-back effect, and those for the Ag and Cu interfaces are due to the formation of the interface states resulting in the charge redistribution ate the interfaces.

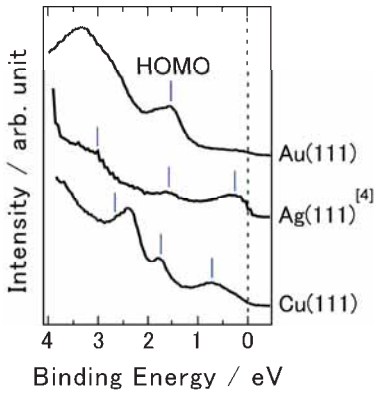

Fig. 2. UPS spectra of 1 ML PTCDA / metal interfaces.

[1] H. Vazquez *et al*., Europhys. Lett. **65** (2004) 802.
[2] S. Narioka *et al*., Appl. Phys. Lett. **67** (1995) 1899.
[3] H. Ishii *et al*., Adv. Mater. **11** (1999) 605.
[4] Y. Zou *et al*., Surf. Sci. **600** (2006) 1240.
[5] A. Ruban *et al*., J. Mol. Catal. A: Chem. **115** (1997) 421.

BL8B2

Valence Electronic Structure of Metal Phthalocyanine Monolayers on Graphite

S. Kera[1], T. Aoki[1], S. Hosoumi[1], N. Mitsuo[1], K. Nebashi[1], T. Kataoka[1], R. Sumii[2], S. Nagamatsu[1], N. Ueno[1]

[1]*Graduate School of Advanced Integration Science, Chiba University, Chiba 263-8522 Japan*

[2]*Graduate School of Science, Nagoya University, Nagoya 464-8602 Japan*

Angle-resolved ultraviolet photoelectron spectroscopy (ARUPS) has been known as a powerful technique to obtain crucial information on electronic band structure for various kinds of materials. Moreover, for organic thin films, information on the molecular orbital (MO) character, bonding nature, can be also discussed in accordance with a quantitative analysis of the ARUPS intensity using photoelectron scattering theory when the geometrical structure of the thin films are considered.

Phthalocyanines(Pcs) are a versatile class of π-conjugated organic semiconductors applicable as device materials. Among these the transition metal Pcs are interesting materials in controlling the device performance via 3d-electron derived MOs. However, information on the electronic structure of these organometallic complexes is still limited. Here, we show the electronic structure of the monolayer of various transition metal (Mn-, Fe-, Co-, Ni-) Pcs on graphite systematically.

The observed electron emission angle (θ) dependences of 2p- and 3d-orbital derived MO bands in ARUPS spectra for well-ordered Pc monolayers were compared.

Experimental

ARUPS spectra were measured at photon incidence angle α=45°, hν=28 or 30 eV, and a sample temperature T=295 K. θ dependence of ARUPS spectra was analyzed using the multiple-scattering theory combined with molecular orbital (MST/MO) calculation [1]. The purified Pc molecules were carefully evaporated onto the graphite (HOPG: grade ZYA). We have found that the molecules are oriented nearly flat to the substrate surface [2].

Results and Discussion

Figure 1 shows θ dependence of ARUPS of annealed-Pc monolayers (MnPc, FePc, CoPc and NiPc) on HOPG. The intensity is normalized to the incidence photon flux. DFT-MO calculation suggests that (i) features A are ascribed to 3d-derived band of Pcs and (ii) features B are assigned to 2p-derived band (a single π MO). Note that the MO calculation to discuss the electronic structure still may have difficulties for organometallic complexes.

Figure 2 shows the comparison between observed and calculated θ dependences of the band A and B intensities for MnPc, CoPc and NiPc (FePc is still under analysis). The θ patterns are completely different between 3d- (A) and 2p-derived (B) bands. In the fitting for π bands (B), the observed θ patterns are well reproduced by the MST/MO calculation of a free molecule for MO (π: a_{1u}), while for 3d-derived bands (A), the observed θ patterns are not fitted by the calculation from MO (3d: a_{1g}). Note that the θ pattern of MO (3d: a_{1g}) depends on the strength of the metal-ligand bonding, that is, on the hybridization between 3d and 2p orbitals.

The results indicate that the 3d-derived band is located at various energy positions due to change in the 3d-electron occupation, while 2p-derived (π) band appears at the similar energy. Further analysis on the intensity of feature A is necessary.

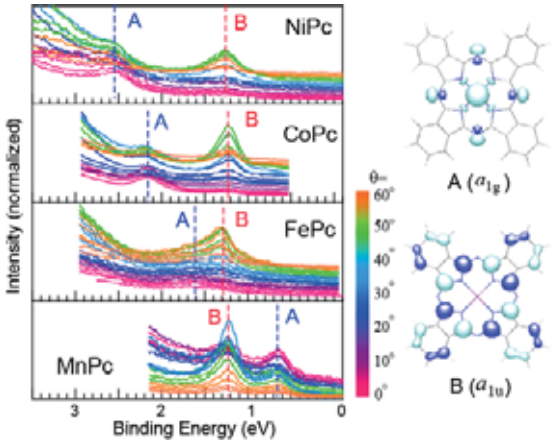

Fig. 1. θ dependences of ARUPS of1-ML-Pcs (MnPc, FePc, CoPc and NiPc) on HOPG. MOs calculated for CoPc are also shown.

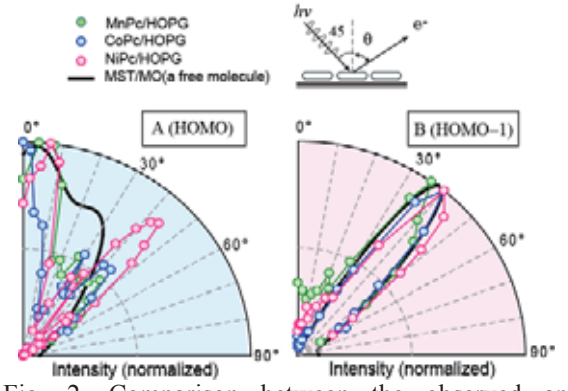

Fig. 2. Comparison between the observed and calculated θ patterns of the band A (left) and B (right).

[1] S. Nagamatsu *et al*, e-J. Surf. Sci. Nano **3** (2005) 461.

[2] T. Kataoka *et al*, Chem. Phys. Lett. **451** (2008) 43.

BL8B2

Angle-Resolved UPS of Thin Films of *o*-Quinonate Complex on Graphite

N. Mitsuo[1], T. Aoki[1], Y. Suzuki[1], S. Nagamatsu[1], R. Sumii[2], S. Noro[3], T. Hosokai[1], K. K. Okudaira[1], N. Ueno[1], S. Kera[1]

[1]*Graduate School of Advanced Integration Science, Chiba University, Chiba 263-8522 Japan*
[2]*Graduate School of Science, Nagoya University, Nagoya 464-8602 Japan*
[3]*Research Institute for Electronic Science, Hokkaido University, Sapporo 060-0812, Japan*

Bis-(*o*-diiminobenzosemiquinonate) nickel(II) complex {Ni(DIBSQ)} is known to have a narrow band-gap of 0.8 eV. Recently, high-performance ambipolar operation in organic field effect transistor of Ni(DIBSQ) was reported [1].

We have investigated the electronic structure and molecular orientation of Ni(DIBSQ) in a thin film by using angle-resolved ultraviolet photoelectron spectroscopy (ARUPS). ARUPS has been known as a powerful technique to obtain crucial information on electronic band structure for various kinds of materials. Moreover, for organic thin films, information on the geometrical structure of the thin films can be also discussed in accordance with a quantitative analysis of the ARUPS intensity using photoelectron scattering theory.

In this report, we show the observed electron-emission-angle (θ) dependence of HOMO bands in ARUPS spectra for the standing Ni(DIBSQ) layer deposited on a graphite substrate.

Experimental

ARUPS spectra were measured at photon incidence angle α=45°, hν=40 eV, and T=295 K. The purified molecules were carefully evaporated onto the graphite (HOPG) substrate. θ dependence was analyzed using the multiple-scattering theory combined with molecular orbital (MST/MO) calculation [2].

Results and Discussion

Figure 1(a) shows the θ dependence of ARUPS of Ni(DIBSQ) (3.5nm) on the HOPG. The intensity is normalized to the incidence photon flux. A top feature appeared around 1.4 eV is ascribed to HOMO band of Ni(DIBSQ). One can see an energy shift of the HOMO about 280 meV depending on the θ (see the guide lines). We found that the molecules are oriented nearly standing to the substrate surface from NEXAFS results (as shown in the right panel in Fig.1). Accordingly we expect that the DOS structure in the HOMO feature of UPS, which comes from the HOMO band dispersion, could be observed even for polycrystalline Ni(DIBSQ) films as in pentacene [3]. ARUPS study for the standing film on the single crystal would be fascinating.

Figure 1(b) shows the comparison between observed and calculated θ dependences of the HOMO intensity. The observed intensity gives the maximum at around 0°. There are large differences between observed and calculated MST/MO patterns. Here we performed the MST/MO calculation for a unit model of 5 molecules to describe the intermolecular scattering effects. We also found that the observed θ pattern depends on the photoelectron kinetic energy and the sample quality (molecular packing and/or crystallinity). These indicate that the impacts of the interference of scattered photoelectron waves are crucial. We are trying to compute the angular dependence by taking into account the intermolecular layer effects.

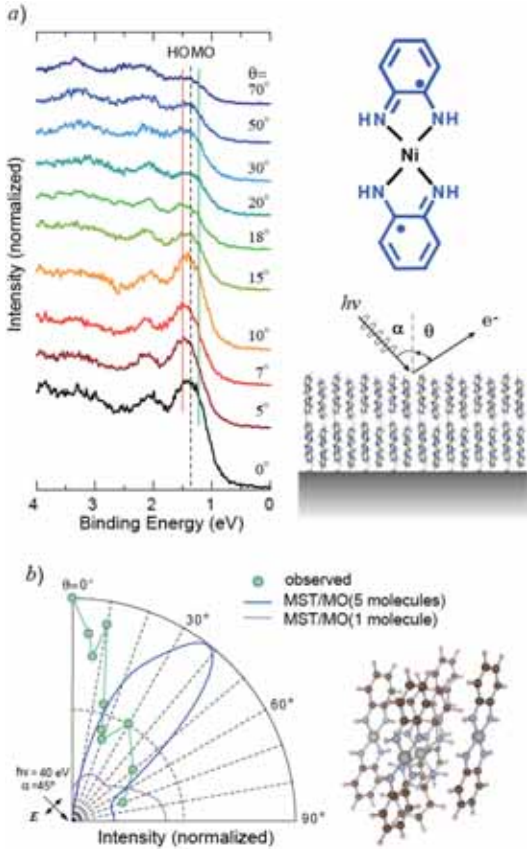

Fig. 1. a) θ dependence of ARUPS of Ni(DIBSQ) on HOPG, b) Observed and calculated θ patterns of the HOMO. Chemical structure, schematic view of the film structure, and a unit model for the calculation are also shown.

[1] S. Noro *et al*, J. Am. Chem. Soc. **127** (2005) 1001.
[2] S. Nagamatsu *et al*, e-J. Surf. Sci. Nanotech, **3** (2005) 461.
[3] H. Fukagawa *et al*, Phys. Rev. B **73** (2006) 245310.

BL8B2

Electronic Structure of $LiNi_{1-x}M_xO_2$ Mixed Oxides (III)

T. Miyazaki[1], R. Sumii[2,3], T. Kamei[1], H. Tanaka[1], S. Hino[1]

[1]*Graduate School of Science and Engineering, Ehime University, Matsuyama 790-8577, Japan*

[2]*Research Center for Materials Science, Nagoya University, Nagoya 464-8602, Japan*

[3]*UVSOR Facility, Institute for Molecular Science, Okazaki 444-8585, Japan*

Hexagonal lithium nickel oxide ($LiNiO_2$) is active for the oxidation coupling of the methane (OCM) with a selective function of oxidation catalyst. We have studied the crystal structure and the surface oxygen species for understanding the selective oxidation mechanism and synthesized hexagonal Li-Ni mixed metal oxides ($LiNi_{1-x}M_xO_2$; M=transition metal). The OCM activity of $LiNi_{1-x}Ti_xO_2$ ($0.05 \leq x \leq 0.2$), which was replaced Ti with a part of Ni of $LiNiO_2$, increased by the metal substitution. In this study, the UPS spectra of $LiNi_{0.95}Ti_{0.05}O_2$ and $LiNi_{0.995}Ti_{0.005}O_2$ were measured with the dependence of the incident photon energy. In addition, the change of the UPS spectra of $LiNiO_2$ thin film was reported by the difference of pre-treating of the sample.

$LiNi_{0.95}Ti_{0.05}O_2$ and $LiNi_{0.995}Ti_{0.005}O_2$ were synthesized by solid state reaction. $LiNiO_2$ thin film was synthesized by Li ion diffusion on Ni plate. The UPS spectra were measured at BL8B2 of UVSOR in Institute for Molecular Science. The argon ion sputtering and IR heating of samples were done in order to imitate rough surface and remove the contamination.

Figure 1 was shown the UPS spectra of $LiNiO_2$ thin film at $h\nu = 40$eV. The valence band spectra consist of five structures at $E_b \leq 15$eV below the Fermi level. The top valence region was almost derived from the Ni3d and O2p states. After the heat treatment the intensity of Ni3d states decreased, but the features of two O2p peaks were cleared. It was analogized that two kinds of oxygen species existed and functioned for the selective oxidation. Figure 2 was shown the UPS spectra of $LiNi_{0.95}Ti_{0.05}O_2$ and $LiNi_{0.995}Ti_{0.005}O_2$ of the incident photon energy at 20-60eV. The valence band spectra of $LiNi_{0.95}Ti_{0.05}O_2$ and $LiNi_{0.995}Ti_{0.005}O_2$ also consist of five structures in this region. The UPS spectral features of $LiNi_{0.995}Ti_{0.005}O_2$ were analogous to those of hexagonal $LiNiO_2$. In the case of $LiNiO_2$ and $LiNi_{0.995}Ti_{0.005}O_2$, the UPS spectra caused the intensity change which depended on the incident photon energy, but only small spectral change of $LiNi_{0.95}Ti_{0.05}O_2$ was observed at 20-60eV. It was speculated that the valence band feeling might be changed by replacing Ti^{4+} in Ni^{3+}.

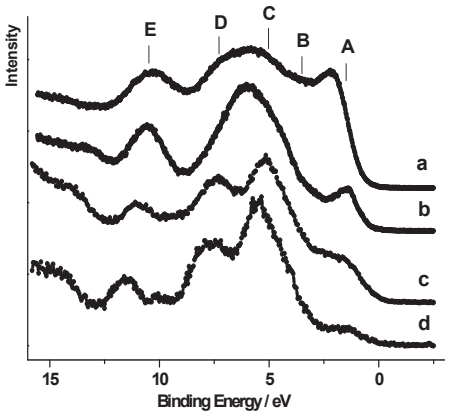

Fig. 1. The UPS spectra of thin film $LiNiO_2$ samples, a) Ar ion sputtering, b) Heating with O_2 at 450℃, c) 450℃ under 10^{-6} Pa, d) 600℃ under 10^{-6} Pa.

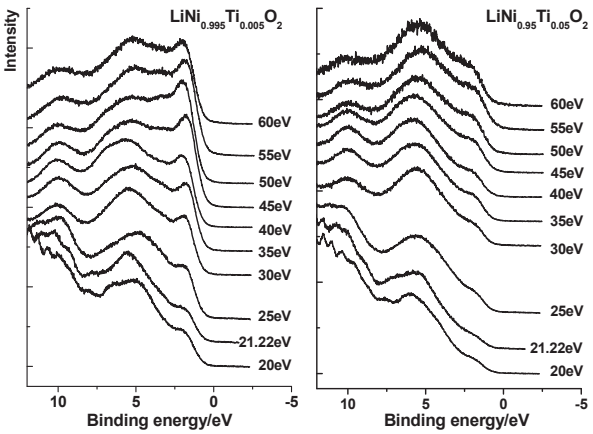

Fig. 2. The UPS spectra of $LiNi_{0.995}Ti_{0.005}O_2$ and $LiNi_{0.95}Ti_{0.05}O_2$ with the dependence of the incident photon energy at 20-60eV.

BL8B2

Electronic Structures of Rubrene and Its Photooxidation Product

Y. Nakayama[1], S. Machida[2], T. Minari[3], K. Tsukagoshi[3], H. Ishii[1,4]
[1]*Center for Frontier Science, Chiba University, Chiba 263-8522 Japan*
[2]*Faculty of Engineering, Chiba University, Chiba 263-8522 Japan*
[3]*Nanoscience Development and Support Team, RIKEN, Saitama 351-0198 Japan*
[4]*Graduate School of Advanced Integration Science, Chiba University, Chiba 263-8522 Japan*

Introduction

Rubrene (5,6,11,12-tetraphenyltetracene) is one of the most promising candidates for a *p*-type organic field effect transistor owing to a high hole mobility in its single-crystalline (SC) phase [1]. Since rubrene easily reacts with oxygen to form its *endo*-peroxide ($RubO_2$) under visible light illumination (Fig.2 inset), it is believed that the surface of rubrene SC is covered with "native" oxide layers and the oxidized product also contributes to the conduction mechanism as a dopant [1,2]. Toward understanding on the transport nature and further improvement of the device performance, information about the electronic structure of not only the pristine rubrene but also its photooxidation product is indispensable.

In the present study, we conducted photoelectron spectroscopy (PES) and photoelectron yield spectroscopy (PYS) measurements for a thin film of rubrene before and after the photooxidation reaction.

Experiment

An amorphous film of rubrene was made on indium-tin-oxide (ITO) by *in-situ* vacuum sublimation. $RubO_2$ was produced by exposing the rubrene film to ambient air under illumination of room light for 3 days. PES measurements were conducted at BL8B2. All the PES spectra presented below were taken at normal emission angle ($h\nu$ = 40 eV). The Fermi-level position was determined from a gold foil. The work function of each sample was estimated from the secondary electron cut-off taken at the sample bias of –5 V. PYS measurements were performed by a home-built system [3].

Results and discussion

Figure 1 shows PES spectra of the pristine rubrene film and the photooxidized film. The peak corresponding to the highest occupied state of rubrene, which is assigned to the tetracene backborn, disappears after photooxidation. It is in good agreement with the previous report for a $RubO_2$ film oxidized in pure oxygen [4]. As shown in Fig. 2, the ionization potential (I_s) estimated from the PES matches that from PYS results in cases of the pristine film and $RubO_2$. No clear sign of the oxidation induced midgap state [2] was identified.

We also conducted PES measurement of a rubrene SC. For SC, however, features at the binding energy (E_b) below 6 eV are absence, and apparent I_s's are completely different between PES and PYS results. Two factors should be taken into account on considering the PES spectra of rubrene SC: the one is surface oxidation, and the other is sample charging. Note that probing depth of PYS is much greater than PES because PYS detects photoelectrons of extremely slow (typically less than 1 eV). Removal of the oxidation product by vacuum heating [4] and/or vacuum cleavage of the crystal will possibly enable us to observe the PES spectra of "pristine crystal" covered with the oxide. Trials to avoid the sample charging problem such as visible light irradiation are now underway.

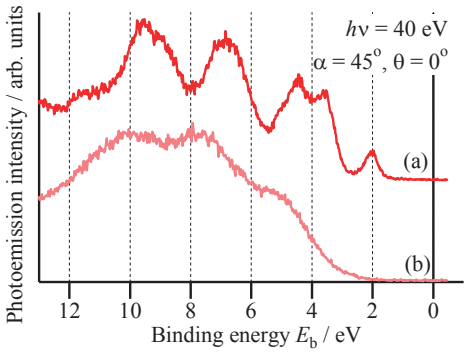

Fig. 1. PES spectra of (a) the pristine rubrene film and (b) the $RubO_2$ film.

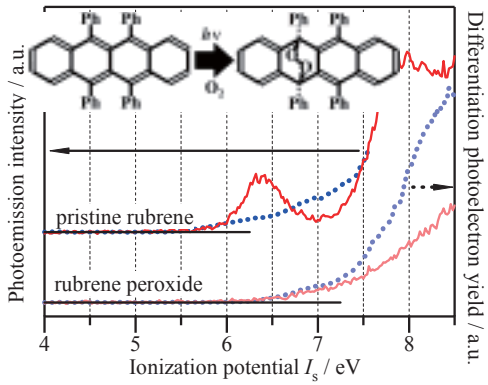

Fig. 2. Magnified PES spectra near the HOMO region (lines, left axis) and differentiation intensity of PYS spectra (dots, right axis). [Inset] Molecular structures before and after the photooxidation.

[1] V. Podzorov, *et al.*, Appl. Phys. Lett. **85** (2004) 6039.
[2] O. Mitrofanov, et al., Phys. Rev. Lett. **97** (2006) 166601.
[3] H. Ishii, *et al.*, Hyomen-kagaku **28** (2007) 264.
[4] Y. Harada, *et al.*, Chem. Phys. Lett. **62** (1979) 283.

BL8B2

ARUPS of Diabenzo-Crown Ether Thin Film on HOPG

K. K.Okudaira[1], T. Hosokai[2], Y. Suzuki[1], S. Kera[1], N. Ueno[1]

[1]*Association of Graduate Schools of Science and Technology, Chiba Univererity,1-33 Yayoi-cho Inage-ku, Chiba 263-8522, Japan*

[2]*Graduate School of Science and Technology, Chiba Univererity,1-33 Yayoi-cho Inage-ku, Chiba 263-8522, Japan*

Introduction

Crown ethers, which consist of flexible oligo-ethers, have remarkable properties of recognizing and binding specific metal atoms, and thus have potential for use in molecular mechanics. [1] In particular, dibenzo-18-crown-6(2,3,11,12–dibenzo-1,4,7,10,13,16- hexaoxacyclo- octadeca- 2,11-diene) (DB18C6), forms a self-organized two-dimensional structure of a Au(111) substrate in $HClO_4$ solution. [2] The DB18C6 has a non-planar and flexible molecular structure, shown in Fig.1.

In this study, we report the results of angle resolved ultraviolet photoelectron spectra (ARUPS) of DB18C6 thin films on HOPG to determine the molecular orientation of DB18C6 thin films quantitatively.

Experimental

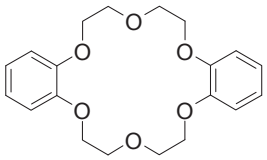

Fig. 1. Molecular structure of DB18C6.

ARUPS measurements were performed at the beam line BL8B2 of the UVSOR storage ring at the Institute for Molecular Science. The take-off angle (θ) dependencies of photoelectron spectra were measured at grazing incidence (incident angle of photon (α) = 70° with the photon energy of 20 eV.
The thin films were prepared in the preparation chamber by vacuum evaporation onto HOPG surfaces which were cleaved under an ultrahigh vacuum. The deposition rate was smaller than 0.1nm /min..

Results and Discussion

The θ dependencies of ARUPS spectra of about 2nm thick film at the binding energy region of 0-5 eV are shown in Fig. 2, where three bands A, B, and C appear. From the comparison of the results of molecular orbital calculation, band A and B are ascribed to the π-orbitals of benzene rings, and band C are n(O) localized at an ether ring.[3] The intensity of the band A, B and C depends on θ, while the energy positions of these bands do not.

The band A, B, and C intensities show characteristic θ dependencies (Fig.3), which reflect the molecular orientation of DB18C6 thin films on HOPG. To determine the molecular orientation quantitatively, it needs to compare the observed θ dependencies with the calculated ones.

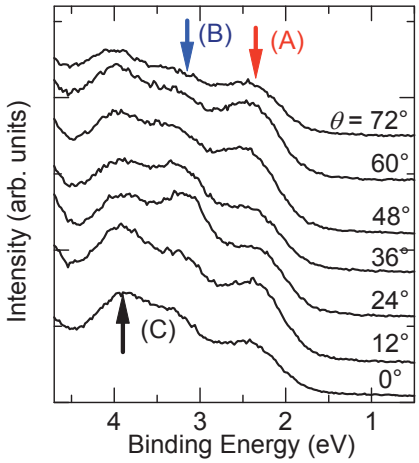

Fig. 2. Take-off angle dependence of ofDB18C6 (three arrows indicate the peak position of A, B, and C).

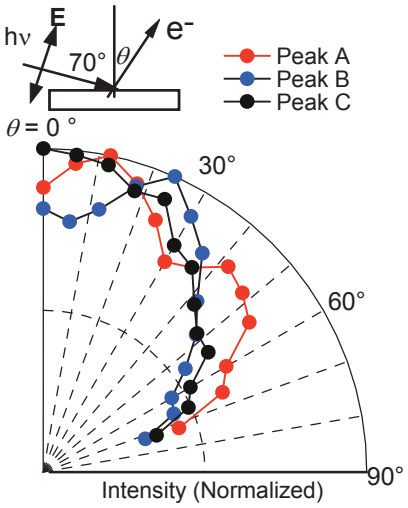

Fig. 3. Take-off angle (q) dependencies of photoelectron intensities of peak A (●), B(●), and C(●).

[1] C. J. Pedersen, J. Am, Chem. Soc. **89** (1976)2495.
[2] A. Ohira, M. Sakata, C. Hirayama, M. Kuntake, Org. Biomol. Chem. **1** (2003) 251.
[3] T. Hosoaki, H. Horie, T. Aoki, S. Nagamatsu, S. Kera, K. K. Okudaira, N. Ueno, J. Phys. Chem. C, *to be published*.

BL8B2

Electronic Structure of Molecular Crystal with CN-I Interaction

R. Sumii[1,2], K. Kanai[2], K. Seki[3]

[1]*Institute of Materials Structure Science, High Energy Accelerator Research Organization, Tsukuba, Ibaraki 305-0801, Japan*

[2]*Research Center for Materials Science, Nagoya University, Nagoya 464-8602, Japan*

[3]*Department of Chemistry, Nagoya University, Nagoya 464-8602, Japan*

Introduction

Some halogen containing molecules, such as *p*-iodo- benzonitrile (*p*-IBN) (Fig. 1(a)), are known to show strong intermolecular interaction. *p*-IBN molecule has a simple structure with I and CN at the opposite sides of a benzene ring. In the crystal, the *p*-IBN molecules form straight chains with CN-I distance nearly 7% shorter than the sum of the van der Waals radii [1]. Thus we can expect that interesting phenomena such as intermolecular charge transfer and anisotropic electrical conductivity may occur in crystals with such CN-I interaction. However, there have been little studies of the electronic structure and electrical properties. The main reason may be sublimation by high vapor pressure in vacuum condition required in such studies and the dissociation of the I-C bond at the contact with clean metal surface.

To solve these problems, in this work we chose a new compound 4-cyano-4'-iodobiphenyl (CIB) and studied the electronic structure of the vacuum deposited thin film by ultraviolet photoemission spectroscopy (UPS). In CIB molecule, the benzene ring of *p*-IBN is substituted with biphenyl (Fig. 1(b)). Like *p*-IBN, the distance between the CN-I is about 5 % shorter than the sum of van der Waals radii and the crystal structure contains straight chains [2]. Moreover, the molecular weight is heavier than *p*-IBN, hindering the sublimation in vacuum. For suppressing possible dissociation by the contact with metal substrate, we used GeS (001) which is an inactive substrate.

(a) p-IBN

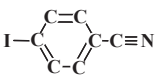

(b) CIB

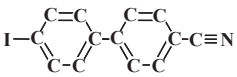

Fig. 1. Molecular structures of IBN and CIB.

Experimental and Theoretical

The CIB film was deposited on a clean GeS (001) surface obtained by cleaving in the vacuum chamber. UPS measurements were performed at BL-8B2 of the UVSOR facility. Molecular orbital (MO) calculations were performed by density functional theory with Gaussian98 package using a B3LYP / 3-21G** basis set.

Results and Discussion

The observed spectra of CIB on GeS (001) and the simulated spectra based on the MO calculations are shown in Fig. 2. In the experimental results, the HOMO at around 3 eV shifts to low binding energy as the film thickness increases,. This shift is well reproduced by MO calculations for molecular chains with increasing length from monomer to tetramer, simulating the formation of crystal structure. For the dimmer, calculations were also performed for various CN-I bond lengths.

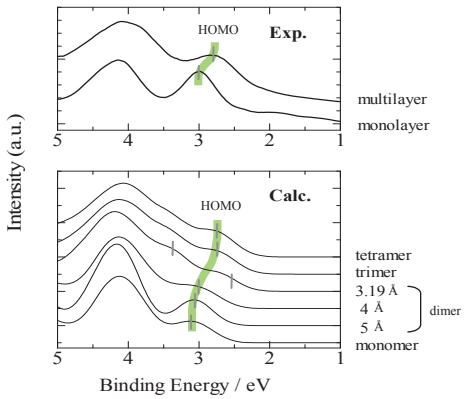

Fig. 2. Experimentally observed UPS spectra and the simulated spectra by the MO calculations for CIB.

Such good correspondence between the observed spectra and the results of MO calculations indicate that the HOMO shift is due to the intermolecular interaction through the CN-I contact. As the detailed mechanism, the HOMO with large component at the iodine is pushed up by the negative charge at the CN part in the neighboring molecule (Fig. 3).

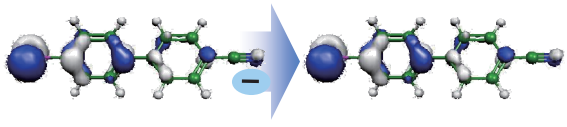

Fig. 3. Unstabilization of the HOMO by the negative charge at the CN group of the neighboring molecule .

[1] E. O. Schlemper, Acta. Cryst. **18** (1965) 419.
[2] D.Britton, Acta. Cryst. **C47** (1991) 2127.

BL8B2

Photoelectron Spectroscopy Study of Photochromic Diarylethene Film

S. Tanaka[1], M. Toba[2], T. Nakashima[2], T. Kawai[2], K. Yoshino[3]

[1]*Center of Integrated Research in Science, Shimane University, Matsue 690-8504, Japan*

[2]*Graduate School of Materials Science, Nara Institute of Science and Technology, NAIST, Ikoma, Nara 630-0192, Japan*

[3]*Shimane Institute for Industrial Technology, Matsue, Shimane 690-0816 Japan*

Photochromic molecules have attracted much attention as a promising material for photonic devices. Photochromism is defined as the reversible transformation between two isomers having different absorption spectra by photoirradiation.[1)] In addition, the geometry and electronic structures in two isomers of the photochromic molecules are also different. The differences in the geometry and the electronic structure relate to the difference in the molecular properties, such as refractive index, fluorescence efficiency, conductivity and magnetism reference. These photoresponsive variations of the molecular properties can be useful for the application to various optoelectronic devices. Among the various photochromic materials, diarylethenes with heterocyclic aryl groups are of particular interest for applications to optoelectronic devices because of their high fatigue resistance and good thermal stability [1]. 1,2-Bis(5-(2,4-diphenylphenyl)-2,4-dimethyl-3-thienyl) perfluorocyclopentene (DAE) is a dithienylethene derivative having bulky substituents [2]. DAE shows blue coloration upon UV light irradiation, and the blue color disappears upon visible (λ□> 450 nm) light irradiation. It is known that DAE undergoes ring cyclization and cycloreversion reactions upon alternate irradiation with UV and visible light (Fig. 1). Hereafter, open-DAE and close-DAE refer to the open- and the closed-ring form isomers, respectively.

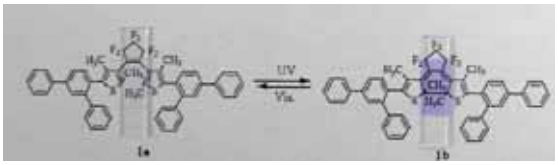

Fig. 1. Molecular structures of open-ring isomer of DAE (left) and closed-ring isomer of DAE (right). The arrows indicate the reversible electrocyclic reaction upon alternate irradiation with UV and visible light.

In this study, the electronic structure of the DAE thin film is revealed using photoelectron spectroscopy. The photoelectron spectra of open- and close-DAE showed clear differences in the density of states around the highest occupied molecular orbital (HOMO). The energy levels of each of the DAE molecules were calculated by the density functional theory (DFT) and it showed good correlation with the photoelectron spectra [3].

The vacuum-deposited DAE film was investigated by photoelectron spectroscopy. The structure of the as-deposited DAE film was considered amorphous. Figure 2 shows the photoelectron spectra of DAE after UV light irradiation (red) and under laser light irradiation (black). The UV lamp was used to induce a coloration of the DAE film. The majority state of the DAE molecule after UV light irradiation was able to assume close-DAE. In the red-line spectrum, a peak that appeared at around 1.5 eV was considered as the photoelectron from HOMO of close-DAE. The black-line in Fig. 2 is a photoelectron spectrum of the DAE under laser light irradiation, where the majority state was considered as open-DAE. It is obvious that the signal intensity around 1.5 eV was decreased compared with the red-line. The spectrum shape around 2 - 4 eV also showed a clear difference. The signal intensity at around 3 eV in the black-line spectrum was larger than that in the red-line spectrum. The appearance and the disappearance of the HOMO peak at 1.5 eV showed good relationship with UV and laser light irradiation, respectively. These variations in the spectra are attributed directly to the photoresponsive change in the electronic structure of DAE.

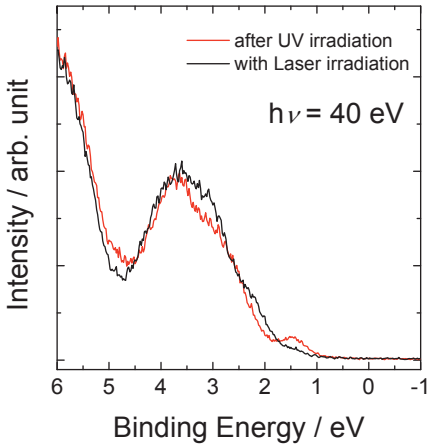

Fig. 2. Photoelectron spectra of DAE.

[1] M. Irie, Chem. Rev. **100** (2000) 1685.
[2] M.-S. Kim, T. Sakata, T. Kawai, M. Irie, Jpn. J. Appl Phys. **42** (2003) 3676.
[3] S. Tanaka, M. Toba, T. Nakashima, T. Kawai, K. Yoshino, Jpn. J. Appl. Phys. **47** (2008) 1215.

BL8B2

Intermolecular Energy Band Dispersion in Highly Ordered Pentacene Multilayer Films on Cu(110)

H. Yamane[1], E. Kawabe[1], R. Sumii[2], K. Kanai[2], Y. Ouchi[1], K. Seki[1]
[1]*Department of Chemistry, Nagoya University, Nagoya 464-8602, Japan*
[2]*Research Center for Materials Science, Nagoya University, Nagoya 464-8602, Japan*

Introduction

The energy band dispersion, $E(\boldsymbol{k})$, is a fundamental basis for understanding charge transport mechanisms of solids. In the field of organic solids, there are two types of band dispersion; the *intra-* and *inter-*molecular band dispersions. In particular, the issue of intermolecular band dispersion is attracting growing attention due to the needs of the interpretation of the charge transport mechanism in (opto)electronic devices using organic semiconductors such as field effect transistors. It is reported that molecules of pentacene (Pn), a high hole mobility material, deposited on Cu(110) in the multilayer regime (more than 10 nm) form a highly ordered structure with an upright-standing orientation, which is virtually identical to the herringbone orientation for Pn films on quartz or polyester substrates [1]. In this work, in order to understand the hole transport mechanism in Pn films, we studied the electronic structure of the highly ordered upright-standing Pn multilayer film on Cu(110) by using angle-resolved UV photoemission spectroscopy (ARUPS).

Experiment

The highly ordered Pn multilayer film was prepared on the clean Cu(110) surfaces in accordance with the sample preparation described in Ref 1.

The photoelectron takeoff angle (θ) dependence of ARUPS spectra was measured at the photon energy of 20 eV, the photon incidence angle of 60° from the surface normal, and the temperature of 300 K.

Results and Discussion

Figures 1(a) and (b) shows the θ dependence of the ARUPS spectra for the 11-nm-thick Pn multilayer film with the upright-standing orientation along (a) the $\bar{\Gamma}$–$\bar{X}_{Pn}$ direction (ϕ = 0°), and (b) the $\bar{\Gamma}$–$\bar{Y}_{Pn}$ direction (ϕ = 90°). At θ = 0°, the topmost peak consists of two prominent components with an energy separation of 0.5 eV (labelled H_1 and H_2 in Fig. 1, respectively). This lineshape shows continuous change with θ. At ϕ = 0°(90°), H_1 shifts to the high E_b side until θ reaches 18°(12°), and turns to the low E_b side until θ reaches 34°(26°). Such a dispersive behaviour can also be seen in H_2. As shown in Fig. 1 (c) and (d), the observed shifts can be explained as the reflection of the two-dimensional intermolecular band dispersion using the unit cell of the upright-standing Pn multilayer film on Cu(110) [2], which was obtained from the previous structural studies [1].

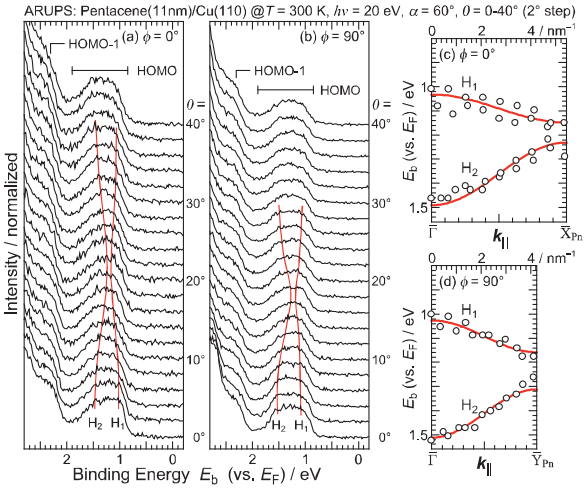

Fig. 1. (a,b) Photoelectron takeoff angle (θ) dependence of the ARUPS spectra for the highly ordered upright-standing Pn multilayer film on Cu(110) measured at ϕ = (a) 0° and (b) 90°. The abscissa is the binding energy (E_b) relative to the Fermi level (E_F) of the substrate, and ordinate is the intensity of the photoelectron, normalized by the incident photon flux. (c,d) $E(\boldsymbol{k}_{\|})$ relation for the highly ordered upright-standing Pn multilayer film on Cu(110) at ϕ = (c) 0° and (d) 90°. The abscissa is the parallel component of the momentum ($\boldsymbol{k}_{\|}$), and ordinate is the E_b relative to the E_F of the substrate.

From the observed $E(\boldsymbol{k}_{\|})$ relation, one can see that the phase of the dispersion for band H_1 is opposite to that for band H_2, and that the size of the dispersion of bands H_1 and H_2 are about 150 and 240 meV, respectively, for both azimuths within the present total energy resolution of 100 meV at 300 K. Since the uppermost band H_1 seems to form a free-electron-like parabolic dispersion, we estimated the effective mass m_h^* to be $3.02m_0$ ($\bar{\Gamma}$–$\bar{X}_{Pn}$) and $1.86m_0$ ($\bar{\Gamma}$–$\bar{Y}_{Pn}$) at 300 K. This result demonstrates the presence of the anisotropy of the hole mobility in Pn crystals also at higher temperatures as suggested by Wijs *et al.* [3].

[1] S. Söhnchen *et al.*, J. Chem. Phys., **121** (2004) 525.
[2] H. Yamane *et al.*, Phys. Stat. Sol. (b), **245** (2008) 793.
[3] G. A. de Wijs *et al.*, Synth. Met., **139** (2003) 109.

BL8B2

Organic/Metal Interface State: Broadening and Splitting Behaviors of Molecular Energy Levels

H. Yamane[1], E. Kawabe[1], R. Sumii[2], K. Kanai[2], Y. Ouchi[1], K. Seki[1]
[1]*Department of Chemistry, Nagoya University, Nagoya 464-8602, Japan*
[2]*Research Center for Materials Science, Nagoya University, Nagoya 464-8602, Japan*

Introduction

The electronic structure at organic(O)/metal(M) interfaces plays a crucial role in the performance of organic electronic devices. In particular, the energies of the highest-occupied and lowest-unoccupied molecular orbital (HOMO and LUMO) levels relative to the Fermi level (E_F) of metals are of fundamental importance in discussing the barrier heights for the charge injection and separation at O/M interfaces. This is still an issue of open question since the interfacial electronic structure is usually modified by various interface-specific phenomena. For deeper understanding of the O/M interface energetics, one of the keys is the elucidation and control of the interface state near E_F, which may dominate the energy level alignment at the interface.

In this work, we studied the electronic structure of various pentacene (Pn) monolayers grown on Au(111), Cu(111), Cu(100), and Cu(110) surfaces using angle-resolved UV photoemission spectroscopy (ARUPS). We observed the evidences of the formation of the interface state, which depends on the type of the metal and its surface structure.

Experiment

All Pn monolayers were prepared on the clean metal surfaces at the temperature of about 500 K, which realizes the formation of flat-lying Pn monolayers. The ARUPS measurements were performed at the surface temperature of 300 K at the photon energy of 20 eV and the photon incidence angle of 60°.

Results and Discussion

Figure 1 shows the ARUPS spectra for the various Pn/metal interfaces as functions of (a) the takeoff angle or (b) the azimuthal angle. For the disordered Pn/Au(111) interface (a1), the Pn-induced peak appears at E_b of 0.96 eV with the linewidth of 0.5 eV, which is slightly broader than that for the Pn/graphite interface of 0.3 eV (not shown), which can be ascribed to the molecular level broadening due to weak O-M interaction [Fig. 1(c1)]. On the other hand, the Pn-induced electronic structure on Cu(111) (a2) is rather different from that on Au(111): the Pn-induced peaks on Cu(111) appear at E_bs of 0.72 and 1.34 eV. These peaks can be ascribed to the molecular levels split due to the hybridization of the molecular orbitals with the substrate wavefunction [Fig. 1(c2)] [1,2], which can modify the energies and orbital symmetries. Such a behavior is observed also for the Pn/Cu(100) (b1) and the Pn/Cu(110) (b2) interfaces. Furthermore, at the single-domain Pn/Cu(110) interface, the resultant split levels show dispersive behavior [2]. This originates from (i) highly ordered film structure and (ii) the intermolecular interaction via the metal substrate due to the hybridization at the interface.

These factors (c1) and (c2) may be dominated by the different O-M bonding distance at the interface, and we consider that the Pn-Cu bonding distance is probably shorter than the Pn-Au bonding distance.

[1] A. Ferretti *et al.*, Phys. Rev. Lett., **99** (2007) 46802.
[2] H. Yamane *et al.*, Phys. Rev. B, **76** (2007) 165436.

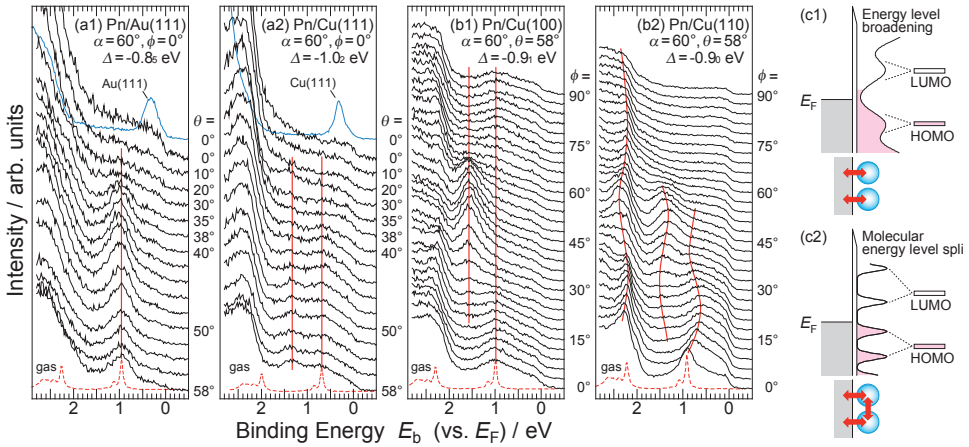

Fig. 1. ARUPS spectra as a function of (a) takeoff angle (θ) and (b) azimuthal angle (ϕ) measured for (a1) the disordered Pn/Au(111) interface, (a2) the disordered Pn/Cu(111) interface, (b1) the multi-domain Pn/Cu(100) interface, and (b2) the single-domain Pn/Cu(110) interface. (c) Possible origins of the interface state: (c1) energy level broadening due to the weak M-O interaction, (c2) energy level splitting due to the hybridization of the molecular orbital with the substrate wavefunction. The vacuum level shift upon adsorption (Δ) is also shown.

BL8B2

Modification of Shockley-Type Surface State and Formation of Charge Transfer State at ZnPc/Cu(111) Interface

H. Yamane[1], K. Kanai[2], Y. Ouchi[1], K. Seki[1]
[1]*Department of Chemistry, Nagoya University, Nagoya 464-8602, Japan*
[2]*Research Center for Materials Science, Nagoya University, Nagoya 464-8602, Japan*

Introduction

The electronic structure at interfaces formed by an organic semiconductor film with a metal electrode is of fundamental importance in discussing the Schottky barrier heights such as the highest-occupied and lowest-unoccupied molecular orbital (HOMO and LUMO) levels at organic-devices interfaces. However, the energetics of organic devices has not yet been understood systematically. To clarify the possibly complicated electrical and structural phenomena at organic/metal interfaces, a more pertinent approach to this issue would be to use a well-characterized system in quantitative electron spectroscopic measurements.

In this work, we studied the electronic structure of thin films of zinc-phthalocyanine (ZnPc), one of the archetypal organic semiconductor, grown on Cu(111) using angle-resolved UV photoemission spectroscopy (ARUPS). We observed the distinctive electronic structure induced by the charge transfer (CT).

Experiment

The ARUPS measurements were performed at the surface temperature of 300 K at the photon energy of 20 eV and the photon incidence angle of 60°.

We obtained a saturated ZnPc monolayer by heating the 5-nm ZnPc film at 700 K; the ARUPS spectra for the heated film shows nearly the same characteristic to that for the 0.3-nm film.

Results and Discussion

Figure 1 shows the film thickness dependence of the ARUPS spectra for the ZnPc/Cu(111) system. In the energy window A, just below the Fermi level (E_F) at around the surface normal (θ = 0°), the Shockley-type surface state of Cu(111) survived even upon formation of the ZnPc monolayer. From the takeoff angle dependence of the ARUPS spectra, we found that the characteristics of the surviving surface state are modified from that of the original one in the peak position at the $\bar{\Gamma}$ point (0.39 → 0.18 eV), Fermi wavelength k_F (2.07 → 2.23 nm^{-1}), and the effective mass m^* (0.42m_0 → 1.08m_0). The adsobate-induced modification of the surface state has been reported for the adsorption of rare gases [1] and a large energy-gap (~ 9 eV) molecule of *n*-alkane (*n*-$C_{44}H_{90}$) [2]. The observed modification of the surface state upon the ZnPc adsorption, which is slightly different from the previous observations [1,2], may be dominated by the combination of (1) the push back (Pauli repulsion) of the surface electrons and (2) the CT between the molecule and the substrate.

For the 1-ML ZnPc spectra at the surface off-normal ($\theta \geq 38°$), one can see two-prominent peaks labelled B and C in Fig. 1. With increasing the film thickness, peak B shifts gradually to higher binding energy side probably due to the change in (i) the final state screening and (ii) the molecular orientation [3], and the intensity of peak C decreases rapidly. Judging from the thickness dependence of the ARUPS spectra, peak B is ascribed to the (original) HOMO-derived level, and peak C may be ascribed to the CT state.

The formation of the CT state at the ZnPc/Cu(111) interface is unexpected just by considering the ionization energy and the electron affinity of the ZnPc solid and the work function of the Cu(111) substrate of I_s = 5.2 eV, A_s = 3.3 eV, and Φ_m = 4.9 eV, respectively, which were obtained from our UPS and inverse photoemission spectroscopy experiments (see Fig. 1). For the origin of the CT state, one has to consider (i) the molecular energy level broadening due to organic-metal interaction and (ii) the change in the intermolecular polarization energy due to the presence of the CT-induced dipole. Since the bonding distance at the interface would be a key for further consideration on the interfacial electronic structure of ZnPc/Cu(111), we will perform the X-ray standing wave experiment for the ZnPc/Cu(111) system at ESRF (Grenoble, FRA).

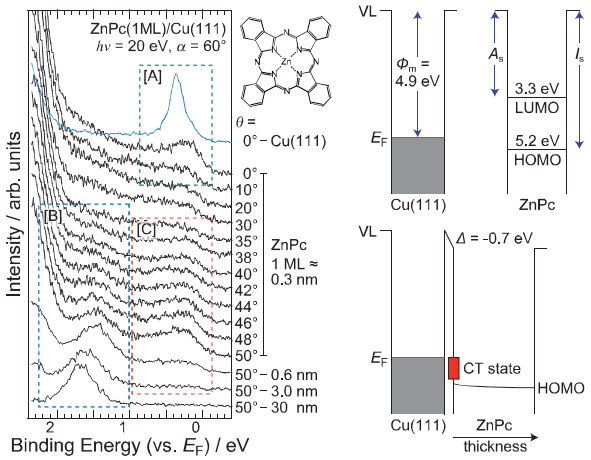

Fig. 1. Film thickness dependence of the ARUPS spectra for the ZnPc/Cu(111) system (left) and the energy level diagrams of the Cu(111) substrate, the ZnPc solid, and the ZnPc/Cu(111) system (right).

[1] F. Reinnert, J. Phys.: Cond. Matter, **15** (2003) S693.
[2] K. Kanai *et al.*, Phys. Rev. B, submitted.
[3] H. Yamane *et al.*, J. Appl. Phys., **99** (2006) 93705.

FEL

Asymmetric Synthesis and Decomposition of Amino Acids by Using UVSOR-FEL

K. Kobayashi[1], T. Ogawa[1], S. Shima[1], T. Kaneko[1], H. Mita[2], J. Takahashi[3], M. Hosaka[4], M. Kato[5]

[1]*Graduate School of Engineering, Yokohama National University, Yokohama 240-8501, Japan*
[2]*Faculty of Engineering, Fukuoka Institute of Technology, Fukuoka 811-0295, Japan*
[2]*NTT Microsystem Integration Laboratory, Atsugi243-0198, Japan*
[3]*Graduate School of Engineering, Nagoya University, Nagoya 464-8601, Japan*
[4]*Masahiro Kato, Institute for Molecular Science, Okazake 444-8585, Japan*

Introduction

The Origin of homochirality of biological molecules such as amino acids has remained one of the most important problems in the field of origins of life and astrobiology. Cronin and Pizzarello reported that some amino acids extracted from carbonaceous chondrites showed significant enantiomeric excesses of L-isomers [1]. Isovaline, a non-proteinous amino acid without a-hydrogen atom, was included in such category of amino acids (Fig. 1). One of the possible scenario for the generation of enantiomeric excesses of amino acids are asymmetric formation or decomposition of amino acids by circular polarized light in space. Bailey found circular polarized light of IR range in space [2]. Takano *et al*. reported that enantiomeric excess of alanine was formed after irradiation of amino acid precursors with UV-CPL [3]. Here we examine decomposition of isovaline by irradiation with UV-CPL from UVSOR-free electron laser (FEL). We also studied possible introduction of chirality to amino acids in thin films by UV-CPL irradiation.

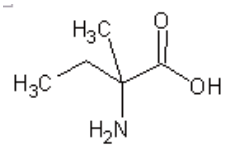

Fig. 1. Isovaline

Experimental

Aqueous solution of isovaline in a quartz cell was irradiated with UV-CPL (Fig. 2): After either R- or L-UV-CPL (wavelength: 216-230 nm) was irradiated, amino acids and amines in resulting products were analyzed by cation-exchange HPLC (Shimadzu LC-10A), and carboxylic acids were determined by capillary electrophoresis (Photal CAPI-3300). D/L ratio of amino acids was measured by reversed-phase HPLC after AQC derivatization (Tosoh DP-8020).

Isovaline aqueous solution was also irradiated with high-energy heavy ions (290 MeV/u carbon ions from HIMAC, NIRS, Japan) or X-rays (6 keV, 27B line of Photon Factory, KEK, Japan).

Thin film of phenylalanine was made by vacuum deposition on an MgF_2 substrate. The film was irradiated with D- or L-CPL. CD spectra were measured after irradiation.

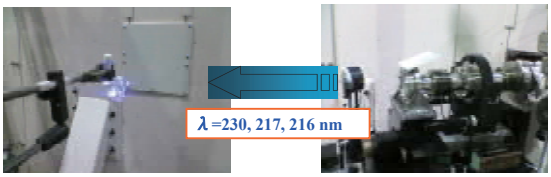

Fig. 2. UV-CPL irradiation of isovaline solution

A gaseous mixture of carbon monoxide, ammonia and water was also irradiated with UV-CPL to examine possible formation of amino acid precursors. The resulting product was acid-hydrolyzed, and amino acids were determined by HPLC (Shimadzu LC-10A).

Results and Discussion

When isovaline solution was irradiated with UV-CPL, isovaline was decomposed: Alanine was found as predominant amino acid products, and 2-butylamine and isovaleric acid were also detected. The release of methyl group, carboxylic group, or amino group from isovaline was specific to UV irradiation, since X-rays or heavy ions irradiation of isovaline solution did not give them as major products. Enantiomeric excesses of isovaline or alanine were not detected in the present experiments. As pH of the solution might be important for asymmetric decomposition, we plan to irradiate isovaline solution in acidic/basic conditions.

When phenylalanine thin films were irradiated L- or R-CPL, the resulting films showed apparent CD spectra at 200 nm and 220 nm. They seem to correspond to π-π* and n-π* transitions, individually. It was proved that CPL irradiation introduced chirality to thin film of aromatic amino acids.

Amino acids were formed by UV-CPL irradiation of the gas mixture: Glycine was predominant, followed by alanine. G-value of glycine was 0.0012, which was smaller than that by proton irradiation or that with UV light from D_2 lamp.

[1] J. R. Cronin, S. Pizzarello, Science **275** (1997) 951.
[2] J. A. Bailey *et al*., Science **281** (1998) 672.
[3] Y. Takano *et al.*, Earth Planet. Sci. Lett. **254** (2007) 106.

List of Publications 2007

T. Awano
Far-Infrared and Millimeter of Wave Spectroscopy of Superionic Copper Conductors
Infrared Phys.Tech. **51** (2008) 458.

S. Bielawski, C. Evain, T. Hara, M. Hosaka, M. Katoh, S. Kimura, A. Mochihashi, M. Shimada, C. Szwaj, T. Takahashi, Y. Takashima
Tunable Narrowband Terahertz Emission from Mastered Laser-Electron Beam Interaction
Nat. Phys. **4** (2008) 390.

K. Chong, T. Hirai, T. Kawai, S. Hashimoto, N. Ohno
Optical Properties of Bi^{3+} Ions Doped in $NaYF_4$
J. Lumin. **122-123** (2007) 149.

M. Fujita, M. Itoh, S. Takagi, T. Shimizu, N. Fujita
Comparative Study of Optical Spectra and Electronic Structures of Ca MoO_4 and $CaWO_4$ Crystals
Phys. Stat. Sol. (b) **243** (2006) 1898.

G. Funabashi, H. Fujiwara, A. Sekiyama, M. Hasumoto, T. Ito, S. Kimura, P. Baltzer, S. Suga
Ultrahigh-Resolution Vacuum Ultraviolet Light Source System for Extremely Low Energy Photoelectron Spectroscopy
Jpn. J. Appl. Phys. **47** (2008) 2265.

D. Fukamaki, T. Takeuchi, K. Soda, M. Hasegawa, U. Mizutani, H. Sato
Electronic Structure and Phase Stability of the Pd-Based Metallic Glass
J. Jpn. Soc. Powder Powder Metalluragy **54** (2007) 754.

M. Hasegawa, T. Takeuchi, K. Soda, H. Sato, U. Mizutani
Electronic Structure and Phase Stability of Glassy Alloys
Mater. Sci. Forum **539-543** (2007) 2048.

M. Hasegawa, K. Soda, H. Sato, T. Suzuki, T. Taketomi, T. Takeuchi, H. Kato, U. Mizutani
Stability and Electronic Structure of Zr-Based Ternary Metallic Glasses and Relevant Compounds
J. Alloys and Compd. **434-435** (2007) 149.

S. Hino, M. Kato, D. Yoshimura, H. Moribe, H. Umemoto, Y. Ito, T. Sugai, H. Shinohara, M. Otani, Y. Yoshimoto, S. Okada
Effect of Encapsulated Atoms on the Electronic Structure of the Fullerene Cage: A Case Study on $La_2@C_{78}$ and $Ti_2C_2@C_{78}$ Via Ultraviolet Photoelectron Spectroscopy
Phys. Rev. B **75** (2007) 125418.

T. Hirai, K. Maeda, M. Yoshida, J. Kubota, S. Ikeda, M. Matsumura, K. Domen
Origin of Visible Light Absorption on GaN-Rich $(Ga_{1-X}Zn_X)(N_{1-X}O_X)$ Photocatalysts
J. Phys. Chem. C **111**(2007) 18853.

T. Hirai, S. Hashimoto, S. Sakuragi, N. Ohno
4f-5d Absorption of Gadolinium Ions on Sodium Gadolinium Tetrafluorides
Chem. Phys. Lett. **446** (2007) 138.

T. Hirai, H. Yoshida, S. Sakuragi, S. Hashimoto, N. Ohno
Transfer of Excitation Energy from Pr^{3+} to Gd^{3+} in YF_3:Pr^{3+}, Gd^{3+}
Jpn. J. Appl. Phys. **46** (2007) 660.

T. Ito, H. Kato, Y. Ohki
Mechanisms of Several Photoluminescence Bands in Hafnium and Zirconium Silicates Induces by Ultraviolet Photons
J. Appl. Phys. **99** (2006) 094106.

M. Itoh, S. Takagi, M. Kitaura, M. Fujita, N. Endo
Luminescence Properties of Piezoelectric Single Crystals with Langasite Structure
J. Lumin. **122-123** (2007) 205.

B. P. Kafle, H. Katayanagi, M. S. I. Prodhan, H. Yagi, C. Huang, K. Mitsuke
Absolute Total Photoionization Cross Section of C_{60} in the Range of 25-120eV: Revisited
J. Phys. Soc. Jpn. **77** (2008) 014302.

T. Kamikake, M. Imamura, Y. Murase, A. Tanaka, H. Yasuda
Electronic Structures of Alkyl-Passivated Si Nanoparticles: Synchrotron-Radiation Photoemission Study
Trans. Mat. Res. Soc. Jpn. **32** (2007) 433.

M. Kamohara, Y. Izumi, M. Tanaka, K. Okamoto, K. Nakagawa
The Optical Oscillator Strength Distribution of Amino Acids from 3 to 250 eV and Examination of the Thomas-Reiche-Kuhn Sum Rule
Rad. Phys. Chem. (2008) *(in press)*.

K. Kanda, J. Igaki, Y. Kato, R. Kometani, A. Saikubo, S. Matsui
NEXAFS Study on Carbon-Based Material Formed by Focused-Ion-Beam Chemical-Vapor-Deposition
Rad. Phys. Chem. **75** (2006) 1850.

S. Kera, H. Yamane, H. Fukagawa, T. Hanatani, K. K. Okudaira, K. Seki, N. Ueno
Angle-Resolved UV Photoelectron Spectroscopy of Titanyl Phthalocyanine Monolayer Film on Graphite
J. Electron Spectrosc. Relat. Phenom. **156-158** (2007) 135.

S. Kimura, H. Im, T. Mizuno, S. Narazu, E. Matsuoka, T. Takabatake
Infrared Study on the Electronic Structure of the Alkaline-Earth-Filled Skutterudites AM_4Sb_{12} (A=Sr, Ba; M=Fe, Ru, Os)
Phys. Rev. B **75** (2007) 245106.

S. Kimura, N. Kimura, H. Aoki
Low-Energy Electrodynamics of Heavy Quasiparticles in $ZrZn_2$
J. Phys. Soc. Jpn. **76** (2007) 084710.

S. Kimura, T. Mizuno, K. Matsubayashi, K. Imura, H. S. Suzuki, N. K. Sato
Infrared Study on the Electronic Structure of SmS in the Black Phase
Physica B **403** (2008) 805.

M. Kitaura, Y. Nakajima, M. Kaneyoshi, H. Nakagawa
Effect of Zr^{4+} Addition on Photoluminescence Properties of YPO_4:Mn^{2+}
Jpn. J. Appl. Phys. **46** (2007) 6691.

E. Kobayashi, K. Mase, A. Nambu, J. Seo, S. Tanaka, T. Kakiuchi, K. Okudaira, S. Nagaoka, M. Tanaka
Recent Progress in Coincidence Studies on Ion Desorption Induced by Core Excitation
J. Phys.: Condens. Matter **18** (2006) S1389.

H. Kobayashi, S. Emura, Y. Arachi, K. Tatsumi
Investigation of Inorganic Compounds on the Surface of Cathode Materials Using Li and O K-edge XANES
J. Power Sources **174** (2007) 774.

H. Kobayashi, Y. Arachi, S. Emura, K. Tatsumi
Investigation on Lithium De-Intercalation Mechanism for $LiNi_{0.45}Mn_{0.45}Al_{0.1}O_2$
Solid State Ionics **178** (2007) 1101.

H. Kobayashi, M. Shikano, S. Koike, H. Sakaebe, K. Tatsumi
Investigation of Positive Electrodes after Cycle Testing of High-Power Li-Ion Battery Cells I. An Approach to the Power Fading Mechanism Using XANES
J. Power Sources **174** (2007) 380.

M. Labat, C. Bruni, G. Lambert, M. Hosaka, M. Shimada, M. Katoh, A. Mochihashi, Y. Takashima, T. Hara, M. E. Couprie
Local Heating Induced by Coherent Harmonic Generation on Electron Beam Dynamics in Storage Ring
Europhys. Lett. **81** (2008) 34004.

Y. S. Lee, Y. Tokunaga, T. Arima, Y. Tokura
Change in Optical Anisotropy with Rotation of Orbital Stripe in a Half-Doped Bilayer Manganite
Phys. Rev. B **75** (2007) 174406.

Y. S. Lee, T. Arima, S. Onoda, Y. Okimoto, Y. Tokunaga, R. Mathieu, X. Z. Yu, J. P. He, Y. Kaneko, Y. Matsui, N. Nagaosa, Y. Tokura
Correlation of Electronic Structure and Ordered Charge and Orbital Patterns for Single-Layered Manganites in a Wide Hole-Doping Range ($0 < x < 1$)
Phys. Rev. B **75** (2007) 144407.

K. Matsubayashi, K. Imura, H.S. Suzuki, T. Mizuno, S. Kimura, T. Nishioka, K. Kodama, N. K. Sato
Effect of Single Crystal Composition on Electrical, Optical, Magnetic and Thermodynamic Properties of SmS
J. Phys. Soc. Jpn. **76** (2007) 064601.

K. Mitsuke, H. Katayanagi, B. P. Kafle, C. Huang, H. Yagi, M. S. I. Prodhan, Y. Kubozono
Relative Partial Cross Sections for Single, Double, and Triple Photoionization of C_{60} and C_{70}
J. Phys. Chem. A **111** (2007) 8336.

H. Miyazaki, T. Ito, S. Ota, M. Kato, S. Yagi, K. Soda, H. J. Im, S. Kimura
Angle-Resolved Photoemission Study on the Ferromagnetic Ordering of EuO Thin Films
Physica B **403** (2008) 917.

T. Miyazaki, D. Yoshimura, K. Okudaira
Ultraviolet Photoemission Study of Lithium Nickel Oxide: A Contact of Valence Band Structure and Selective Oxidation
Appl. Catalysis A: General **338** (2008)79.

H. Oakamura, T. Watanabe, N. Tsujii, T. Ebihara, T. Nanba
Mid-Infrared Absorption in Strongly Correlated Yb Compounds
Physica B **378-380** (2006) 756.

J. Onoe, T. Ito, S. Kimura, K. Ohno, Y. Noguchi, S. Ueda
The Valence Electronic Structure of a Peanut-Shaped C_{60} Polymer: In Situ High-Resolution Photoelectron Spectroscopic and Density-Functional Studies
Phys. Rev. B **75** (2007) 233410.

J. Onoe, Y. Ochiai, T. Ito, S. Kimura, S. Ueda, Y. Noguchi, K. Ohno
Electronic and Electron-Transport Properties of Peanut-Shaped C_{60} Polymers
J. Phys.: Conf. Ser. **61** (2007) 899.

J. Onoe, T. Ito, S. Kimura, K. Ohno
In Situ High-Resolution Valence Photoelectron Spectra of a Peanut-Shaped C_{60} Polymer
Eur. Phys. J. D **43** (2007) 141.

I. Ouchi, I. Nakai, M. Ono, S. Kimura
Features of Fluorescence Spectra of Polyethylene 2,6-Naphthalate Films
J. Appl. Polym. Sci. **105** (2007) 114.

A. Saikubo, K. Kanda, Y. Kato, J. Igaki, R. Kometani, S. Matsui
Angle-Dependent Measurement of Near Edge X-ray Absorption Fine Structure of Annealing Effect on Local Structure of Focused-Ion-Beam Chemical Vapor Deposition Diamond-Like Carbon
Jpn. J. Appl. Phys. **46** (2007) 7512.

Y. Sakurai, S. Kimura, K. Seki
Infrared Reflection-Absorption Spectroscopy of Alq_3 Thin Film on Silver Surface Using Synchrotron Radiation
Appl. Phys. Lett. **91** (2007) 061922.

M. Shimada, M. Katoh, S. Kimura, A. Mochihashi, M. Hosaka, Y. Takashima, T. Hara, T. Takahashi
Intense Terahertz Synchrotron Radiation by Laser Bunch Slicing at UVSOR-II Electron Storage Ring
Jpn. J. Appl. Phys. **46** (2007) 7939.

J. Sichelschmidt, S. Kimura, C. Krellner, C. Geibel, F. Steglich
Optical Properties of $YbRh_2Si_2$ and $YbIr_2Si_2$: a Comparison
Physica B **403** (2008) 775.

K. Soda, S. Ota, T. Suzuki, H. Miyazaki, M. Inukai, M. Kato, S. Yagi, T. Takeuchi, M. Hasegawa, H. Sato, U. Mizutani
Electronic Structure of Pd- and Zr-Based Bulk Metallic Glasses Studied by Use of Hard X-Ray Photoelectron Spectroscopy
AIP Conf. Proc. **879** (2007) 1821.

N. Tagami, M. Okada, N. Hirai, Y. Ohki, T. Tanaka, T. Imai, M. Harada, M. Ochi
Dielectric Properties of Epoxy/Clay Nanocomposites -Effects of Curing Agent and Clay Dispersion Method-
IEEE Trans. Dielectr. Electr. Insul. **15** (2008) 24.

A. Tanaka, R. Saito, T. Kamikake, M. Imamura, H. Yasuda
Optical and Photoelectron Spectroscopic Studies of Alkyl-Passivated Silicon Nanoparticles
Euro. Phys. J. D **43** (2007) 229.

A. Tanaka, T. Kamikake, M. Imamura, Y. Murase, H. Yasuda
Spectroscopic Characterization of Alkyl-Passivated Si Nanoparticles Synthesized by a Solution Route
Mater. Res. Soc. Symp. Proc. **958** (2007) 0958-L10-29.

T. Takeuchi, D. Fukamaki, H. Miyazaki, K. Soda, M. Hasegawa, H. Sato, U. Mizutani, T. Ito, S. Kimura
Electronic Structure and Stability of the Pd-Ni-P Bulk Metallic Glass
Mater. Trans. **48** (2007) 1292.

S. Tanaka, Y. Yoshida, M. Nonomura, K. Yoshino, I. Hiromitsu
Effect of Insertion of a Thin Bathocuproine Layer at Au/Zn-Phthalocyanine Interface on Energy Level Alignment and Morphology
Thin Solid Films **516** (2008) 1006.

S. Tanaka, M. Toba, T. Nakashima, T. Kawai, K. Yoshino
Photoelectron Spectroscopy Study of Photoresponsive Change in Electronic Structure of Amorphous Photochromic Diarylethene Film
Jpn. J. Appl. Phys. **47** (2008) 1215.

M. Yamaga, Y. Ohsumi, T. Nakayama, N. Kashiwagura, T. P. J. Han
Long-Lasting Phosphorescence in Ce-Doped Oxides
J. Mater. Sci. : Materials in Electronics (2008) *(in press)*.

H. Yamane, D. Yoshimura, E. Kawabe, R. Sumii, K. Kanai, Y. Ouchi, N. Ueno, K. Seki
Electronic Structure at Highly Ordered Organic/Metal Interfaces: Pentacene on Cu(110)
Phys. Rev. B **76** (2007) 165436.

H. Yamane, E. Kawabe, D. Yoshimura, R. Sumii, K. Kanai, Y. Ouchi, N. Ueno, K. Seki
Intermolecular Band Dispersion in Highly Ordered Monolayer and Multilayer Films of Pentacene on Cu(110)
Phys. Stat. Sol. (b), **245** (2008) 793.

H. Yoshida, K. Fujikawa, H. Toyoshima, S. Watanabe, K. Ogasawara
Luminescence Properties of $YAl_3(O_3)_4$ Substituted with Sc^{3+} Ions
Phys. Stat. Sol. (a) **203** (2006) 2701.

H. Yoshida, T. Yamazaki, H. Toyoshima, S. Watanabe, K. Ogasawara, H. Yamamoto
Experimental and Theoretical Investigations for Excitation Properties of $Ba_{1-x}Eu_xMgAl_{10}O_{17}$
J. Electro. Soc. **154** (2007) J196.

H. Yoshida, H. Toyoshima, S. Watanabe, K. Ogasawara, H. Yamamoto
P-202L: *Late-News Poster:* Luminescence and Excitation Properties of Host Lattice and Eu^{2+} Ions in $BaMgAl_{10}O_{17}:Eu^{2+}$ Phosphor
SID Symposium Digest of Technical Papers **38** (2007) 526.

T. Yoshida, S. Muto, T. Tanabe
Measurement of Soft X-Ray Excited Optical Luminescence of a Silica Glass
AIP conf. Proc. **882** (2007) 572.

T. Yoshida, S. Muto, J. Wakabayashi
Depth Selective Electronic State Analysis of Implanted Nitrogen in Visible-Light Response TiO_2 Photocatalyst
Mater. Sci. Forum **561-565** (2007) 567.

S. Yoshioka, F. Oba, R. Huang, I. Tanaka, T. Mizoguchi, T. Yamamoto
Atomic Structures of Supersaturated ZnO-Al_2O_3 Solid Solutions
J. Appl. Phys. **103** (2008) 014309.

(in Japanese)
H. Yamane, Y. Tanaka, E. Kawabe, K. Kanai, K. Seki
Elucidation and Control of Energy Level Alignment at Organic/Metal Interfaces
J. Surf. Sci. Soc. Jpn. **29** (2008) 99.

UVSOR Users Meeting

Place: Okazaki Conference Center

November 15, 2007

13:00 - 14:10	
Opening Remarks	S. Hino (Ehime Univ.)
Preface	N. Kosugi (UVSOR)
Present Status of UVSOR-II Accelerators	M. Katoh (UVSOR)
High-Resolution VUV ARPES Beamline BL7U	S. Kimura (UVSOR)
14:20 - 15:20	
A Project for Constructing a New Undulator Beamline BL6U	E. Shigemasa (UVSOR)
Evaluation of Higher Diffracted Light Contaminations in BL5B	F. Suzuki (Univ. Fukui)
Present Status of Application Experiments of the UVSOR-II FEL	M. Hosaka (Nagoya Univ.)
15:30 - 16:30	
Intense THz Coherent Synchrotron Radiation at UVSOR-II	M. Shimada (UVSOR)
Measurement of Photoabsorption Cross Sections of Fullerenes and Study on Their Photodissociation Dynamics at BL2B	H. Katayanagi (IMS)
How the Encapsulated Atoms Affect the Electronic Structure of the Fullerene Cages?	S. Hino (Ehime Univ.)
16:30 - 18:20 Poster Session	
18:30 Banquet	

November 16, 2007

9:00 - 10:00	
Optical Reflectance, Photoluminescence, and Photoluminescence Excitation Spectra of AlN	K. Fukui (Univ. Fukui)
Exciton Decay Processes in AlGaN Alloys	T. Sakai (Univ. Fukui)
Impurity Band Structure of Boron Doped Diamond	T. Inushima (Tokai Univ.)
10:10 - 11:30	
Development of Radiation Watching by Nuclear Emulsion	Y. Taira (Nagoya Univ.)
Optical Response of Heavy Electron Meterials by Infrared Spectroscopy	T. Nanba (Kobe Univ.)
Chemical Evolution Study Using Synchrotron Radiation - Chirality Emergence in Amino-Acid-Films by Circularly Polarized FEL -	J. Takahashi (NTT Microsystem Integration Laboratories)
VUV・SX Spectroscopy of Amino Acid Films	K. Nakagawa (Kobe Univ.)
11:40 - 12:40	
Photoemission Study of Surface-Chemical-Controlled Surface-Passivated Si Nanoparticle	A. Tanaka (Kobe Univ.)
Electronic Structure of Crown Ether Ultrathin Films	K. Okudaira (Chiba Univ.)
Present Status of Angle-Resolved Photoemission End Stations at UVSOR-II	T. Ito (UVSOR)

Poster Session

P1	Characterization of Catalytically Active Mo Species for Methane Dehydroaromatization by Means of Mo L-Edge XANES	H. Aritani (Saitama Inst. Tech., Osaka Prefectute Univ.) et al.
P2	Luminescence and Excitation Spectra of Tl^{+} Centers-Doped Phosphors	Y. Danhara (Osaka Electro-Communication Univ.) et al.
P3	Carrier concentration dependence of thermoelectric properties in layered cobalt oxides $NaCoO_2$	S. Kuno(Nagoya University) et al.
P4	Electronic structure and phase stability of Pd-based bulk metallic glasses	D. Fukamakia (Nagoya Univ.) et al.
P5	Investigation into the origin of unusual behaviors in thermoelectric power of $La_{2-x}Sr_xCuO_4$ by means of angle-resolved photoemission spectroscopy	H. Komoto (Nagoya University) et al.
P6	Photolysis of Isovaline by UV ray and various irradiation	T.Ogawa (Yokohama National Univ.) et al.
P7	Local structure analysis of trace elements in bioceramic materials	Y. Kawashima (Waseda Univ.) et al.
P8	XANES analysis of local environment of Ga ions in $SrTiO_3$:(Pr,Ga)	S. Matsuda (Waseda Univ.) et al.
P9	Theoretical analysis of impurity-induced phonon by first-principles lattice dynamics calculations	H. Murata (Waseda Univ.) et al.
P10	Optical Properties of Transparent Conductive Oxides β-Ga_2O_3	T. Ishikawa (Gifu Univ.) et al.
P11	Optical Properties in VUV to Visible Regions for Fluoride Crystals Doped with Rare Earth Ions	T. Nakamura (Gifu Univ.) et al.
P12	Phosphorescence Property of Rare Earth Ion-doped Hydroxyapatite excited by UVSOR	M. Ohta (Niigata Univ.) et al.
P13	Absolute Photoionization cross section of C_{70} at 25-120 eV	B. P. Kafle (Grad. Univ. Adv. Studies) et al.
P14	Temperature dependence of the optical reflectance spectra of InN	T. Yanagawa (Univ. Fukui) et al.
P15	Crystal anisotropy effect on excitonic luminescence in AlGaN	M. Kishida (Univ. Fukui) et al.
P16	Correlation between Coloration and Optical Properties in Yttrium Oxysulfide Single Crystals	S. Tokunaga (Univ Fukui) et al.
P17	Comparative study of photoluminescence properties between YPO_4:Zr^{4+},Mn^{2+} and $ScPO_4$:Zr^{4+},Mn^{2+} phosphors	Y. Inada (Univ Fukui) et al.
P18	Dependence of photoluminescence properties on Br^{-} ion concentrations- ion concentrations in $PbCl_2$:Br^{-} crystals	S. Izuhara (Univ Fukui) et al.
P19	Measurements of time resolved decay spectra by using ICCD detector at the single bunch operation	F.Suzuki (Univ. Fukui) et al.
P20	The concentration dependency of Eu ions for excitation spectra of $BaMgAl_{10}O1_{7}$:Eu	H. Yoshida (Kwansei Gakuin Univ.) et al.
P21	Nd^{3+}:$(La_{1-x},Ba_x)F_{3-x}$ Grown via Micro-Pulling Down as Vacuum Ultraviolet Scintillator and Potential Laser Material	S. Ono (Nagoya Inst. Tech.) et al.
P22	Ultraviolet Photoemission Spectra of Layered Metal Oxide Thin Film	T. Miyazaki (Ehime Univ.) et al.
P23	Electron structure of halogen bonding studied by UPS	R. Sumii (KEK-PF) et al.
P24	Nano-clusters in Pd-Ni-P Bulk Metallic Glasses Studied by Synchrotron Spectroscopy	T. Mochizuki (Nagoya Univ.) et al.
P25	Electronic Structure of Fe-based Heusler-type Thermoelectric Alloys	T. Mochizuki (Nagoya Univ.) et al.
P26	Photoinduced Phenomena in Amorphous Semiconductor Materials by UVSOR	K. Hayashi (Gifu University)
P27	XANES Spectra of Sulfur amino acids at S K-edge	Y. Izumi (Kobe Univ.) et al.
P28	A study of a molecular orientation of crown ether in thin films by ARUPS	Y. Suzuki (Chiba Univ.) et al.
P29	A study of molecular orientation of Bis-(o-diiminobenzosemiquinonate)Nickel(II) Complex in the films by AR-UPSin the films by AR-UPS	N. Mitsuo (Chiba Univ.) et al.
P30	Photoluminescence Analysis of Lanthanum Aluminate Single Crystals	K. Kanai (Waseda University) et al.
P31	Characterization of Mg-modified titanias synthesized by the glycothermal method	Y. Sazanami (Kyoto Univ.) et al.
P32	Change in the Metal 3d derived molecular electronic state due to Metal-phthalocyanine/Ag(111) interaction	T.Aoki (Chiba Univ.) et al.
P33	Change of electronic structure of para – ferro magnetic phase transition on EuO : Three-dimensional angle-resolved photoemission spectroscopy	H. Miyazaki (Nagoya Univ., UVSOR) et al.
P34	Infrared-Terahertz Spectroscopy of $CeIn_3$ under a pressure	T. Iizuka (Kobe Univ., UVSOR) et al.
P35	Terahertz Spectroscopy of SmS under Pressure	T. Mizuno (Grad. Univ. Adv. Studies, UVSOR) et al.
P36	Soft x-ray magnetic circular dichroism at high magnetic field and low temperature	T. Nakagawa (IMS) et al.
P37	Electronic states of a single crystal of Rubrene studied by Photoelectron Yield Spectroscopy	Y. Nakayama (Chiba Univ.) et al.
P38	Systematic Study of Quantum Criticality in $Ce_{1-x}Gd_xCoSi_3$:Ce and Gd 4d-4f resonant photoemission spectroscopy	H.J. Im (Sungkyunkwan Univ., UVSOR) et al.

UVSOR Lunch Seminar

FY2007

July 23 Prof. Yunsang LEE, Department of Physics, Soongsil University, Korea
Charge-orbital ordered state in half-doped layered manganites

Feb. 8 Mr. Masahiro ITO, Graduate School of Science and Technology, Niigata University and UVSOR
Metastability of carbonyl sulfide (OCS) dications

Feb. 8 Mr. Takuya IIZUKA, Graduate School of Science and Technology, Kobe University and UVSOR
Infrared-to-Terahertz Spectroscopy of $CeIn_3$ under pressure

Mar. 13 Dr. Miho SHIMADA, UVSOR Facility, Institute for Molecular Science
Generation of Coherent Synchrotron Radiation (CSR) produced by an interaction between electron beam and external laser

Mar. 13 Dr. Tatsuo KANEYASU, UVSOR Facility, Institute for Molecular Science
Development of an electron-ion coincidence spectrometer and its application to decay dynamics in molecules following core hole creation

UVSOR Workshop on Terahertz Coherent Synchrotron Radiation

Place: Okazaki Conference Center and UVSOR Facility

September 23th, 2007

15:00- Registration and UVSOR site tour.
18:00- Get together party

September 24th, 2007

8:30- Breakfast
9:15- Opening Remark — M. Katoh (UVSOR)

1. Light Source (1); Linac

9:30- Status of Coherent Radiation Beamline at KURRI-LINAC — T. Takahashi (Kyoto U.)
9:55- Bunch compression at the SPring-8 linac for successive generation of THz pulse train in the isochronous ring — Y. Shoji (New SUBARU)
10:20- Coffee break

2. Light Source (2-1); Storage Ring

10:50- The BESSY (and MLS) Low Alpha Optics and the Generation of Coherent Synchrotron Radiation — G. Wuestefeld (BESSY)
11:15- Coherent THz radiation at NewSUBARU — Y. Shoji (New SUBARU)
11:40- Observation of THz CSR burst in UVSOR-II — M. Shimada (UVSOR)
12:05- Lunch

3. Light Source (2-2); Storage Ring

13:20- Status of the ANKA Short Bunch Operation — A.-S. Mueller (ANKA)
13:45- CSR studies at the ALS and optimizing a storage ring for THz — M.C. Martin (ALS)
14:10- Generation of THz CSR with laser-bunch slicing in UVSOR-II electron storage ring — A. Mochihashi (UVSOR)

4. Light Source (3); ERL

14:35- Applications of Intense CSR from a cw Linac at Jefferson Lab — G. P. Williams (J-lab)
15:00- An Intense Terahertz Radiation Source at the Compact ERL — K. Harada (KEK)
15:25- Coffee break

5. Applications

15:55- Scientific Experiments at BESSY using Coherent Synchrotron Radiation — U. Schade (BESSY)
16:20- Coherent Synchrotron Edge Radiation and Applications at ANKA — Y-L. Mathis (ANKA)
16:45- Coherent THz radiation from photo-injected linac and applications to studies of materials — L. Carr (NSLS)

17:10- Closing remark — S. Kimura (UVSOR)

18:30- Banquet at an Izakaya restaurant (Japanese pub)

September 25th, 2007

9:00- Move to Awaji Island by public transportations.

Status of Coherent Radiation Beamline at KURRI-LINAC

T. Takahashi
Research Reactor Institute, Kyoto University, Japan

In the electron linear accelerator at Research Reactor Institute in Kyoto University (KURRI-LINAC), properties of several types of coherent radiation (synchrotron radiation [1], transition radiation [2], Cherenkov radiation [3], diffraction radiation, and Smith-Purcell radiation [4], pre-bunched FEL [5]) in the THz-wave and millimeter-wave regions have been experimentally investigated since 1991. The beamline for the millimeter-wave spectroscopy has been constructed [6], in which coherent transition radiation (CTR) has been used as a light source and the spectroscopic research of N_2O gas [6] and electron spin resonance using a pulsed magnet [7] have been demonstrated.

The KURRI-LINAC consists of an injector, pre-buncher, two accelerator tubes. The specifications are represented in Table. 1.

Table 1. Specifications of KURRI-LINAC

Operation Mode	Short Pulse	Long Pulse
RF frequency	1300 MHz	
Energy	46 MeV	30 MeV
Pulse Width	2～100 ns	0.1～4 μs
Repetition Rate	1～300 Hz	1～200 Hz
Peak Current	8 A	500 mA
Beam Power	Max. 10 kW	

This linac has been operated for collaboration research programs with other universities since 1964 and research activities have covered the nuclear data with pulsed neutron source, electron irradiation, and coherent radiation. The time of operation in 2006 was about 2,700 hr. The distributed user-time to the research of coherent radiation is about ten weeks per year. The schematic diagram of the beamline is shown in Fig. 1.

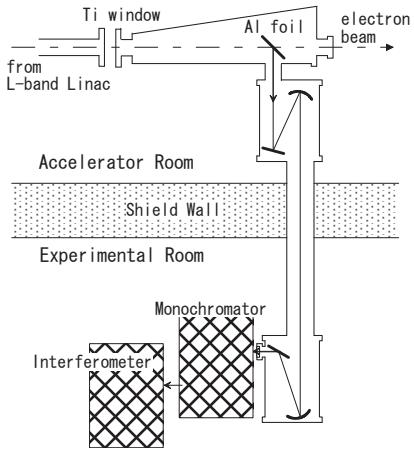

Fig. 1. The schematic diagram of the coherent radiation beamline.

The forward coherent transition radiation emitted from a Ti window and the backward one from an Al-foil are used as a light source. The beamline is equipped with a grating-type monochromator and a Martin-Puplett type interferometer in series. When the interferometer is used as a spectrometer the grating in the monochromator is replaced with a flat mirror. Three types of detectors are prepared, i.e. a liquid-helium-cooled Si bolometer (Infrared Lab.), a hot-electron InSb bolometer (Infrared Lab.), and a millimeter-wave diode-type detector (DXP-10, Millitec) according to the sensitivity and the response time. The degree of instability of the observed intensity is within 2%.

Coherent radiation is especially useful as a pico-second pulsed light source for the time-resolved spectroscopy and the pulseradiolysis study. Since the accelerating frequency of this linac is 1.3 GHz (L-band), the interval between pulses in the CTR pulse train is 770 ps (23 cm). The spectrum from the successive bunches is constituted of the higher harmonics of 1.3 GHz [6]. As a result, the CTR can be treated as a light source with a continuous spectrum only when the spectral resolution is lower than $1/23 = 0.0434$ cm^{-1} and the delay in the time-resolved measurement is restricted within 770 ps. In order to lift these restrictions, the single-bunch beam has been generated by installing a high-speed avalanche-type pulser in the electron injector. The degree of impurity of single bunch was estimated to be 1.5% by means of the cross-correlation interferogram.

The following researches in the millimeter-wave region are in progress at this beamline:

a) Optical conductivity of superionic conductors (collaboration research),
b) Optical properties of water (collaboration research),
c) Optical properties of polymeric materials under irradiation (collaboration research),
d) Development of pulseradiolysis system.

[1] Y. Shibata, *et al.*, Phys. Rev. A **44** (1991) R3449.
[2] Y. Shibata, *et al.*, Phys. Rev. A **45** (1992) R8340.
[3] T. Takahashi, *et al.*, Phys. Rev. E **50** (1994) 4041.
[4] Y. Shibata, *et al.*, Phys. Rev. E **57** (1998) 1061.
[5] Y. Shibata, *et al.*, NIM **528** (2004) 162.
[6] T. Takahshi, *et al.*, Rev. Sci. Instrum. **69** (1998) 3770.
[7] Y. H . Matsuda, *et al.*, Physica B **346-347** (2004) 519-523.

Bunch compression at the SPring-8 linac for successive generation of THz pulse train in the isochronous ring

T. Asaka, H. Dewa, H. Hanaki, Y. Hisaoka*, T. Kobayashi, T. Matsubara*, T. Mitsui*, A. Mizuno, Y. Shoji*, S. Suzuki, T. Taniuchi, H. Tomizawa, and K. Yanagida
SPring-8, JASRI, Sayo-cho, Sayo-gun, 679-5198, Japan
**NewSUBARU, LASTI, University of Hyogo, Kamigori-cho, Ako-gun, 678-1205, Japan*

Abstract

We have already demonstrated our idea of circulating a short and intense bunch in a synchrotron radiation ring. The idea is based on the understanding that it is almost impossible to store short and high-charged electron bunch in a storage ring but it is not difficult to produce that kind of bunch at a linac. When the short bunch is produced at a linac and injected into an ideal isochronous ring, the time structure of the bunch is frozen and it emits short-pulsed radiation for every turn. It would supply a strong coherent radiation pulse train in THz region for beam lines in the storage ring.

In our previous work [1] we compressed the bunch of the SPring-8 linac to a few picoseconds (r.m.s.) by means of an energy compression system and a beam transport line from the linac to NewSUBARU. The bunch charge was about 0.02 nC. The NewSUBARU storage ring was set at quasi-isochronous condition and the bunch circulated for about 50 turns after injection while maintaining the short bunch length. A strong coherent radiation was observed using a Shottkey diode detector, which was sensitive to 0.1 - 0.14 THz radiation. Fig. 1 shows the turn-by-turn radiation power after injection in the storage ring. The radiation power at the initial turn was raised by the bunch compression. This high power radiation lasted longer by setting the ring quasi-isochronous. At the present, the imperfection of the isochronous condition produces the increase of bunch length and the reduction of coherent radiation power.

Our plan for the next few years, which is not yet approved, is to install the photo-cathode electron gun developed at SPring-8. According to the expected beam parameters listed in Table 1, the beam would be shorter and stronger with the smaller energy spread. Consequently it would supply more lasting shorter pulses in the ring. The smaller energy spread is important not only because this parameter is a trade-off of the bunch compression, but also that the small energy spread reduces the bunch elongation due to the higher order momentum compaction factor. Many improvements of the linac since 1998 for stability and reliability were also essential for this research.

Our method is partly very similar to ERL (Energy Recovery Linac). There is no stationary state in the ring or bending arc, therefore its performance as a light source strongly depends on the initial beam. Performance of the electron gun is essential. The quasi-isochronous ring as a circulator can be a model of a bending arc of ERL. Many circulations in the ring would enhance problems, which would occur in ERL arc.

We hope that this new beam handling would bring us new understandings on beam physics. What we would see is a transient process starts from a short pulsed intense beam. We can observe energy spreading by instabilities or CSR in time domain. The turn-by-turn time structure of a bunch will be measured using a streak camera and a beam profile by a fast gated ICCD camera. The diode detector in THz region is a diagnostic on fine time structure in a bunch.

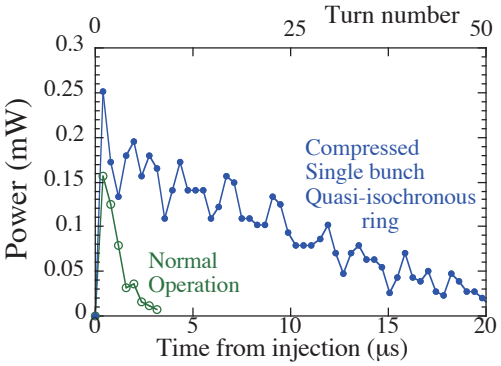

Fig. 1. The turn-by-turn coherent radiation power after injection. The line with open circles shows the power obtained with the parameters of normal operation, where there were three bunches in a pulse. The line with filled circles shows the power obtained from one compressed bunch in the quasi-isochronous ring. The bunch charge was about 0.02 nC/bunch in both cases.

Table 1. Beam parameters at 1.0 GeV with the present thermionic electron gun and the expected parameters with the new photo-cathode electron gun.

	Present	Next
Electron Gun	Thermionic	Photo-Cathode
Energy Spread	(+/-) 0.5%	(+/-) 0.1%
Bunch Length	2.2 ps	< 1 ps
Bunch Charge	< 0.1 nC	> 1 nC

The BESSY (and MLS) Low Alpha Optics and the Generation of Coherent Synchrotron Radiation

J. Feikes, K. Holldack, H.-W. Huebers[1], P. Kuske, G. Wuestefeld
BESSY, and [1]DLR, Berlin (Germany)

The BESSY II optics is tuned to a low alpha optics for bunch shortening. This machine mode is offered 4 times per year for 3 days for users experiments. About 1mm short bunches emit coherent synchrotron radiation in the THz range and short x-ray pulses. Characteristics of the machine optics and measured THz signals are discussed. Limitations to produce ultra short bunches and a possible upgrading scheme for intense, short bunches are discussed.

The presently commissioned Metrology Light Source (MLS) next to the BESSY site includes the option for low alpha operation. Plans for the short bunch generation are presented.

Coherent THz radiation at NewSUBARU

Y. Shoji
NewSUARU, LASTI, University of Hyogo, Kamigori-cho, Ako-gun, 678-1205, Japan

Abstract

NewSUBARU is a 1.5 GeV synchrotron radiation ring at the SPring-8 site. Laboratory of Advanced Science and Technology for Industry (LASTI) at the University of Hyogo is in charge of its operation, collaborating with SPring-8. The beam is injected from the SPring-8 linac with 1.0 GeV of electron energy. Three types of CSR (coherent synchrotron radiation) from three types of electron beam were detected in the storage ring, NewSUBARU.

One was quasi-dc CSR (in other wards, steady state CSR) from a low-current, short-bunched beam, which is used for application experiment at BESSY-II. The ring was operated in a quasi-isochronous mode (with a low momentum compaction factor), in which it a short-bunched beam can be stored stationary. At NewSUBARU a quasi-dc CSR was obtained at low current of 1 pC/bunch and short bunch length of 3.4 ps FWHM. In this state, the longitudinal coherent oscillation amplitude depended on the stored beam current probably because of a burst of CSR by a longitudinal instability. Burst CSR could produce a sudden energy loss and excite a coherent synchrotron oscillation. Fig. 1 shows the FFT power spectrum of the pulsed CSR signal. This quasi-isochronous operation requires delicate tuning and high stability of the storage ring.

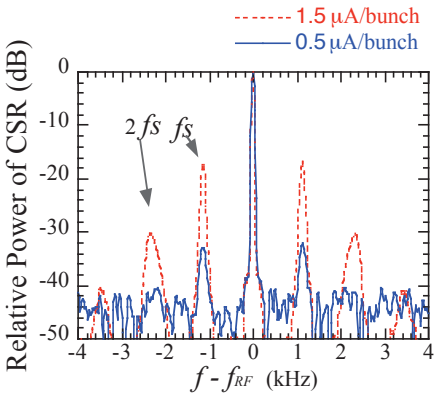

Fig. 1. Beam current dependence of the power spectrum of CSR signal. The main peak (rf frequency f_{RF}) is normalized to 0dB.

The second type was a radiation pulse following injection. A short-bunch linac beam, with a base width of 20 ps and a charge of 50 pC/bunch, emitted short-pulse CSR in the storage ring. It was almost impossible to store short and high-charged electron bunch in a storage ring but the production of short and intense bunch at a linac is not difficult. When the short bunch is injected into an ideal isochronous ring, the time structure of the bunch is frozen and it emits short-pulsed radiation for every turn. It would supply a strong coherent radiation pulse train in THz region for beam lines in the storage ring. This plan will be presented in the other presentation titled "Bunch compression at the SPring-8 linac for successive generation of THz pulse train in the isochronous ring" at the workshop.

The third type was a radiation burst from a high-density, single-bunch beam. Although its radiation power is extremely high and easy to be obtained in any electron storage ring, this type is not used for experiments. This is because the source of the CSR burst is a fine time structure in the bunch due to longitudinal beam instabilities, and is not stable. However, it could be used for some kind of application experiments with an appropriate time averaging. We investigated the time structure of the CSR burst using Schottky diode detector, which had a high time resolution. When we took an averaging period of 10ms (=25250 revolutions), the fluctuation of the integrated power was about 10% (standard deviation). In this time range, the relative fluctuation decreases with the period length faster than the square root scaling law as shown in Fig. 2. It is thought that the CSR burst can be obtained in most storage rings. This type does not require fine and delicate machine tuning as the quasi-isochronous operation does. However for a user operation, two accelerator techniques, an accurate bucket selection in the injection process, and the top-up operation are required. These two techniques are not common at the existing storage rings but coming to be a standard of new rings.

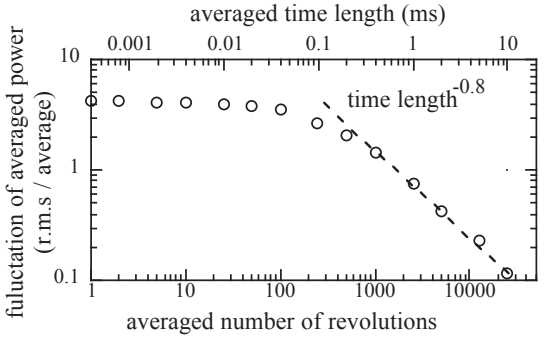

Fig. 2. Fluctuation of time-averaged power of CSR burst. The broken line is a guide which shows the dependence of period$^{-0.8}$.

Observation of THz CSR burst at UVSOR-II

M. Shimada[1], M. Katoh[1,2], M. Hosaka[2], A. Mochihashi[1*], Y. Takashima[2], S. Kimura[1], T. Takahashi[3]

[1]*UVSOR Facility, Institute for Molecular Science, Japan*
[2]*Graduate School of Engineering, Nagoya University, Japan*
[3]*Research Reactor Institute, Kyoto University, Japan*
**Present affiliation : JASRI Spring-8, Japan*

In 2004, we reported the first result from the observation of bursts of Terahertz Coherent Synchrotron Radiation (THz CSR) at UVSOR-II [1]. In this experiment, UVSOR-II electron storage ring was operated in a single-bunch mode with the electron beam energy of 600 MeV. The bursts were observed at the infrared/THz beamline BL6B which has a large solid angle, 215 × 80 mrad^2 [2]. A hot-electron bolometer, which is sensitive from a few cm^{-1} to 50 cm^{-1}, was used as a detector.

Figure 1 shows the average intensity of the terahertz radiation measured by using a mechanical chopper and a lock-in-amplifier, in the single bunch mode (black circles) and in the multi-bunch mode (gray circles) against the average beam current. Large fluctuations can be seen in two beam current regions around 80 mA and above 130 mA. In these regions, very intense bursts were observed. They appeared quasi-periodically at the lower current while chaotically at the extremely higher current. The time structure of each burst sometimes showed periodicity which was approximately same as twice of synchrotron frequency..

After the upgrade of RF cavity at 2005 [3], a correlation between the bursts and a vertical beam instability was discovered. The threshold beam current came to be lower down to around 40 mA. The quisi-periodic structure in each burst cannot be seen.

At 2006, a schottky THz diode detector was introduced for measurement with high time resolution of around 100 ps. We have successful in observing the THz CSR at each revolution of the electron bunch (5.6 MHz). The bursts seems to contain rapid temporal structure which could not resolved with the bolometer.

We have constructed a laser bunch slicing system by introducing a Titanium Sapphire (Ti:Sa) femto-second laser [4]. The minimum duration of Ti:Sa laser is 130 fs and the maximum power per pulse is 2 mJ. We could observe both bursting THz CSR and CSR produced by the bunch slicing simultaneously in some beam current region. So far, we have not observed that the slicing induced the bursts.

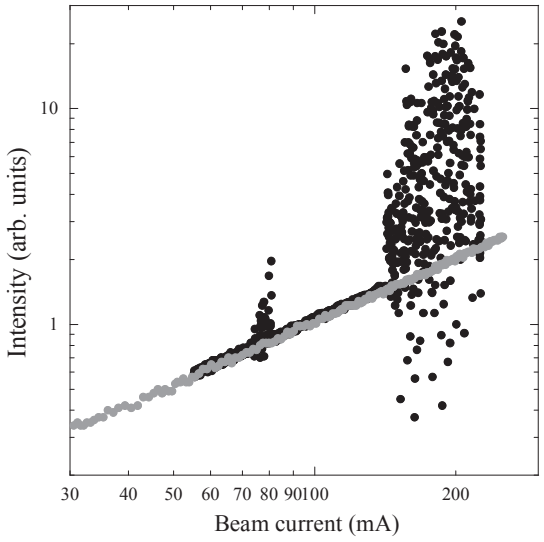

Fig. 1. Average intensity of the terahertz radiation in the single bunch mode (black circles) and in the multi-bunch mode (gray circles) as a function of the average beam current, measured by using a mechanical chopper and a lock-in-amplifier.

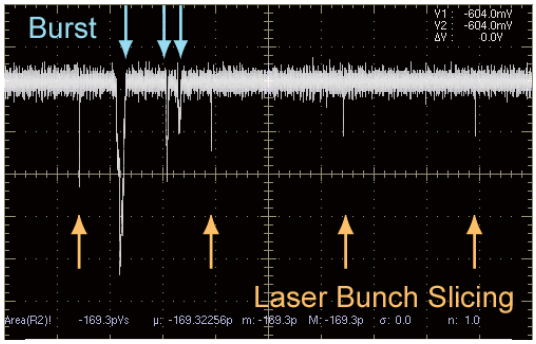

Fig. 2. THz CSR produced by the laser bunch slicing with the CSR bursts.

Reference

[1] Y. Takashima, *et. al.*, *Jpn. J. Appl. Phys.*, **44,** (2005) L1131
[2] S. Kimura, *et. al.*, *Infrared Phys. Tech.*, **49,** (2006) L 147
[3] A. Mochihashi *et. al.*, Proc. EPAC2006 (2006, Edinburgh), 1268-1270
[4] M. Shimada *et al.*, accepted for publication by Jpn. J. Appl. Phys.

STATUS OF THE ANKA SHORT BUNCH OPERATION

A.-S. Müller, I. Birkel, E. Huttel, S. Casalbuoni, B. Gasharova,
Y.-L. Mathis, D.A. Moss, P. Wesolowski
Karlsruhe Research Center, Germany

The ANKA electron storage ring located at the Research Centre Karlsruhe in Germany operates in the energy range from 0.5 to 2.5 GeV. To generate coherent radiation in the far IR (THz) region, a dedicated operation mode with reduced momentum compaction factor is used. The beam behaviour with short bunches has been studied under various conditions and at different beam energies (see Fig. 1). This presentation gives an overview over the status and perspectives of the operation of the ANKA storage ring with short bunches.

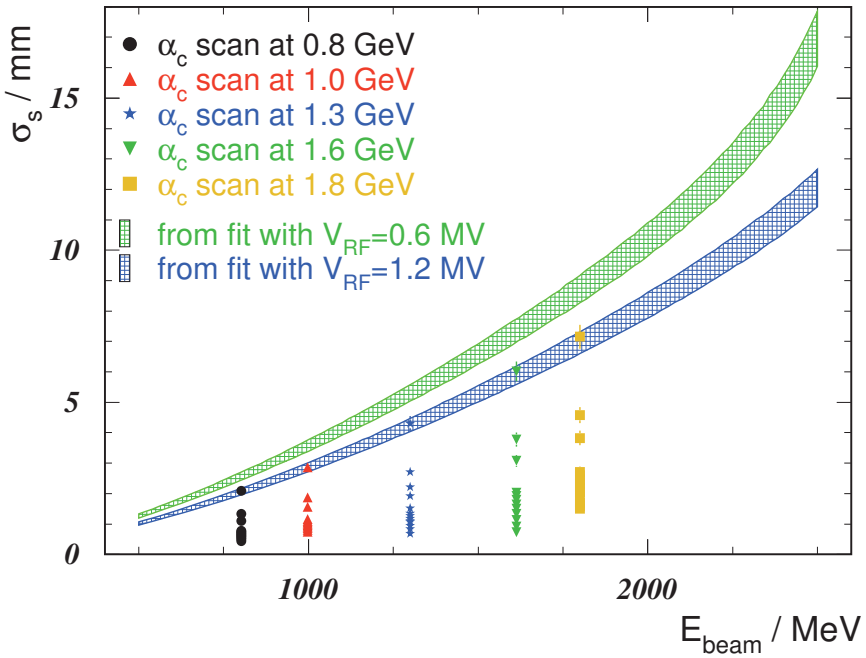

Figure 1: RMS Bunch length derived from measurements of the synchrotron frequency as a function of beam energy. The hatched regions are error bands obtained by a full error Monte Carlo. The markers represent bunch lengths derived from synchrotron frequency measurements for different beam energies.

Generation of THz CSR with laser-bunch slicing in UVSOR-II electron storage ring

A. Mochihashi[1]*, M. Shimada[1], M. Katoh[1], S. Kimura[1], M. Hosaka[2], Y. Takashima[2], T. Hara[3], T. Takahashi[4], S. Bielawski[5], C. Szwaj[5] and C. Evain[5]

[1] *UVSOR Facility, Institute for Molecular Science, Japan*

[2] *Graduate School of Engineering, Nagoya University, Japan*

[3] *RIKEN/SPring-8, Japan*

[4] *Research Reactor Institute, Kyoto University, Japan*

[5] *Universite des Science et Technologies de Lille, France*

* *Prsent affilation : JASRI/SPring-8, Japan*

abstract

We have performed experiments for generation of THz CSR with laser-bunch slicing in UVSOR-II electron storage ring. A mode-locked Ti:Sa laser system generates femto-second high power laser pulse and injects the pulses into an undulator section of the UVSOR-II electron storage ring. The laser pulse induces energy modulation on an electron bunch in the undulator section and the energy modulation changes to longitudinal density modulation on the bunch by passing through a bending magnet section which is beyond the undulator section. The THz radiation generates at the bending magnet section where infra-red beam line (BL6B) is settled. Quadratic dependence of the intensity of the intense THz radiation on the peak bunch current indicates the coherent synchrotron radiation (CSR). Spectral measurement with an interferometer settled in the beam line shows dependence of the bandwidth and spectral range on the laser pulse duration; that indicates possibility to control the frequency and bandwidth of the THz CSR. To control both the frequency and the bandwidth of the THz CSR, we have performed a bunch-slicing experiment with amplitude-modulated laser pulse. The amplitude-modulated pulse laser is generated by 'chirped pulse beating' method[1]. The THz CSR spectral bandwidth by the modulated laser pulse becomes narrower than that by single laser pulse. Because the spectral peak frequency and the bandwidth depend on the modulation of the laser pulse, it is possible to tune the THz CSR frequency and bandwidth only by adjusting the optics for the laser modulation. Introduction of the laser-bunch slicing system in UVSOR-II, experimental results of the bunch-slicing with single and amplitude-modulated laser pulses are presented in the workshop.

[1] Weling, A.S. & Auston, D. H., J. Opt. Soc. Am. B **13**, 2783-2791 (1996)

Applications of Intense CSR from a cw Linac at Jefferson Lab

Gwyn P. Williams, Mike Klopf & The Jefferson Lab Team
Jefferson Lab
Newport News, Virginia 23606

At Jefferson Lab we operate a superconducting linac with continuous-wave radio-frequency excitation to produce 135 pC sub-ps bunches of electrons at repetition rates

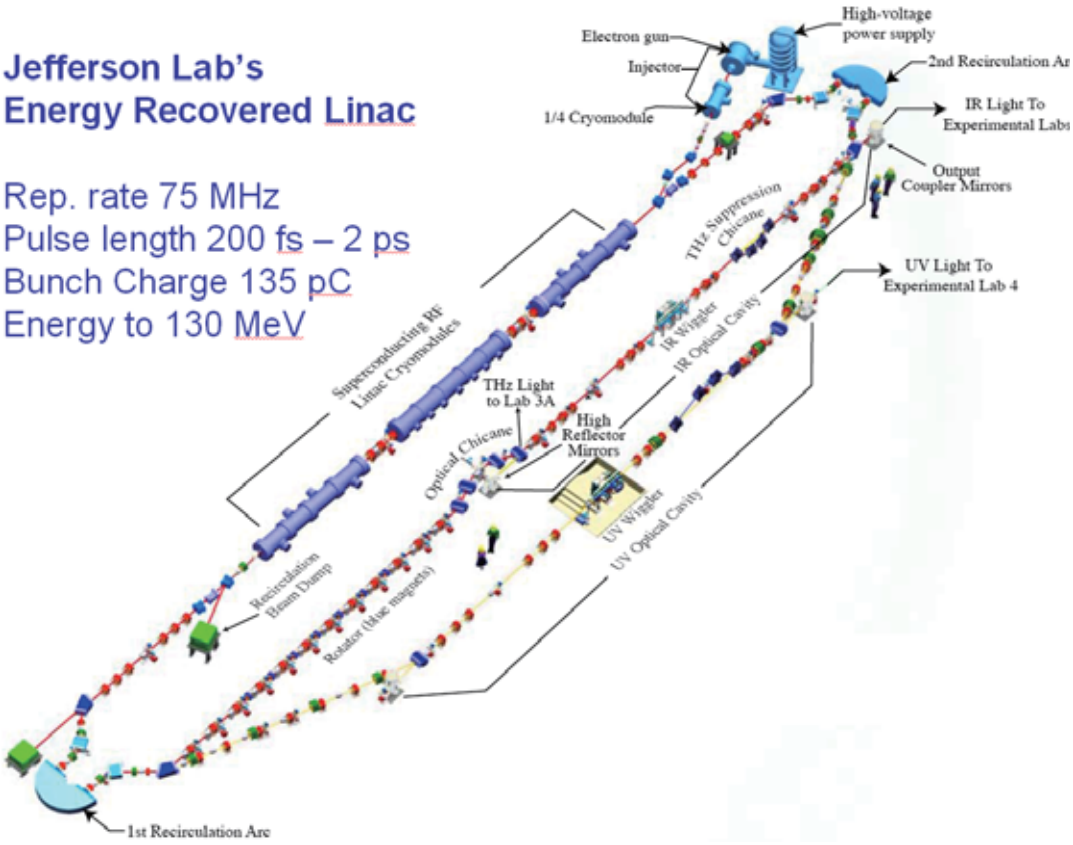

up to 75 MHz. CSR, or multiparticle coherently enhanced emission is produced by modulating this bunch in a Free Electron Laser cavity, and is also produced for wavelengths that are longer than twice the bunch length. With electron beam energies of 100 MeV, the electron beam energy is 1 MW. Therefore we energy recover the electrons in a return loop.

We will describe the operation of the facility, and then applications of this intense beam. The applications fall into 2 categories, real-time imaging, and out-of-equilibrium dynamics.

G.R. Neil et al "The JLab High Power ERL Light Source", Nucl. Instr. & Methods **A557** 9 (2006).

J.M. Klopf, et al., Nucl. Instr. and Meth. A (2007), doi:10.1016/j.nima.2007.08.081.

This work supported by the Office of Naval Research, the Joint Technology Office, the Commonwealth of Virginia, the Air Force Research Laboratory, The US Army Night Vision Lab, and by DOE under contract DE-AC05-060R23177.

An Intense Terahertz Radiation Source at the Compact ERL

Kentaro Harada, *Photon Factory, High Energy Accelerator Research Organization (KEK), Oho, Tsukuba, Ibaraki 305-0801, Japan*
Miho Shimada, *UVSOR, Institute for Molecular Science, National Institutes of Natural Sciences, Myodaiji-cho, Okazaki, Aichi 444-8585, Japan*
Ryoichi Hajima, *ERL Development Group , Japan Atomic Energy Agency (JAEA), Tokai, Naka, Ibaraki 319-1195, Japan*

The Compact ERL is the energy recovery linac (ERL) test facility that will be constructed at KEK Tsukuba campus as a joint project of the KEK, JAEA, and other institutes. The Compact ERL has a great feasibility of producing intense terahertz radiation using coherent synchrotron radiation (CSR) from its electron beams. Although the primary purpose of the facility is the demonstration of the key technologies that are essential to build ultra-brilliant new synchrotron light source based on the ERL, the limited user operation with the terahertz CSR is now examined. In this presentation, we show the parameters of the Compact ERL and discuss expected performances of the terahertz radiation.

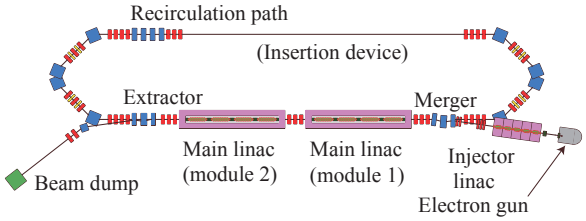

Fig. 1. Lattice of the Compact ERL.

Table 1 Tentative parameters of the test facility

	Parameters (final goal)
Injection energy	5 MeV (10-15 MeV)
Injector beam power	500 kW (1 MW)
Beam energy in the recirculation path	~60 MeV (160-200 MeV)
SC cavities for main linac	9 cells x 4: single module (two modules)
Normalized emittance	1 mm·mrad (0.1 mm·mrad)
Beam current	10 mA (100 mA)
RMS bunch length	Usual mode : σ_τ = 1-2 ps (Short bunch : σ_τ = 0.1 ps)

Figure 1 shows the plan of the Compact ERL and Table 1 lists the tentative parameters. In order to generate the CSR of the wavelength λ_{CSR} , the electron bunch length should be shorter than

$$\sigma_z = \frac{\lambda_{CSR}}{2}.$$

For example, the electron bunch with the bunch length of 0.2 ps (60μm) can generate the CSR of the energy 10 meV (120 μm). In order to achieve such short bunch length, however, the bunch compression is inevitable.

For the bunch compression [1],[2], the off-crest acceleration at the main acceleration module firstly generates the energy gradient in the electron bunch. Then the difference of the orbit length depending on the particle energy at the arc section can compress the bunch length. The linear path length difference of the arc, R_{56}, can be optimized by the quadrupoles and the second order effect, T_{566}, by the sextupoles. Furthermore, in order to suppress the emittance growth by the CSR, Twiss parameter α at the end of the arc section is fixed. Finally, the simulation results show that, if the bunch charge is smaller than about 0.5nC, the bunch length can be compressed to about 0.2ps at the 65MeV beam energy [3]. The estimated photon flux from the bending magnet at the arc of the ERL test facility is shown in Fig. 2.

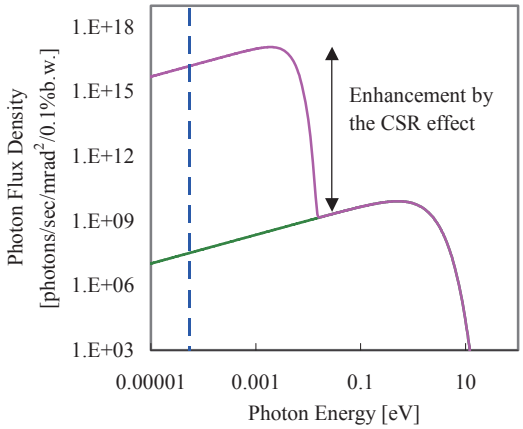

Fig. 2. Radiation spectrum from the bending magnet of the arc section of the Compact ERL. The beam current is 100 mA (= 77 pC x 1.3 GHz), the bunch length 0.2ps, and the beam energy 65MeV.

[1] M. Shimada, K. Yokoya, T. Suwada and A. Enomoto, "Lattice and beam optics design for suppression of CSR-induced emittance gowth at the KEK-ERL test facility", NIM A 575, (2007) 315
[2] R. Hajima, "Emittance commpensation in a return arc of an energy recovery linac", NIM A 528, (2004) 335
[3] M. Shimada, K. Harada, R. Hajima, "Bunch compression and the emittance growth dur to CSR", Proc. of ERL 2007

Scientific Experiments at BESSY using Coherent Synchrotron Radiation

U. Schade

Berliner Elektronenspeicherring-Gesellschaft für Synchrotronstrahlung m.b.H. (BESSY)

Albert-Einstein-Strasse 15

12489 Berlin, Germany

ulrich.schade@bessy.de

Coherent synchrotron radiation (CSR) from a storage ring is a new spectroscopic source between microwaves and thermal black body radiation offering broadband radiation in the THz range. During the past few years, this new technique to generate powerful, stable, coherent sub-THz and THz radiation from the electron storage ring has been established at the electron storage ring in Berlin (BESSY). The spectral range between 3 and 30 wavenumbers (0.1 – 1 THz) which can be only poorly accessed by conventional sources is now covered by operating BESSY in special machine modes. Here, up to 10^8 more brilliance than from a black body source has been achieved. The production of stable, high power, coherent synchrotron radiation at THz and sub-THz frequencies at BESSY opens a new region in the electromagnetic spectrum offered at synchrotron radiation sources which now can be applied for imaging, spectroscopic and microscopic methods in solid state physics, material sciences and life sciences. The feasibility of using the coherent synchrotron radiation in scientific applications has been proven at the infrared beamline IRIS. Beside the characterization of the coherent synchrotron radiation source this talk will present a couple of applications spanning from spectroscopic investigations of new superconducting materials to scanning near-field microspectroscopy.